Soviet Physics
CRYSTALLOGRAPHY

Vol. 1, No. 6, pp. 485-599

November-December, 1956

LETTER TO THE EDITORS

ANSHELES'S COMMENTS* ON "A TRADITIONAL ERROR AND THE MANY WAYS IN WHICH IT APPEARS"†

A. V. Shubnikov

Soviet Physics
CRYSTALLOGRAPHY
Institute of Crystallography, Academy of Sciences of the USSR
Translated from Kristallografiya, Vol. 1, No. 5, pp. 611-612, September-October, 1956
Original article submitted November 21, 1956

In my paper on the above title I assert that a crystal occurs in a variety of forms in accordance with crystallography. It is essentially by this considerable development of the asymmetric figure as point by the most symmetrical figure, i.e., a sphere or a point by implies that one gives the symmetry of a sphere.

Ansheles criticizes not my entirely clear formulation, but some idea entirely my own, which is concerned not with the regular part of an asymmetric figure by a symmetrical point, but with the replacement of a symmetrical figure by some unspecified point. "In using analogy to compare

by the other. In which no species of whole crystals or the ph shown in my illustrations, whereas the latter do not show any crystals. Ansheles's comments, and those by the editors of the journal, are irrelevant to my paper, as they require an explanation from me. It remains only to note that such comments could appear in a journal published by the Academy, whereas the objections to them were not published.

COLOR SYMMETRY GROUPS

N. V. Belov and T. N. Tarkhova

Institute of Crystallography, Academy of Sciences of the USSR
Gor'kii State University
Translated from Kristallografiya, Vol. 1, No. 6,
pp. 619-620, November-December, 1956
Original article submitted September 11, 1956

The task has been completed of compiling colored plane mosaics corresponding to all 15 symmetry groups, using elementary "tiles" with straight-line outlines only.

In our basic article on this question [1], we used as an illustration of the group $P4_1$ two four-color mosaics (I, II) which were formally correct, but not very successful. With the crystallographically equivalent two sorts of 4_1 axis present (as required by group theory), we found that at the point of emergence at one-half of each of these axes, eight elementary triangular "tiles" converged, while for the other half there were only four. This was a natural result of choosing an elementary figure containing only one right angle. A shape with two right angles is desirable. To achieve this we could use either a quadrilateral of the most general type (Fig. 1a on the attached color table), or a rectangle (Fig. 1b on the same table).

In the same article, we took an erroneous path from the two tetragonal mosaics with the centered group $I4_1md = F4_1dm$ to the corresponding orthorhombic mosaics with the group Fdd; elongation and contraction of the cell must take place along d, the diamond planes, i.e., along the diagonal of the square shown in Fig. V, so that we then obtain Fig. VII and Fig. VIII in the form in which they are shown in the color table in the present article.

Although mosaic IV is made up of strictly square tiles, the screw and colored 4_1 and 4_3 axes on it nonetheless only lie at the meeting places of four tiles, because (see Fig. 1) through the center of each tile there passes only an ordinary, two-fold rotation axis. Here, using the same square outline and with the same conditions imposed (4_1 and 4_3 axes at intersections and two-fold rotation axes at the centers of the tiles), we can obtain another kind of elementary figure by losing part of the area of each component square tile in the direction of one mirror plane and gaining the same area from two adjacent square tiles along the perpendicular mirror plane. The resulting mosaic (Fig. IVa in the color table) has an elementary figure showing the re-entrant angles which are very common in Moresque decorative work [2]. This corresponds to the group $I4_1md = F4_1dm$, and an orthorhombic version is also possible, with symmetry Fdd (Fig. VIIa on the color table).

If each of the one-color squares in mosaic IV is left, in accordance with symmetry mm2, with only two triangles colored out of the four formed in each square by its two diagonals, then the empty triangles (see Fig. 2) can be arranged in a different fashion, but with retention of the same mosaic symmetry of $I4_1md = F4_1dm$.

These can be colored in the same color as the triangles of adjacent squares, which gives mosaic V, again with square tiles, but with the areas of these only half those of the original tiles, and with their edges lying at 45° to the edges of the original square tiles. The centers of these smaller tiles do

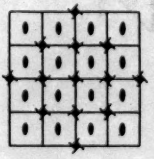

Fig. 1

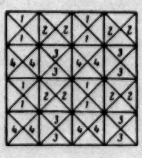

Fig. 2

not contain the two-fold axes, which now emerge at the intersections of four tiles, where they alternate with 4_1 and 4_3 axes (Fig. V).

In the second version the empty triangles, which are equal in number to the retained colored triangles, are colored in four new colors so that the latter are related by exactly the same symmetry $I4_1md = F4_1dm$, but remain completely independent of the basic triangles, and in particular are not related to the latter through any normal or colored symmetry relationships. The possibility of simultaneous existence in a lattice of given symmetry of two analogous, interpenetrating, but independent mosaics, each with a symmetry equal to that of the whole, has already been pointed out more than once [3].

In Fig. IVb the four main colors are the same as in the original Fig. IV, while the four additional colors will be white, orange, gray, and lilac.

The drawbacks noted for the tetragonal mosaics also apply to some of the mosaics given in [1] to illustrate hexagonal colored groups. In order for a mosaic of symmetry $P3_1$ not to have six tiles converging on each three-fold axis, as occurred in the formally correct Fig. X of [1], the corresponding elementary tile must be an n-sided polygon with three angles of 120° (cf. the tetragonal symmetry case), and this is only possible when n is not less than 5. Two mosaics made up of pentagonal tiles, both of symmetry $P3_1$, are shown in Figs. Xa and Xb, and we see that only three tiles converge at the points of emergence of the three kinds of three-fold axes.

In Fig. XI, which should illustrate group R3, curved edges were wrongly given to the hexagonal colored tiles, and the mosaic took on the higher symmetry of R3m. In Fig. XIa, the correctly assigned curved tile edges destroy the plane of symmetry, and the colored group will, in fact, be only R3. This group can also be illustrated without curved edges, if we return to the pattern of mosaic XIII in [1], but use here only three colors instead of six. Two versions of such a mosaic are shown in Fig. XIb and XIc. A mosaic like XIc but in six colors would be another illustration of group R3c.

The same arrangement as that in mosaic XIII can be used to illustrate the group $P6_1$, if the tile outlines do not contain curved lines and if it is not necessary for six tiles to converge at the points of emergence of both the six-fold axis and of the two kinds of three-fold axes, as was the case in mosaic XIV. The corresponding two mosaics are shown in Figs. XIVa and XIVb.

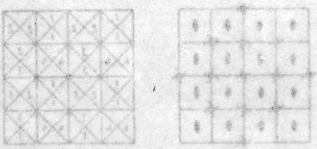

LITERATURE CITED

1. N.V. Belov and T.N. Tarkhova, "Colored symmetry groups," Kristallografiya, 1, 1, 4-13 (1956).
2. N.V. Belov, "Medieval Moresque ornamental work," Kristallografiya, 1, 5, 609-610 (1956).
3. N.V. Belov, "Space groups of cubic symmetry," Tr. Inst. Kristallogr., 9, 21-34 (1954).

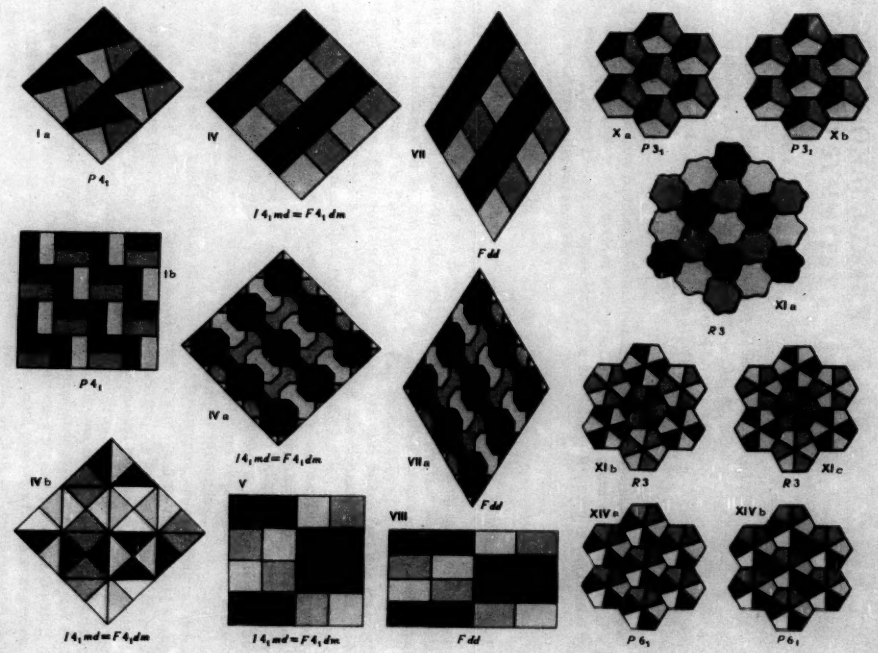
Ia
P4₁
IV
I4₁md=F4₁dm
VII
Fdd
Xa
P3₁
Xb
P3₁
XIa
R3
Ib
P4₁
IVa
I4₁md=F4₁dm
VIIa
Fdd
XIb
R3
XIc
R3
IVb
I4₁md=F4₁dm
V
I4₁md=F4₁dm
VIII
Fdd
XIVa
P6₁
XIVb
P6₁

SOVIET PHYSICS - CRYSTALLOGRAPHY VOL. 1, NO. 6 NOV.-DEC., 1956

THREE-DIMENSIONAL MOSAICS WITH COLORED SYMMETRY

N. V. Belov

Institute of Crystallography, Academy of Sciences of the USSR

Translated from Kristallografiya, Vol. 1, No. 6,
pp. 621-625, November-December, 1956
Original article submitted November 11, 1956

A method has been devised for constructing simple three-dimensional mosaics. The simplest solutions are obtained when starting from the plane colored mosaics corresponding to the 15 colored symmetry groups. A Klein V-group is illustrated by a colored crystallographic group.

When working with two colors, three-dimensional mosaics are derived most simply from the plane mosaics corresponding to the 46 two-color groups [1] by adding layers of identical plane mosaics (of a certain thickness) in the third direction, but with the colors rearranged so that a unit "tile" of one color lies above a tile of the other color. This operation is repeated for each new layer. In other words, we introduce a vertical colored translation. The corresponding two-color lattices were listed in [2].

Colored translations may, however, also be inclined to the vertical (the layer direction), and this occurs in several simple mosaics derived from Fedorov systems of parallelohedra.

If we use the usual set of nine heptaparallelohedra (Fedorov cubo-octahedra with 14 faces) to depict a body-centered lattice (i.e., its unit cell), and we make the middle cubo-octahedron a different color, we will obtain a very simple three-dimensional mosaic with a two-color cubic Bravais lattice (one of the 50 such lattices, see [2]), with the oblique colored translation $P_I m3m$. The unit cell of this lattice will contain one cubo-octahedron of each of the two colors.

If we start from the simplest system of triparallelohedra, namely, close-packed normal cubes, and color alternate cubes along each of the coordinate directions in two different colors, then we obtain a three-dimensional chessboard pattern, which is often used to describe the structure of fluorite (CaF_2) by saying that occupied cubes alternate with empty ones (Fig. 1); here, however, we will prefer to speak of the alternation of cubes of two different colors (but identical in all other respects). The corresponding Bravais lattice will be cubic face-centered, with all edges color-centered according to $F_S m3m$ (cf. [2]).

It is easy to see that this packing is a special case of the mosaics mentioned at the beginning of this article, i.e., it can be broken up into layers of identical plane mosaics with the two colors in each plane mosaic interchanged on passing from one layer to the next. In this particular three-dimensional mosaic, however, this operation of breaking up into layers is possible along three mutually perpendicular directions.

By applying uniform Fedorov deformations to the original (and thus two-color) systems of parallelohedra, we arrive at the corresponding three-dimensional mosaics of lower symmetry.

Starting from the system of hexaparallelohedra used for the cubic face-centered lattice (rhombic dodecahedra), we immediately find that we cannot apply the simplest technique to obtain a three-dimensional mosaic with the same cubic symmetry, because the unit cell contains four rhombic dodecahedra. If these are colored in levels along a four-fold axis, the symmetry is lowered to tetragonal. There is then no reason to have a base-centered lattice, and we go over to a primitive tetragonal lattice with $P_I 4/mmm$ color body-centering and with one rhombic dodecahedron of each color in the unit cell.

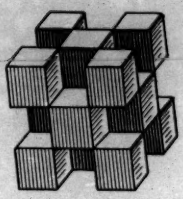

Fig. 1

If the rhombic dodecahedra are colored in levels along a three-fold axis, this leads to the rhombohedral symmetry $R\bar{3}m$ (cf. [2]), with two rhombic dodecahedra of different colors in the primitive rhombohedral unit cell.

The packing of rhombic dodecahedra does, however, retain cubic symmetry if all four of the dodecahedra in the unit cell are given different colors. This first representative of a multi-color (here, four-color) three-dimensional Bravais lattice mosaic will be primitive cubic, with inclined colored translations which center the different faces of the unit cell: this can be conventionally written (cf. [2]) in the form $P_{A'B'C'}$.

Using ordinary descriptive terms, this three-dimensional mosaic with rhombic dodecahedra of four colors can be described as a set of four "interpenetrating" primitive lattices, all geometrically identical, but of different colors. All the rhombic dodecahedra in each of the four lattices are related by a system of translations of the primitive cubic lattice, translations which are noncolored or, more precisely, which do not change the colors of the rhombic dodecahedra. This set of translations will be denoted by T = 1. Any lattice will be related to the other three through three-color diagonal translations (along faces) of the primitive cube, denoted by T'_A, T'_B, and T'_C (or, more exactly, by the set of these), i.e., these translations not only displace the rhombic dodecahedra by half a face-diagonal, but they simultaneously alter their color.

In three-dimensional colored mosaics it is not possible to compare the coloring with a level which is higher by a certain fraction of the full repeat distance [1], and the relationships between colors have a general character. In our case, the compatibility of these relationships is easily established by examining Figs. 2a and 2b, which depict the unit cell of our mosaic. If the transition from the zero (black) lattice to the first (yellow) lattice occurs by means of the translation T'_A, that to second (blue) lattice by the translation T'_B, and that to the third (red) lattice by the translation T'_C, then it is not difficult to see that the transition 1 – 0 (yellow to black) can be described by the translation T'_A, the transition 1 – 2 (yellow to blue) by the translation T'_C, and the transition 1 – 3 (yellow to red) by the translation T'_B.

If we consider all points (of the rhombic dodecahedron) in the same system (i.e., of the same color) to be equivalent, we find that

$$T'^3_A = T'^3_B = T'^3_C = T = 1,$$

$$T'^{-1}_A = T'_A \text{ etc.}, \quad T'_A \cdot T'_B = T'_C, \quad T'_B \cdot T'_C = T'_A, \quad T'_C \cdot T'_A = T'_B.$$

From this it follows that $T'_A \cdot T'_B \cdot T'_C = 1$, whatever the order of the factors.

These relationships join together the four translations T, T'_A, T'_B, and T'_C (or, rather, their combinations) into a mathematical group; the basic property, according to which the product of two colored translations is equal to a third, shows that in this combination of translations $P_{A'B'C'}$,[1] we have another example of a mathematical V-group (Klein group [3], or fourth-order equation group), for which only three representatives were previously known in crystallography [4], namely, the point groups $V = D_2 = 222$, $C_{2v} = mm2$, and $C_{2h} = 2/m$.[2]

	$V = D_2$	C_{2v}	C_{2h}	$P_{A'B'C'}$	
a_0	1	1	1	T	$a_1^2 = a_2^2 = a_3^2 = a_0$
a_1	2_x	m_x	m	T'_A	$a_1 = a_2 a_3$; $a_2 = a_3 a_1$; $a_3 = a_1 a_2$
a_2	2_y	m_y	$\bar{1} = \frac{2}{m}$	T'_B	$a_1 a_2 a_3 = a_0$
a_3	2_z	2_z	2	T'_C	

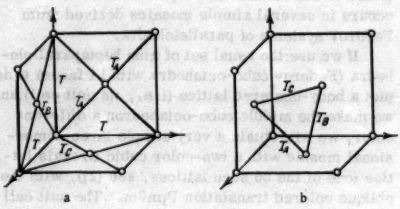

Fig. 2

[1] As in [2], the primes mean that the corresponding translations, or symmetry elements in general, are colored.

[2] This is formally not quite true, because the Klein V-groups also include the corresponding black–white groups [2]: 2'2'2, m'm'2, mm'2', 2'/m, 2/m', 2'/m'. However, the properties of these groups are extremely close to those of the noncolored crystallographic groups, and so we will only mention them here.

It will be obvious that the groups of translations $P_{A'B'C'}$ will also be retained as such after uniform deformation of the system of hexaparallelohedra or rhombic dodecahedra. A more important point is that the system formally loses its cubic symmetry even earlier, as a result of the imposition of the four colors. Although the colored figure in the center of face A can be superimposed in turn on the centers of faces B and C, and then on itself, where it regains its color, this is brought about through the sequence of different operations $T'_A \cdot T'_B \cdot T'_C = 1$, and not by repeating the same operation three times, e.g., a left-handed (or right-handed) rotation about a three-fold axis. These latter axes are absent from the system of colored rhombic dodecahedra, and it is these four three-fold axes which would determine that a system of figures belonged to the cubic system. It is easy to see that the spatial symmetry retained by our packing will only be the orthorhombic $P_{A'B'C'}mmm$ with the three unit-cell constants the same only "by chance." With a rhombically deformed cell the three-fold axis will evidently not be present, but the face centers will translate one into the other as before through the colored translations, so that a fourth translation will bring a face center back to its original position.

We will arrive at a particularly simple pseudocubic system of figures, with the same symmetry of $P_{A'B'C'}mmm$, if we start off from the fluorite structure examined above when it is represented in the form of Pauling cubes (Fig.1), and apply three new colors to the "occupied" cubes at the centers of all the faces of the unit cube. In actual fact this will be the same mosaic as that which we have just examined, because a rhombic dodecahedron is the same as a cube with a pyramid added on each face, where the pyramid is obtained by cutting the cube in six along its diagonal symmetry planes (Fig.3). If then these pyramidal attachments are taken off, it is easy to see that spaces will be left between the cubes which will also be cubes of identical size, and, as we have repeatedly emphasized, the symmetry of this identical system of empty cubes will be the same as the symmetry of the system of occupied cubes, and also the same as that of the combination of both cube systems.

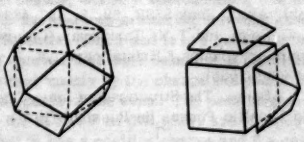

Fig. 3

In the symmetry groups of those mosaics which we constructed from parallelohedron systems, the basic colored operation was a second-order translation. In order to obtain groups with colored operations of third and higher order, it would be simplest to revert to the 15 multicolored plane groups, and their corresponding mosaics, which were given in [1,5]. If we consider the latter to actually be plane mosaics of a certain thickness and possessing colored elements, in particular colored symmetry axes, we can extend these upward by adding layers of similar mosaics but with the colors altered by a colored translation, in the same order as that which the colors follow around the colored axes (or along glide planes, particularly the d-planes). Thus, if we use the four tiles in mosaics I, II, Ia, and Ib (from the color tables in [1,5]), which appear in the order yellow (y), green (g), red (r), and blue (b) around the four-fold colored axis, we will add on four tiles with the color order g-r-b-y, and then the four r-b-y-g and b-y-g-r, finishing up with the original order of y-g-r-b. The colored vertical translations are fourth order. Operated once, they raise a color by 90°, twice by 180°, then by 270°, and so on: $y.T_{IV} = g$, $y.T_{IV}^2 = r$, $y.T_{IV}^3 = y.T_{IV}^{-1} = b$, $y.T_{IV}^4 = y$, $g.T_{IV} = r$, etc.

If we obtain a plane mosaic by starting with a 4_1 axis and noting the change in color with each raise along this axis, we then find that our mosaic has a 4_{col} axis, and because of the layering of the tiles through the action of the colored translations we restore the ordinary one-color 4_1 axis, which is fixed on the four tile levels by the four differently colored spirals (Fig.4).

The symmetry group of the colored mosaic formed may be denoted by either $P_{c'}/4_{col}$ or $P_{c'}/4_1$. In the first notation the derived symmetry element will be $4_1 = 4_{col} \cdot c'/4$. We also have it that $4_1^2 = 2_1 = 4_{col} \cdot c'/2$. With the second notation the derived symmetry elements will be

$$4_{col} = 4_1 \cdot (c'/4)^{-1}, \quad 4_{col}^2 = 2_{col} = 2_1 \cdot (c'/4)^2.$$

Similarly, from the mosaics belonging to other colored symmetry groups depicted in [1], we must be able to find in these the multicolored symmetry elements 6_{col}, $6_{col}^2 = 3_{col} \cdot 2$, 3_{col}, d_{col} and the plane three-color lattice H_{col} which correspond to the lattice R. By piling up layers of identical mosaics, using colored translations of the same order as that of the major symmetry element of the plane mosaic, we "reconstruct" the one-color symmetry

Fig. 4

elements 6_1, 6_2, 3_1, d, and R from which we started off in [1] to derive the colored plane symmetry groups, and which now will be realized in the form of the corresponding packings of each color.

We note that the three-dimensional mosaic $R_c\,'/_3 3m$, derived from the plane mosaic R3m (XII in [1]), gives the spatial pattern of ilmenite, $FeTiO_3$, if we take it that the empty octahedron in this structure plays the same crystallographic role as the octahedra with Fe and Ti [6].

Although the mosaic XIII has the symmetry group R3c, and six colors, the R(H) lattice in the plane pattern corresponds to a sequence of only three colors, and the corresponding vertical translation will break down into three colored translations 120° apart, i.e., along the vertical we will have either black (bk)–red (r)–blue (b) or white (w) –yellow (y)–green (g) alternating, in accordance with our accepted cyclic color sequence w–b–y–bk–g–r–w (Fig. 5).

We can form more three-dimensional mosaics by making the colored translation 180° instead of 90° for a four-fold colored axis, and by having translations of 120° and 180° as well as 60° with a six-fold axis. The resulting (one-color) groups will respectively replace $P4_1(4_3)$ by the monoclinic $P2_1/m$, and $P6_1(6_5)$ by $P2_1/m$ again (180°) and $P3_1$ (120°). Higher symmetry will only occur with four-fold and six-fold colored axes.

We cannot use the above principle to obtain

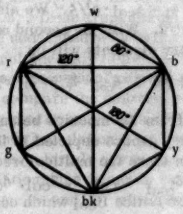

Fig. 5

three-dimensional mosaics from plane mosaics with a three-fold colored symmetry axis (in [1, 5], the mosaics X–$P3_1$, XI–R3, XII–R3m, XIII–R3c, XV–$P6_3$). A horizontal mirror plane can be introduced into the appropriate three-dimensional mosaic by other means, namely, by the use of further colors (by raising each of the three basic colors by 180°). This is most simply achieved with mosaic XIII, where the additional colors are already present [1]. On the layer depicted in mosaic XIII we stack a similar layer with the colors interchanged on the complementary principle, and this is repeated for each new layer. In the three-dimensional mosaic the colored translation $c/_2$ appears, but the lattice R will be absent. The retained glide planes plus the horizontal mirror plane generate a horizontal two-fold axis, i.e., the noncolored symmetry will be P3/mc2 = P6c2 = D^2_{3h}.

To introduce a horizontal mirror plane into the three-dimensional mosaic constructed from mosaic XII, which has the symmetry group R3m, we alternate layers of the latter with layers of a similar mosaic made up with colors raised through 180°, according to mosaics XIII and XIV. The space (noncolored) group of the resulting three-dimensional mosaic will be P3/mm2 = P$\bar{6}$m2 = D^1_{3h}.

In the same way, an m plane present with a perpendicular colored translation (180°) can be introduced into the three-dimensional mosaic based on mosaic XV, with colored group $P6_2$. The resulting noncolored (space) group will, however, only be the monoclinic group P2/m.

LITERATURE CITED

1. N.V. Belov and T.N. Tarkhova, "Colored symmetry groups," Kristallografiya, 1, 1, 4-13 (1956).
2. N.V. Belov, N.N. Neronova, and T.S. Smirnova, "The 1651 Shubnikov groups," Tr. Inst. Kristallogr., 11, 33-67 (1955).
3. P.S. Aleksandrov, Introduction to Group Theory, 2nd ed. [in Russian] (Moscow, 1951).
4. E.N. Belova, N.V. Belov, and A.V. Shubnikov, "The number and composition of abstract groups corresponding to the 32 crystal classes," Dokl. Akad. Nauk SSSR, 59, 3, 487-489 (1948).
5. N.V. Belov and T.N. Tarkhova, "Colored symmetry groups," Kristallografiya, 1, 6, 619-620 (1956).
6. N.V. Belov, The Structures of Ionic Crystals and Metallic Phases [in Russian] (1947).

SOVIET PHYSICS - CRYSTALLOGRAPHY VOL. 1, NO. 6 NOV.-DEC., 1956

EFFECTS OF BONDING ON ELECTRON SCATTERING BY ATOMS

B. K. Vainshtein and V. F. Dvoryankin

Institute of Crystallography, Academy of Sciences of the USSR
Translated from Kristallografiya, Vol. 1, No. 6,
pp. 626-630, November-December, 1956
Original article submitted October 2, 1956

It is now reasonably well established that the theoretical curves for electron scattering derived from the Born approximation agree well with experiment, at least for atoms of low and medium atomic number. This is confirmed by recent experiments [1,2], which also gave the deviations for the heaviest element used (gold). It has been pointed out [3] that the Born approximation is inadequate for heavy atoms. The establishment of the scattering law applicable to a crystal in essence consists of two stages: 1) type identification (kinematic or dynamic), and 2) derivation of the atomic scattering curve. The first aspect must be settled before the second can be discussed; but the scattering type (critical thickness) is itself dependent on the atomic amplitude [4], which makes the two aspects related. This is not surprising, because the physical basis of the Born approximation is neglect of secondary waves within the atom, the secondary waves throughout the crystal being neglected in the kinematic approximation [5].

The Born approximation is reliable for light atoms, so their f_e curves are of interest in relation to bond effects. These f_e curves are much more sensitive to changes in the outer parts of the electron shells than are the x-ray f curves, because

$$f_e \sim \frac{Z - f}{(\sin\Phi/\lambda)^2} \qquad (1)$$

at small angles, where f approaches Z (the nuclear charge), the electron scattering becomes essentially a differential effect; and it is a general property of the f curves that their behavior at small angles is governed mainly by the charge and potential of the outer parts of the atom. The peak heights and shapes for Si and F in $(NH_4)_2SiF_6$ are [6] such as to show that Si has a positive charge and F a negative one. The shape of the f_e curves may also be examined directly without Fourier synthesis of the potential.

Li_2O is very convenient here, for it has a face-centered structure of antifluorite type; the structure amplitude is finite for unmixed indices and takes the form

$$\Phi_{hkl} = \begin{cases} f_{e,O} + 2f_{e,Li} & \text{for} \quad h+k+l = 4n \qquad (2a) \\ f_{e,O} & \text{for} \quad h+k+l = 2n+1 \qquad (2b) \\ f_{e,O} - 2f_{e,Li} & \text{for} \quad h+k+l = 4n+2 \qquad (2c) \end{cases}$$

One of the species of atom (Li) thus takes no part in the scattering if the reflection indices are odd, and this gives $f_{e,O}$ directly. Again, this curve may be deduced from half the sum of the curves drawn through the Φ_{hkl} that satisfy (2a) and (2c), the combination (2a)-(2c) then giving $f_{e,Li}$.

The Li_2O was made by distilling lithium metal onto collodion films at about 10^{-4} mm Hg in the diffraction apparatus; this pressure is such as to produce complete oxidation in nearly all cases (the lines of metallic Li are only occasionally seen among those of Li_2O). Multiple exposures and microphotometry were used as in [6,7] to deduce the intensities. The specimens were usually textured, but the measurements were based only on polycrystalline Li_2O showing no signs of texture, as deduced from oblique-incidence patterns [1]. Very weak reflections gave no peaks on the microphotometer trace, so these were evaluated visually. The intensities I_{hkl} were converted to the Φ_{hkl} via

$$\Phi_{hkl} = \sqrt{I_{hkl}/d^3_{hkl}\,p}.$$

Averages over four specimens were taken; the I were measured to about 10% so the Φ were found to about 5%.

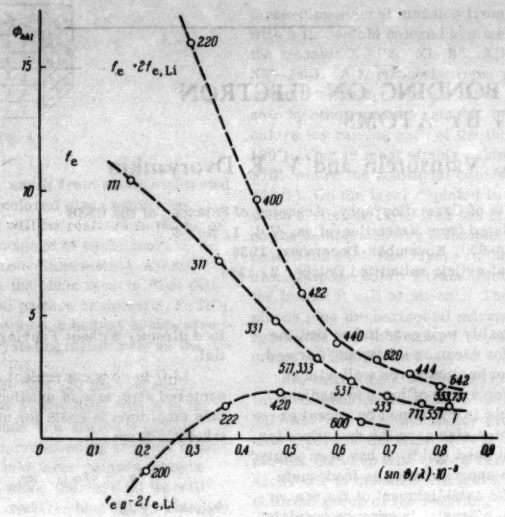

Fig. 1. Relative values of Φ_{hkl} for Li_2O.

TABLE 1. Experimental Φ_{hkl} for Li_2O (a = 4.60 A)

hkl	Φ	hkl	Φ	hkl	Φ
111	10.6	420	1.9	533	1.7
200	−1.3	422	5.9	444	2.6
220	16.0	333, 511	3.2	711, 551	1.5
311	7.2	440	3.7	642	2.0
222	1.4	531	2.2	553, 731	1.4
400	9.7	600, 442	0.5		
331	4.7	620	3.1		

The lines were broad and indicated a small crystal size, while the f_e curves fell even more rapidly than the theoretical ones (see Fig. 2; this is due to the temperature factor); the two features together point to kinematic scattering. Table 1 gives the relative values of the Φ_{hkl}; Fig. 1 gives the resulting curves. All except Φ_{200} are positive (Fig. 1). These f_e curves must be normalized in some way for comparison with experiment; it is convenient to do this for $\sin\vartheta/\lambda$ small, because the temperature factor here has only a small effect; but this is precisely the region where the other effects on f_e are pronounced. For this reason, we neglect the temperature factor temporarily and normalize the curves by equating $f_{e,O}$ to the theoretical value for $\sin\vartheta/\lambda = 0.3 \cdot 10^8$ cm, the theoretical value being taken from the tables of [8], which themselves are based on McWeeny's f [9] for light elements. This $\sin\vartheta/\lambda$ represents roughly the point at which the f (and hence the f_e) found in different ways come into agreement. Figure 2 shows the experimental and theoretical f_e curves calculated from (1) in accordance with [8, 9] and also with [10] for free O and Li atoms, and also for O^{2-} and Li^+. Table 2 gives the f_e for the elements as normalized in this way (without allowance for the thermal motion).

Figure 2 compares theory with experiment; small $\sin\vartheta/\lambda$ are of special interest. The features of (1) are such as to produce very marked discrepancies between the theoretical curves; the experimental $f_{e,O}$ (curve 1) is clearly closer to that given by [8] (curve 2), which is based on the data of [9], than it is to that given by [10] (curve 3). This shows that McWeeny's basic assumption (the need to allow for bonding in the lattice) gives (as would be expected) closer agreement with experiment than does the calculation of [10], which was based on Hartree's method for free (unbonded) atoms. But curve 1 for $f_{e,O}$ runs below curve 3 at small

TABLE 2. Experimental f_e*

$(\sin\vartheta/\lambda)\cdot 10^{-8}$	0.15	0.2	0.25	0.3	0.4	0.5	0.6	0.7	0.8
$f_{e,O}$	0.55	0.51	0.47	0.425	0.315	0.215	0.135	0.085	0.065
$f_{e,Li}$		0.30	0.24	0.195	0.120	0.070	0.040	0.029	0.022

* The factor required to convert to absolute f_e is $2.393 \cdot 10^{-8}$ cm.

$\sin\vartheta/\lambda$, because Li_2O does not have a purely covalent lattice. Curve 4 gives $f_{e,O^{2-}}$ as calculated from (1) for the free anion from the data of [10]. The lower level of curve 1 is thus to be ascribed to a certain proportion of ionic bonding. Our results show that the common view (that the bonds in compounds of Li_2O type are mainly ionic) is wrong, for here the proportion of ionic character is low. It is difficult to draw more detailed conclusions because Li_2O has $a = 4.60$ Å only, so the experimental f_e can be found only from $\sin\vartheta/\lambda \approx 0.15 \cdot 10^8$ cm.

The theoretical results [9,10] for Li (curve 5) agree extremely closely; ionization effects appear only around $\sin\vartheta/\lambda$ of about $0.1 \cdot 10^8$ cm (curve 6), which is inaccessible to measurement for Li_2O. This makes it difficult to draw any conclusions for Li, although the experimental $f_{e,Li}$ curve 7 does deviate somewhat from the theory, especially in that it does not show the predicted sharp upward trend.

The experimental f_e curves in the range $\sin\vartheta/\lambda = 0.3\text{-}0.8 \cdot 10^8$ cm allow us to select suitable temperature factors for the theoretical f_e curves, the B in $e^{-B(\sin\vartheta/\lambda)^2}$ being $B_O \approx 1.0$ Å^2 and $B_{Li} \approx 1.5$ Å^2. The former is the larger because, for remote regions of $\sin\vartheta/\lambda$ we should have $f_{e,O}/f_{e,Li}$ close to $Z_O/Z_{Li} = 8/3 = 2.66$, if we neglect the thermal motion, whereas experiment gives it as about 2.9.

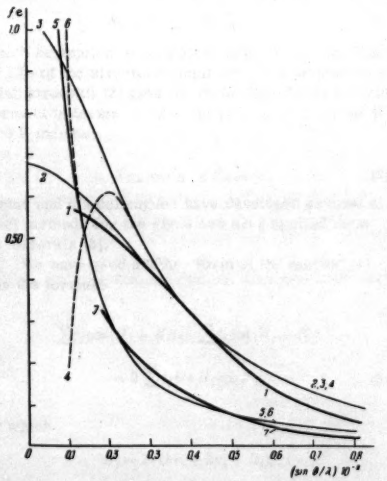

Fig. 2. Theoretical and normalized experimental f_e curves; the factor required to convert to absolute f_e is $2.393 \cdot 10^{-8}$ cm: 1) oxygen, experiment; 2) theory [8,9] for bound oxygen; 3) free oxygen [10]; 4) free O^{2-} [10]; 5) lithium [8-10]; 6) Li^+ [10]; 7) lithium, experiment.

LITERATURE CITED

1. I.I. Yamzin and Z.G. Pinsker, "An experimental test of the theory of elastic scattering for fast electrons," Dokl. Akad. Nauk SSSR, 65, 645-649 (1949).
2. S. Lennander, "Measurements of electron diffraction intensities by means of Geiger counters," Arkiv Fysik, Bd. 8, No. 54, 551-613 (1954).
3. J.M. Cowley, "Electron diffraction study of the structure of basic lead carbonate," Acta Cryst., 9, 391-396 (1956).
4. B.K. Vainshtein, "Kinematic scattering of electrons by an ideal crystal," Dokl. Akad. Nauk SSSR, 104, 537-539 (1955).
5. B.K. Vainshtein, Structural Electron Diffraction [in Russian] (Izd. AN SSSR, 1956).
6. B.K. Vainshtein and M.M. Stasova, "An electron-diffraction study of cryptohalite," Kristallografiya, 1, 311-320 (1956).
7. M.M. Stasova and B.K. Vainshtein, "Refinement of the structure of the NH_4 group in ammonium chloride," Tr. Inst. Kristallogr., 12, 18-24 (1956).
8. B.K. Vainshtein, "Atomic scattering factors for electrons," Zh. Éksperim. i Teor. Fiz., 25, 158-168 (1953).

9. R. McWeeny, "X-ray scattering by aggregates of bonded atoms," Acta Cryst., 4, 513-519 (1951).

10. Internationale Tabellen zur Bestimmung von Kristallstrukturen (Berlin, 1935), Vol. II.

USE OF DIRECT X-RAY STRUCTURE ANALYSIS METHODS IN CHEMICAL CRYSTALLOGRAPHY

Z. V. Zvonkova

Karpov Institute of Physical Chemistry

Translated from Kristallografiya, Vol. 1, No. 6,
pp. 631-633, November-December, 1956
Original article submitted October 5, 1956

A direct method (statistical equations) is shown to be applicable to a compound characterized by 60 atomic parameters.

Direct methods are much used in chemical crystallography, especially the statistical method for the signs, which is used in various forms.

Zachariasen [1], in 1952, proposed a relation between the signs of the amplitudes F_H, F_K, and F_{H+K}:

$$S_H = S(\overline{S_{K_i} \cdot S_{H+K_i}}), \qquad (1)$$

which he applied to metaboric acid; it gave the signs of 13% of the structure amplitudes (the largestones). Kitaigorodskii [2] gave the theoretical basis for this formula in terms of the structural product of the H and K indices:

$$X_{HK} = \hat{F}_H \hat{F}_K \hat{F}_{H+K}. \qquad (2)$$

Belov and his colleagues have developed several direct methods for the signs and have applied these to minerals [3].

We have used another form of the method [4] via the formula

$$\sum_j f_j \cos(H_j + K_j) + \sum_j f_j \cos(H_j - K_j) = 2 \sum_j f_j \cos H_j \cos K_j, \qquad (3)$$

in which

$$H_j = 2\pi(hx_j + ky_j + lz_j),$$

which relates the signs of F_{H+K}, F_{H-K}, F_H, and F_K. This formula becomes, in the particular case, $\cos K_j = 1$

$$S_{H+K} \cdot |F_{H+K}| + S_{H-K} |F_{H-K}| = 2 \cdot S_K \cdot S_H \cdot |F_H|. \qquad (4)$$

This shows that only the signs of two amplitudes appear here, as against the three of (1), and only two amplitudes, namely, F_H and F_K, so (4) may be put in general form as $S_{H+K} = S_H S_K$ or $S_{H-K} = S_H \cdot S_K$, provided that the moduli of the structure amplitudes satisfy

$$|F_{H+K}| > |F_{H-K}| \text{ or } |F_{H-K}| > |F_{H+K}|.$$

Equation (4) can be used only via a statistical survey, except where there is a heavy atom in a special position, because any deviation of the cos K_j from unity gives rise to errors in the signs; statistical averaging of the signs then involves as necessary and sufficient condition that the modulus of only one structure amplitude in the product $|F_K|$ should be large. It is of interest to apply the method implied by (3) to complex structures; we first used it to advantage in joint work with G.S. Zhdanov and K.I. Tobelko on the structure of realgar, As_4S_4 [5]. The method was subsequently applied to the coordination compound $F_3B \leftarrow NC_5H_5$, which contains only light atoms. The x-ray results on this are a = 17.71, b = 5.89, c =

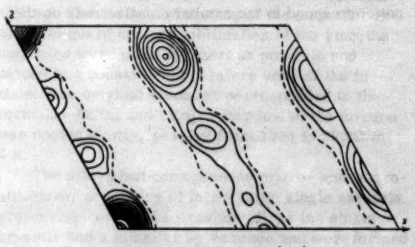

Fig. 1. Patterson projection on the (010) plane.

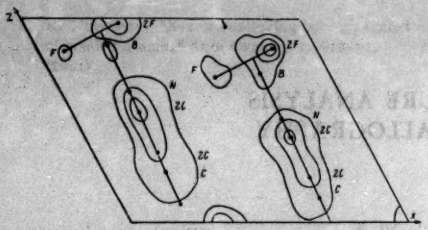

Fig. 2. Electron-density projection on (010) plane; signs of the F(h0l) determined directly from statistical equations.

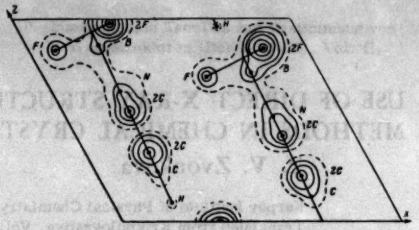

Fig. 3. Electron-density projection on the (010) after successive approximations.

14.34 Å; $\beta = 118°40'$; $\sigma_p = 1.48$ g · cm^{-3}, $\sigma_x = 1.49$ g · cm^{-3}, z = 8; space group $C_{2h}^5 = P2_1/c$.

The general fourfold position 4(e) in group $P2_1/c$ is taken twice for z = 8. Figure 1 shows the Patterson projection first calculated; this revealed the layered structure, but the outline of the molecule was not seen. The signs of the F(h0l) were then deduced via the statistical equations on the basis of 112 reflections of h0l type, four equations being drawn up for each amplitude. The statistical averaging was based on structure amplitudes giving moduli [F_K] greater than 0.25.

Figure 2 shows the resulting electron-density projection, which reveals all of the atoms. The mutual displacement of the molecules explains the largest peak in Fig. 1; the calculated intensities also confirmed the configuration. The signs were refined successively by reference to the coordinates of the atoms; Fig. 3 shows the resulting electron density projection. The final coordinates showed that the direct method gave errors in the coordinates less than 0.1 Å, and that 75% of the signs had been determined directly; about 15% of the signs for weak reflections were undefined, while 10% of the F(h0l) had been given incorrect signs. This led to distortion of the shape and size of the electron-density peaks, so the heights of these at first did not correspond to the numbers of electrons on the atoms. Electron-density series based on the correct signs gave electron numbers approximately proportional to the peak heights (see [6]). A point here is that for NaCl, with $Z_{Na^+} = 10$ and $Z_{Cl^-} = 18$, the correction for deviation from proportionality is 1/3 of an electron for Z_{Na^+}, which lies at the limit of detection for x-ray methods. The coordinates were further refined from three-dimensional series. The statistical method is thus applicable to a coordination compound characterized by 60 atomic parameters.

LITERATURE CITED

1. W.H. Zachariasen, Acta Cryst., 5, 68 (1952).
2. A.I. Kitaigorodskii, Tr. Inst. Kristallogr., 10, 27 (1954).
3. E.G. Fesenko, I.M. Rumanova, and N.V. Belov, Dokl. Akad. Nauk SSSR, 102, 275 (1955).
4. Z.V. Zvonkova and G.S. Zhdanov, Dokl. Akad. Nauk SSSR, 86, 529 (1952); Z.V. Zvonkova, X-Ray Methods of Examination in the Chemical Industry [in Russian] (1953).
5. K.I. Tobelko, Z.V. Zvonkova, and G.S. Zhdanov, Dokl. Akad. Nauk SSSR, 96, 749 (1954).
6. G.S. Zhdanov and Z.V. Zvonkova, Zh. Éxperim. i Teor. Fiz., 22, 356 (1952).

SOVIET PHYSICS – CRYSTALLOGRAPHY VOL. 1, NO. 6 NOV.-DEC., 1956

CRYSTAL STRUCTURE OF Th_2Zn_{17} AND U_2Zn_{17}

E. S. Makarov and S. I. Vinogradov

Translated from Kristallografiya, Vol. 1, No. 6,
pp. 634-643, November-December, 1956
Original article submitted May 21, 1956

Following x-ray diffraction studies of single crystals, the crystal structures of Th_2Zn_{17} and U_2Zn_{17}, constituting new structural types, have been completely determined.

Introduction

In 1946 there appeared a paper by Nowotny [1] indicating that the thorium–zinc system contained a compound $ThZn_9$ with hexagonal structure and lattice spacings

$$a = 5.237\ kX,\ c = 4.442\ kX.$$

As regards positioning of the atoms in $ThZn_9$, Nowotny found that the structure constituted a modification of the $CaZn_5$ type, in which the place of calcium was occupied by a "statistical atom" $(Th_{0.6}Zn_{0.4})$, while the zinc sites were fully occupied by zinc atoms. Hence, the composition of $ThZn_9$ should be given the formula $(Th_{0.6}Zn_{0.4})Zn_5$.

It should be noted that Nowotny prepared his alloys in open crucibles, using flux, which apparently led to severe oxidation and contamination. He observed that the rotation x-ray photographs contained not only layer lines corresponding to the spacing 4.442 kX along the z axis, but also other layer lines which he ascribed (without adequate grounds, in our opinion) to impurities of thorium dioxide.

In 1953 we began an x-ray structural study of single crystals and powders of a uranium–zinc compound with composition initially taken as corresponding to the formula UZn_9 (in analogy with $ThZn_9$). Further study, however, showed that the real compositions of these compounds corresponded to the formulas Th_2Zn_{17} and U_2Zn_{17}, and their crystal structure, although quite akin to that of $CaZn_5$, was considerably more complex and belonged to a new structural type.

In this paper we present results of our solution of the crystal structures of Th_2Zn_{17} and U_2Zn_{17}. In the initial stages of the work it became clear that the two structures were very similar and that solution of U_2Zn_{17} should be preceded by solution of the simpler structure of Th_2Zn_{17}. By combining harmonic analysis with the method of trial and error, we were able to make a complete determination of the atomic positions in crystals of Th_2Zn_{17} and U_2Zn_{17}.

Preparation of the Alloys

For preparing the alloys we used metallic uranium of 98.95% purity produced in the Soviet Union, metallic thorium of 100% purity from Germany, and 99.95% pure zinc from our own industry. By roughly filing monolithic pieces of these metals, we obtained powders; after taking the appropriate proportions of the components these were pressed into 12-g tablets. The tablets were placed in a beryllium-oxide crucible provided with a cover, which was then inserted into a thin-walled quartz ampoule. The ampoule was evacuated to the region of 10^{-4} mm Hg and after sealing placed in a vertical tubular electric furnace. The temperature was raised gradually, holding at 400°C for 1 h, 800°C for 1 h, and at the maximum for 10 min; this was 1000°C for uranium alloys and 1250°C for thorium alloys. There was no bursting of the ampoule. In order to guard against sublimation of the zinc, the ampoules were made as short as possible and placed in a constant-temperature zone of the furnace. The original mixtures corresponded to the formulas $ThZn_9$ and UZn_9. After fusion the furnace was cooled slowly, passing from 1200 to 800°C in 3 h.

The alloys had homogeneous micro- and macrostructure, consisting of fairly large single crystals grown together. In the uranium alloys the single crystals had a lamellar appearance and were formed

as stacks growing together along the base. In the thorium alloys the single crystals had the form of fragments showing various faces.

We selected the finest fragments with well-formed faces and 0.1 to 0.3 mm in size for x-ray examination.

The single crystals of the uranium compound were extremely stable in air and retained the luster of their faces for two years. The single crystals of the thorium compound were less stable and tarnished in air after a few months.

Chemical Composition of the Single Crystals

For an exact determination of the chemical composition of the compounds, we made a chemical analysis of single crystals selected by means of a lens. The weights of the single crystals were 0.5 to 1 g.

The method of determining the uranium was based on its reduction from the hexavalent state into the tetravalent by means of zinc amalgam with subsequent titration of the solution with potassium permanganate. From two analyses with 0.53 and 1.04 g of the specimen we determined uranium contents of 29.5 and 29.9 wt.%. The mean uranium content of the uranium–zinc compound was thus 29.7 wt.%, corresponding to 10.4 at.%, or the formula $UZn_{8.6}$, i.e., on rounding off to whole numbers, U_2Zn_{17}.

The thorium was determined as ThO_2. From three parallel analyses of 0.5 to 0.7 g we determined percentage contents of 31.00, 31.15, and 31.19 wt.% Th, giving a mean value of 31.11 wt.%. This gave the formula $ThZn_{7.9}$, close to $ThZn_8$.

Thus, chemical-analysis data show that the single crystals of the uranium compound had composition U_2Zn_{17} and those of the thorium compound $ThZn_8$. However, as we shall show below, the composition of the latter compound is really nearer to Th_2Zn_{17} than $ThZn_8$. We note that the structural data also allow the compositions $ThZn_8$ and UZn_8 as a result of a variation in the number of zinc atoms in the unit cell of the variable-composition phases $Th_2Zn_{15\rightarrow17}$ and $U_2Zn_{15\rightarrow17}$. In this case, it is more or less immaterial which composition we take as fundamental for determining the structure, AB_8 or A_2B_{17}.

As initial composition of the compounds we took Th_2Zn_{17} and U_2Zn_{17}, which was later confirmed by the number of atoms in the cell obtained from experimental densities.

The Unit Cell

(a) Th_2Zn_{17}. Rotation x-ray photographs with a Th_2Zn_{17} single crystal rotating around the c and *a* axes were obtained in unfiltered cobalt radiation, using an RKV-86 camera. The c-rotation photograph gave six layer lines and the *a* photograph gave four. The symmetry of the Laue and oscillation photographs showed that the Th_2Zn_{17} crystals belonged to the hexagonal system. Measurement of these photographs gave the following lattice spacings:

$$a = 9.03 \text{ Å}, \quad c = 13.20 \text{ Å}.$$

Thus, our spacings are, respectively, $\sqrt{3}$ and 3 times larger than those proposed by Nowotny [1].

The experimental density of Th_2Zn_{17} single crystals determined pycnometrically in benzene was 8.32 g/cm^3. Hence, the number of atoms per cell becomes 56.3. If we round this off to 57, the unit cell contains three formula units of Th_2Zn_{17}. The x-ray density of Th_2Zn_{17} will be equal to 8.39 g per cm^3.

(b) U_2Zn_{17}. Rotation x-ray photographs of U_2Zn_{17} single crystals taken around the c and *a* axes were obtained in filtered cobalt radiation, using the RKV-86 camera.

From the symmetry of the Laue and oscillation photographs, hexagonal symmetry was assigned to the U_2Zn_{17} crystals.

Measurement of the x-ray photographs gave the periods:

$$a = 8.99 \text{ Å}, \quad c = 26.35 \text{ Å}.$$

We note that the *a* spacings of Th_2Zn_{17} and U_2Zn_{17} are approximately the same, while the c spacings of U_2Zn_{17} are twice those of Th_2Zn_{17}.

The experimental density value of the U_2Zn_{17} single crystals was 8.50 g/cm^3.

This gave 113.1 atoms in the unit cell.

This number agrees closely with the figure of six formula units of U_2Zn_{17} in the cell, in all 114 atoms. On this basis the x-ray density of U_2Zn_{17} equals 8.57 g/cm^3.

Determination of the Space Group

In order to determine the reflection intensities and to effect indexing, a series of oscillation photographs was obtained in the RKV-86 camera around the *a* and c axes, the oscillation range being 15°. The relative intensities were determined by standard blackening marks.

(a) Th_2Zn_{17}. On considering the indices of the spots on a series on oscillation photographs

of Th_2Zn_{17}, it became clear that all satisfied the rhombohedral extinction conditions; this yields the following possible space groups: $D_{3d}^5 = R\bar{3}m$, $D_3^5 = R32$, $C_{3v}^5 = R3m$, $C_{3i}^2 = R\bar{3}$, $C_3^4 = R3$.

From the symmetry of the Laue and oscillation photographs, the last two groups drop out, since the diffraction class is determined as D_{3d}. Since we had no experimental indications suggesting noncentrosymmetric groups, we chose the centrosymmetric $D_{3d}^5 - R\bar{3}m$.

(b) U_2Zn_{17}. It follows from the symmetry of the Laue and oscillation photographs that U_2Zn_{17} belongs to the diffraction class D_{6h}. Among indices of the $00l$ type, only those satisfying the condition $l = 3n$ are present. From this it would be possible to select x-ray group No. 93 [3], including the space groups $D_6^4 = C6_32$ and $D_6^5 = C6_42$. It is also possible, however, that spots with indices $00l$, where $l \neq 3n$, were absent because of low intensity. This supposition found support in later study which showed that it was more correct to state that there were no systematic extinctions in this case. Thus, we have the following space groups of class D_{6h} to consider: $D_{6h}^1 = C6/mmm$, $D_6^1 = C62$, $C_{6v}^1 = C6mm$, $D_{3h}^1 = C\bar{6}m2$, and $D_{3h}^2 = C\bar{6}2m$.

Subsequently, on the basis of the close structural kinship of U_2Zn_{17} and Th_2Zn_{17}, we found that a satisfactory disposition of atoms in regular systems of points could only be set up in the space group $D_{3h}^1 = C\bar{6}m2$.

Determination of Atomic Coordinates

The rotation x-ray photographs of Th_2Zn_{17} and U_2Zn_{17} around corresponding axes are very similar to one another both in the dispositions and intensities of the spots. The powder photographs of the two compounds are even more alike. These experimental facts indicate that the structures of the compounds are also very similar.

In the unit cell of Th_2Zn_{17} we have to site 6 Th atoms and 51 Zn. In the unit cell of U_2Zn_{17} we must site 12 U atoms and 102 Zn. From the similar intensities of corresponding reflections in the two compounds we may suppose that the heavy metal atoms are analogously situated in both structures, and that the doubling of the c spacing of U_2Zn_{17} as compared with Th_2Zn_{17} is due to the appearance of a horizontal mirror plane on passing from the rhombohedral group $D_{3d}^5 = R\bar{3}m$ to the hexagonal group $D_{3h}^1 = C\bar{6}m2$.

The procedure for determining the coordinates of the atoms in the two cases was in general respects as follows. First, we constructed Patterson-Harker cross sections along the basal planes (using 101 reflections) and diagonal plane ($11\bar{2}0$) (using 285 reflections) for U_2Zn_{17}, with 7.5° and 3° strips. The interatomic vectors U–U could clearly be determined on these sections; there were no clear indications of the U–Zn and Zn–Zn vectors.

From the sections referred to the basal plane it was concluded that the horizontal coordinates of the heavy atoms had values $0,0,\frac{1}{3},\frac{2}{3}$, and $\frac{2}{3},\frac{1}{3}$. From the diagonal section it was established that the z coordinates of the uranium atoms could have values $z = 0,\frac{1}{6},\frac{1}{3},\frac{1}{2},\frac{2}{3},\frac{5}{6}$.

From considerations of the analogous disposition of heavy atoms in U_2Zn_{17} and Th_2Zn_{17}, we assumed that the thorium atoms in Th_2Zn_{17} could only have the following values of z coordinates: $0,\frac{1}{3},\frac{2}{3}$. Only the six-fold position 6(c) with parameter $z = \frac{1}{2}$ satisfies this condition in the space group $D_{3d}^5 = R3m$. In this case we may suppose that the arrangement of uranium atoms in one half of the U_2Zn_{17} cell will be similar to that of the thorium atoms in the Th_2Zn_{17}, while the other half of the U_2Zn_{17} cell will be the mirror image of the first half. These relationships are illustrated in Fig. 1, which shows the cross section of the two cells in the ($11\bar{2}0$) plane.

The coordinates of the majority of the zinc atoms in the two structures were established by trial and error on the basis of a model with the $CaZn_5$ structure.

As seen from the above relationships for the cell dimensions, the volume of our Th_2Zn_{17} cell is nine times that of the $(Th_{0.6}Zn_{0.4})Zn_5$ cell of the $CaZn_5$ type proposed by Nowotny [1].

Structure of the $CaZn_5$ type belongs to the space group $D_{6h}^1 = C6/mmm$. The Ca and Zn atoms in this structure have the following coordinates: 1 Ca in 1(a): 000; 2 Zn_I in 2(c): $\frac{1}{3},\frac{2}{3},0$, $\frac{2}{3},\frac{1}{3},0$; 3 Zn_{II} in 3(g): $\frac{1}{2},0,\frac{1}{2}$, $0,\frac{1}{2},\frac{1}{2}$, $\frac{1}{2},\frac{1}{2},\frac{1}{2}$.

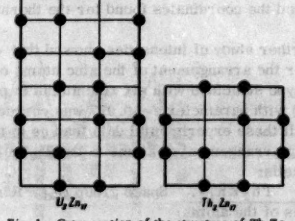

Fig. 1. Cross section of the structure of Th_2Zn_{17} and U_2Zn_{17} along the diagonal plane ($11\bar{2}0$).

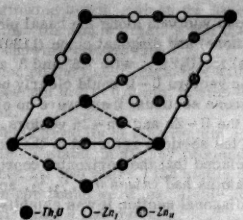

●–Th,U ○–Zn, ◎–Zn,

Fig. 2. Projection of Th_2Zn_{17} and U_2Zn_{17} structure on the basal plane.

We started from the assumption that the zinc atoms in Th_2Zn_{17} and U_2Zn_{17} were arranged according to the $CaZn_5$ motif as in Fig. 2, which gives a projection of the $CaZn_5$ structure (cell indicated by broken lines) on the basal plane of the Th_2Zn_{17} cell. The structural motif of the $CaZn_5$ type gives us positions for 45 zinc and 9 calcium atoms, six of which are occupied by thorium atoms in the Th_2Zn_{17} cell, as shown above. In the three remaining positions not occupied by thorium we must have the remaining six atoms of zinc. Geometrical analysis showed that these six zinc atoms could only occupy positions on certain vertical axes containing thorium atoms. A Harker section with respect to the hexagonal axis confirmed this conclusion and led to the value $z = 0.097$ for Th_2Zn_{17}.

From the proposed arrangement of the zinc atoms and the coordinates found for the thorium atoms, we determined the signs of the structure amplitudes for the $0kl$ and $hk0$ zones and constructed electron-density projections on the basal plane and the diagonal plane $(11\bar{2}0)$. The synthesis was made in an orthohexagonal cell from 56 independent $0kl$ reflections and 11 reflections of the $hk0$ type. In view of the considerable truncation of the series, good agreement was only found for the thorium atoms in the electron-density synthesis. Very large maxima on both electron-density charts confirmed the coordinates found for the thorium atoms.

Further study of intensities showed that our motif for the arrangement of the zinc atoms on the $CaZn_5$-type structure with six zinc atoms in position 6(c) with parameter $z = 0.097$ was correct. Thus, all these experimental data lead us to the following arrangement of atoms in the Th_2Zn_{17} and U_2Zn_{17} cells:

(a) Th_2Zn_{17}. Space group $D_{3d}^5 = R\bar{3}m$. Coordinates of the atoms:

6 Th in $6(c)_I$, $z = \frac{1}{3}$,

9 Zn in $9(d)$,

18 Zn in $18(f)$, $x = \frac{1}{3}$,

18 Zn in $18(h)$, $x = \frac{1}{2}$, $z = \frac{1}{6}$,

6 Zn in $6(c)_{II}$, $z = 0.097$.

(b) U_2Zn_{17}. Space group $D_{3h}^1 = C\bar{6}m2$. Coordinates of the atoms:

1 U in $1(c)$, 2 U in $2(g)_I$, $z = \frac{1}{6}$,

1 U in $1(d)$, 2 U in $2(g)_{II}$, $z = \frac{1}{3}$,

1 U in $1(e)$, 2 U in $2(h)_I$, $z = \frac{1}{3}$,

1 U in $1(f)$, 2 U in $2(i)_I$, $z = \frac{1}{6}$

6 Zn in $6(l)$, $x = \frac{1}{3}$, $y = 0$,

6 Zn in $6(m)$, $x = \frac{1}{3}$, $y = 0$,

12 Zn in $12(o)_I$, $x = \frac{1}{3}$, $y = 0$, $z = \frac{1}{6}$,

12 Zn in $12(o)_{II}$, $x = \frac{1}{3}$, $y = 0$, $z = \frac{1}{3}$,

6 Zn in $6(n)_I$, $x = \frac{1}{2}$, $z = \frac{1}{12}$,

6 Zn in $6(n)_{II}$, $x = \frac{1}{2}$, $z = \frac{1}{4}$,

6 Zn in $6(n)_{III}$, $x = \frac{1}{2}$, $z = \frac{5}{12}$,

6 Zn in $6(n)_{IV}$, $x = \frac{1}{6}$, $z = \frac{1}{12}$,

6 Zn in $6(n)_V$, $x = \frac{1}{6}$, $z = \frac{1}{4}$,

6 Zn in $6(n)_{VI}$, $x = \frac{1}{6}$, $z = \frac{5}{12}$,

6 Zn in $6(n)_{VII}$, $x = \frac{5}{6}$, $z = \frac{1}{12}$,

6 Zn in $6(n)_{VIII}$, $x = \frac{5}{6}$, $z = \frac{1}{4}$,

6 Zn in $6(n)_{IX}$, $x = \frac{5}{6}$, $z = \frac{5}{12}$,

2 Zn in $6(g)_I$, $z = 0.049$,
2 Zn in $2(g)_{II}$, $z = 0.451$,
2 Zn in $2(h)_{II}$, $z = 0.118$,
2 Zn in $2(h)_{III}$, $z = 0.784$,
2 Zn in $2(i)_{II}$, $z = 0.284$,
2 Zn in $2(i)_{III}$, $z = 0.618$.

Figure 3 gives a comparison between the theoretically calculated and experimental values of F^2 for the zero layer line of oscillation x-ray photographs of Th_2Zn_{17} around the c axis. Here we have used averaged values of the experimental intensities for spots of a given hkl family.

Figures 4 and 5 give a comparison between the experimental intensities of the leading lines on pow-

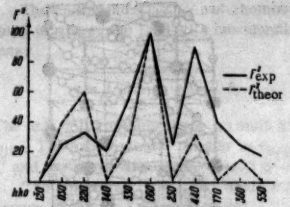

Fig. 3. Comparison between theoretical and experimental values of F^2_{hk0} for the oscillation x-ray photographs of a Th_2Zn_{17} single crystal rotated around the c axis.

der photographs of Th_2Zn_{17} and U_2Zn_{17} estimated visually from blackening standards and those calculated for the above coordinates. The agreement between experimental and theoretical values is entirely satisfactory; this confirms the validity of our assumed structures for the two compounds. In view of the difficulty of calculating the true absorption factor for the single crystals, we preferred to use intensities from powder photographs, where this factor varies monotonically with scattering angle.

For the U_2Zn_{17} structure we calculated theoretical intensities for several lines of the $00l$ type with $l \neq 3n$ and the hkl type with $l = 1$ and 5. Results showed that the intensities of these lines were not zero, but very small. Thus, for example, for the 0.0.10 reflection the intensity was 0.0007, while for the weakest observed reflection, the 322, the intensity was 0.5. These results confirm the validity of the conclusion regarding the absence of any systematic extinctions and the choice of space group $D^1_{3h} = C\bar{6}m2$.

We also calculated the theoretical intensities for composition $ThZn_8$, corresponding to 6 Th and 48 Zn atoms in the cell, three atoms being in the 3(a) positions (at the sites corresponding to the absence of thorium atoms in the $CaZn_5$ model). The

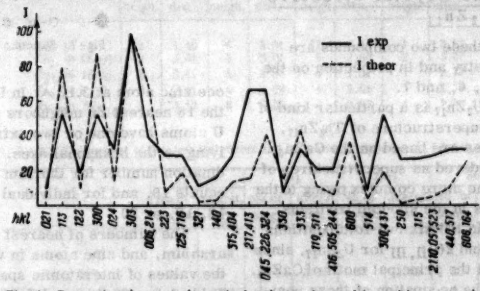

Fig. 4. Comparison between theoretical and experimental intensities on powder photographs of Th_2Zn_{17}.

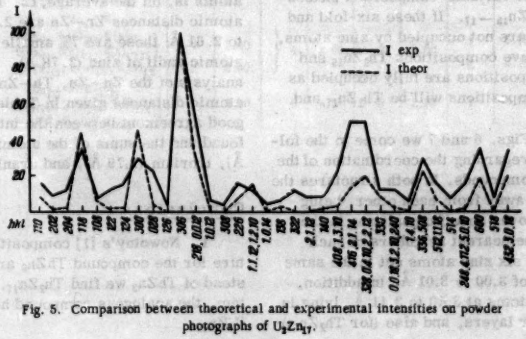

Fig. 5. Comparison between theoretical and experimental intensities on powder photographs of U_2Zn_{17}.

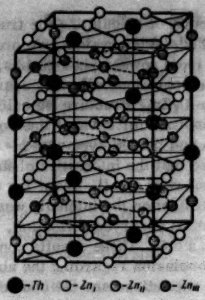

Fig. 6. Structure of Th_2Zn_{17}.

agreement between theoretical and experimental intensities in this case was not so good as for composition Th_2Zn_{17} with 6 atoms in the 6(c)$_{II}$ position.

Description of the Crystal Structure of Th_2Zn_{17} and U_2Zn_{17}

The unit cells of these two compounds are shown both in axonometry and in projection on the basal plane in Figs. 2, 6, and 7.

The structure of U_2Zn_{17} is a particular kind of noncentrosymmetric superstructure of Th_2Zn_{17}. Both of these structures are based on the $CaZn_5$ motif and can be considered as superstructures of $CaZn_5$. Matters become more complex owing to the presence of zinc atoms in the six-fold positions 6(c)$_{II}$ for Th_2Zn_{17} and in the six two-fold positions 2(g)$_{III,IV}$, 2(h)$_{II,III}$, and 2(i)$_{II,III}$ for U_2Zn_{17}, since these positions disrupt the principal motif of $CaZn_5$. We may suppose that the occupation of these positions by zinc atoms is statistical, thus providing for the formation of variable-composition phases $Th_2Zn_{15\rightarrow17}$ and $U_2Zn_{15\rightarrow17}$. If these six-fold and two-fold positions are not occupied by zinc atoms, the crystals will have compositions Th_2Zn_{15} and U_2Zn_{15}. When the positions are fully occupied as in our case the compositions will be Th_2Zn_{17} and U_2Zn_{17}.

By analyzing Figs. 6 and 7 we come to the following conclusion regarding the coordination of the atoms in the two compounds. In both structures the heavy atoms stand away from each other, being evenly distributed over specific positions in the hcp Zn lattice. The nearest neighbors of each heavy atom will be six zinc atoms set in the same layer at distances of 3.00 to 3.01 Å. In addition, there are 12 zinc atoms at 3.40 to 3.41 Å, lying in the upper and lower layers, and also (for Th_2Zn_{17})

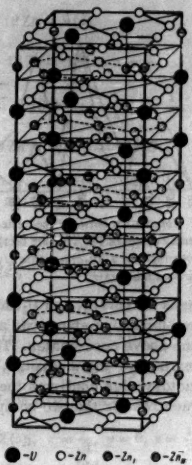

Fig. 7. Structure of U_2Zn_{17}.

one zinc atom at 3.12 Å. In U_2Zn_{17}, in addition to the 18 nearest Zn neighbors mentioned, individual U atoms have one or two extra Zn atoms at 3.10 Å lying on the hexagonal axes. Thus, the total coordination number for thorium atoms in Th_2Zn_{17} equals 19, and for individual U atoms in U_2Zn_{17} it is 18, 19, or 20.

The numbers of nearest neighbors for thorium, uranium, and zinc atoms in various complexes and the values of interatomic spacings are given in Table 1 for Th_2Zn_{17} and Table 2 for U_2Zn_{17}.

The over-all coordination number of the zinc atoms is, on the average, 12. The minimum interatomic distances Zn–Zn are 2.56 to 2.58 and 2.60 to 2.61 Å; these are 7% smaller than the sum of the atomic radii of zinc (2.78 Å). On the whole, the analysis of the Zn–Zn, Th–Zn, and U–Zn interatomic distances given in Tables 1 and 2 shows good agreement between the interatomic distances found and the sums of the atomic radii of zinc (1.39 Å), thorium (1.79 Å), and uranium (1.52 Å).

Conclusions

1. Nowotny's [1] composition and crystal structure for the compound $ThZn_9$ are erroneous. Instead of $ThZn_9$ we find Th_2Zn_{17}. In the U–Zn system, the analogous compound has composition U_2Zn_{17}.

2. The compound Th_2Zn_{17} has rhombohedral structure (space group D_{3d}^5) with hexagonal-lattice spacings:

$$a = 9.03\,\text{Å},\ c = 13.20\,\text{Å}.$$

The unit cell contains three formula groups Th_2Zn_{17}. The experimental density is $d_{exp} = 8.32$ g/cm^3 and the x-ray density $d_x = 8.39$ g/cm^3.

3. The compound U_2Zn_{17} has hexagonal structure (space group D_{3h}^4) with spacings:

$$a = 8.99\,\text{Å},\ c = 26.35\,\text{Å}.$$

The unit cell contains six formula units U_2Zn_{17}. The experimental density is $d_{exp} = 8.50$ g/cm^3, and the x-ray density $d_x = 8.57$ g/cm^3.

4. The structural data obtained suggest the possibility of a variable-composition range in these compounds; this may be represented by the chemical formulas Th_2Zn_{15-17} and U_2Zn_{15-17}.

LITERATURE CITED

1. H. Nowotny, "Die Kristallstrukturen von Zn_3Th, Cd_3Ca, und $(Ag, Mg)_3Ca$," Metallforschung, 1, 1/2, 31-33 (1946).
2. International Tables for X-Ray Crystallography (Birmingham, England, 1952), Vol. 1.
3. G. S. Zhdanov and V. Pospelov, "Determination of crystal symmetry from the x-ray diffraction picture. II. Rational tables of extinctions for determination of x-ray groups," Zh. Éxperim. i Teor. Fiz., 15, 709 (1945).

TABLE 1. Number of Nearest Neighbors and Interatomic Spacings (Å) for Th_2Zn_{17}

	Th		Zn_I		Zn_{II}		Zn_{III}	
	No. of neigh.	interat. dist.	No. of neigh.	interat. dist.	No. of neigh.	interat. dist.	No. of neigh.	interat. dist.
Th in 6 $(c)_I$	1	4.40	6	3.01	12	3.41	1	3.12
Zn_I in 18 (f)	2	3.01	3	3.01	6	2.66	2	3.27
Zn_{II} in 18 (h)	3	3.41	4	2.66	4	2.61	1	2.77
Zn_{II} in 9 (d)	2	3.41	4	2.66	4	2.61	2	2.77
Zn_{III} in 6 $(c)_{II}$	1	3.12	6	3.27	6	2.77	1	2.56

TABLE 2. Number of Nearest Neighbors and Interatomic Spacings (Å) for U_2Zn_{17}

	U		Zn_I		Zn_{II}		Zn_{III}	
	No. of neigh.	interat. dist.	No. of neigh.	interat. dist.	No. of neigh.	interat. dist.	No. of neigh.	interat. dist.
U in $I(e)$, $I(d)$	2	4.39					—	—
$I(c)$, $I(f)$	—	—	6	3.00	12	3.40	2	3.10
$2(g)_I, 2(g)_{II}, 2(h)_I, 2(i)_I$	1	4.39					1	3.10
Zn_I in 6 (i), 6 (m) $12(o)_I$; $12(o)_{II}$	2	3.00	3	3.00	6	2.66	2	3.27
Zn_{II} in $6(n)_I$, $6(n)_{III}$, $6(n)_V$, $6(n)_{VI}$, $6(n)_{VII}$, $6(n)_{VIII}$	3	3.40	4	2.66	4	2.60	1	2.75
$6(n)_{II}$, $6(n)_{IV}$, $6(n)_{IX}$	2	3.40					2	2.75
Zn_{III} in $2(g)_{III}$, $2(g)_{IV}$, $2(h)_{II}$, $2(h)_{III}$, $2(i)_{II}$, $2(i)_{III}$	1	3.10	6	3.27	6	2.75	1	2.58

CRYSTAL STRUCTURE OF UGa AND UGa_2

E. S. Makarov and V. A. Levdik

Translated from Kristallografiya, Vol. 1, No. 6, pp. 644-649, November-December, 1956
Original article submitted May 21, 1956

The existence of compounds UGa and UGa_2 in the U-Ga system is established from chemical and x-ray examination and their crystal structures are determined. The structure of UGa determined from single-crystal data constitutes a new type. The structure of UGa_2 found by the powder method is of the AlB_2 type.

Introduction

There is no published information on the phase diagram of the U-Ga system. It is merely known that the compound UGa_3 has a fcc structure of the $AuCu_3$ type [1].

Between 1949 and 1955 we studied the U-Ga system by x rays and discovered compounds UGa and UGa_2.

We here present results relating to the crystal structures of these compounds.

Preparation of the Alloys

Uranium-gallium alloys 10-17 g in weight were prepared from 99.86% pure uranium and chemically pure gallium in a high-frequency vacuum furnace. After filling with the charge, the furnace was evacuated to 10^{-4} mm Hg. In the course of heating and fusion, the vacuum fell to 10^{-1} mm Hg. On reaching the melting point, there was a short rest for 2-4 min in order to achieve better mixing of the components. The cooling rate between 150 and 1000° was, on the average, never greater than 50 deg/min. The temperature was regulated visually.

The shrinkage cavities of alloys with composition close to 50 at.% contained fine single crystals. Chemical analysis of these gave the figures shown in Table 1.

TABLE 1

Percentages	Determination of gallium		Determination of uranium	
	% Ga	% U = 100 - % Ga	% Ga = 100 - % U	% U
Weight	21.45	75.55	21.95	78.05
Atomic	48.25	51.75	49.99	51.01

The chemical analysis was conducted by A.I. Elovatskii under the direction of A.G. Karabash by the Hillebrandt method [2], based on separating the gallium from the uranium by extraction of gallium chloride with ether from a solution of the alloy in 6% hydrochloric acid.

Crystal Structure of UGa

The single crystals selected for x-ray examination had the form of interlinked rhombic scales with dimensions of the order of tenths of a millimeter (Fig. 1).

The x-ray study was carried out with filtered cobalt radiation. The symmetry of the Laue photographs showed that the crystals had rhombic structure. The unit-cell parameters calculated from rotation x-ray photographs (RKV-86 camera) had the following values: $a = 9.40$ Å, $b = 7.60$ Å, $c = 9.42$ Å.

Rotation photographs taken around the cell diagonal indicated that the *ab* face was centered.

In order to determine the reflection intensities, we took three series of 10° oscillation photographs

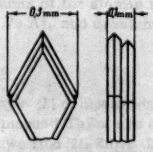

Fig. 1. Form and dimensions of a UGa single crystal.

around the three principal axes of the crystal. The intensities were estimated with the help of a scale of film blackening. The cobalt radiation enabled us to fix only 245 independent reflections. On changing from intensities to structure amplitudes, we allowed for the Lorentz, polarization, and kinematic factors.

The results of measuring and calculating the oscillation photographs reveal the following extinction laws:

$$hkl: h + k = 2n$$
$$h0l: \quad l = 2n,$$

This corresponds to x-ray group No. 29, consisting of three space groups D_{2h}^{17} = Cmmc, C_{2v}^{12} = Cmc2, C_{2v}^{16} = C2cm. The smallest multiplicity of points in each of these groups is 4.

The number of atoms per cell was determined from the additive density, preserving the smallest multiplicity and the least deviation from the composition given by chemical analysis of the single crystals. The cell contains 16 uranium and 16 gallium atoms.

The additive density of $U_{16}Ga_{16}$ equals 12.8 g per cm^3 (d_r^U = 18.97 g/cm^3; d_r^{Ga} = 6.087 g/cm^3). The x-ray density of $U_{16}Ga_{16}$ is 12.1 g/cm^3.

Analysis of the cross sections of three-dimensional F^2 series based on space-group symmetry shows that, when the structure contains atoms in the general position, the (u0w) section gives an unequivocal indication of the space group. The absence of atoms in general positions reduces the reliability of the determination and demands the construction of additional cross sections. After analyzing the cross sections of the F^2 series in the plane (0vw) and parallel to the coordinate axes, we arrived at a single centrosymmetric group D_{2h}^{17} = Cmcm.

By analyzing the cross sections of a series of interatomic vectors, examining the intensities, and making a geometrical analysis by trial and error, we produced a structural model giving good agreement between the experimental and computed values of F(0k*l*) and F(h0*l*). The computed series of F(hk0) values was in poor agreement with experiment. Introduction of a correction for absorption in the sample [3] improved agreement to a satisfactory extent. This was apparently because the crystal was least "transparent" for the (hk0) zone (see Fig. 1).

Graphs comparing the structure amplitudes F_{meas} and F_{calc} for the zero zones are shown in Fig. 2. Our electron-density projections on the coordinate planes (001), (010), and (100) appear in Fig. 3. The uranium-atom peaks appear clearly in all projections [except the 4(a) group in the projection on the (010) plane]. The gallium-atom peaks are comparable in magnitude with the effects of

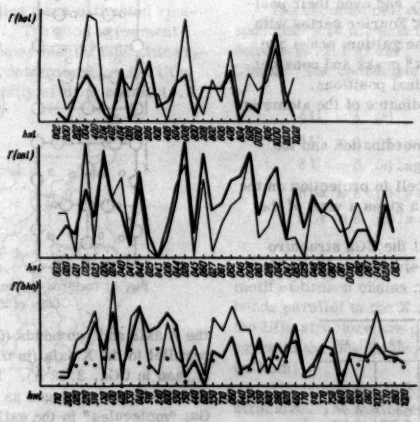

Fig. 2. F_{meas} and F_{calc} for UGa. Thick lines = F_{meas}; thin lines = F_{calc}; circles = $F(hk0)_{meas}$, without allowing for absorption.

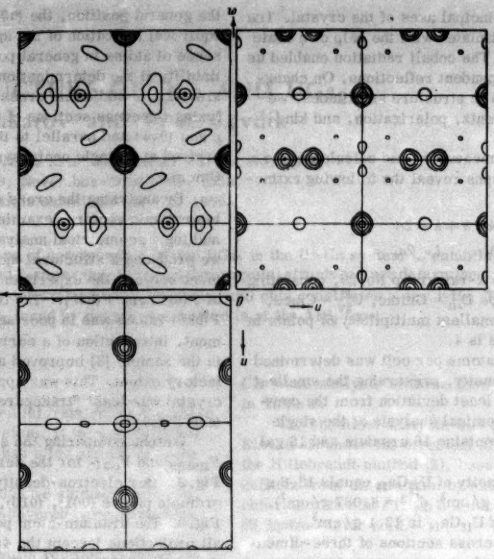

Fig. 3. Electron-density projection on the face of the UGa cell.

truncating the Fourier series, so that only those with double "weight" appear, and even their positions are shifted. In a check Fourier series with computed values of F(h0l) the gallium peaks are also comparable with "ghost" peaks and considerably shifted from their original positions.

Table 2 shows the coordinates of the atoms in the cell.

Table 3 gives data on coordination and the shortest interatomic spacings.

Figure 4 indicates the cell in projection on the coordinate planes, and Fig. 5 gives a view of the cell in axonometry.

It is not hard to see that the UGa structure preserves the α U [4] motif of broken chains along

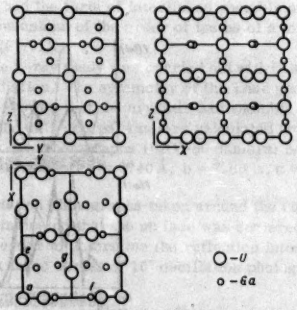

Fig. 4. Positions of atoms in projections on the faces of the UGa cell.

TABLE 2

Atom	Position	x/a	y/b	z/c
4 U	4 (a)	0	0	0
4 U	4 (c)	0	0.212	0.250
8 U	8 (e)	0.300	0	0
8 Ga	8 (f)	0	0.689	0.118
8 Ga	8 (g)	0.260	0.354	0.250

the Z axis and two bonds (for positions 4a and 8e) parallel to the X axis (in α U the distance is 2.85 Å, and in UGa, 2.82 Å). The gallium atoms in position 8(f) are arranged as pairs analogous to the Ga_2 "molecules" in the gallium structures (distance in Ga, 2.45 Å, and in UGa, 2.48 Å) [5].

TABLE 3

Atoms	Position	Distance A	No. of nearest neighbors
U — U	(a) — (e)	2.85	2
	(a) — (e)	2.82	2
U — Ga	(a) — (f)	2.61	2
	(e) — (f)	2.605	2
	(e) — (g)	2.66	2
	(e) — ( )	2.66	2
Ga — Ga	(f) — (f)	2.48	1
	(g) — (f)	2.86	2

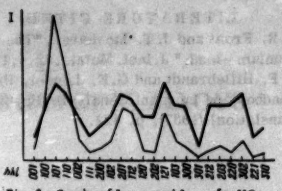

Fig. 6. Graphs of I_{meas} and I_{calc} for UGa_2. Thick line = I_{meas}; thin line = I_{calc}.

Crystal Structure of UGa_2

On indexing the x-ray photographs of UGa_2 by means of Hull curves, we found that it had hexagonal structure with lattice constants: $a = 4.21$ Å, $c = 4.01$ Å, $c/a = 0.954$.

The x-ray photographs also showed two lines which could not be indexed: these were apparently due to impurities.

From crystal-chemical considerations it appeared the UGa_2 had the crystal structure of the AlB_2 type (space group D_{6h}^1 = C6/mmm) with atomic positions:

1 U in 1(*a*),
2 Ga in 2(*d*).

Figure 6 gives a comparison of the theoretical and experimental line intensities for the powder photograph of UGa_2. The theoretical intensities were calculated without allowance for absorption. The experimental intensities were estimated visually on a nine-point scale. The good agreement between theoretical and experimental intensities indicates that the structure determined for the UGa_2 is correct. The x-ray density of UGa_2 equals 10.3 g/cm³. The closest interatomic distances in the UGa_2 structure are: Ga — Ga = 2.43 Å; U — Ga = 3.15 Å; U — U = 4.01 Å.

We may conclude from these data that the uranium atoms are not in contact with each other; the gallium atoms form a plane hexagonal lattice parallel to the basal plane, each atom having three nearest neighbors at a distance of 2.43 Å equal to the smallest distance in the structure of pure gallium.

The uranium — gallium distance equals the sum of the maximum interatomic radii found in the structures of gallium and α-uranium.

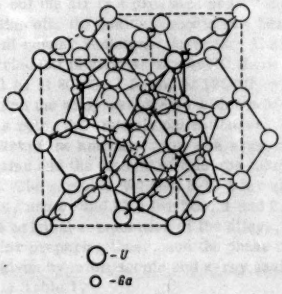

Fig. 5. Unit cell of UGa.

Conclusions

X-ray study of UGa single crystals shows that this compound belongs to a new structural type of rhombic symmetry. The lattice constants are $a = 9.40$ Å, $b = 7.60$ Å, $c = 9.42$ Å.

The rhombic cell contains 32 atoms, corresponding to 16 formula units of UGa. The x-ray density is 12.1 g/cm³. The space group is D_{2h}^{17} = Cmcm. The coordinates of the atoms are:

4 U in 4 (*a*)
4 U in 4 (*c*): $y = 0.212$
8 U in 8 (*e*): $x = 0.300$
8 Ga in 8 (*f*): $y = 0.689$, $z = 0.118$
8 Ga in 8 (*g*): $x = 0.260$, $y = 0.354$.

The UGa structure preserves the α-uranium motif of broken chains along the Z axis and two bonds parallel to the X axis. The gallium atoms in the UGa structure are disposed in pairs, in analogy with the Ga_2 "molecules" in the structure of gallium.

The compound UGa_2 crystallizes in the AlB_2 structure. The lattice constants are: $a = 4.21$ Å, $c = 4.01$ Å, $c/a = 0.954$. The x-ray density is 10.3 g/cm³.

LITERATURE CITED

1. B.R. Frost and J.T. Moskarey, "The system uranium–lead," J. Inst. Metals, 82, 4, 171 (1953).
2. V.F. Hillebrandt and G.E. Lendel, Practical Handbook on Inorganic Analysis [Russian translation] (1937), p. 422.
3. D.M. Kheiker, "Simple method of calculating the absorption factor for strongly absorbing samples in x-ray structural analysis," Zh. Éxperim. i Teor. Fiz., 25, 6(12), 759 (1953).
4. Strukturbericht, VI (1941).
5. Strukturbericht, II (1937).

X-RAY DIFFRACTION STUDY OF THORIUM-ZINC ALLOYS

E. S. Makarov and L. S. Gudkov

Translated from Kristallografiya, Vol. 1, No. 6,
pp. 650-656, November-December, 1956
Original article submitted May 21, 1956

Chemical, x-ray structural, and phase analysis was used to establish the existence of the following compounds in the Th-Zn system: $Th_{2\pm x}Zn$, $ThZn_3$, $ThZn_4$, Th_4Zn_7, and Th_2Zn_{11}. The crystal structure of the first three of these was determined.

Introduction

No phase diagram of the Th-Zn system has so far been published. There are certain indications that the system contains compounds $ThZn_3$ [1] and Th_2Zn [2]. Data of Nowotny [1] on the structure of $ThZn_3$ are erroneous (see Makarov and Vinogradov [3]). Data on the composition and structure of the Th_2Zn phase are confirmed in the present paper.

Preparation of Alloys

The original materials were 100% pure thorium and 99.95% pure zinc. Solid pieces of these metals were coarsely filed to give powders, which were mixed in due proportion and pressed into tablets in a steel mold.

In order to obtain an alloy the tablet was placed in a beryllium-oxide crucible provided with a cover, and this was placed in a quartz ampoule. After pumping out the air to a pressure of 10^{-4} mm Hg and sealing off, the quartz ampoule was heated in a vertical tubular resistance furnace. The heating was carried out in stages: at ~400°C there was a rest of 1 h; at 800°C, 1 h; and at 1250°C, ~10 min, after which the alloy was cooled with the furnace.

As a rule, the ampoule did not burst. In the upper part of the ampoule there was some condensed zinc and the amount of this was taken into account. The samples weighed 8-10 g for alloys Nos. 3, 4, and 5, and 23 g for Nos. 1 and 2.

The original composition of the alloys, the conditions for preparing these, and the phase composition as given by microscopic and x-ray analysis, appear in Table 1.

The chemical composition of individual phases was determined from the microstructure and chemical analysis.

The temperature was measured with a calibrated Pt-PtRh thermocouple placed at the level of the tablet in the immediate neighborhood of the outer wall of the ampoule.

The surface of the alloys showed thin plates of rectangular form, having a silver-white metallic color similar to hoar frost. These single-crystal plates were studied by the Laue and rotation methods; they had tetragonal symmetry and the following lattice constants: $a = 4.16$ Å, $c = 14.43$ Å.

Considering the way in which these single-crystal plates were formed, we came to the conclusion that they developed by condensation from the gas phase and constituted the result of interaction between the thorium and silicon reduced from the quartz ampoule by zinc vapor. The single-crystal plates were in fact the compound $\alpha ThSi_2$. According to published data [2], $\alpha ThSi_2$ has a tetragonal lattice with spacings $a = 4.13$ Å, $c = 14.35$ Å, which are in good agreement with the above results.

Chemical Analysis

A weighed portion of alloy of the order of 0.5 g was dissolved in aqua regia by heating. The solution was evaporated almost to dryness, 3-5 ml concentrated nitric acid was added, and the result again evaporated almost to dryness. The thorium and zinc nitrates obtained in the dry residue were dissolved in a small quantity of water with the addition of 1 ml of 5% nitric acid solution.

The resultant solution was brought up to a volume of 40 ml, 2 g ammonium nitrate was added,

TABLE 1

No. of alloys	Composition in original mixture wt.% Zn	at.% Zn	Phase composition of alloy	Remarks
1	21.98	50.0	Alloy consists of two parts: (a) uniform silver-white, easily oxidized phase $Th_{2\pm x}$ with small inclusions of an unknown phase; (b) loose, dark-gray mass of thorium dendrites and cubic phase X	Very small α-$ThSi_2$ crystals formed on surface
2	36.03	66.66	Single-phase alloy, Th_4Zn_7	Zinc (1.2 g) sublimes. Crystals of α-$ThSi_2$ formed on alloy
3	46.0	75.0	Alloy consists mainly of phase $ThZn_4$ and traces of $ThZn_2$	
4	52.99	80.0	Alloy consists mainly of phase $ThZn_4$	Crystals of α-$ThSi_2$ formed on surface
5	71.71	90.0	Alloy consists of phase Th_6Zn_{17}	Large α-$ThSi_2$ crystals formed on surface

and the result heated to 60-80°C. From the hot solution thus obtained, thorium was precipitated as the peroxide by adding a 15% solution of H_2O_2. The filtered and washed residue was roasted to constant weight in a porcelain crucible at about 1000°C and weighed as ThO_2.

In order to determine the zinc, the remaining filtrate was evaporated almost to dryness. The dry residue was dissolved in water with 1-2 ml hydrochloric acid added and diluted with water to a volume of 100 ml, after which 1 g ammonium acetate and 5 ml concentrated acetic acid were added. The zinc was precipitated as ZnS by H_2S. The resultant ZnS residue was washed and roasted so as to transform it to ZnO, from which the original zinc content was determined by weighing.

Crystal Structure of $Th_{2\pm x}Zn$

From alloy No. 1 we were able to isolate a few single-crystal fragments around 0.1 mm in size and to study these by the Laue and rotation methods. The Laue x-ray photographs indicated tetragonal symmetry and the rotation (around the $\sqrt{2}a$ and c directions) photographs gave periods of 10.68 and 5.62 Å, respectively. Hence, the dimensions of the tetragonal cell are: a = 7.62 Å, c = 5.62 Å.

According to published data [2], the cell dimensions of Th_2Zn are: a = 7.95 Å, c = 5.64 Å.

The slight difference in the a values may be due to the variable composition of the $Th_{2\pm x}Zn$ phase. This is partly confirmed by the fact that, according to chemical analysis, the unbroken part of alloy No. 1, in which the $Th_{2\pm x}Zn$ single crystals were found had composition 8.19 to 8.94 wt.% Zn, corresponding to 24.1 to 25.8 at.% Zn, instead of the theoretically expected value of 33.33 at.% Zn for the composition Th_2Zn.

From crystal-chemical considerations and the cell dimensions, it appeared that $Th_{2\pm x}Zn$ had the $CuAl_2$-type structure [4]. In this case, the theoretically calculated density equals 10.7 g/cm³, in satisfactory agreement with the value 10.2 g/cm³ for the additive density of $Th_{2\pm x}Zn$. It was very hard to determine the experimental density owing to the small weight of the single crystals, and it was in fact not determined.

In the case of the $CuAl_2$ structure (space group D_{4h}^{18}), the positions of the atoms in $Th_{2\pm x}Zn$ for composition Th_2Zn will be:

4 Zn in 4(*a*), 8 Th in 8(*h*).

For the parameter u we took roughly 1/6.

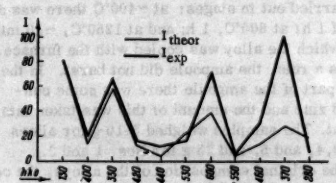

Fig. 1. Comparison between calculated and experimental spot intensities for the zero-layer line of Th_2Zn.

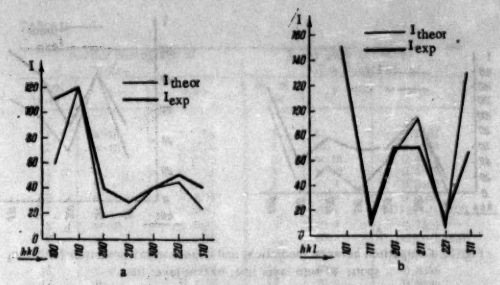

Fig. 2. Comparison between calculated and experimental intensities for $ThZn_2$ spots: a) zero layer line; b) first layer line.

Figure 1 gives a comparison between calculated intensities for the ideal composition Th_2Zn and the experimental values for spots on the zero layer line of rotation photographs taken around the c axis of a $Th_{2\pm x}Zn$ single crystal.

Remembering that in calculating the theoretical intensities the absorption factor was not taken into account, we may consider the agreement between theory and experiment as quite satisfactory. This leads to the conclusion that $Th_{2\pm x}Zn$ does in fact have the $CuAl_2$ structure.

The interatomic distances calculated from the cell dimensions obtained together with the parameter $u = 1/6$ generally agree with the corresponding sums of atomic radii of thorium and zinc; in order to obtain the exact interatomic spacings, however, the exact value of u is required, and this we did not have. The interatomic distances in $Th_{2\pm x}Zn$ have the following values:

$$Zn-2Zn = 2.81\,Å,\quad Zn-8Th = 3.18\,Å,$$
$$Th-4Zn = 3.18\,Å,$$
$$Th-2Th = 3.33\,Å,\quad Th-1Th = 3.59\,Å.$$

Crystal Structure of $ThZn_2$

As seen from Table 1, alloy No. 3 contained the phase $ThZn_2$. We were able to select a few very fine acicular single crystals with clearly expressed hexagonal-prism faces. The thickness of the crystallites was less than 0.1 mm and the length about 0.3 mm. In air the $ThZn_2$ crystals were quite stable and lasted for several days.

Rotation and oscillation x-ray photographs gave coarse values for the identity periods of the hexagonal $ThZn_2$ cell; these were used to index the powder photograph, which gave the following lattice spacings: $a = 4.20$ Å; $c = 4.17$ Å.

By comparing the atomic radii, cell dimensions, and additive density, we considered that $ThZn_2$ had the AlB_2-type structure with three atoms per unit cell.

A comparison of the theoretically calculated and experimental spot intensities of the zero and first layer lines of the rotation x-ray photographs of $ThZn_2$ is given in Figs. 2a and 2b.

In calculating the theoretical intensities we considered the Lorentz and recurrence factors. The agreement between the experimental and theoretical intensities is entirely satisfactory, indicating the correctness of the hexagonal AlB_2-type structure for $ThZn_2$.

The closest interatomic distances in $ThZn_2$ have the following values:

$$Zn-3Zn = 2.42\,Å,\quad Th-12Zn = 3.18\,Å,$$
$$Zn-6Th = 3.18\,Å,\quad Th-2Th = 4.17\,Å.$$

If we assume that the atomic radii of thorium and zinc are, respectively, 1.80 and 1.38 Å, then the Zn–3Zn distance in the hexagonal layers is 12.3% below the atomic diameter. The Th–Zn distance found agrees exactly with the sum of the atomic radii of thorium and zinc.

Crystal Structure of $ThZn_4$

According to microscope analysis, alloy No. 3 (see Table 1) had an almost single-phase microstructure. A slight accumulation of acicular $ThZn_2$ crystals occurred owing to segregation in the lower part of the ingot obtained from alloy No. 3.

Chemical analysis of monolithic fragments of alloy No. 3 gave a zinc content of 52.22 wt.%, corresponding to 79.5 at.% Zn, close to $ThZn_4$.

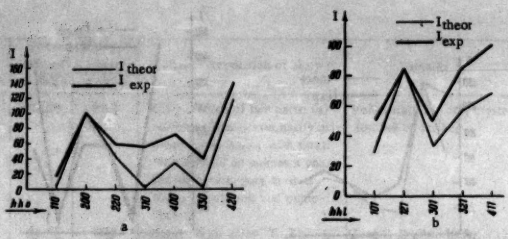

Fig. 3. Comparison between theoretical and experimental intensities for $ThZn_4$ spots: a) zero layer line; b) first layer line.

Single crystals of $ThZn_4$ could easily be isolated in alloy No. 3; these had the form of lamellas with curved edges. From x-ray rotation photographs we obtained the following parameters for the tetragonal cell of $ThZn_4$: $a = 4.26$ Å, $c = 10.4$ Å.

From the x-ray densities of thorium, zinc, and the intermediate phases $Th_{2\pm x}Zn$ and $ThZn_2$, we constructed a curve for the x-ray densities of the Th–Zn alloy system. The value interpolated on this curve for $ThZn_4$ was 8.6 g/cm^3, giving ten atoms per cell, or two $ThZn_4$ groups.

From crystal-chemical considerations we gathered that $ThZn_4$ had the AlB_4 type of structure. This was confirmed on comparing theoretical and experimental intensities for the spots on the zero and first layer lines of the rotation photographs, as seen in Figs. 3a and 3b.

The space group is $D_{4h}^{17} - I4/mmm$. The coordinates of the atoms are: 2Th in 2(a); $4Zn_I$ in 4(d); $4Zn_{II}$ in 4(e). We took the z parameter as 0.38.

The closest interatomic spacings in $ThZn_4$ have the values:

$$Th - 8Zn_I = 3.26Å, \quad Th - 8Zn_{II} = 3.36Å,$$
$$Zn_I - 1Zn_I = 2.48Å, \quad Zn_I - 4Zn_{II} = 2.52Å,$$
$$Zn_I - 4Th = 3.26Å, \quad Zn_{II} - 4Zn_I = 2.52Å,$$
$$Zn_{II} - 4Th = 3.36Å.$$

Comparing these with the sums of the atomic radii, we see that the Zn–Zn distances are severely shortened. This indicates the presence of a homopolar or covalent bond.

The Th_4Zn_7 Phase

As seen from Table 1, alloy No. 2 had original composition 66.6 at.% Zn. In the course of fusion, part of the original zinc volatilized and condensed in the upper part of the ampoule. The condensed zinc was weighed and the composition of the alloy corrected for the actual zinc content, equal to 32.6 wt.% (63.6 at.%). Chemical analysis of alloy No. 2 gave 34.38 wt.% Zn, or 65.2 at.%. Alloy No. 2, as shown by study in the microscope, was single-phase. Thus, the chemical composition indicates the formula Th_4Zn_7, or possibly Th_8Zn_{15}.

We were unable to find single crystals corresponding to this phase, since the alloy constitutes a continuous monolithic formation. Hence, powder photographs were obtained from alloy No. 2, using copper radiation. The Th_4Zn_7 phase was very brittle and susceptible to work-hardening, as indicated by the reduced line intensities. In Table 2 we therefore present a calculation of two x-ray photographs somewhat differing from one another in the number and intensity of the lines observed and corresponding to a fragment of the alloy and Th_4Zn_7 powder, respectively, the latter obtained by grinding in an agate mortar. We could not index the x-ray photographs, and the question of the crystal structure of Th_4Zn_7 remains open.

Phase X

As seen from Table 1, the upper part of alloy No. 1 contains a loose dark-gray metallic mass of thorium dendrite and a cubic phase X. Since we were unable to obtain phase X in pure form so as to analyze it chemically, the chemical composition of this phase remains uncertain.

As regards the ratios of the line intensities, the x-ray photograph of phase X is very similar to that of α Th, and also that of ThO_2. The lattice constant of thorium dioxide ($a = 5.58$ Å) is close to that of the phase in question ($a = 5.684$ Å), which suggests that phase X may have an oxide nature. We can imagine that the increased lattice constant of phase X (by comparison with thorium dioxide) is due to the dissolution of zinc oxide in thorium di-

TABLE 2

Powder photograph of Th_4Zn_7			X-ray photograph of Th_4Zn_7 fragment		
No. of lines	i	sin θ	No. of lines	i	sin θ
1	w-m	0.2014	1	s.	0.2862
2	w-m	0.2636	2	m.	0.3423
3	s.	0.2904	3	w-m	0.4470
4	w.	0.3121	4	w-m	0.4637
5	m-s	0.3447	5	m-s	0.5400
6	m.	0.4057	6	m-s	0.5659
7	m.	0.4184	7_d	m-s	0.7128—0.7250
8	w-m	0.4480	8	m-s	0.7424
9	w.	0.4651	9_d	m.	0.7923—0.7997
10	v.w.	0.4909	10_d	m-s	0.8119—0.8180
11	v.w.	0.5038	11	m-s	0.8345
12	w.	0.5356	12	m-s	0.8494
13	w.	0.5400	13	m-s	0.8601
14	w-m	0.5659	14	m-s	0.8839
15	w-m	0.5955	15_d	s.	0.9237—0.9289
16	w.	0.6298	16	m.	0.9350
17	w.	0.6576	17_d	s.	0.9446—0.9484
18	w.	0.6693	18	m.	0.9613
19_d	w.	0.7143—0.7288	19_d	m-s	0.9640—0.9667
20_d	w-m	0.7383—0.7441	20_{α_2}	s.	0.9762
21	w-m	0.8165	21_{α_1}	m.	0.9795
22	w-m	0.8369	22_d	s.	0.9849—0.9864
23	w-m	0.8625			
24	m.	0.8840			
25	m.	0.9484			

oxide. The true nature of phase X awaits further study.

The Th_2Zn_{17} Phase

As already indicated in the introduction, Nowotny's data [1] on the chemical composition and crystal structure of $ThZn_9$ are erroneous. Makarov and Vinogradov showed [3] that instead of Nowotny's phase of composition $ThZn_9$, the actual phase formed was Th_2Zn_{17}, having a structure with the following hexagonal lattice spacings: $a = 9.03$ Å, $c = 13.20$ Å.

Details of the Th_2Zn_{17} structure are given in [3].

Conclusions

1. X-ray phase analysis of alloys in the Th–Zn system, taken together with chemical analysis and a study of microstructure, have established the existence of the following chemical compounds:

$Th_{2\pm x}Zn$, $ThZn_2$, $ThZn_4$, Th_4Zn_7, Th_2Zn_{17}

and a phase X of unknown chemical composition. The crystal structures of some of these phases have been determined by x-ray diffraction study of powders and single crystals.

2. The phase $Th_{2\pm x}Zn$ has variable composition shifted to the side of greater thorium content and a structure of the $CuAl_2$ type with spacings $a = 7.62$ Å, $c = 5.62$ Å.

3. The phase $ThZn_2$ has the structure of AlB_2 with spacings $a = 4.20$ Å, $c = 4.17$ Å.

4. The phase $ThZn_4$ has the structure of AlB_4 with spacings $a = 4.26$ Å, $c = 10.4$ Å.

5. The phase Th_4Zn_{17} has rhombohedral structure with spacings $a = 9.03$ Å, $c = 13.20$ Å.

6. Phase X has an unknown chemical composition, but its fcc lattice has constant $a = 5.68_4$ Å.

LITERATURE CITED

1. H. Nowotny, "Die Kristallstrukturen von Zn_9Th, Cd_2Ca, und $(Ag,Mg)_2Ca$," Metallforschung, 1, 1/2, 31 (1946).
2. O.N. Carlson, P. Chiotti, G. Murphy, D. Peterson, B.A. Rogers, J.F. Smith, M. Smutz, M. Voss, and H.A. Wilhelm, "The metallurgy of thorium and its alloys," International Conference on the Peaceful Uses of Atomic Energy, A. Conf., (1955), Vol. 8, p. 556.
3. E.S. Makarov and S.I. Vinogradov, "Crystal structure of Th_2Zn_{17} and U_2Zn_{17}," Kristallografiya, 1, 6, 634-643 (1956).

X-RAY DIFFRACTION STUDY OF THE $PbTiO_3$-"$PbSnO_3$" SYSTEM

Yu. N. Venevtsev, G. S. Zhdanov, and T. N. Shendrik

L. Ya. Karpov Physicochemical Institute

Translated from Kristallografiya, Vol. 1, No. 6,
pp. 657-665, November-December, 1956
Original article submitted June 4, 1956

A wide range of $Pb(Ti, Sn)O_3$ solid solutions extending from 0 to 75 mol.% "$PbSnO_3$" was found to exist in the $PbTiO_3$–"$PbSnO_3$" system. The phase diagram of this solid solution is similar to that of $Pb(Ti, Zr)O_3$ but differs from that of $Ba(Ti, Sn)O_3$. Conclusions are drawn regarding differences in the mechanism of spontaneous electric polarization in the ferroelectrics $BaTiO_3$ and $PbTiO_3$, which have hitherto been regarded as completely analogous.

Introduction

We showed earlier [1,2] that, when the oxides PbO and SnO_2 were sintered in the temperature range 800 to 1050°C, no single compound $PbSnO_3$ resulted; samples of composition $PbSnO_3$ contained two phases, Pb_2SnO_4 and SnO_2. The samples examined in the present paper may thus be regarded as belonging to a linear section of the ternary system $PbTiO_3 - Pb_2SnO_4 - SnO_2$, which can only nominally be written in the form of a binary system $PbTiO_3$–"$PbSnO_3$." Despite the two-phase nature of its components, however, this system $PbTiO_3$–"$PbSnO_3$" may be expected to contain a wide range of solid solutions, in view of the similarity between the radii of the tetravalent ions of titanium (0.64 Å) and tin (0.67 Å), which belong to the same group of the Mendeleev periodic table. The likelihood of this being so is supported by the fact that there are continuous series of solid solutions in systems similar to the one considered, namely, $BaTiO_3$–$BaSnO_3$ [3, 4] and $PbTiO_3$–$PbZrO_3$ [5,6].

A study of the $PbTiO_3$–"$PbSnO_3$" and $BaTiO_3$–$BaSnO_3$ systems is necessary for a deeper understanding of the properties of the ferroelectrics $PbTiO_3$ and $BaTiO_3$. Those who have studied the ferroelectric properties of $PbTiO_3$ [7-11] and the atomic displacements in these [12], consider the two compounds to be completely analogous. It is supposed that in the cells of both compounds the displacement of the titanium ion (below the Curie temperature) from the center of the oxygen octahedron along the four-fold axis leads to the development of electric polarization in the crystal in the same direction. If the properties of these two compounds are similar, then the phase diagrams of the solid solutions $Ba(Ti, Sn)O_3$ and $Pb(Ti, Sn)O_3$ should also be similar. A study of the solid solution $Pb(Ti, Sn)O_3$ is also interesting for elucidating the effects of the different sizes and electron configurations of the mutually interchangeable cations of titanium and tin on the ferroelectric properties.

Characteristics of the Samples

Samples of the $PbTiO_3$–"$PbSnO_3$" system were prepared in the Physics Laboratory of the Institute of Silicate Chemistry, Academy of Sciences of the USSR, by the well-known technique for preparing ceramic ferroelectrics containing lead [9]. The original materials included titanium dioxide and tin ("pure" type) and commercial red lead. The temperature of the final anneal fell from 1060 to 1000 °C with increasing "$PbSnO_3$" content. The dielectric properties of these samples were studied simultaneously in the same laboratory. The results of these dielectric studies are presented in [13].

Method

X-ray photographs were taken at room temperature in the RKU-114 camera. For high- and

low-temperature work special cameras of diameters 120 and 114 mm, respectively, were used. Both the low-temperature camera and the special apparatus for blasting and glazing the samples were developed in the L. Ya. Karpov Physicochemical Institute [14,15] and enabled photographs to be taken from room temperature down to the temperature of liquid nitrogen. In selecting radiation for the precision measurement of parameters, a special nomogram was used [16]. All the samples were taken in Cu Kα radiation, and the sample 40% $PbTiO_3$–60% "$PbSnO_3$" in Ni K and Cr K radiation as well. For work with Cu Kα radiation the 314 and 413 lines of lead titanate lay at angles θ of 76 and 80.5°, respectively.

The films were placed in the RKU-114 camera in an asymmetric fashion. The positions of the lines used for calculating the cell parameters were measured to an accuracy of $\Delta(2L) = \pm 0.1$ mm, and the value of πD_{eff} determined to an accuracy of ±0.01-0.02 mm. Under these conditions the accuracy of determining the cell parameters should have been ±0.001 Å. However, owing to the large thermal-expansion coefficient along the c axis of the lead-titanate cell (about $5 \cdot 10^{-5}$/deg) [11], the error in determining the cell parameters reached ±0.0015 Å for a temperature variation of 3 to 5°. Thus, the errors in determining the axial ratio c/a and volume v of the cell will, respectively, be $\Delta(c/a) = \pm 0.0007$ and $\Delta v = \pm 0.07$ Å^3. For the rhombohedral cells the angle α_{rh} was determined both by the usual method (solution of two equations with two unknowns) and by the method described by Megaw [17]. The values of α_{rh} calculated for several groups of lines: 422 (Cu Kα radiation), 332 (Ni K radiation), and 222 (Cr K radiation) differed by ±1'. This accuracy in determining c/a, v, and α_{rh} gave a reliable check on changes taking place in the cell of the $Pb(Ti, Sn)O_3$ solid solution with varying chemical composition. The wavelength values for the calculation were taken from [18].

Results of Examining Samples at Room Temperature

Our x-ray diffraction photographs showed that the $PbTiO_3$–"$PbSnO_3$" system contained a wide range of solid solutions on the $PbTiO_3$ side, extending from 0 to 75 mol.% "$PbSnO_3$." The range from 75 to 100% "lead stannate" was not single-phase. In this region, x-ray examination revealed the phases $Pb(Ti, Sn)O_3$, X, Pb_2SnO_4, and $(Sn, Ti)O_2$. Conditions for obtaining phase X in the $PbO-SnO_2$ system were indicated in [1,2]. The probable boundaries between these phases in the range 75 to 100 mol.% "$PbSnO_3$" appear in Fig. 1.

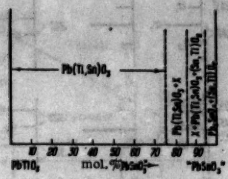

Fig. 1. Phase composition of the samples in the $PbTiO_3$–"$PbSnO_3$" system studied.

For pure lead titanate we confirmed a tetragonal cell with parameters close to those given in [17, 19]. With increasing "lead stannate" content, the tetragonal distortion of the cell diminished and for a 55 mol.% content of "$PbSnO_3$" the tetragonal cell transformed into rhombohedral. The rhombohedral distortion fell with increasing "lead stannate" content but still existed up to the boundary of the solid solution $Pb(Ti, Sn)O_3$. The phase transformation at 55 mol.% "$PbSnO_3$" was confirmed by the following. On the x-ray photographs of samples containing 0-50 mol.% "$PbSnO_3$," as the concentration of the latter increased the components of all groups of lines gradually moved closer together; between 50 and 60 mol.% there was a considerably greater change in the diffraction pictures than that corresponding to a 10% change in the lower range (0 to 50%). Careful analysis of the way in which various groups of lines (especially the 332 group) behaved in the x-ray photographs of these samples showed that between 50 and 60 mol.% "$PbSnO_3$" the cell of the $Pb(Ti, Sn)O_3$ solid solution passed from tetragonal to rhombohedral. Figure 2 gives a schematic representation of the 332 group of lines found on the 60-mol.% photograph for Cu and Ni radiations and the 222 group for Cr radiation. In the same figure (for comparison) we have the same groups of lines for the tetragonal and rhombohedral distortions of the lattice, respectively. We see from Fig. 2 that the observed 332 and 222 groups of lines on the x-ray diffraction picture of $Pb(Ti_{40}, Sn_{60})O_3$ are indexed on the assumption of a rhombohedral distortion of the cell and not on that of a tetragonal distortion.

Figure 3 shows the results of a precision measurement of the cell parameters of solid solution $Pb(Ti, Sn)O_3$. According to [20,21] the transformation of one form into another takes place over a certain range, and the nature of the change in pa-

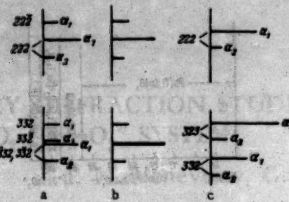

Fig. 2. Groups of 332 and 222 lines for: a) rhombohedral and c) tetragonal distortion of the cell, and also b) for the experimental x-ray diffraction picture of the sample $Pb(Ti_{60}Sn_{40})O_3$.

rameters must be similar to that shown in Fig. 3. In the transitional region in which the tetragonal and rhombohedral forms coexist simultaneously, the parameters change sharply on passing from one form to another. The axial ratio c/a for the tetragonal cell at the beginning of the transitional range is, moreover, larger than at the end.

Figure 4 shows the variation of the axial ratio c/a and angle α_{rh} of the solid-solution cell on the "$PbSnO_3$" content. Figure 5 shows the change in unit-cell volume for the solid solution as a function of composition. The unit-cell volume of the solid solution rises with increasing content of "$PbSnO_3$". This is because the tetravalent tin ion has a larger radius (0.67 Å) than the tetravalent titanium ion (0.64 Å). In the range 0 to 20 mol% "$PbSnO_3$," the cell volume rises nonlinearly, and in the range 20 to 75 mol.%, linearly. On transforming from the tetragonal to the rhombohedral form, the unit-cell volume changes smoothly (within the limits of measuring error), although we might have expected a sharp change, since ferroelectric transformations are transformations of the first kind [22].

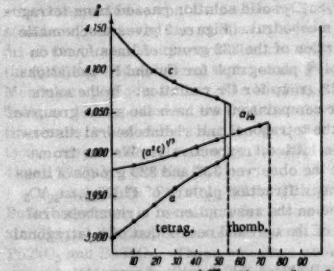

Fig. 3. Unit-cell parameters a and c of solid solution $Pb(Ti,Sn)O_3$ as a function of composition.

Phase Diagram of the Solid Solution $Pb(Ti,Sn)O_3$

In order to construct the phase diagram of the solid solution $Pb(Ti,Sn)O_3$ experiments at room temperature are insufficient. We therefore made some high- and low-temperature measurements of $Pb(Ti_{60},Sn_{40})O_3$ and low-temperature measurements of $PbTiO_3$.

The x-ray diffraction photographs of $PbTiO_3$ and the sample containing 40 mol.% "$PbSnO_3$" taken at liquid-oxygen temperature (–183°C) showed an absence of phase transformations in these samples between –183°C and room temperature.

The cell parameters of lead titanate at –183°C and room temperature are given in Table 1. We see from this table that the axial ratio at –183°C is slightly larger than at room temperature. The unit-cell volume is practically constant over this range. At the same time it is well known that between the Curie point (490°C) and room temperature the unit-cell volume of lead titanate rises [10,11]. The observed fact that the volume remains constant may

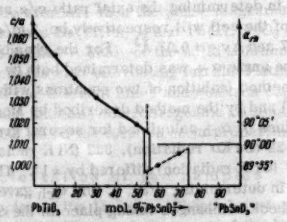

Fig. 4. Variation of c/a and α_{rh} of the solid solution $Pb(Ti,Sn)O_3$ with composition.

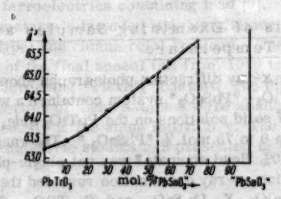

Fig. 5. Variation of the unit-cell volume of solid solution $Pb(Ti,Sn)O_3$ with composition.

TABLE 1. Cell Parameters of Lead Titanate

Temp.	a Å	c Å	c/a	v
Control	3.900	4.153	1.064$_5$	63.1$_8$
–183°C	3.891	4.167	1.071$_1$	63.0$_3$

be explained if the increase in unit-cell volume due to the temperature variation of polarization is compensated by ordinary thermal compression.

The absence of phase transformations in $PbTiO_3$ on cooling with liquid oxygen agrees with dielectric measurements given in [10,11]. The sample containing 40 mol.% "$PbSnO_3$" was also photographed at high temperature. The main aim of the high-temperature work was to discover the Curie point. For the sample in question the Curie temperature as found by x-ray diffraction was 320 ± 5°C. This shows that the Curie point of the solid solution $Pb(Ti,Sn)O_3$ falls as the "$PbSnO_3$" content rises, since, for pure $PbTiO_3$ the Curie temperature is 490°C [9,11,23].

The transformation of the tetragonal form of the solid solution into rhombohedral and the reduction in the Curie point as the "$PbSnO_3$" content rises indicates a similarity between variations in the properties of the solid solution in question, $Pb(Ti,Sn)O_3$, and the well-known solid solution $Pb(Ti,Zr)O_3$ [5,6,24-26], the phase diagram of which is shown in Fig. 6. On replacing the titanium in $PbTiO_3$ by either tin or zirconium, the Curie temperature falls. Moreover, for a certain content of either tin or zirconium there is a transformation from the tetragonal modification to the rhombohedral.

Let us take the variation in the Curie temperature in the $PbTiO_3$ – "$PbSnO_3$" system as linear and, in analogy with the $PbTiO_3$ – $PbZrO_3$ system, the boundary between the tetragonal and rhombohedral forms on the phase diagram as vertical. In this case

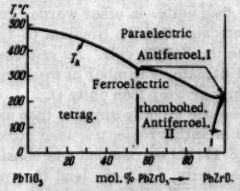

Fig. 6. Phase diagram of $Pb(Ti,Sn)O_3$ from data of [6].

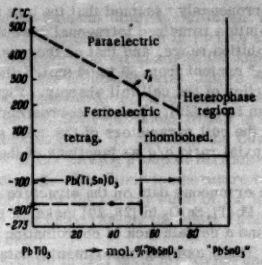

Fig. 7. Phase diagram of solid solution $Pb(Ti,Sn)O_3$.

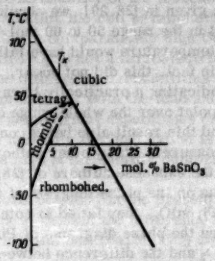

Fig. 8. Phase diagram of solid solutions $Ba(Ti,Sn)O_3$ from data of [27].

the diagram of the phase state of the solid solution $Pb(Ti,Sn)O_3$ will appear as indicated in Fig. 7.

As established in [22], the similarity between the ways in which zirconium and tin ions act on the ferroelectric properties of $PbTiO_3$ on introducing them into its lattice instead of titanium ions is due to the fact that the dimensions of the Zr^{4+} ion (0.82 Å) and Sn^{4+} ion (0.67 Å) exceed those of the Ti^{4+} ion (0.64 Å).

The phase diagram of the solid solution $Pb(Ti,Sn)O_3$ differs from the well-known phase diagram of $Ba(Ti,Sn)O_3$ [27] shown in Fig. 8.

While the present investigation was being carried out, two other papers [28,29] were published on the dielectric and structural properties of the $PbTiO_3$ – "$PbSnO_3$" system. Our conclusions regarding the existence of a solid solution in the range 0 to 75 mol.% "$PbSnO_3$" agree with the results of these papers. At the same time the two-phase nature of the samples with composition $PbSnO_3$ and the presence of phase X in the heterogeneous region was not noted by the other authors, who, more-

over, erroneously assumed that the unit cell of the solid solution remained tetragonal over the whole solid-solution range, and that on increasing the "$PbSnO_3$" content from 50 to 60 mol.% the tetragonal distortion of the cell fell sharply. Figures 9 and 10, taken from [29], show the corresponding variations in the cell parameters of the solid solution and the axial ratio c/a as functions of the "$PbSnO_3$" content.

The erroneous data on the structure of the solid solution $Pb(Ti,Sn)O_3$ in [28,29] make it possible to understand a certain lack of coordination in these papers. Thus, existing experimental data on a number of solid solutions show that the behavior of the Curie temperature in a system may be judged from that of the axial ratio. Assuming the validity of the x-ray data given in [28,29], we should then have expected that in the range 50 to 60 mol.% "$PbSnO_3$" the Curie temperature would have fallen sharply, whereas, in fact, this did not occur, the papers in question indicating a practically linear variation of the Curie point over the whole range of the solid solution and this result also being confirmed by dielectric measurements by other authors [13].

Since the Japanese authors of [28,29] lacked correct data on the phase diagram of the solid solution $Pb(Ti,Sn)O_3$, they failed to note the similarity between the phase diagrams of $Pb(Ti,Sn)O_3$ and $Pb(Ti,Zr)O_3$ and the difference between these and that of $Ba(Ti,Sn)O_3$. This is perhaps why these authors mistakenly assigned a leading role to the difference in the electron structures of the titanium and substituted tin ions. As we have already

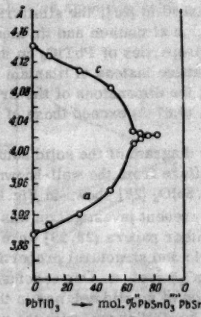

Fig. 9. Variation of a and c cell parameters of solid solution $Pb(Ti,Sn)O_3$ with composition, according to [29].

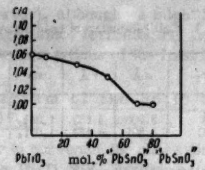

Fig. 10. Variation of axial ratio c/a for the cell of solid solution $Pb(Ti,Sn)O_3$ with composition, according to [29].

pointed out, our own results lead to a different conclusion, namely, that the properties of the solid solution $Pb(Ti,Sn)O_3$ depend substantially on the different sizes of the substituent cations; the difference between the electronic structures of titanium and tin is of subsidiary significance.

Discussion of Results

Our most important experimental result is the establishment of a difference between the phase diagrams of solid solutions $Pb(Ti,Sn)O_3$ and $Ba(Ti,Sn)O_3$, which indicates a lack of agreement between the properties of $PbTiO_3$ and $BaTiO_3$. In this connection it is interesting to compare the properties of these two solid solutions. From the results of [6,27,30], which were published while the present work was in progress, we may conclude that the phase diagram of the solid solution $Ba(Ti,Zr)O_3$ is similar to that of $Ba(Ti,Sn)O_3$, but different from that of $Pb(Ti,Zr)O_3$. Thus, the difference between the phase diagrams of solid solutions $Pb(Ti,Zr)O_3$ and $Ba(Ti,Zr)O_3$ also indicates that $PbTiO_3$ and $BaTiO_3$ are not completely analogous.

Let us consider the factors which may lead to a difference in the properties of these two ferroelectrics.

According to existing estimates of the geometrical criterion t for different compounds of the perovskite type [7,17,31], the value of t for $BaTiO_3$ is greater than unity. In other words, geometrical analysis indicates that the titanium (B-type) cation is "free" in the $BaTiO_3$ cell. As regards the t factor of lead titanate, a number of workers give a value slightly greater than unity [7,31], while Megaw gives one slightly smaller than unity [17]. In the case of antiferroelectric lead zirconate, everyone [6,17,31] agrees that t is considerably smaller than unity, i.e., the lead (A-type) cation is "free" in the cell of this compound. It is apparently for this reason that it is assumed in [32]

that ferroelectrics may include ABO_3 compounds of the perovskite type, in the cells of which the B cations are free ($t > 1$), while antiferroelectrics include only those compounds where this applies to the A cations ($t < 1$).

There are some experimental data, however, which disagree with this last conclusion. Thus, in [6, 33] it was shown by x-ray diffraction that, in the cells of both the ferroelectric rhombohedral and antiferroelectric pseudo-monoclinic form of the solid solution $Pb(Ti, Zr)O_3$, cations of the same type (lead) were free, so that at room temperatures the lead cations in the cells of these solid solutions were considerably displaced relative to the compact $BO_6 = (Zr, Ti)O_6$ octahedra along three-fold and two-fold axes of the original cells, respectively. Thus not only compounds with free B cations, but also those with free A cations, may have ferroelectric properties.

The difference between the properties of the ferroelectrics $BaTiO_3$ and $PbTiO_3$ is primarily connected with the fact that in the case of $PbTiO_3$ the lead (A) cation is free in the cell rather than the titanium (B) cation as in $BaTiO_3$.

On replacing the titanium ions in $PbTiO_3$ by tin or zirconium ions, the geometrical possibilities for the displacement of the lead cation increase. For the solid solution $Pb(Ti, Zr)O_3$ it may be shown that cations of the A type (Pb in the present case) may be displaced along the four-fold (tetragonal form), three-fold (rhombohedral form), and two-fold (pseudo-monoclinic form) axes, in the same way as B-type cations (for example, Ti in $BaTiO_3$).

The displacement of the titanium cation in $BaTiO_3$ (below the Curie point) from the center of the oxygen octahedron leads to a polar rearrangement of the cell. In this sense the titanium cation in $BaTiO_3$ is a ferroactive cation. From this point of view the ferroactive cation in $PbTiO_3$ is the lead.

Workers studying atomic displacements in $PbTiO_3$ by x-ray and neutron diffraction [12] established a picture of atomic displacements in $PbTiO_3$ differing somewhat from that in $BaTiO_3$ and explained this as being due simply to the different polarizabilities of the barium and lead cations; they had no doubts regarding the similarity between the properties of $BaTiO_3$ and $PbTiO_3$, but found confirmation for this in the continuous variation of the Curie temperature and cell parameters of solid solution $(Ba, Pb)TiO_3$ with composition, as established in [34, 35]. No attention was paid to the anomalous temperature dependence of the cell parameters of solid solution $(Ba, Pb)TiO_3$ in the concentration range 10-25 mol.% $PbTiO_3$, established in [36].

Up to the present time, the different mechanisms of electric polarization in $PbTiO_3$ and $BaTiO_3$ have not been considered in any of the known publications [9, 37-39] dealing with factors responsible for the different Curie temperatures of these compounds. Hence, the conclusions drawn in these papers regarding factors affecting the Curie temperatures of the $BaTiO_3$ group of ferroelectrics require checking. The Curie temperature of $PbTiO_3$ is determined by the energy state of the lead cation, and that of $BaTiO_3$ by the energy state of the titanium cation.

We showed in [22] that, for ferro- and antiferroelectrics with $t < 1$ and cations A of the same valence, the Curie temperature was the higher, the greater the polarizability of the ferroactive A cation and the smaller the cell parameters. The fact that $PbTiO_3$ has a comparatively high Curie point (490°C) and $SrTiO_3$ is not a ferroelectric is explained by the different polarizabilities of the lead and strontium cations. Both the lead and strontium cations have geometrical capabilities of displacement, but in fact only the lead cation is ferroactive in view of its high polarizability compared with that of strontium.

The results obtained in the present investigation enable us to explain the difference in the properties of solid solutions $(Ba, Sr)TiO_3$ and $(Ba, Pb)TiO_3$.

Conclusions

1. A range of solid solutions extending from 0 to 75 mol.% "$PbSnO_3$" has been established in the $PbTiO_3$ – "$PbSnO_3$" system.

2. For a "$PbSnO_3$" content up to 55 mol.% the cell remains tetragonal; in the range 55 to 75 mol.% it becomes rhombohedral.

3. The phase diagram of solid solution $Pb(Ti, Sn)O_3$ has been obtained for various temperatures from x-ray data; it is similar to that of $Pb(Ti, Zr)O_3$, but differs from that of $Ba(Ti, Sn)O_3$.

4. The mechanisms of electric polarization in ferroelectrics $BaTiO_3$ and $PbTiO_3$, hitherto considered completely analogous, are apparently different.

5. The different properties of $BaTiO_3$ and $PbTiO_3$ are mainly explained by the fact that in $BaTiO_3$ the ferroactive cation is titanium (B type), while in $PbTiO_3$ it is lead (A type).

We consider it our duty to thank Doctor of Physicomathematical Sciences G. A. Smolenskii for providing the samples for study and discussing some of the results.

Note Added in Proof

Some of the experimental results in our earlier paper [1] are independently confirmed by B. Jaffe, R. S. Roth, and S. Marzullo (J. Res. Nat. Bur. Stds., 55, 239-254, 1955); we only became aware of this after going to press.

LITERATURE CITED

1. Yu. N. Venevtsev and G. S. Zhdanov, "X-ray study of solid solutions of ferroelectrics with the perovskite structure," Izv. Akad. Nauk SSSR, ser. fiz., 20, 2, 178-184 (1956).
2. Yu. N. Venevtsev and G. S. Zhdanov, "On lead metastannate ($PbSnO_3$)," Zh. Fiz. Khim., 30, 6, 1324-1326 (1956).
3. G. A. Smolenskii, M. A. Karamyshev, and K. I. Rozgachev, "Ferroelectric properties of some solid solutions," Dokl. Akad. Nauk SSSR, 79, 1, 53-56 (1951).
4. R. H. Dungan, D. F. Kane, and L. R. Bickford, "Lattice constants and dielectric properties of barium titanate–barium stannate–strontium titanate bodies," J. Am. Ceram. Soc., 35, 12, 318-321 (1952).
5. G. Shirane, K. Suziki, and A. Takeda, "Phase transition in solid solution of $PbZrO_3$ and $PbTiO_3$. II. X-ray study," J. Phys. Soc. Japan, 7, 1, 12-18 (1952).
6. E. Sawaguchi, "Ferroelectricity versus antiferroelectricity in solid solutions of $PbZrO_3$ and $PbTiO_3$," J. Phys. Soc. Japan, 8, 5, 615-629 (1953).
7. G. H. Jonker and J. H. van Santen, "Dielectric properties of titanates of perovskite type," Chem. Weekblad, 43, 672-679 (1947).
8. J. H. Van Santen and G. H. Jonker, "Effect of temperature on the permittivity of barium titanate," Nature, 159, 4036, 333 (1947).
9. G. A. Smolenskii, "Ferroelectric properties of certain titanates and zirconates of divalent metals with the perovskite structure," Zh. Tekhn. Fiz., 20, 2, 137 (1950); "New ferroelectrics," Dokl. Akad. Nauk SSSR, 70, 3, 405 (1950); Dissertation: Ferroelectrics with the Perovskite Structure [in Russian] (IKhS, AN, Leningrad, 1954).
10. G. Shirane, S. Hoshino, and K. Suzuki, "X-ray study of phase transition in lead titanate," Phys. Rev., 80, 6, 1105 (1950).
11. G. Shirane and S. Hoshino, "On the phase transition in lead titanate," J. Phys. Soc. Japan, 6, 4, 265 (1951).
12. G. Shirane, R. Pepinsky, and B. C. Frazer, "X-ray and neutron diffraction study of ferroelectric $PbTiO_3$," Phys. Rev., 97, 4, 1179-1780 (1954); Acta Cryst., 9, 131-140 (1956).
13. G. A. Smolenskii, A. I. Arganovskaya, A. M. Kalinina, and T. M. Fedotova, "Ferroelectric properties of solid solutions (Pb, Ba)SnO_3, Pb(Ti, Sn)O_3, and Pb(Zr, Sn)O_3," Zh. Tekhn. Fiz., 25, 12, 2134 (1955).
14. M. M. Umanskii, G. S. Zhdanov, G. A. Gol'der, A. G. Kapyshev, and L. A. Lebedev, "X-ray photography of single crystals and polycrystalline samples at low temperatures," Zavod. lab., 6, 703 (1952).
15. A. G. Kapyshev and G. S. Zhdanov, "X-ray camera for low-temperature photography with a frame cassette," Scientific-Information Bulletin "Pribory i Stendy" (in press).
16. G. S. Zhdanov, "Nomogram for selection of anode in precision measurements of lattice constants," Zavod. lab., 8, 999 (1939).
17. H. D. Megaw, "Crystal structure of double oxides of the perovskite type," Proc. Phys. Soc., 58, 133 (1946).
18. K. Lonsdale, "International tables: x-ray wavelength values," Acta Cryst., 3, 400 (1950).
19. J. Naray-Szabo, "Structure of compounds ABO_3 sister structures," Naturwiss., 31, 466 (1943).
20. H. F. Kay and P. Vousden, "Symmetry changes in barium titanate at low temperatures and their relation to its ferroelectric properties," Phil. Mag., 7, 40, 1019 (1949).
21. K. Suzuki, "On the phase transition in barium–lead titanate," J. Phys. Soc. Japan, 6, 5, 340 (1951).
22. Yu. N. Venevtsev, Dissertation: X-Ray Structural Study of Solid Solutions of Ferroelectrics with the Perovskite Structure [in Russian] (MIFI, Moscow, 1955).
23. H. H. Rogers, Technical Report No. 56, Laboratory for Insulation Research, Mass. Inst. Tech. (1953).
24. G. Shirane and A. Takeda, "Phase transition in solid solutions of $PbZrO_3$ and $PbTiO_3$. I. Small concentration of $PbTiO_3$," J. Phys. Soc. Japan, 7, 1, 5-11 (1952).
25. G. Shirane and K. Suzuki, "Crystal structure of Pb(Zr–Ti)O_3," J. Phys. Soc. Japan, 7, 333 (1952).
26. B. Jaffe, R. S. Roth, and S. Marzullo, "Piezoelectric properties of lead zirconate–lead titanate solid solution ceramic ware," J. Appl. Phys., 25, 809-810 (1954).
27. G. A. Smolenskii and V. A. Isupov, "Phase

transformations in certain solid solutions having ferroelectric properties," Dokl. Akad. Nauk SSSR, 96, 1, 53 (1954); "Ferroelectric properties of solid solutions of barium stannate in barium titanate," Zh. Tekhn. Fiz., 24, 8, 1375-1386 (1954).

28. S. Nomura and S. Sawada, "Dielectric substances having high permittivity. III. Solid solutions of titanates," Rept. Inst. Sci. Techn. Univ. Tokyo, 7, 83-86 (1953).
29. S. Nomura, "Dielectric properties of titanates containing Sn^{4+} ions. I," J. Phys. Soc. Japan, 10, 2, 112-119 (1955).
30. M. McQuarrie and F. Behnke, "Structural and dielectric studies in the system (Ba, Ca) · $(Ti, Zr)O_3$," J. Am. Ceram. Soc., 37, 11, 539 (1954).
31. J. Naray-Szabo, "The perovskite structure family," Müegyetemi Közlemények, 1, 30 (1947).
32. E. Wainer and C. Wentworth, "Niobate and tantalate dielectrics," J. Am. Ceram. Soc., 35, 8, 207 (1952).
33. E. Sawaguchi, H. Maniwa, and S. Hoshino, "Antiferroelectric structure of lead zirconate," Phys. Rev., 83, 5, 1078 (1951).
34. G. Shirane and K. Suzuki, "On the phase transition in barium–lead titanate," J. Phys. Soc. Japan, 6, 4, 275-277 (1951).
35. G. Shirane and A. Takeda, "On the phase transition in barium–lead titanate. II," J. Phys. Soc. Japan, 6, 5, 329 (1951).
36. K. Suziki, "On the phase transition in barium–lead titanate," J. Phys. Soc. Japan, 6, 5, 340 (1951).
37. H. D. Megaw, "Ferroelectricity and crystal structure. II," Acta Cryst., 7, 187 (1954).
38. P. Vousden, "A study of the unit-cell dimensions and symmetry of certain ferroelectric compounds of niobium and tantalum at room temperature," Acta Cryst., 4, 373 (1951).
39. A. Hippel, "Piezoelectricity, ferroelectricity, and crystal structure," Z. Phys., 133, 5, 158-173 (1952).

DETERMINATION OF THE STRUCTURE OF SiB_6 BY X-RAY DIFFRACTION

N. N. Zhuravlev

M.V. Lomonosov State University, Moscow

Translated from Kristallografiya, Vol. 1, No. 6, pp. 666-668, November-December, 1956
Original article submitted March 15, 1956

The compound SiB_6 crystallizes with cubic symmetry and is isostructural with CaB_6. The lattice parameters are $a = 4.142 \pm 0.002$ kX, $\sigma_{pycn} = 2.15$, $\sigma_{x\ ray} = 2.18$ g/cm³; Z = 1, space group O_h^1.

Moissan [1] was the first to report a compound of silicon with boron. He reported that the fusion of silicon with boron gave two compounds, SiB_3 and SiB_6, which were very hard and conducted electricity. In a handbook [2] it is stated that SiB_3 consists of black rhombic crystals with a density of 2.52 g per cm³, while black crystals of SiB_6 have a density of 2.47 g/cm³.

The samples of SiB_6 which we have studied were prepared by G.V. Samsonov (Moscow Institute of Nonferrous Metals and Gold) from elemental silicon and boron and also by reducing a mixture of boric oxide and quartz with magnesium. The synthesis from the elements was carried out by sintering a mixture of powdered boron and silicon in a hot press. The samples were black powders.

The x-ray photographs were taken in a 114.4 mm RKU camera with CuKα radiation. Initial calculations indicated the presence of a cubic phase with a lattice parameter of $a = 4.14$ kX, and this suggested the presence of a silicon hexaboride with a structure of the cubic hexaboride type. A comparison of the x-ray photographs of polycrystalline CaB_6 and SiB_6 showed their similarity and confirmed the suggestion that they were isomorphous.

The intensities I and the positions of the lines were measured on x-ray photographs of samples of SiB_6, and the value of d was subsequently calculated (Table 1).

From an exact determination the lattice period of SiB_6 was found to be $a = 4.142 \pm 0.002$ kX. The interplanar distances calculated on this basis (see Table 1) were in excellent agreement with the measured values. It should be noted that the period a for SiB_6 is very close to those of the known hexaborides (CaB_6, LaB_6, etc.) [3].

The density of the crystals of SiB_6 was determined as $\sigma_{pycn} = 2.15$ g/cm³ by hydrostatic weighing [4] in carbon tetrachloride; with Z = 1, we obtained $\sigma_{x\text{-}ray} = 2.18$ g/cm³. The density of SiB_6 is less than those of silicon and boron and this probably has some effect on the conditions for obtaining the compound. In structures of the CaB_6 type, the atoms take up the a and f positions in space group O_h^1 – Pm3m [5]

$$\text{Si } 1(a),\quad 000,$$

$$\text{B } 6(f),\quad \pm\left(x\ \tfrac{1}{2}\ \tfrac{1}{2}\right).$$

The structure amplitude is:

$$F_{hkl} = f_{Si} + 2f_B\left[\cos 2\pi\left(hx + \frac{k+l}{2}\right) + \cos 2\pi\left(kx + \frac{h+l}{2}\right) + \cos 2\pi\left(lx + \frac{h+k}{2}\right)\right].$$

A value of 0.21 was taken for x. The line intensities were calculated according to the formula

$$I \sim L_p p F^2,$$

where L_p is the Lorentz polarization factor and p is the frequency factor.

TABLE 1. Data from Measurements and Calculations on the X-Ray Photograph of SiB_6

hkl	d_{calc}	d_{exp}	I_{exp}	I_{theor}	
100	4.14	—	—	0.1	
110	2.93	2.93	very strong	463	
111	2.39	2.40	strong	190	
200	2.07	2.07	mod. strong	123	
210	1.85	1.85	strong	166	
211	1.69	1.69	mod. weak	14.5	
220	1.46	1.46	mod. weak	15.8	
300	1.38	1.38	strong	0.7	216.7
221	1.38			216	
310	1.31	1.31	strong	133	
311	1.25	1.25	average	35	
222	1.19	—	—	0.3	
320	1.15	1.15	mod. weak	12.0	
321	1.108	1.107	average	32.3	
400	1.036	1.035	mod. weak	30.9	
410	1.004	1.004	average	3.5	60.8
322	1.004			57.3	
411	0.977	0.976	mod. strong	22.5	78.1
330	0.977			55.6	
331	0.951	—	—	1.4	
420	0.927	0.927	mod. weak	42.7	
421	0.904	0.904	mod. strong	81	
332	0.884	0.884	mod. weak	36	
422	0.845	0.845	very strong	3.2	
500	0.828	—	—	1.2	2.8
430	0.828			1.6	
510	0.8123	0.8124	strong	101	249
431	0.8123			148	
511	0.7972	0.7972	mod. strong	134	134.2
333	0.7972			0.2	

A comparison of the calculated and measured intensities (Table 1) showed excellent agreement.

The samples studied contained, apart from the basic phase of SiB_6, small amounts of impurities, probably SiO_2 and SiC, which produced additional weak lines on the x-ray photograph (2-5 lines). The difference in density obtained by us and in the literature [2] probably resulted from the presence of different quantities of impurities, denser than SiB_6 in the different samples. The isostructural hexaborides have a simple cubic lattice in which the boron atoms form a three-dimensional skeleton in the holes of which the metal atoms are found – silicon atoms in the case of SiB_6. The boron atoms are at the vertices of octahedra, and each boron atom is surrounded by five others at a distance of 1.72 kX. Four of these atoms are in the same octahedron while the fifth is in a neighboring octahedron. In addition, each boron atom is surrounded by four metal atoms in such a way that the four metal atoms and the boron atom form a tetragonal pyramid with the metal atoms at the base.

The metal atoms have a high coordination number. They are surrounded by 24 boron atoms and six metal atoms. The metal–boron distance is considerably greater than the sum of the atomic radii. This indicates the formation of a stable skeleton from the boron atoms with the metal atoms distributed in its holes. The metal–boron bond is weakened as the atomic radius of the metal decreases [6].

In the case of SiB_6, the atomic radius of silicon is considerably less than those of the other light metals which form hexaborides, and the silicon–boron distance is very different from the sum of the atomic radii ($Si + B = 3.05$ kX; $R_{Si_{12}} + R_{B_{12}} = 1.34 + 0.91 = 2.25$). This peculiarity of the SiB_6 structure may explain the difficulty in making the compound SiB_3 [7].

The author thanks Professor G.S. Zhdanov (Head of the Department of Solid State Physics), and dozent M.M. Umanskii for discussion of the results, aspirant A.A. Stepanova for the gift of x-ray photographs of some hexaborides, and dozent G.V. Samsonov (Department of Rare Metal Metallurgy, Mintsvetmetzoloto) for presenting the samples.

LITERATURE CITED

1. H. Moissan and A. Stock, Compt. rendus, Acad. Sci., 131, 139 (1900).
2. C.D. Hodgman, Handbook of Chemistry and Physics, 33rd edition (1951-1952), p. 468. Chemical Rubber Publishing Co., Cleveland, Ohio.

3. A.A. Stepanova and M.M. Umanskii, Proc. Conference on the Chemistry of Boron and Its Compounds [in Russian] (1955).
4. É.M. Bronshtadt-Kupletskaya, Determination of the Specific Gravity of Minerals [in Russian] (1951), pp. 43-55.
5. G.B. Bokii, Introduction to Crystal Chemistry [in Russian] (1954), p. 325.
6. R. Kiessling, Acta. Chem. Scand., 4, 209 (1950).
7. G.V. Samsonov and V.P. Latysheva, Dokl. Akad. Nauk SSSR, 105, 3, 499 (1955).

THE CRYSTAL STRUCTURE OF TETRAPHENYL-PHOSPHONIUM IODIDE AND THE CONFIGURATION OF TETRAARYL IONS AND MOLECULES

T. L. Khotsyanova and Yu. T. Struchkov

Institute of Hetero-organic Compounds

Translated from Kristallografiya, Vol. 1, No. 6, pp. 669-676, November-December, 1956
Original article submitted May 19, 1956

Solution of the Structure

The crystals of tetraphenylphosphonium iodide $[(C_6H_5)_4P]I$ were light yellow tetragonal prisms with dimensions of 4.0 × 0.3 × 0.3 mm.[1] Goniometry of the crystals showed the presence of faces of only one simple form {110} (relative to our chosen axis). The x-ray study was by the oscillation method and by photographing the reciprocal lattice in copper radiation. The lattice parameters were:

$a = b = 11.88 \pm 0.06$ Å, $c = 6.96 \pm 0.02$ Å (prism axis), $V = 982$ Å^3,

$M = 466.3$, $p \approx 1.5$ g/cm^3 ($p_{x\,ray} = 1.58$), $n = 2$ (1.89).

By rotation about the c axis in a camera for photographing the reciprocal lattice, the zero-, first-, second-, and third-layer lines were developed. The intensities of the reflections were estimated visually and converted to a general scale via the oscillation photograph. The number of independent reflections of which the intensities were measured was 231. In converting the intensities to structure factors, only the Lorentz and polarization factors were taken into account.

The symmetry of the reflections indicated that the crystals belonged to the Laue class 4/m, and the presence of systematic absences with $h + k + l \neq 2n$ indicated three possible space groups: I4/m, I/4, and $I\bar{4}$. A distinct piezoelectric effect ruled out the first of these space groups; in the other two the I^- and $(C_6H_5)_4P^+$ ions must occupy special positions on the symmetry axes when the multiplicity is two, but since the cation has a tetrahedral configuration, the choice of space group is unambiguous, namely, $I\bar{4} = S_4^2$. This group is one of four which permit close packing of molecules with symmetry $\bar{4}$ [1].

Because of the absence of a center of symmetry, the atomic coordinates were determined by calculation of a three-dimensional interatomic vector series:

$$P(xyz) = \sum\sum\sum [(F_{hkl}^2 + F_{h\bar{k}l}^2)\cos 2\pi hx \cos 2\pi ky - (F_{hkl}^2 - F_{h\bar{k}l}^2)\sin 2\pi hx \sin 2\pi ky] \cos 2\pi lz.$$

In practice, a section was calculated along the c axis through the region of the maxima in a projection on the *ab* face. (The side of the lattice was divided into 60 parts.) In this projection (independent of the region $a/4$, $b/2$) the maxima next in height above the background were at $x = 0$, $y = \frac{1}{2}$. Consequently, the cation and anion are on different $\bar{4}$ axes; the iodine atoms occupy the 2 (*a*) positions :000, while the phosphorus atoms occupy the 2(c) positions: $0, \frac{1}{2}, \frac{1}{4}$. Since the I – P and I–C maxima are considerably larger than the P–P, P–C, and C–C maxima, only the maxima of the first two types are revealed in the interatomic function which appears as the union of two structures joined by a plane of symmetry through the iodine atoms and perpendicular to the $\bar{4}$ axis. Hence, the "untangling of the structure" is reduced to the choice of one of two values of the z coordinate for each maximum (atom). The choice was made by taking geometrical considerations into account (interatomic distances for P–C and C–C) and appeared to be unambiguous for all atoms. The coordinates found are given in Table 1. The coordi-

[1] The authors thank G. A. Razuvaev for presenting the sample for study.

nates of the maxima were determined by interpolation, while those of the hydrogen atoms were calculated with the usual assumptions (C–H = 1.08 Å, and the C–H bond is the bisector of the C – C – C angle).

The structure amplitudes F_{hk0} were calculated from the coordinates of Table 1. They showed that all were positive and the corresponding centrosymmetric electron density projection (Fig. 1) gave practically the same x and y coordinates.

Description of the Structure

The structure of tetraphenylphosphonium iodide is constructed from I^- anions and tetrahedral $(C_6H_5)_4P^+$ cations which occupy special positions on the 4 axes of different sets (Fig. 2).

We shall first discuss the structure of the cation. The length of the P–C bonds is 1.80 Å, i.e., 0.07 Å less than the sum of the single-bond covalent radii ($r_C + r_P = 0.77 + 1.10 = 1.87$ Å). This shortening is not remarkable, since interatomic distances between an element and a carbon atom of a benzene ring are usually shorter than the sums of the corresponding single-bond covalent radii. It should be noted that there is only one recorded P–C bond length in the literature [2], and this was obtained from an electron-diffraction study of trimethylphosphine vapor, $(CH_3)_3P$, and is equal to 1.87 Å. The bond lengths in the benzene ring were:

$C_1 - C_2$	1.42	$C_4 - C_5$	1.44
$C_2 - C_3$	1.41	$C_5 - C_6$	1.41
$C_3 - C_4$	1.38	$C_6 - C_1$	1.37

Average 1.41±0.02 Å

The equation for the plane of the benzene ring (nucleus IV of Fig. 2) was found by the least-squares method and has the form $0.707x - 0.150y + 0.692z - 0.098 = 0$. The distances of the carbon atoms from this plane are:

C_1	−0.02 Å,	C_4	0.02 Å,
C_2	0.03,	C_5	−0.03,
C_3	−0.02,	C_6	0.04.

Thus, the average divergence from the plane is ±0.03 Å and, consequently, the error in determining the bond lengths is not greater than 0.05 Å. Hence, the bond lengths in the benzene ring are the same within the limits of experimental error. For the error in determination of the bond angles, the divergence of the P–C_1 bond from the C_1–C_4 diagonal of the benzene ring should be taken; it did not exceed 2°.

The bond angles at phosphorus were not tetrahedral: $\psi = C_1(I) - P - C_1(II) = 112.5°$, $\omega = C_1(I) - P - C_1(III) = 103°$ (the numbering of the benzene rings is shown in Fig. 2). It appears that the divergence of the bond angles does not gainsay the $\bar{4}$ symmetry and it has a natural explanation, as is shown below. The angle between the planes of the benzene rings I and II is 118.5°, and that between the planes of rings I and III is 92.5°. It is not difficult to show that the mutual orientation of the benzene rings of the cation in the crystal is real and corresponds to a minimum energy.

We shall discuss the cation $(C_6H_5)_4P^+$ with symmetry $\bar{4}$. Its configuration is described by the bonding angles ψ and ω, and by the angle φ between the normal to the plane of a benzene ring and the "vertical" plane which passes through the $\bar{4}$ axis and the P–C_1 bond (Fig. 3). The presence of $\bar{4}$ symmetry requires that the angle φ should be the same for all four benzene rings (I, II, III, IV) of the cation.

A characteristic of the tetraphenylphosphonium ion is the steric hindrance between the carbon and hydrogen atoms of different benzene nuclei. For example, the distance between the "bound" atoms C_1 of two benzene nuclei with an ideal configuration about phosphorus is $2 \cdot 1.80 \cdot \sin(109°28'/2) = 2.04$ Å (Fig. 3), whereas twice the intermolecular radius for carbon is 3.4–3.6 Å. For simplicity we shall assume that all the bond angles of the cation have the theoretical value, i.e., $\psi = \omega = 109°28'$, and we shall find the relation of the steric hindrance in the cation to the angle of rotation φ of the benzene rings about the P–C bonds. This relation is shown in Fig. 4. Here, Δ is the sum of the reductions in the distances between nonbonded atoms relative to the sum of the intermolecular radii:

$$\Delta = \sum_{i,k} \delta_{ik} = \sum_{i,k} R_i + R_k - d_{ik},$$

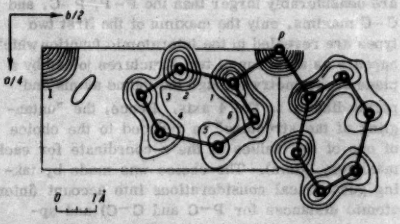

Fig. 1. Electron-density projection on the *a b* face. The electron density was calculated in arbitrary units. The contour lines for iodine are about three times as far apart as in the remainder of the diagram.

TABLE 1. Coordinates of the Symmetry-Independent Atoms

Atom	Å			Relative		
	x	y	z	x	y	z
I	0	0	0	0	0	0
P	0	5.94	1.74	0	1/2	1/4
C_1	0.80	4.78	0.83	0.067	0.402	0.091
C_2	0.48	3.40	0.59	0.040	0.286	0.085
C_3	1.14	2.46	−0.22	0.096	0.207	−0.032
C_4	2.06	2.98	−1.11	0.173	0.251	−0.160
C_5	2.38	4.38	−1.07	0.200	0.369	−0.154
C_6	1.70	5.31	−0.26	0.143	0.447	−0.037
H_2	−0.25	3.03	1.23	−0.021	0.255	0.177
H_3	0.92	1.36	−0.20	0.077	0.115	−0.029
H_4	2.55	2.29	−1.78	0.215	0.193	−0.256
H_5	3.11	4.77	−1.71	0.262	0.402	−0.246
H_6	1.89	6.41	−0.28	0.159	0.540	−0.040
Center of gravity of benzene ring	1.43	5.94	−0.24	0.120	0.327	−0.035

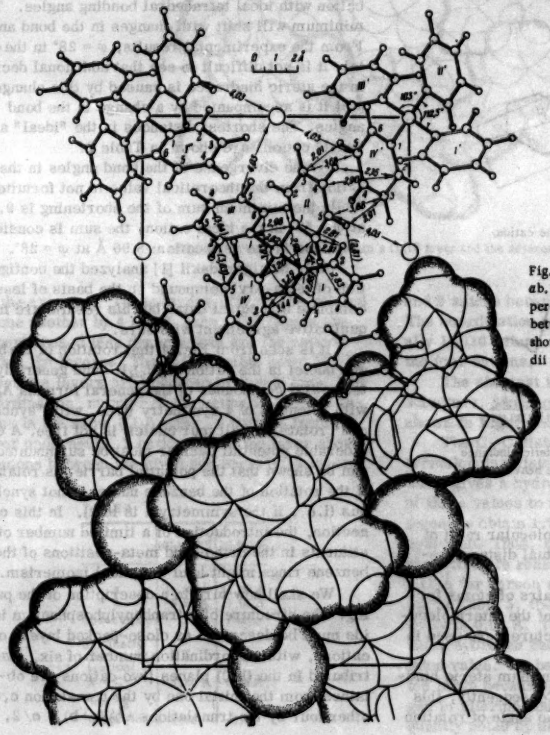

Fig. 2. Projection of the structure on the face ab. A "skeletal" diagram is shown in the upper half, together with the shortest distances between nonbonded atoms. The lower half shows the packing with the intermolecular radii used in the calculations.

TABLE 2. Shortening of the Distance (A) Between Nonbonded Atoms in the Cation

Distance	No. of distances	"Real cation" $\phi = 112.5°$, $\omega = 169°$, $\varphi = 28°$		"Ideal" cation $\phi = \omega = 109°28'$ $\varphi = 28°$		"Ideal cation" $\phi = \omega = 109°28'$, $\varphi = 52°$	
		d_{ik}	s_{ik}	d_{ik}	s_{ik}	d_{ik}	s_{ik}
$C_1(I) - C_1(II)$ . .	4	2.96	0.64	2.94	0.68	2.94	0.68
$C_2(I) - C_6(II)$ . .	4	3.47	0.15	3.43	0.19	3.86	—
$C_3(I) - C_3(II)$ . .	4	3.29	0.33	3.13	0.49	3.19	0.43
$C_5(I) - C_4(II)$ . .	4	3.44	0.18	3.22	0.40	3.51	0.11
$H_2(I) - C_1(II)$ . .	4	2.81	0.06	2.60	0.27	2.70	0.17
$H_6(I) - C_6(II)$ . .	4	2.81	0.06	2.49	0.38	2.70	0.17
$C_2(I) - C_1(III)$ . .	2	2.82	0.80	2.94	0.68	2.94	0.68
$C_3(I) - C_6(III)$ . .	4	3.20	0.42	3.47	0.15	3.27	0.35
$C_4(I) - C_4(III)$ . .	2	>3.70	—	>3.70	—	3.34	0.28
Sum of the shortenings	—	—	8.96	—	11.60	—	9.56

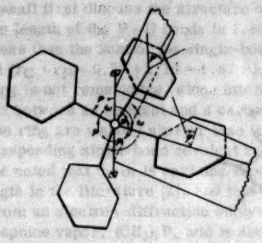

Fig. 3. Configuration of the cation.

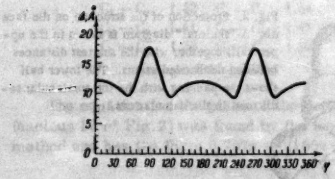

Fig. 4. Relation between the steric hindrance and the angle of rotation of the benzene rings about the P–C bond.

where R_i and R_k are the intermolecular radii of atoms i and k, and d_{ik} is the actual distance between them.

Sums were taken over all pairs of atoms for which $R_i + R_k > d_{ik}$ (the values of the intermolecular radii found in the given structure were used in the calculation; see below).

It is shown in Fig. 4 that minimum steric hindrance corresponds to $\varphi = 52°$. Consequently, this is the energetically most suitable angle of rotation of the benzene rings and should occur in the "free" cation with ideal tetrahedral bonding angles. The minimum will shift with changes in the bond angle. From the experimental results, $\varphi = 28°$ in the crystal. It is not difficult to see that additional decrease in the steric hindrance is caused by this change in φ if it is accompanied by a change in the bond angles. The shortest distances in the "ideal" and "real" cations are shown in Table 2.

So the divergence of the bond angles in the real cation from the theoretical value is not fortuitous. While the minimum sum of the shortening is 9.56 Å at $\varphi = 52°$ in the ideal cation, the sum is considerably less in the real cation: 8.96 Å at $\varphi = 28°$.

A. I. Kitaigorodskii [1] analyzed the configuration of tetra-aryl compound on the basis of less complete structural data, but his results are in qualitative agreement with ours.

It is seen from Fig. 4 that rotation of the benzene nuclei in the cation $(C_6H_5)_4P^+$ (and generally in tetra-aryl compounds of the general formula A_4X) with retention of $\bar{4}$ symmetry (i.e., with "synchronous" rotation of all four nuclei) is not free. A considerable potential barrier must be surmounted. It can be shown that the potential barrier is retained if the rotation of the benzene nuclei is not synchronous (i.e., if the symmetry $\bar{4}$ is lost). In this connection, the introduction of a limited number of substituents in the ortho- and meta-positions of the benzene rings might lead to optical isomerism.

We shall now turn to a description of the packing. The structure of tetraphenylphosphonium iodide must be described as close-packed layers of cations, with a coordination number of six, distributed in the (110) planes [two cations are obtained from the initial one by the translation c, the other four by the translations $\pm\frac{1}{2}(a+b) \pm c/2$, or

TABLE 3. Shortest Intermolecular Distances

Atoms	Bonds	Dist., A	Sum of radii, A	Diff., A	Atoms	Bonds	Dist., A	Sum of radii, A	Diff., A
$C_2(I) - C_5(II)$	e	3.63	3.62	0.01	$C_6(II) - H_3(IV')$	2_1	2.90	2.87	0.03
$C_2(I) - H_3(II)$	e	2.81	2.87	0.06	$H_4(II) - H_3(IV')$	2_1	2.16	2.12	0.04
$C_3(I) - C_5(II)$	e	3.64	3.62	0.02	$C_3(II) - C_3(IV')$	2_1	3.68	3.62	0.06
$C_3(I) - H_4(II)$	e	2.83	2.87	0.04	$H_3(II) - C_3(IV')$	2_1	2.91	2.87	0.04
$C_4(I) - H_4(II)$	e	2.88	2.87	0.01	$C_3 - I$	—	4.03	—	—

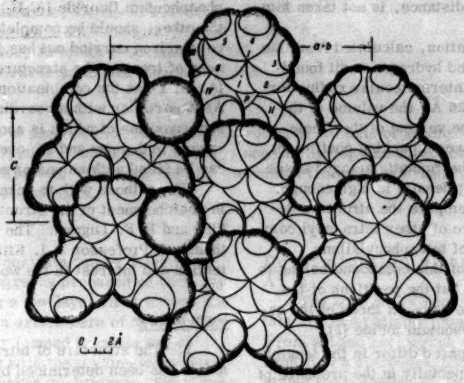

Fig. 5. Packing of the cations in a (110) layer and the adjacent anions.

by the axes 2_1]. These layers (Fig. 5) are related to one another by $\bar{4}$ and 2_1 axes. The layers are superimposed less densely than are the cations within the layers. The considerable holes left between the layers are occupied by iodide ions. The coordination number of the cation is 14: six cations in the same (110) layer, 2 cations from the layer underneath, 2 cations from the layer above, 2 anions between the given and underlying layers, and 2 anions between the given and overlying layers. The coordination number of the anion is also formally 14 (10 anions and 4 cations) but it only touches the four cations.

TABLE 4

	$[(C_6H_5)_4P]I$	$(C_6H_5)_4Sb]I$
a	11.88 Å	11.30 Å
c	6.96 Å	7.08 Å
Space group	$I\bar{4}$	$P\bar{4}2_1c$
n	2	2
Symmetry of molecule (cation)	$\bar{4}$	$\bar{4}$
X – C	1.80 Å	1.94 Å
Packing coefficient	0.76	0.71

The shortest intermolecular distances in the structure, which correspond to atomic contacts are shown in Figs. 2 and 5 and cited in Table 3.

The C–C distance leads to a normal carbon intermolecular distance of 1.83 Å and the H–H distance gives a hydrogen radius of 1.08 Å. Using one of these values to find the other from the C–H distance we obtain 1.79 Å for carbon and 1.04 Å for hydrogen. Thus, the intermolecular radii in this structure are reasonably constant and are equal to 1.81 Å for carbon and 1.06 Å for hydrogen. According to Table 3, the average divergence from additivity is 0.03 Å. The value found for the intermolecular hydrogen radius is 0.1 Å less than the tabulated value. We believe that the tabulated value is too large because of the "compression" of hydrogen in intermolecular contacts which has been frequently noted by us and by other workers (e.g., in

the structure of naphthalene [3]). The ionic radius of iodine in this structure is 2.22 Å, which is somewhat larger than the normally accepted value (2.16 Å according to Pauling). Evidently, the value of 2.22 Å may be taken as the radius of the free iodide ion since the polarizing effect of P^+ can be neglected because it is so far from the I^-. On the other hand, the values of the ionic radius given in the literature are determined from structures with monatomic cations – polarization of the iodide ion, which would shorten the interatomic distance, is not taken into account.

The volume of the cation, calculated from the intermolecular carbon and hydrogen radii found above and the tabulated intermolecular radius for phosphorus (1.9 Å), is 326 $Å^3$; the volume of the anion is 46 $Å^3$, so that the volume of the "molecule" is 372 $Å^3$. This gives a packing coefficient of 0.76. Thus, despite the "unsatisfactory" shape of the cation, the packing density is high enough.

It is of interest to compare the structure described with the structure of other tetra-aryl compounds, e.g., with that of tetraphenylsilane $(C_6H_5)_4Si$. The crystals of this compound belong to space group $P\bar{4}2_1c = V_d^4$, but the positions of the molecules are exactly the same as those of the cations in tetraphenylphosphonium iodide [1].

The structures compared differ in the lengths of the X–C bonds and especially in the presence of large anions in the phosphorus compound. Nevertheless, the similarity is very great. This indicates that there are considerable holes in the structures of tetra-aryl compounds, and these can be filled with anions on going to structures of the type $[(C_6H_5)_4X]^+Y^-$ without important changes in the character of the packing. The packing coefficient in $[(C_6H_5)_4P]I$ is 0.66 without taking into account the anions. Thus, the "ready-made" holes between the filled (110) layers of molecules in the structures of tetra-aryl compounds are somewhat small for iodide ions. The introduction of the iodide ions causes the layers to shift apart (the parameter a increases from 11.30 to 11.88 Å), but this is compensated by filling of the holes (the packing coefficient increases from 0.71 to 0.76). Introduction of the anions cannot cause an increase in the parameter c. The increase in this from 6.96 to 7.08 Å results from the increase in X – C bond length: $7.08 - 6.96 = 0.12$ Å $\approx 2(1.94 - 1.80)\sin(109°28'/2) = 0.15$ Å.

We shall now discuss the hypothetical structure $(C_6H_5)_4P$ with densest superposition of the layers. Shortening of the bond length from 1.94 (Si–C) to 1.80 Å (P–C) should lead to a decrease in the parameter $a = 11.30$ Å by $2(1.94 - 1.80) \cdot \cos(109°28'/2)/\sqrt{2} = 0.16$ Å. Thus, the parameter a in the hypothetical structure should be 11.14 Å, i.e., 0.74 Å less than the parameter a in the real structure of $[(C_6H_5)_4P]I$. Thus, the replacement of iodine with a small cation with a radius $R \leq R_I - 0.74 = 1.48$ Å requires no change in the structure of Ar_4X with space group $P\bar{4}2_1c$ and it is to be expected that the unchanged compounds $(C_6H_5)_4C$, $(C_6H_5)_4Si$, etc., on the one hand, and tetraphenylphosphonium fluoride $[(C_6H_5)_4P]F$ ($r_{F^-} = 1.36$ Å) on the other, should be completely isostructural. The comparison carried out has justified the correctness of treating the structures of Ar_4X and $[Ar_4X]^+Y^-$ as the combination of densest layers of Ar_4X particles with a coordination number of 6, the superposition of which is accompanied by a decrease in density and the creation of holes which can be filled with anions or can remain vacant.

The authors with to acknowledge the part taken in decipherment of the structure by L. A. Kamashkina and K. F. Lugova. The authors express their thanks to Professor A. I. Kitaigorodskii for his attention and interest in the work.

Summary

1. The structure of tetraphenylphosphonium iodide has been determined by calculating the three-dimensional interatomic vector series.

2. The following were determined: P–C = 1.80 Å, angle C–P–C = 103° and 112.5°, and the intermolecular radii of C, H, and I are 1.81, 1.06, and 2.22 Å, respectively.

3. The configuration of tetra-aryl molecules and cations and steric hindrance and internal rotation in them have been discussed.

4. The packing in the crystal of tetraphenylphosphonium iodide has been analyzed and compared with that in structures of neutral tetra-aryl compounds.

LITERATURE CITED

1. A. I. Kitaigorodskii, Organic Crystal Chemistry [in Russian] (1955), p. 149.
2. H. D. Springall and L. O. Brockway, "The molecular structures of the methyl derivatives of phosphorus and arsenic," J. Am. Chem. Soc., 60, 996 (1938).
3. S. C. Abrahams, J. M. Robertson, and J. G. White, "The crystal and molecular structure of naphthalene," Acta Cryst., 2, 238 (1949).

SOVIET PHYSICS - CRYSTALLOGRAPHY VOL. 1, NO. 6 NOV.-DEC., 1956

THE STUDY OF POORLY-FORMED SINGLE CRYSTALS OF UNKNOWN SYMMETRY WITH AN X-RAY GONIOMETER

E. Sándor

Physics Institute, Budapest University
Translated from Kristallografiya, Vol. 1, No. 6,
pp. 677-680, November-December, 1956
Original article submitted March 28, 1956

A method is proposed for finding the direction of the axis of an important zone in poorly formed crystals of unknown symmetry, and of aligning this direction with the goniometer rotation direction. The zone axis is determined from a single Laue photograph prepared on a cylindrical film.

All the unit-cell constants can be determined from oscillation photographs prepared on an x-ray goniometer, and from a few layer lines around one axis [1]. The problem arises here of determining the zone axis in poorly formed crystals and of aligning this direction with the goniometer rotation axis. In principle it makes no difference which zone axis is selected for the job, because any unit cell can be transformed by the appropriate methods into the Bravais cell characteristic of the lattice symmetry of the particular crystal [2]. However, for practical reasons it is best to choose an important zone axis, if possible one corresponding to one of the crystallographic axes of the crystal.

Determination of an Important Zone Axis

The zone axis directions in poorly formed crystals are most simply found from Laue photographs. From a Laue photograph it is always possible to construct a stereographic projection of the planes giving the reflections, and this projection can then be used in the same way as the stereogram obtained from optical measurements of angles in a morphological study of a crystal. However, the treatment of an arbitrarily obtained Laue photograph is usually much more complex than that of an "optical" stereogram, because of the following two factors:

Fig. 1. Laue photographs obtained on a cylindrical film from a monoclinic crystal. The most important nodal points are circled and numbered. This group of points also includes one which is formed by the intersection of zone curves outside the photograph.

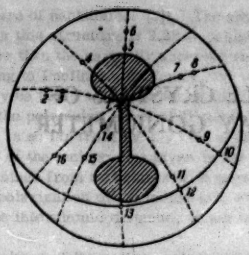

Fig. 2. Stereographic projection of the points marked by circles on Fig. 1.

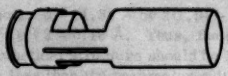

Fig. 3. Screening cylinder with a wide aperture, used in obtaining four Laue photographs on an x-ray goniometer film.

(a) If the x rays do not fall on the crystal along the direction of an axis of symmetry or normal to a plane of symmetry, then it is impossible to see the crystal symmetry on the stereographic projection.

(b) Quite a large proportion of the Laue spots are high-order reflections, which makes analysis of the stereographic projection even more difficult.

A systematic method of overcoming these difficulties has been worked out by Gross [3]. The basis of his method is that a series of flat Laue photographs, selected in a certain way, will give a unique result for the symmetry system (or rather the Laue class) of the crystal, which establishes the directions of the crystallographic axes. However, even in the simplest case this means preparing at least 16 photographs, and for crystals of higher symmetry even more are required. Kvitka and Umanskii have subsequently shown [4] that it is possible to choose important plane networks and zones in a simple manner from the Laue photographs and use these to establish the directions of the crystallographic axes and also the indices of the most important spots. This method requires only three suitably chosen Laue photographs.

A method is described below, by means of which it is possible to determine the axis direction of an important zone from only one Laue photograph, obtained on a cylindrical film in an x-ray goniometer. The exposure time needs to be chosen so as to give clear images of the spots with the highest possible ϑ (Fig. 1). On the photograph, 10-15 spots are chosen which lie at the intersections of the largest possible numbers of zonal curves; these will be the spots with the largest empty areas around them. With the aid of the appropriate (S, Φ) diagram and a stereographic net, these "nodal points" can be transferred to a stereographic projection (Fig. 2).

Immediately after this, a check is made to see whether mirror planes can be detected on the stereogram or not. Since the normal to a mirror plane is simultaneously a zone axis, on the stereographic projection a mirror plane can be recognized because, on the zone circle corresponding to it, there appear the images of points belonging to other zones. With a stereographic net it is easy to find the nodal points, which are the poles of zones passing simultaneously through images of points belonging to other zones. Each of these "nodes" is the stereographic projection of a mirror plane.

The shaded dumbbell-shaped area in Fig. 2 does not contain points because the corresponding spots were lacking on the photograph. This area is so small that it generally will not interfere with the treatment of the Laue photograph. In this particular case, for example, it is easy to see that the zonal curve, which has its pole at the No. 1 point which did not appear on the photograph, is a mirror plane, with the circle corresponding to it on the stereographic projection passing through the points 10, 12, and 13, respectively. Since the photograph was obtained without a beam catcher for the primary beam, there will actually be a narrow annular region around the edge of the stereographic projection where no spots will fall. This region has not been drawn in on the stereographic projection, because, by using a suitable beam catcher it could be made very small.

A search for mirror planes can, in principle, lead to the following four alternatives:

(1) no mirror planes observed on the projection;

(2) one mirror plane found;

(3) several mirror planes found, all lying at similar angles to one another (30, 45, 60, or 90°); or

(4) several mirror planes found, with angles of 30 or 45° between them, and, in addition, at least one more mirror plane perpendicular to these planes.

In the first case it can be assumed that the crystal belongs to one of the two Laue classes without a mirror plane ($\bar{1}$ or $\bar{3}$).

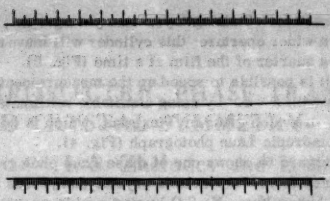

Fig. 4. Rule for measurement of quadruple Laue photographs.

In accordance with this, an important zone is chosen on the Laue photograph (i.e., the line with the highest number of spots on it and with the widest empty space on either side of it), and the axis of this zone is lined up with the axis of rotation of the goniometer. This approach will usually lead to a triclinic unit cell, which can always be converted into a unit cell characteristic of the particular symmetry system by using the well-known Delaunay methods. If the crystal should happen to belong to the trigonal Laue class $\bar{3}$, this will be shown up during the conversion.

In the second case, the crystal obviously belongs to the monoclinic Laue class 2/m, when it is best to line up the goniometer rotation axis with the normal to the single mirror plane.

In the third case, according to the interplanar angle shown, it may be assumed that the crystal belongs to the Laue class 6/m, 4/m, or 3/m, respectively, or, when the angles are equal to 90°, to the class mmm or m3. In this case, it is best to choose the goniometer rotation axis to coincide with the line of intersection of any two planes.

Finally, if, in addition to the planes lying at angles of 30 or 45° to each other, there is a further plane perpendicular to these, the crystal can only belong to the Laue class 6/mmm, if the angle is 30°, or the classes 4/mmm or m3m, if the angle is 45°. In this case it is also best to have the goniometer rotation axis lined up with the line of intersection of any two planes making an angle of 30 or 45° with each other.

Where the above method is concerned, the following additional points are worth noting:

(1) Since the overwhelming majority of crystals belong to Laue classes possessing at least one plane of symmetry, in most cases a check for mirror planes will give a positive result.

(2) Even though Laue photographs obtained on a crylindrical film include a spot-recording area extending over almost all of the stereographic projection, it may nevertheless happen that the reflection corresponding to a mirror plane will be absent from the Laue photograph. An example of this can be seen in Fig. 1, where the reflection corresponding to the only mirror plane of the monoclinic crystal (the point of intersection of zonal curves lying outside the photograph) is missing from the Laue photograph.

However, on the stereographic projection it is easy to establish that this particular missing spot corresponds to a mirror plane.

Aligning the Chosen Axis with the Axis of Rotation of the X-ray Goniometer

After the position of an important zone axis has been established, it can be lined up with the axis of rotation of the goniometer using the goniometer head arcs. However, since the graphical treatment of the cylindrical Laue photograph cannot be expected to be accurate to more than 1-2°, the accuracy of the resulting setting will generally not be great enough

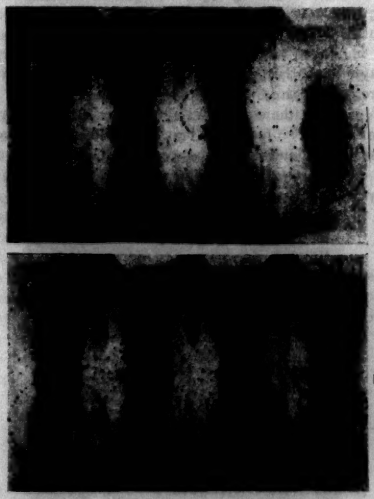

Fig. 5. Quadruple Laue photograph, to refine the setting of a monoclinic ($Na_2S_2O_3$) crystal along the normal to the mirror plane. a) Photograph in an inaccurate setting; b) control photograph from an accurately positioned crystal.

to satisfy the requirements for a goniometer photograph. In practice, the positioning is complicated by the fact that the required angle of rotation very often cannot be achieved through the use of the goniometer head arcs alone, so that the crystal can be brought to the desired position only through applying other auxiliary methods (with a small universal joint, etc.), or by regluing, which reduces the accuracy of the setting even further. The rough setting obtained from the stereographic projection must, therefore, be further refined.

On an x-ray goniometer this refinement is most simply brought about by the four-photograph Laue method (see Winchell [5]), in which four Laue photographs are obtained side by side on a cylindrical film. The first photograph is taken in a position such that the direction of the x-ray beam coincides with the plane of one of the goniometer arcs; the other three photographs are taken after rotating the goniometer axis through 180, 90, and 270°. If the zone axis coincides exactly here with the goniometer axis, the corresponding zone on the four photographs will be parallel to the equatorial line, and if the chosen zone axis is a normal to a mirror plane, then all four photographs will also show a mirror symmetry plane (Fig. 5b). Two difficulties arise in the use of this method:

(a) the four Laue photographs partially overlap one another, which greatly complicates their treatment; and,

(b) on the equatorial-zone curves the spots are sometimes so far apart that it is quite difficult to measure the distances between curves when $\vartheta = 90°$.

The first difficulty is most simply overcome by using a screening cylinder with the film, like that used for obtaining layer-line photographs, but with a wider aperture; this cylinder will leave free only a quarter of the film at a time (Fig. 3).

It is possible to speed up the measurement of spots with $\vartheta = 90°$ by using a suitable millimeter rule, drawn on glass or Plexiglas, which is laid on the quadruple Laue photograph (Fig. 4).

Figure 5a shows one of these Laue photographs, obtained from a monoclinic crystal (anhydrous sodium hyposulfate, $Na_2S_2O_3$) using a wide-aperture screening cylinder. The zone axis chosen is the normal to the mirror plane. From the control photograph (Fig. 5b) it can be seen that even in the unfavorable case where the original position was quite inaccurate, and the equatorial zone spots lay some distance away from each other, the method described here leads to a satisfactory result.

LITERATURE CITED

1. M. J. Buerger, X-Ray Crystallography (New York, 1942).
2. B. Delaunay, "Neue Darstellung der Geometrischen Kristallographie," Z. Krist., 84, 109-149 (1933).
3. R. Gross, "Erweiterte Lauemethode," Zentralbl. f. Miner., 52-64 (1920).
4. S. S. Kvitka and M. M. Umanskii, "X-ray goniometer measurements on polychromatic fixed-crystal photographs," Zh. Tekhn. Fiz., 20, 901-909 (1950).
5. H. Winchell, "Crystal orientation on the Weissenberg goniometer," Acta Cryst., 3, 396 (1950).

SOVIET PHYSICS - CRYSTALLOGRAPHY VOL. 1, NO. 6 NOV.-DEC., 1956

FERROELECTRIC PHASE TRANSITIONS AND CRYSTAL SYMMETRY

I. S. Zheludev and L. A. Shuvalov

Institute of Crystallography, Academy of Sciences of the USSR
Translated from Kristallografiya, Vol. 1, No. 6
pp. 681-688, November-December, 1956
Original article submitted June 10, 1956

A study has been made of changes in morphological symmetry for all classes of crystal during possible ferroelectric phase changes.

1. Introduction

At certain temperatures, the Curie points, ferroelectric crystals undergo a sharp change in a number of their physical properties. These changes in properties are due to the fact that a phase change of the first or second kind occurs at the Curie points. Some ferroelectric crystals have several ferroelectric phases, and thus have several phase transition points. The Curie point usually refers to the temperature at which the crystal goes over from the nonferroelectric to the ferroelectric state (or vice versa). The temperature of transition from one ferroelectric phase to another is usually called simply a phase transition point. In what follows, by a ferroelectric phase change we will mean either type of transition. Incidentally, it should be noted that ferroelectric phase changes are reversible. For simplicity in what follows, unless otherwise stated, we will consider changes in one direction only, but this does not reduce the generality of the arguments used.

Changes in the physical properties of ferroelectric crystals during ferroelectric phase changes are always accompanied by microstructural changes, as structural investigations show, so that the space symmetry group of the crystal alters. When an area in a ferroelectric crystal changes from a nonferroelectric to a ferroelectric phase, a domain structure arises in that area. In cases where a crystal alters from one ferroelectric state to another, the nature of the domain orientation changes.

It is important to note that experiments show that the morphological (point) symmetry of a domain differs from the symmetry which the crystal (or domain) had before the phase change. In other words, the structural changes occurring during a ferroelectric phase change in a ferroelectric crystal are accompanied by a change in the point symmetry.

Thus, for example, a crystal of Rochelle salt belongs to the orthorhombic class 2:2 above a temperature of 24.5°C (the upper Curie point); in the temperature interval between the Curie points (−18.5°C to +24.5°C) the crystal domains belong to the monoclinic symmetry class 2. Similar symmetry changes can also be observed in other ferroelectric crystals.

A careful scrutiny of the fundamental changes taking place during phase transitions in ferroelectric crystals leads to the conclusion that the changes in crystal or domain symmetry are governed by certain definite laws, from which it is possible, for example, to accurately foretell how the point symmetry of a crystal belonging to a given class will alter if the crystal passes through a ferroelectric transition, how many transitions can occur in crystals of a given class, etc. The present article is devoted to a discussion of these questions.

2. Symmetry Changes during Ferroelectric Phase Transitions

The most important characteristic feature of a phase change in a ferroelectric is the creation, or disappearance, or change in direction, of spontaneous polarization in the crystal. This feature also governs changes in other properties of ferroelectrics, i.e., electrical, optical, mechanical

properties, etc. Spontaneous polarization in a crystal is defined by a polar vector $\overline{P}_s$, which has the symmetry $\infty \cdot m$. The individual domains in a ferroelectric crystal can, therefore, only belong to one of the pyroelectric classes which are subclasses of the class $\infty \cdot m$, which means only the following:

$$1,\ 2,\ 3,\ 4,\ 6,\ m,\ 2 \cdot m,\ 3 \cdot m,\ 4 \cdot m,\ 6 \cdot m.$$

The change in point symmetry which takes place during a ferroelectric phase change can be found in two ways. The first of these uses the Curie symmetry principle [1]. According to this principle, the symmetry which a crystal attains when spontaneous polarization arises in it is given by the highest subgroup of the symmetry group of the crystallographic class which is common both to the crystal under consideration, when in the nonferroelectric phase, and to the symmetry group of the polar vector $\overline{P}_s$, for a given arrangement of the symmetry elements of both groups.

In the general case, spontaneous polarization may be assumed to arise in a crystal in any direction. Since there is an infinite number of different directions in a crystal, then formally each crystal can have an infinite number of physically different ferroelectric phases. However, we will limit ourselves to considering phases which differ in their symmetry. It is easy to see that the number of phases which differ in symmetry is not great and may be calculated simply.

As an example, let us consider a crystal belonging to the class $m \cdot 2 : m$. If spontaneous polarization arises along one of the two-fold axes in this crystal, its symmetry drops to $2 \cdot m$; if the vector $\overline{P}_s$ lies in a plane of symmetry and does not coincide with any of the symmetry axes, the crystal symmetry is lowered to the class m; and, finally, if the vector $\overline{P}_s$ does not lie in any of the symmetry planes, the symmetry of the crystal is reduced to the class 1.

The second method of determining a change in symmetry is more graphical, and comes down to a direct examination of the uniform spontaneous deformation. This deformation is piezoelectric and electrostrictional in nature, but in crystals which do not have piezoelectric properties in their initial phase (whether in general or along the direction of the vector $\overline{P}_s$), it is only electrostrictional. Here, the character of this deformation can be found from an examination of the electrostrictional tensor or the piezoelectric constant tensor. It is easy to see that in a crystal belonging to, say, the class 2:2, spontaneous polarization arising along the X axis will lead to shear deformation about the X axis (in accord with the form of the piezoelectric constant tensor), which will result in the crystal becoming monoclinic, with the symmetry class 2. (This example corresponds to the ferroelectric phase change in Rochelle salt.) If the direction of the vector $\overline{P}_s$ does not coincide with any of the two-fold symmetry axes, the crystal will undergo shear deformation about all three axes, which will result in the symmetry being lowered to symmetry class 1.

For crystals not possessing piezoelectric properties in their initial nonferroelectric phase, the change in symmetry can be found in a similar manner from the electrostrictional tensor. There is no need to examine electrostrictional deformation in crystals possessing piezoelectric properties in their initial nonferroelectric phase, because the electrostrictional deformation leads to the same symmetry changes as the corresponding piezoelectric deformation.

Thus, by using either the first or the second method, it is possible to find the symmetry change occurring during ferroelectric transitions in any of the 32 crystal classes, i.e., when the vector $\overline{P}_s$ arises or changes its direction. Tables 1-4 give the results of such an examination for crystals of all classes.[1]

Tables 1-4 show symmetry changes for all classes during possible ferroelectric phase changes. In other words, it does not follow from the tables that a crystal of a given class will necessarily undergo the transformation indicated when the temperature is altered, because it may either not undergo any transformation at all, or it may be transformed without spontaneous polarization arising (a nonferroelectric transformation). However, it does follow from the table that if the crystal does undergo a ferroelectric phase change when the temperature is altered, then this transition can only lead to the symmetry change shown in the table. It may be observed here that all known ferroelectric transitions conform completely with these tables.

3. Discussion of Some Possible Ferroelectric Transitions. Orientation of Domains

1. For crystals belonging in their initial phases to one of the pyroelectric classes, two al-

[1] All these examinations were essentially based on one assumption, that the change in crystal symmetry during a phase change was due only to the formation of spontaneous polarization. This assumption is quite natural and, as can be seen from examples, is supported by all known ferroelectric transitions.

ternatives are formally possible. The first alternative relates to those crystals which, although belonging to the classes in question, are not spontaneously polarized in their initial states. In this case the formation of spontaneous polarization along the existing special polar direction cannot be considered as a ferroelectric transition, because, in view of the uniqueness of this special direction, the spontaneous polarization cannot arise with equal probability in any other direction, and, consequently, the crystal cannot undergo a change in symmetry and cannot be split into domains; splitting into domains is a necessary condition for a ferroelectric transition.

There may also occur the other alternative, when the crystal has spontaneous polarization in its initial state, but is not split up into domains, i.e., it is a simple pyroelectric. It could theoretically be assumed that such a crystal would, at a certain temperature, undergo an abrupt change in the absolute value of its spontaneous polarization (without changing its direction). It is easy to see that this would not be a ferroelectric transition, since the direction of the vector $\vec{P}_s$ would still be unique, and the crystal could not split up into domains (and the crystal symmetry also could not change).

Thus, the transitions of the $6 \cdot m \rightarrow 6 \cdot m$, $4 \cdot m \rightarrow 4 \cdot m$ type listed in Tables 1–4 cannot be considered as ferroelectric transitions, and they are only included in these tables because they resulted from the complete and rigorous derivation procedure used.

As well as these transitions, the pyroelectric classes listed in Tables 1–4 may formally be transformed into the classes m and 1. Such transitions are not met with in practice and, moreover, in our view, would be unrealistic. It can, therefore, be considered that if a crystal from a pyroelectric class does not split up into domains, it cannot undergo ferroelectric transformations.

It should be noted here that the above observation regarding unrealistic transitions to classes m and 1 does not relate solely to pyroelectric classes, but to all classes.

2. The conclusion arrived at in the preceding section, that none of the pyroelectric classes could be the initial class for a series of ferroelectric phase changes, in no way contradicts the known fact that some ferroelectric crystals can pass from one ferroelectric phase into another, because, in the latter case, not only does the magnitude of the spontaneous polarization change, but also its direction. A change in polarization like this is always bound up with a change in symmetry of the crystal. Examples of such transitions are those of $BaTiO_3$ at +5°C, from a tetragonal to an orthorhombic phase, and at –70°C, from an orthorhombic to a rhombohedral phase.

These transitions are generally possible because, in its initial nonferroelectric phase, the crystal has a symmetry such that for different directions of the vector $\vec{P}_s$ (along simple crystallographic directions) the initial symmetry can alter in different ways. It thus turns out to be possible to have several adjoining ferroelectric phases for a single initial nonferroelectric phase. (In $BaTiO_3$, for example, the possible transitions are $\bar{6}/4 \rightarrow 4 \cdot m$, $4 \cdot m \rightarrow 2 \cdot m$, $2 \cdot m \rightarrow 3 \cdot m$, etc.)[2]

Because of this feature, it may be asserted that the character of symmetry changes in any ferroelectric transition is determined, not by the symmetry possessed by the domains before the ferroelectric transition occurs, but by the symmetry which the whole crystal has in its initial nonferroelectric state; moreover, the spontaneous deformation in any transition is described by the electro-

[2] The order in which the ferroelectric phases follow one another is not strictly constant within a particular transformation series (for example, the perovskite solid-solution ferroelectrics may show the transitions $\bar{6}/m \cdot \rightarrow 4 \cdot m \rightarrow 2 \cdot m \rightarrow 3 \cdot m$ or $\bar{6}/m \rightarrow 4 \cdot m$ or $6/4 \rightarrow 3 \cdot m$, etc., for different compositions). Because of this, the order cannot be forecast in the tables of possible transitions for any particular series.

TABLE 1. Transitions from Cubic Classes

Set of P_s directions	Initial phase				
	$\bar{6}\|4$	$3\|4$	$3\|\bar{4}$	$\bar{6}\|3$	$3\|3$
	Possible ferroelectric phases				
<100>	$4 \cdot m(6)$	$4(8)$	$2 \cdot m(6)$	$2 \cdot m(6)$	$2(6)$
<111>	$3 \cdot m(8)$	$3(8)$	$3 \cdot m(4)$	$3(8)$	$3(4)$
<110>	$2 \cdot m(12)$	$2(12)$	$m(12)$	$m(12)$	$1(12)$
<hk0>	$m(24)$	$1(24)$	$1(24)$		
<hkk>			$m(12)$	$1(24)$	
<hhk>					
<hkl>	$1(48)$		$1(24)$		

TABLE 2. Transitions from Hexagonal and Rhombohedral Classes

Set of $\vec{P}_S$ directions	Initial phase: $6 \cdot m \cdot m$	$\bar{6} \cdot m$	$6 : m$	$6 \cdot 2$	6	$m \cdot 3 \cdot m$	$2 : m$	$\bar{6} \cdot m$	$\bar{6}$	$4 \cdot m$	$3 \cdot 2$	$3 \cdot m$	3
Possible ferroelectric phases													
⟨0001⟩	$6 \cdot m(2)$	$6 \cdot m(1)$	$6(2)$	$6(2)$	$6(1)$	$3 \cdot m(2)$	$3(2)$	$3 \cdot m(2)$	$6(2)$	$3 \cdot m(1)$	$3(2)$	$3 \cdot m(1)$	$3(1)$
⟨11$\bar{2}$0⟩	$2m(6)$	$m(6)$	$m(6)$	$2(6)$		$2 \cdot m(3)$	$m(3)$	$2(6)$		$2(6)$	$2(3)$	$m(3)$	
⟨10$\bar{1}$0⟩	$m(12)$	$1(12)$	$1(12)$		$1(6)$	$m(6)$	$1(12)$	$1(12)$	$1(6)$	$1(6)$		$1(6)$	$1(3)$
⟨hki0⟩	$m(12)$	$m(6)$	$1(12)$			$m(6)$	$1(12)$	$m(6)$		$m(3)$			
⟨hh2hl⟩	$1(24)$	$1(12)$				$1(12)$		$1(12)$		$1(6)$			
⟨h0hl⟩													
⟨hkil⟩													

Note. Symbols are given for Bravais conditions (see, for example, [4]).

strictional and (where applicable) the piezoelectric deformations of the initial, nonferroelectric phase.

3. If spontaneous polarization arises along a particular direction in a ferroelectric crystal, then it could arise with equal probability along other crystallographically equivalent directions. In a multidomain crystal, therefore, the domain polarization directions are found to be equally distributed among the complete set of these crystallographically equivalent directions.

The number of spontaneous polarization directions n for each transition may be found from the ratio of the order of the symmetry group of the initial nonferroelectric phase N_1, to the order of the symmetry group of one of the domains N_2, arising on transition:

$$n = N_1 : N_2$$

Thus, for example, when $BaTiO_3$ transforms from class $\bar{6}/4$ (symmetry group order 48) to class $4 \cdot m$ (group order 8) the number of orientations of the vector $\vec{P}_S$ will be 6, while for transition to class $3 \cdot m$ (group order 6), the number of $\vec{P}_S$ orientations will be 8, etc. In Tables 1-4 the numbers of orientations are given in brackets for each transition, after the symbol for the class into which the crystal is transformed.

Thus, the general character of domain orientation in a multidomain ferroelectric crystal is determined by the symmetry of the initial nonferroelectric phase and the $\vec{P}_S$ direction in the given ferroelectric phase.

4. The ordering of domain orientations along crystallographically different directions of spontaneous polarization leads to the position where the multidomain crystal is in essence a polysynthetic twin (or a special texture specimen with axes of finite order), and the domains are the components of this twin. The twinning elements are formed by the loss of the symmetry elements present in the initial nonferroelectric phase when it goes over into the ferroelectric phase. (This holds for any ferroelectric phase.)

Here, the multidomain crystal, with respect to statistically averaged macrosymmetry, consequently, reverts to the symmetry of its initial nonferroelectric phase.[3] This applies not only to its morphological symmetry, but also to all its physical properties when taken as a whole (its macroscopic

[3] This fact, noted for Rochelle salt by Chernysheva [2], has recently been examined in detail by us [3].

TABLE 3. Transitions from Tetragonal Classes

Set of $\vec{P}_s$ directions	Initial class						
	$4 \cdot m : m$	$4 \cdot m$	$4 : m$	$4 : 2$	4	$\bar{4} \cdot m$	$\bar{4}$
Possible ferroelectric phases							
<001>	$4 \cdot m(2)$	$4 \cdot m(1)$	$4(2)$	$4(2)$	$4(1)$	$2 \cdot m(2)$	$2(2)$
<100>	$2 \cdot m(4)$	$m(4)$	$m(4)$	$2(4)$		$2(4)$	
<110>		$1(8)$			$1(4)$	$1(8)$	$1(4)$
<hk0>	$m(8)$	$m(4)$	$1(8)$	$1(8)$		$m(4)$	
<h0l>			$1(4)$			$1(8)$	
<0kl>							
<hkl>	$1(16)$	$1(8)$					

TABLE 4. Transitions from Orthorhombic, Monoclinic, and Triclinic Classes

Set of $\vec{P}_s$ directions	Initial class							
	$m \cdot 2 : m$	$2 \cdot m$	$2 : 2$	$2 : m$	m	2	$\bar{1}$	1
Possible ferroelectric phases								
<001>	$2 \cdot m(2)$	$2 \cdot m(1)$	$2(2)$	$2(2)$	$m(1)$	$2(1)$	$1(2)$	$1(1)$
<010>		$m(2)$		$m(2)$	$1(2)$			
<100>		$1(4)$		$1(4)$	$m(1)$			
<hk0>	$m(4)$	$m(2)$	$1(4)$	$m(2)$	$1(2)$	$1(2)$		
<h0l>		$1(4)$		$1(4)$				
<0kl>								
<hkl>	$1(3)$	$1(4)$						

properties); this has been rigorously proved by us for the example of Rochelle salt [3].

In particular, if a crystal belongs to a nonpiezoelectric class in its initial nonferroelectric state, then the multidomain crystal (e.g., $BaTiO_3$) will not possess piezoelectric properties in any ferroelectric phase. If the initial nonferroelectric phase belongs to a piezoelectric class, then in any ferroelectric phase the multidomain crystal will show piezoelectric properties (e.g., Rochelle salt).

It is natural that the conclusion concerning reversion to the symmetry of the initial phase is only statistical, as an average. If for some reason or other the domains in a multidomain crystal had a certain preferred orientation, this conclusion would not be valid. This would apply, in particular, if we were dealing with a specimen cut from a particular growth pyramid, rather than with a whole crystal.

5. Analysis of Tables 1-4[4] reveals that not all the formally possible ferroelectric phase changes shown in these tables are equally possible. Some have specific features which have not been met with up to now, and these changes appear unlikely. (We noted above the formal nature of the series of transformations with initial pyroelectric classes, and of transitions into classes m and 1.) In fact, several of the transitions included in Tables 1-4 ($\bar{6}/2 \rightarrow 3$, $6 : m \rightarrow 6$; $\bar{6} \cdot m \rightarrow 2$; $3 : m \rightarrow 3$, etc.) are such that the reversion of a multidomain crystal to the symmetry of the initial class (see section 4) can only occur under conditions where the crystal in a ferroelectric phase contains equal numbers (twin components) of left-handed and right-handed enantiomorphs. Such transitions do not seem to be very probable.

In the transitions $m : 3 : m \rightarrow 2 \cdot m$, $3 : 2 \rightarrow 2$, $3/2 \rightarrow 3$, the vector $\vec{P}_s$ is directed along the polar axis of the initial phase, so that in this case an antiparallel arrangement of domains is not possible. In the transitions $6 : 2 \rightarrow 6$, $m : 3 : m \rightarrow 3 \cdot m$, $3 : 2 \rightarrow 3$, etc., although the initial phases belong to piezoelectric classes, the spontaneous deformation is electrostrictional because, in these cases, the vector $\vec{P}_s$ is directed along the Z axis of the cell, a direction in which the initial phase does not possess piezoelectric properties. In spite of this, it appears to us that in crystals with averaged symmetry a ferroelectric transition with a $\vec{P}_s$ vector directed along a high-order axis is more favorable than transitions with other $\vec{P}_s$ directions.

[4] It is pointed out that these tables may also be used to determine the symmetry changes in a crystal when any influence described by a polar vector is applied to it. Thus, with the aid of the tables, it can be easily seen how the crystal symmetry will change if an electret is obtained from it, or from what crystal symmetries and through what action a Kerr cell may be obtained, etc.

4. Conclusions

From Tables 1-4, which are in complete agreement with all known ferroelectric phase transitions, it is possible to make a series of predictions, which are quite unambiguous when the low probability (or even impossibility) of some of the formally possible transitions is taken into account.

From Tables 1-4 it is possible to make an unambiguous forecast, for a particular ferroelectric belonging to a given series of transformations, of the absence or presence of new ferroelectric transitions, i.e., the number of possible ferroelectric phases differing in symmetry can be predicted. In order to discover whether these possibilities are realized in practice, it is, of course, necessary to carry out the appropriate studies in each particular case.

The authors are deeply grateful to Academician A.V. Shubnikov for much valuable advice and for discussing the manuscript.

LITERATURE CITED

1. A.V. Shubnikov, "The work of Pierre Curie in the field of symmetry," UFN, 59, 4, 591-602 (1956).
2. M.A. Chernysheva, Thesis: Twinning in Rochelle Salt Crystals (Institute of Crystallography, 1955).
3. I.S. Zheludev and L.A. Shuvalov, "The symmetry and physical properties of multidomain Rochelle salt crystals," Tr. Inst. Kristallogr., 12, 59-66 (1956).
4. A.V. Shubnikov, E.E. Flint, and G.B. Bokii, Fundamentals of Crystallography [in Russian] (1940).

SOVIET PHYSICS - CRYSTALLOGRAPHY VOL. 1, NO. 6 NOV.-DEC., 1956

BEHAVIOR OF ROCHELLE SALT DOMAINS IN ALTERNATING ELECTRIC FIELDS

I. S. Zheludev and R. Ya. Sit'ko

Institute of Crystallography, Academy of Sciences of the USSR
Translated from Kristallografiya, Vol. 1, No. 6,
pp. 689-691, November-December, 1956
Original article submitted September 3, 1956

The characteristics of the behavior of Rochelle salt domains in alternating electric fields of a strength of about 50 V/cm and at frequencies of 32 and 1000 cps are described with reference to microcinematographic frames. Hysteresis of the reorientation of the domains in alternating fields is followed by means of microcinematographic frames.

It is generally accepted to associate the polarization processes of ferroelectrics with reorientation of the domains. Such a connection may be based on the observed variations of domain structure when constant electric fields are applied to ferroelectrics. Considerable interest, however, attaches to the behavior of the domain structure in alternating electric fields. For this purpose, we have made a cinematographic study of the domain structure of Rochelle salt when electric fields of a frequency of 32 and 1000 cps were applied to the crystal.

For the cinematography of even comparatively slow processes, high-speed filming is necessary. However, we used another method, the ordinary filming method (about 32 frames per second), but using stroboscopic illumination. By the use of stroboscopic illumination, the observation of rapidly ensuing processes can be extended in time. The possibility of such an observation is evidence of the fact that for given field strength and given frequency, the process of movement of the domains takes place reproducibly from cycle to cycle.

In filming at the frequency of 32 cps, the stroboscopic effect was obtained from the difference between the frequency with which the camera objective was closed by the shutter and the frequency of the electric field. The resulting slowing down of about 40 times made it possible to examine the polarization reversal process as if occurring in one cycle of the electric field. For the frequency of 1000 cps, a mechanical stroboscope was used, by means of which filming took place with a slowing down of about 4000 times. Filming was carried out at the different frequencies in a microcinematograph camera especially constructed for the purpose. The specimens used were plates of X-cut Rochelle salt, 20 × 20 × 1 mm in size. The electrodes on the specimens were silver leaf, but in the observation area, instead of the silver coating, a transparent conducting layer about 1 mm^2 in area was applied. The specimen was thermostatically controlled during observation. Observation was carried out at a temperature of 11.5°C.

Figure 1 shows the variation in domain structure at a frequency of the electric field of 32 cps and a field strength of 36 V/cm. Concurrently with the observation and cinematography of the domain structure, observations were made on the character of the polarization of the specimens using an oscillograph and the usual circuit for recording hysteresis loops. In accordance with this, the frames selected to illustrate the variations in domain structure were arranged on a curve corresponding qualitatively to the curve observed on the oscillograph.

As will be seen from Fig. 1, the polarization curve is far from saturation for the given field strength, but the dependence of polarization hysteresis on the field strength is fairly clearly shown on the curve. In addition to the polarization curve, the figures also show the sinusoidal variation of the electric field with time (in the present case, the

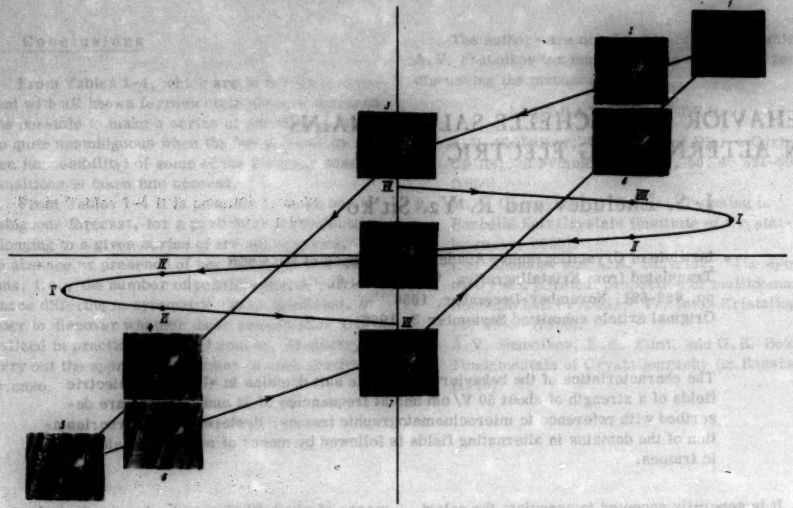

Fig. 1. Variation in domain structure of Rochelle salt at a frequency of 32 cps. The Roman numerals on the field variation curve correspond to the Arabic numerals (frame numbers) on the polarization variation curve. The amplitude value of the electric field strength, 36 V/cm.

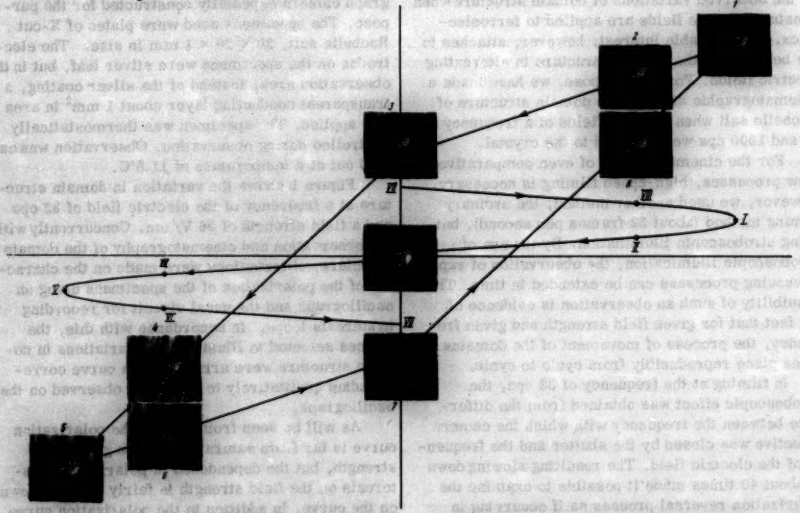

Fig. 2. Variation in domain structure at a frequency of 1000 cps. The Roman numerals on the field variation curve correspond to the Arabic numerals (frame numbers) on the polarization variation curve. Amplitude value of the electric field strength, 56 V/cm.

time axis is the axis of ordinates). The points shown in Roman numerals on the sinusoid correspond to the frames shown on the polarization curve and marked with the corresponding Arabic numerals (the point on the sinusoid corresponding to frame 3 is underneath the frame situated in the center of the figure).

In the center of the figure is the frame corresponding to the domain structure of the portion filmed in the absence of a field. As will be seen from this frame, the domains of opposite orientations in the limits of the filmed portion have unequal areas. The part corresponding to the light component occupies the predominant area, while the part corresponding to the dark component occupies an insignificant area. Thus, the domain structure in this portion is unipolar. It should be noted that unipolarity of the domain structure in the limits of the observed region is not evidence of unipolarity of the specimen as a whole.

The frames located on the polarization curve correspond to field strengths differing from each other in phase by 45° (0°, 45°, 90°, 135°, etc.). Frame 1 corresponds to the amplitude value of the field strength. It may be seen from frame 1 that the light component of the domains occupies practically the whole field, while the dark component, antiparallel to the field, is practically absent. Reduction in the field strength from the amplitude value to zero (frames 2 and 3) results in the formation of the dark component, but its proportion is still insignificant.

Increase in the field strength of opposite sign already leads to a sharper increase in the proportion of dark component (frames 4 and 5). The fact that at the amplitude value of the field (frame 5) the dark component does not occupy the entire field of view (in contradistinction to what occurs at the amplitude value of the field strength of reverse polarity – frame 1), is understandable, since, in the initial state (frame in the center of the figure) in the field of view the dark component was quite weakly pronounced. The reduction in the field (from frame 5 to frame 7) does not result in any substantial change in domain structure; it is as if the crystals "remembered" the state of domain structure which existed at the amplitude value of the field strength (frame 5). Increase in the field strength, illustrated by frames 7-1, shows the more pronounced variation in the domain structure in this portion. In this respect, the portion marked by frames 7-1 is similar to the portion marked by frames 3-5.

In addition to the foregoing features characterizing the variations in domain structure in an alternating field, careful examination of these variations brings to light two facts. The first and more important is that, for the same field strength and the same direction of the field, the domain structure has a different form, depending on whether these strengths are attained on increasing or decreasing the field. This is quite clearly shown by a comparison of frames 2 and 8, 3 and 7. This indeed constitutes the hysteresis of the variations in domain structure on the application of electric fields.

The second interesting fact is that the domain structure in the absence of a field (frame in the center of the figure) in its arrangement does not occupy an intermediate position compared with the domain structure obtained when the field passes through zero value (frames 3 and 7). This fact is readily understandable if it is borne in mind that in the initial state the domain structure in the field of view was unipolar. Evidently, under the action of the alternating field, in the first polarization reversal cycles, this unipolarity diminishes somewhat, there is some averaging out of the proportions of the two components, and the specimen assumes, in the field of view, so to speak, a new initial state which, however, after removal of the field is lost fairly soon, and the domain structure again assumes the form shown on the frame in the center.

Figure 2 shows the variation of the same portion of domain structure shown in Fig. 1. In this case, filming was conducted at an electric field strength of 56 V/cm and frequency 1000 cps. The characteristics of the variation in domain structure that were pointed out in the foregoing discussion of Fig. 1, apply wholly in this case. It should, however, be noted that at a frequency of 1000 cps, unipolarity of the domain structure is less marked; in both limit positions (frames 1 and 5), the specimen is approximately equally remote from saturation. As our observations show, this circumstance is due precisely to the change in frequency, and not to the fact that the field strength at the frequency of 1000 cps was rather higher, since, at the frequency of 32 cps, unipolarity was quite definite for the same field strength.

Observations at different field strengths but at the same frequencies show that with increase in field strength, the variations in domain structure occur not only by the growth of some domains at the expense of others, but also by the formation of fresh small domains in the limits of large domains previously existing (at smaller field strengths).

The authors thank V. F. Parvov for assistance in the work.

DEPOLARIZATION OF PHOTOPOLARIZED SULFUR SINGLE CRYSTALS AT VARIOUS TEMPERATURES

V. M. Fridkin

Institute of Crystallography, Academy of Sciences of the USSR

Translated from Kristallografiya, Vol. 1, No. 6,
pp. 692-695, November-December, 1956
Original article submitted October 15, 1956

The depolarization rate of the photoelectret state in sulfur single crystals is examined as a function of temperature; the thermophotoelectret state is discussed.

We have previously [1] examined the charge on single crystals in relation to photopolarization conditions, the charge being measured by depolarization by repeated illumination. Here we report depolarization tests made at various temperatures.

As previously [1], the specimens were plates of area 1 cm^2 and thickness about 1 mm cut perpendicular to the acute bisector of the optic axes from natural sulfur crystals. The depolarization current was measured with the vacuum-tube electrometer previously described [2]. A stabilized power supply was used in the polarization.

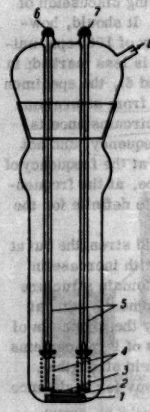

Fig. 1. Apparatus for examining depolarization: 1) aluminum electrode; 2) specimen; 3) grid; 4) springs; 5) quartz tubes; 6,7) thermocouple leads; 8) pumping tube.

The specimen was mounted in the evacuable quartz vessel shown in Fig. 1. The electrodes were the aluminum plate 1 and the brass grid 3, to which the polarizing voltage was applied. The specimen 2 was gripped by the pressure of the springs 4 supported by the quartz tubes 5. Electrode 1 was joined to the electrometer via a special lead (not shown). Grid 3 acted as a transparent electrode and was at the high potential. The temperature of the specimen was measured with a copper-constantan differential thermocouple attached to grid 3, with leads via tubes 5. Figure 1 shows light incident parallel to the polarizing field.

The lower part of the apparatus of Fig. 1 was fitted with a heater; it could also be inserted in a Dewar containing liquid nitrogen. The effects could be examined at a variety of temperatures, including continuously changing ones.

The polarizing voltage was 300 V, which was applied for 10 min with the specimen exposed to the unfiltered light of a quartz–mercury lamp. The light was then cut off, the apparatus was placed in a Dewar containing liquid nitrogen, the required temperature was attained, the polarizing voltage was cut off, and the electrodes were short-circuited. The depolarization was begun 5 min later, by exposing the specimen to the above light, whose intensity was as during the polarization.

Figure 2 shows the depolarization of a single crystal; the initial falling part of the curve is for –103°C and corresponds to only partial depolarization. It is clear that this initial process was very largely complete within 10 min; at that time, the

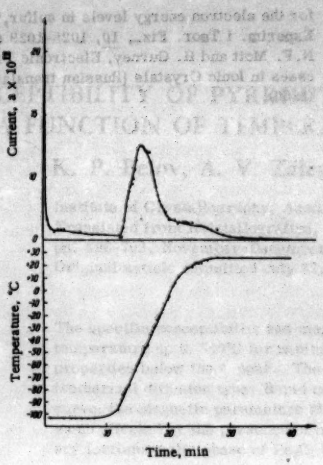

Fig. 2. Discharge-current curve for a photoelectret heated and illuminated, with the corresponding temperature curve.

heater was switched on, the specimen still being illuminated.

The heating produced a characteristic peak in the discharge current, which fell to zero shortly after the specimen had reached room temperature. The shape of the peak is governed by the heating rate; the curve of Fig. 2 is that appropriate to the initial temperature and rate of change shown. Similar curves were obtained with other initial temperatures.

These depolarization curves resemble those reported (e.g., in [2]) for thermoelectrets in the course of total-charge measurement by heating and integration of the discharge current; here the heating was combined with continuous illumination, of course.

This photoelectret state is thus also a thermoelectret one, because illumination at a low temperature removes only part of the charge; total depolarization requires heating to the temperature used in the polarization (here room temperature). Also, the state is not of purely thermoelectret type, because the heating must be accompanied by illumination; lack of the latter gives no measurable discharge current, although there is a slight loss of total

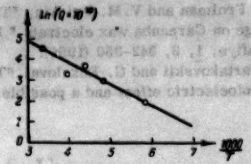

Fig. 3. Relation of $\ln(Q \cdot 10^{18})$ to $10^3/T$; Q is charge released (coulombs) and T is absolute temperature.

charge. The state may be called the thermophotoelectret one.

This state arises by electron trapping at localized levels and on account of a thermal activation energy (gap between the excitation levels and the conduction band). The light excites the electrons to the latter levels, from which they can pass to the conduction band, but the transition probability is dependent on the temperature. This is the mechanism that has been proposed [4] to explain photoconduction in alkali halides; it gives an explanation of the depolarization rate as a function of temperature and, hence, of the peak in the discharge during depolarization by simultaneous illumination and heating.

The activation energy may be deduced as in [2] for specimens polarized as above at room temperature. The depolarization curves were recorded at a variety of temperatures; the discharge current was integrated for each temperature, the charge being proportional to the area under the falling branch of the curve in Fig. 2. The logarithmic plot of Fig. 3 is a straight line, and it gives the activation energy as U = 0.09 eV ($1.4 \cdot 10^{-13}$ erg), which is very small, as is to be expected [3]. The result for the Carnauba wax thermoelectrets of [2] was rather larger ($1.3 \cdot 10^{-12}$ erg). Polycrystalline sulfur gives photoelectrets of much lower activation energy, which may be measured as described here.

We are indebted for assistance to Yu. N. Martyshev and A.I. Delova, and we are indebted for discussions to Academician A.V. Shubnikov, G. Nadzhakov (Bulgarian Academy of Sciences), and I.S. Zheludev. Advice on the method from A. I. Froiman is also gratefully acknowledged.

LITERATURE CITED

1. V.M. Fridkin, "Some results on the photoelectret state in sulfur single crystals," Kristallografiya, 1, 5, 557-583 (1956).

2. A.I. Froiman and V.M. Fridkin, "The heterocharge on Carnauba wax electrets," Kristallografiya, 1, 3, 342-350 (1956).
3. P. Tartakovskii and G. Rekalova, "The internal photoelectric effect and a possible scheme for the electron energy levels in sulfur," Zh. Éxperim. i Teor. Fiz., 10, 1025-1029 (1940).
4. N.F. Mott and H. Gurney, Electronic Processes in Ionic Crystals [Russian translation] (1950).

SOVIET PHYSICS – CRYSTALLOGRAPHY VOL. 1, NO. 6 NOV.-DEC., 1956

SUSCEPTIBILITY OF PYRRHOTINE AS A FUNCTION OF TEMPERATURE

K. P. Belov, A. V. Zalesskii, and A. S. L'vova

Institute of Crystallography, Academy of Sciences of the USSR

Translated from Kristallografiya, Vol. 1, No. 6,
pp. 696-702, November-December, 1956
Original article submitted July 27, 1956

The specific susceptibility and magnetization have been measured as functions of temperature up to 600°C for natural pyrrhotine; thermal hysteresis occurs in these properties below the λ peak. The transition around the λ peak is shown to be of isothermal diffusion type. Rapid cooling suppresses the λ peak in the susceptibility curve; the magnetic parameters above the Curie point (about 300°C) are also very much affected by the presence of oxygen. This is discussed in relation to a secondary ferromagnetic phase of Fe_3O_4 type with a Curie point of 570°C.

Introduction

Compounds of the transition metals (especially Fe and Cr) with sulfur, selenium, and tellurium are of considerable interest [1,6,8], because these belong to the class of substances that can become ferromagnetic under appropriate conditions.

Natural pyrrhotine is hexagonal and has the composition $FeS_{1.1}$–$FeS_{1.2}$, and is already one such substance; it has some very unusual magnetic properties.

There are two views on the cause of the ferromagnetism. Néel's view [2] is that the lattice has vacant sites that are not filled by iron, whose disposition is such that the mineral has two sublattices, whose spontaneous magnetizations are opposite in direction and unequal in magnitude. This gives rise to uncompensated antiferromagnetism, which is responsible for the strong magnetization. Néel considers that the vacant sites may become ordered at a certain temperature, which gives rise to even greater uncompensated antiferromagnetism. The second view is that taken by Japanese workers [3,4]. They neglect this vacant-site structure and consider that the uncompensated antiferromagnetism arises from inequality of the two sublattices, one of which contains only Fe^{2+} ions, while the other contains Fe^{3+} and Fe^{2+}. No final decision has been reached on the nature of the ferromagnetism; new experimental evidence is needed.

We have measured the magnetic parameters as functions of temperature to obtain more detailed evidence on the behavior near the Curie point.

Methods

A specimen in the form of a disc, ellipsoid, or cylinder a few millimeters in size was suspended on a quartz fiber in a furnace with a bifilar winding, which was placed between the poles of an electromagnet. The susceptibility χ was deduced from the force of attraction F via

$$\chi = \frac{F}{mH\,dH/dx},$$

where m is the mass of the specimen and dH/dx is the field gradient. H(dH/dx) was measured with substances of known susceptibility. The force was measured with a VR-NV-2O direct-reading balance. The field was measured with a small probe coil whose size was comparable to that of the specimen. The demagnetization factor for the specimen was derived from tables. The specific magnetization is given by $\sigma = \chi H$. The measurements were made with fields of 1300 to 7500 Oe in air and with the specimen sealed in a bulb. The order of error in the susceptibility was about 5%.

Measurements Near the Curie Point

The susceptibility decreases somewhat between room temperature and 200°C, but it rises

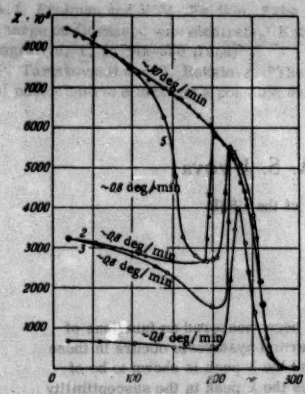

Fig. 1. Susceptibility over the range 20-300°C in a field of 1340 Oe. Arrows show the sense of the temperature change, the numbers being the stages of heating and cooling.

sharply at 220°C to give the λ peak [5], which represents very unusual behavior. The usual Weiss curve is followed between this peak and the Curie point (about 300°C). Temperature hysteresis occurs in the susceptibility curve below 200°C; the position and height of the λ peak are dependent on the rates of heating and cooling [6].

Figure 1 shows the susceptibility for one specimen at 1340 Oe at several rates of heating and cooling used in sequence. Curve 1 is the initial heating; cooling (curve 2) at the same rate gave a higher susceptibility below the λ point. Curve 3 lies below the previous cooling curve, which shows that the transition had not gone to completion during the cooling. Curve 4 of Fig. 1 shows that no λ peak is produced when the cooling is very rapid, the entire curve from the Curie point down to room temperature being of the usual Weiss form.

Néel's explanation for the λ peak and the hysteresis is that the vacancies become ordered at that point (superlattice I, in the terminology used by the Japanese workers [6]). Superlattice I is converted to another type of vacancy ordering below 220°C (superlattice II), which reduces the deviation from equivalence in the sublattices. The kinetic behavior suggests that the transition involves diffusion; Fig. 2 provides strong evidence for this by reference to the susceptibility as a function of time at fixed temperatures of 221°C (this corresponds to the λ peak after heating, curve a) and 208°C after cooling (curve b). The relaxation time for the transition from I to II is finite, so structure II is not perfected during rapid cooling, structure I persisting to a certain extent. This explains why there is no λ peak on rapid cooling (curve 4 of Fig. 1), be-

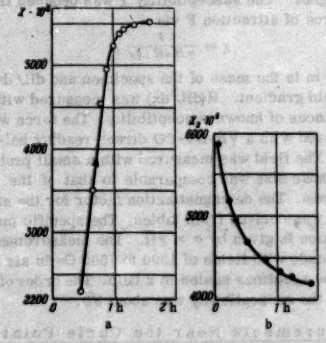

Fig. 2. Susceptibility as a function of time at a fixed temperature in a field of 1340 Oe. a) 221°C, halt during heating; b) 203°C, halt during cooling.

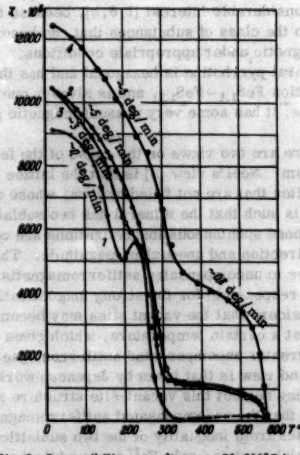

Fig. 3. Susceptibility over the range 20-800°C in a field of 1340 Oe. Arrows show the sense of the temperature change, the numbers being the stages of heating and cooling. The rates of change of temperature are also shown.

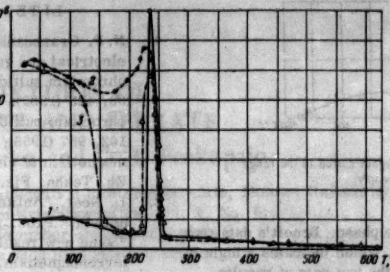

Fig. 4. Susceptibility over the range 20-640°C in a field of 1340 Oe without access to air. Arrows show the sense of the temperature change, the numbers being the stages of heating and cooling.

cause structure II scarcely forms at all, the material consisting almost entirely of the ferromagnetic phase I. Subsequent slower heating (curve 5 of Fig. 1) allows diffusion and accelerates the conversion of structure I to structure II.

Measurements Above the Curie Point

The only paper on this region is that by Benoit [7], who found that the susceptibility fell rapidly near 570°C. It has been supposed [2, 7] that structure I is destroyed at this temperature, but our results show that the effect at 570°C is of secondary origin.

Measurements in air (Fig. 3) show a marked sensitivity to oxygen. The initial heating above

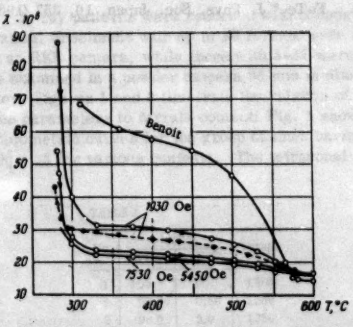

Fig. 5. Susceptibility of pyrrohotine at various field strengths over the range 300-600°C. The arrows indicate the direction of temperature change.

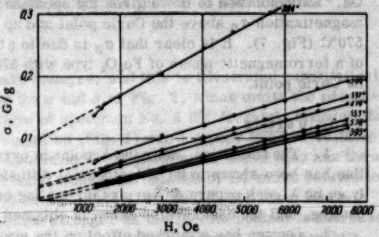

Fig. 6. Magnetization isotherms in the range 280-600°C.

300°C (broken line of Fig. 3) sometimes causes the susceptibility first to rise and then to fall at 570°C. Cooling curve 2 (after a certain time at 600°C) runs above the curve for the previous heating and has the typical shape of a curve for a two-phase state with two Curie points. This indicates that the mineral takes up much oxygen at high temperatures and produces a second ferromagnetic phase whose Curie point is 570°C; this may be Fe_3O_4 (magnetite), whose Curie point is 570°C.

A similar effect from a magnetite-type phase has been observed for FeTe, which falls in the FeS class of compounds [8].

We have recorded χ(T) curves over the range 20 to 600°C for specimens heated and cooled in tubes without access to air. Figure 4 shows that there is then no characteristic point at 570°C. Figure 5 shows the range 300-600°C on a larger scale. The susceptibility shows a slight dependence on the field in this range, which almost vanishes at 570°C (the material becomes paramagnetic). Natural pyrrhotine crystals evidently contain a small propor-

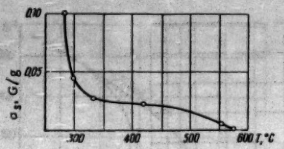

Fig. 7. Spontaneous magnetization in the range 280-600°C.

tion of the magnetite-type phase. Benoit's data give a curve lying above ours, which indicates a higher proportion of magnetite; the two sets of results give very similar susceptibilities above 570°C.

The magnetite phase is indicated also by the magnetization isotherms from the Curie point to 600°C (Fig. 6), which are straight lines above 2000 Oe. Extrapolation to H = 0 gives the spontaneous magnetization σ_S above the Curie point and up to 570°C (Fig. 7). It is clear that σ_S is due to a trace of a ferromagnetic phase of Fe_3O_4 type with 570°C as Curie point.

Conclusions

1. The transition near the λ point in pyrrhotine has been shown to be of isothermal diffusion type; no λ peak occurs on very rapid heating or cooling, and the usual Weiss curve is obtained.

2. Oxygen has a marked effect on the magnetic properties of pyrrhotine above the Curie point. The fall in susceptibility at 570°C is due to a phase of magnetite type formed on heating the mineral in air.

We are indebted to Professor G. P. Barsanov for providing the specimens of natural pyrrhotine.

LITERATURE CITED

1. N. P. Grazhdankina and I. G. Fakidov, "The electrical and galvanomagnetic properties of chromium sulfides," Dokl. Akad. Nauk SSSR, 93, 429 (1953); "The inherent conductivity of chromium sulfides," Dokl. Akad. Nauk SSSR, 102, 957 (1955); F. S. Smirnov, "The ferromagnetism of chromium–sulfur compounds," Zh. Tekhn. Fiz., 23, 50 (1953).
2. L. Néel, "Antiferromagnetism and ferrimagnetism," Proc. Phys. Soc., A65, 869 (1952); "Some new results on antiferromagnetism and ferromagnetism," Rev. Mod. Phys., 25, 60 (1953).
3. K. Joshida, "On the magnetic properties of pyrrhotite, chromium, sulphide, and α-hematite," Phys., 17, 794 (1951); "Note on the magnetic properties of FeS_n system," Progr. Theoret. Phys., 6, 356 (1951).
4. Hirone and Tsuya, "On the origin of magnetism in iron sulfides with various sulfur contents," Phys. Rev., 83, 1063 (1951).
5. H. Haraldsen, "Eine thermomagnetische Untersuchung der Umwandlungen im Troilit–Pyrrhatin–Gebiet des Eisen–Schwefel–Systems," Z. anorg. allg. Chem., 231, 78 (1937); "Über die Eisen (II)–Sulfidmischkristalle," Z. anorg. allg. Chem., 246, 169 (1941).
6. Hirone, Maeda, and Tsuya, "On the λ-shaped ferrimagnetism of FeS_n," J. Phys. Soc. Japan, 9, 736 (1954).
7. B. Benoit, "Sur le paramagnetisme des sulfures de fer," Compt. rend., 234, 2175 (1952).
8. Uchida and Kondoh, "Magnetic properties of FeTe," J. Phys. Soc. Japan, 10, 357 (1955).

SOVIET PHYSICS – CRYSTALLOGRAPHY VOL. 1, NO. 6 NOV.-DEC., 1956

ISOMORPHOUS MIXTURES OF BARIUM TITANATE AND FERRATE

E. G. Fesenko and O. I. Prokopalo

Physics and Mathematics Research Institute, Molotov University, Rostov

Translated from Kristallografiya, Vol. 1, No. 6,
pp. 703-707, November-December, 1956
Original article submitted July 30, 1956

Structure and dielectric properties are reported for $Ba(Ti, Fe)O_3$ with $BaFeO_3$ contents from 0 to 5%; a discontinuity in properties occurs at about 3% $BaFeO_3$. A previous discussion [1] of the properties of cubic barium ferrate (perovskite structure) is extended to the titanates and to isomorphous barium titanate–ferrate mixtures, whose properties are reported here.

1. Synthesis

The cubic titanate and ferrate of barium were used as initial components for the $Ba(Ti, Fe)O_3$. The titanate was made [3] by firing $Ba(OH)_2 \cdot 8H_2O$ with TiO_2 in stoichiometric proportions for 20 h at 400°C.

The components were ground together in a ball mill for 5 h, and mixtures were pressed into discs, which were fired for 2 h at various temperatures in a silite oven. Table 1 gives the conditions used for some of the specimens.

2. Structure

X-ray patterns were recorded with copper radiation. Specimens with up to 3% ferrate were used in an RKE camera, while those with 3-5% were also examined in a powder camera 86 mm in diameter. Figures 1 and 2 illustrate the relation of lattice parameters to ferrate content; Fig. 1 shows photometric curves for the group of lines having $\Sigma h_1^2 = 26$ for various contents. The tetragonal ratio here changes, and this is illustrated quantitatively by the c and a of Fig. 2, which omits the parameters of specimen No. 4 (3% ferrate), because the resolution (Fig. 1) was too poor to allow reliable calculation. This photometer curve also has the additional weak peak denoted by H, which relates to the hexagonal form of $BaTiO_3$ [2]. This line becomes stronger as the ferrate content is increased, while the lines corresponding to the perovskite structure become weaker.

TABLE 1

No.	Mol.% $BaTiO_3$	Mol.% $BaFeO_3$	Temp.
1	100	0	1380
2	99.50	0.50	1380
3	98.0	2.0	1380
4	97.0	3.0	1380
5	95.0	5.0	1360

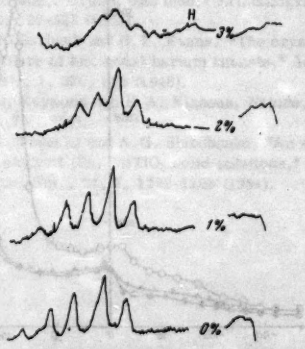

Fig. 1. Photometer curves for reflections having $\Sigma h_1^2 = 26$ for $BaTiO_3$ containing $BaFeO_3$ (shown as mol.% on the curves).

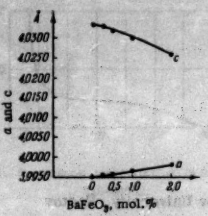

Fig. 2. Relation of cell parameters to $BaFeO_3$ content for $BaTiO_3$.

3. Dielectric Measurements

The above change at 3% ferrate is revealed also by dielectric measurements.

a. High Frequencies. Figures 3 and 4 show the dielectric constant at $5 \cdot 10^5$ cps and E = 100 V/cm as a function of temperature; the substitution method was used in conjunction with a heterodyne measurement of the resonance frequency. Figure 3 shows that the peaks in ε corresponding to the first and second phase transitions (120°C and about 0°C, respectively) shift to lower temperatures as the ferrate content increases. Figure 4 shows that ferrate contents of 3-5% reduce ε (especially at the peak), as well as the Curie temperature. The last is linearly related to concentration (Fig. 5) up to 2% ferrate, but not above this.

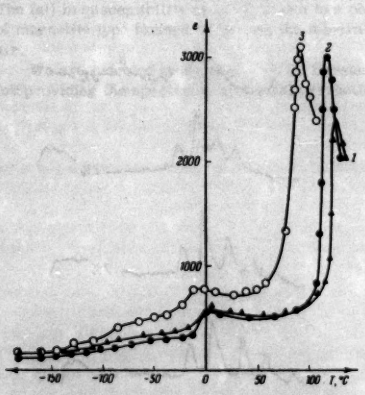

Fig. 3. Relation of ε to temperature at $5 \cdot 10^5$ cps and E = 100 V/cm; curves 1, 2, and 3 correspond to specimens 1, 2, and 3 of Table 1.

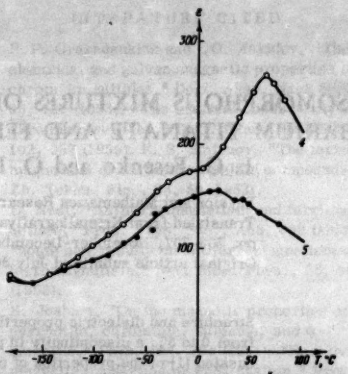

Fig. 4. Relation of ε to temperature at $5 \cdot 10^5$ cps and E = 100 V/cm; curves 4 and 5 correspond to specimens 4 and 5 of Table 1.

b. Low Frequencies. Figure 6 shows $\varepsilon = f(T)$ as recorded with an MDP bridge at 50 cps with E = 550 V/cm; as in Figs. 3 and 4, there is a rise in ε up to 2%, this being especially prominent around the high-temperature transition, but there is only a slight fall in the transition temperature. There is a sharp rise in ε and a displacement of the weak high-temperature peak toward higher temperatures at 3-5%. The $\tan\delta = f(T)$ curves at this frequency for 0-2% ferrate resemble the curve for pure $BaTiO_3$, but the curves shift toward lower temperatures as the ferrate content increases, the minima in these curves occurring at the temperatures corresponding to maxima in $\varepsilon = f(T)$. The $\tan\delta = f(T)$ curves for 3 and 5% ferrate have

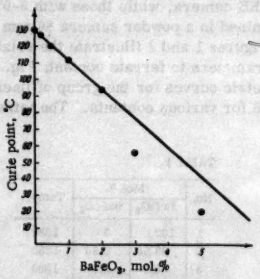

Fig. 5. Relation of Curie point to $BaFeO_3$ content for $BaTiO_3$.

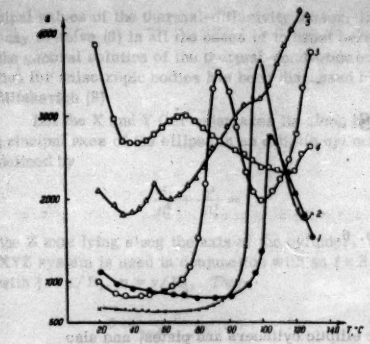

Fig. 6. Relation of ε to temperature at 50 cps and E = 550 V/cm; curves 1-5 correspond to specimens 1-5 of Table 1.

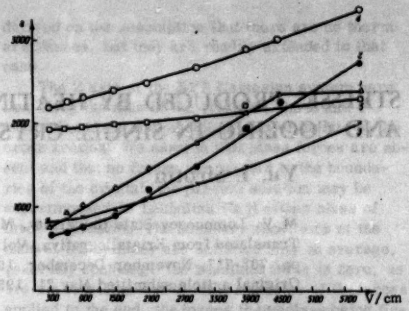

Fig. 7. Relation of ε to field strength at 50 cps; curves 1-5 correspond to specimens 1-5 of Table 1.

minima, but they differ greatly in shape from the others.

Figure 7 shows $\varepsilon = f(E)$; ε in all cases increases with E, but the gradient is inversely related to the ferrate content.

4. Discussion and Conclusions

The structure and dielectric properties show that isomorphous replacement of Ti by Fe has marked effects. The material remains ferroelectric at low iron contents, but the phase transitions shift to lower temperatures. We have previously assumed [1] that ideal $BaFeO_3$ with the perovskite structure would show a phase transition above the temperature found for $BaTiO_3$; on this basis, and from the properties of other isomorphous series such as $(Ba, Pb)TiO_3$ [4], we would expect the Curie point to increase with the iron content, but this is not found. The reason appears to be that iron of valency four is unstable; the iron enters the lattice of $BaTiO_3$ in trivalent form, which reduces the Curie point.

The structure becomes increasingly irregular as the proportion of iron is raised; the collective interaction of the ions is reduced, and a hexagonal phase appears when the ferrate content attains 3%, this being detectable in specimens cooled slowly from 1380°C. The reduced stability range for the spontaneous polarization is easily explained if quadrivalent titanium is replaced by trivalent iron, as are the increase in the relaxation-type polarization and the other effects.

LITERATURE CITED

1. E.G. Fesenko and O.I. Prokopalo, "Isomorphism of the titanates and ferrates of strontium, barium, and lead," Kristallografiya, 1, 5, 520-523 (1956).
2. R.D. Burbank and H.T. Evans, "The crystal structure of hexagonal barium titanate," Acta Cryst., 1, 330, 336 (1948).
3. M.G. Harwood and H.A. Klasens, Nature, 165, 75 (1950).
4. E.G. Fesenko and A.G. Slabchenko, "An x-ray study of $(Ba, Pb)TiO_3$ solid solutions," Zh. Tekhn. Fiz., 24, 7, 1288-1290 (1954).

STRESSES PRODUCED BY HEATING AND COOLING IN SINGLE CRYSTALS

Yu. I. Sirotin

M. V. Lomonosov State University, Moscow

Translated from Kristallografiya, Vol. 1, No. 6, pp. 708-717, November-December, 1956
Original article submitted May 21, 1956

These stresses are calculated for anisotropic elliptic cylinders and plates, and also for spheres of cubic crystals; constant rates of heating or cooling are assumed. Detailed formulas are given for some particular cases.

1. General

These thermal stresses must be known in order to choose the best conditions for growing or annealing single crystals; they are also relevant to the design of piezoelectric and pyroelectric devices for use under conditions of rapidly changing temperature. It is general knowledge [1-4] that these stresses are relevant to all forms of heat treatment of materials, and the basic aspects of thermoelasticity for isotropic bodies are considered in the papers cited. Anisotropic bodies have begun to be considered only recently. Shubnikov [5] has examined the geometry of thermal expansion for crystals, and calculations have been reported [6] for the stresses in cylinders of cubic and hexagonal crystals for the cases of the cylinder axis along four-fold and six-fold crystallographic axes. In collaboration with others, we [7] have deduced the stresses in anisotropic plates with arbitrary linear anisotropy subject to the condition that the only temperature gradient is along the direction of the thickness. Results have been given [8] for the cylindrically orthotropic thick-walled cylinders. Here we give results for elliptic cylinders, plates with very general anisotropy, and spheres of cubic crystals.

The first requirement is to find the temperature distribution produced by the heating or cooling. We assume that the temperature at the boundaries of the crystal changes at a constant rate h (deg/sec), which is taken as positive for heating and negative for cooling. The temperature distribution is then given by

$$\varkappa^{ik}\frac{\partial^2 T}{\partial x^i \partial x^k}=\frac{\partial T}{\partial t}\quad (i,k=1,2,3) \tag{1}$$

subject to the boundary conditions $T_b = T_0 + ht$, $T(x,y,z;t) < \infty$, and to the additional condition $T(x,y,z;0) = T_0$. Here, $\varkappa^{ik}$ is the thermal-diffusivity tensor. The superscripts represent contravariance with respect to both, i.e., that on transforming the coordinates from x^i to $x^{i'}$ we have

$$\varkappa^{i'k'}=\frac{\partial x^{i'}}{\partial x^i}\frac{\partial x^{k'}}{\partial x^k}\varkappa^{ik},$$

as distinct from covariant tensors, for which

$$\alpha_{i'k'}=\frac{\partial x^i}{\partial x^{i'}}\frac{\partial x^k}{\partial x^{k'}}\alpha_{ik}.$$

Summation with respect to the various repeated indices is assumed.

An approximate solution to (1) is

$$T(x,y,z;t)=T_0+ht+\Phi(x,y,z), \tag{2}$$

where Φ satisfies

$$\varkappa^{ik}\frac{\partial^2\Phi}{\partial x^i \partial x^k}=h\quad (i,k=1,2,3);\quad \Phi_b=0.^1 \tag{3}$$

The relative error arising from this approximation does not exceed ε provided that the time since the start is not less than

$$t_*=\frac{R^2}{\varkappa}\ln\frac{1}{\varepsilon},$$

where R is the largest of the characteristic dimensions of the crystal, and $\varkappa$ is the least of the prin-

[1] See [3], for example.

cipal values of the thermal-diffusivity tensor. It is easy to solve (3) in all the cases of interest here; the general solution of the thermal-conduction equation for anisotropic bodies has been discussed by Mitskevich [9].

Let the X and Y Cartesian axes lie along the principal axes of the ellipse in an elliptic cylinder defined by

$$\frac{x^2}{R_1^2} + \frac{y^2}{R_2^2} = 1,$$

the Z axis lying along the axis of the cylinder. The XYZ system is used in conjunction with an $\xi\,\eta\,Z$ one, with $\xi = x/R_1$, $\eta = y/R_2$. Then,

$$\Phi = \frac{h}{2(\varkappa^{xx} + \varkappa^{yy})}(\xi^2 + \eta^2 - 1). \tag{4}$$

For an unbounded layer $-R < z < R$, heated at the surfaces $z = R$ and $z = -R$, we have

$$\Phi = \frac{h}{2\varkappa^{zz}}(z^2 - R^2). \tag{5}$$

For a sphere (radius R) cut from a cubic crystal, we have

$$\Phi = \frac{h}{6\varkappa}(x^2 + y^2 + z^2 - R^2). \tag{6}$$

To find the stresses we have to solve a system of equations that in the general case consists of three Cauchy equations for elastic equilibrium and six equations for consistency. In the latter the components ε_{ik} of the deformation tensor must be expressed in terms of the generalized form of Hooke's law

$$\varepsilon_{ik} = s_{iklm}\sigma_{lm} + \alpha_{ik}T \quad (i, k, l, m = 1, 2, 3)$$

via the components σ_{lm} of the stress tensor, the components α_{ik} of the thermal-expansion tensor, those of the elasticity s_{iklm}, and the temperature T. The boundary conditions are deduced from the absence of forces applied to the boundaries of the crystal.

2. Stresses in an Anisotropic Elliptic Cylinder

These stresses are completely determined by the temperature distribution of (4), so they also will be functions only of x and y or ξ and η. Lekhnitskii ([10], sections 17 and 21, pp. 87-97 and 109-110) has used stress functions to solve this class of problem and has derived a system of equations that these functions must satisfy; they were derived on the assumption that there are no thermal stresses, but they are readily extended to that case.

The Z axis of the XYZ Cartesian system here lies along the axis of the cylinder, the X and Y axes lying along the principal axes of inertia of the cross section. We assume that mass forces are absent and that no forces are applied to the boundaries of the crystal; the present solution may be superimposed on Lekhnitskii's if either class of force is present. The boundary conditions at the ends of the cylinder are satisfied only on average, generally speaking: the resultant force is zero, as are the torsional and bending moments of the forces applied to the end, the forces themselves being finite. We follow Lekhnitskii and introduce two stress functions $F(x, y)$ and $\Psi(x, y)$, with

$$\sigma^{xx} = \frac{\partial^2 F}{\partial y^2}, \quad \sigma^{yy} = \frac{\partial^2 F}{\partial x^2}, \quad \sigma^{xy} = -\frac{\partial^2 F}{\partial x\,\partial y},$$

$$\sigma^{xz} = \frac{\partial \Psi}{\partial y}, \quad \sigma^{yz} = -\frac{\partial \Psi}{\partial x}. \tag{7}$$

The stresses given by (7) satisfy the equations of equilibrium identically; these stresses are related to the deformations and the temperature via the generalized form of Hooke's law, and they must also satisfy the equations of compatibility and the conditions at the ends. For this to be so, it is necessary and sufficient that the stress functions are solutions of the following system of equations[2]:

$$L_4 F + 2L_3 \Psi = -L_{11} T,$$

$$L_3 F + 2L_2 \Psi = -L_1 T + (\alpha_{yz} - \gamma_{yz})\frac{\overline{Tz}}{y^2} - (\alpha_{xz} - \gamma_{xz})\frac{\overline{Ty}}{y^2} = 0, \tag{8}$$

subject to the boundary conditions[3]

$$\frac{\partial F}{\partial x}\Big|_b = \frac{\partial F}{\partial y}\Big|_b = \Psi_b = 0.$$

Here, the symbols are

$$L_4 = n_{yyyy}\frac{\partial^4}{\partial x^4} - 2n_{xxyy}\frac{\partial^4}{\partial x\,\partial y} + n_{xxxx}\frac{\partial^4}{\partial y^4},$$

$$L_3 = -n_{yyyz}\frac{\partial^3}{\partial x^3} + (n_{yyxz} + 2n_{xyyz})\frac{\partial^3}{\partial x^2 \partial y}$$

$$-(n_{xxyz} + 2n_{xyxz})\frac{\partial^3}{\partial x\,\partial y^2} + n_{xxxz}\frac{\partial^3}{\partial y^3},$$

[2] See [10], pp. 91-92, formulas (17.17) and (17.18).

[3] These are applicable only to a singly coupled body; see [10], p. 93, for extension to more general cases.

$$L_4 = n_{yyyy}\frac{\partial^4}{\partial x^4} - 4n_{yyyx}\frac{\partial^4}{\partial x^3\partial y} + 2(n_{xxyy} + 2n_{xyxy})\frac{\partial^4}{\partial x^2\partial y^2} - 4n_{xxxy}\frac{\partial^4}{\partial x\partial y^3} + n_{xxxx}\frac{\partial^4}{\partial y^4}, \tag{9}$$

$$L_1 = -\gamma_{yz}\frac{\partial}{\partial x} + \gamma_{xz}\frac{\partial}{\partial y},$$

$$L_{11} = \gamma_{yy}\frac{\partial^2}{\partial x^2} - 2\gamma_{xy}\frac{\partial^2}{\partial x\partial y} + \gamma_{xx}\frac{\partial^2}{\partial y^2},$$

$$n_{iklm} = s_{iklm} - \frac{s_{iklz}s_{zzlm}}{s_{zzzz}} \quad (i, k, l, m = 1, 2, 3),$$

$$\gamma_{ik} = \alpha_{ik} - \frac{s_{ikzz}\alpha_{zz}}{s_{zzzz}} \quad (i, k = 1, 2, 3).$$

The bar denotes averaging over a cross section perpendicular to the axis:

$$\overline{f} = \frac{1}{S}\iint_S f(x, y)\,dx\,dy.$$

Also, ϑ is a constant defined by the condition

$$\overline{\Psi} = 0, \tag{10}$$

which expresses the fact that there is no torque.

The above system may be solved by noting that $\overline{Tx} = \overline{Ty} = 0$ in this particular case, and that n_{iklm} and γ_{ik} are covariant tensors in respect of coordinate transformations in planes z = const; then we put (7) and (8) in the $\xi\,\eta\,Z$ system as

$$\sigma^{\xi\xi} = \frac{1}{R^4}\frac{\partial^2 F}{\partial\eta^2}, \quad \sigma^{\eta\eta} = \frac{1}{R^4}\frac{\partial^2 F}{\partial\xi^2}, \quad \sigma^{\xi\eta} = -\frac{1}{R^4}\frac{\partial^2 F}{\partial\xi\partial\eta},$$

$$\sigma^{\xi z} = \frac{1}{R^2}\frac{\partial\Psi}{\partial\eta}, \quad \sigma^{\eta z} = -\frac{1}{R^2}\frac{\partial\Psi}{\partial\xi}, \tag{11}$$

$$L_4' F + 2R^2 L_3'\Psi = -R^4 L_{11}'\Phi,$$

$$L_3' F + 2R^2 L_2'\Psi = -R^4 L_1'\Phi - R^6\vartheta, \tag{12}$$

in which the operators L' are derived from the corresponding operators L by replacing x by ξ and y by η, with $R = \sqrt{R_1 R_2}$, and Φ defined by (4).

The solution to (12) is found in the form

$$F = -\frac{1}{4}hR^4 qa(1 - \xi^2 - \eta^2)^2,$$

$$\Psi = -\frac{1}{2}hR^2 q(b\xi - c\eta)(1 - \xi^2 - \eta^2). \tag{13}$$

Condition (10) gives $\vartheta = 0$, while a, b, c, and q are given by

$$a = \frac{\Delta(\gamma_{\xi\xi} + \gamma_{\eta\eta}) + (KQ_\eta - K_\xi Q_\xi)\gamma_{\xi z} + (KQ_\xi - K_\eta Q_\eta)\gamma_{\eta z}}{\Delta D + 2KQ_\xi Q_\eta - K_\xi Q_\xi^2 - K_\eta Q_\eta^2},$$

$$b = \frac{1}{\Delta}[(KQ_\xi - K_\eta Q_\eta)a - K\gamma_{\xi z} + K_\eta\gamma_{\eta z}],$$

$$c = \frac{1}{\Delta}[(KQ_\eta - K_\xi Q_\xi)a - K\gamma_{\eta z} + K_\xi\gamma_{\xi z}],$$

$$q = \frac{1}{2(\varkappa^{\xi\xi} + \varkappa^{\eta\eta})}. \tag{14}$$

Here,

$$K = 2n_{\xi\eta\xi\eta},$$
$$K_\xi = 3n_{\eta\eta\xi\xi} + n_{\xi\xi\xi\xi},$$
$$K_\eta = 3n_{\xi\xi\xi\xi} + n_{\eta\eta\xi\xi},$$
$$Q_\xi = 3n_{\xi\xi\xi\xi} + 2n_{\xi\eta\eta\xi} + n_{\eta\eta\xi\xi},$$
$$Q_\eta = 3n_{\eta\eta\eta\eta} + 2n_{\xi\eta\xi\eta} + n_{\xi\xi\eta\eta},$$
$$\Delta = K_\xi K_\eta - K^2,$$
$$D = 3n_{\xi\xi\xi\xi} + 3n_{\eta\eta\eta\eta} + 2n_{\xi\xi\eta\eta} + 4n_{\xi\eta\xi\eta}. \tag{15}$$

The stress distribution is then

$$\sigma^{\xi\xi} = hqa(1 - \xi^2 - 3\eta^2),$$
$$\sigma^{\eta\eta} = hqa(1 - 3\xi^2 - \eta^2),$$
$$\sigma^{\xi\eta} = 2hqa\xi\eta,$$
$$\sigma^{\xi z} = \frac{1}{2}hq[c(1 - \xi^2 - 3\eta^2) + 2b\xi\eta],$$
$$\sigma^{\eta z} = \frac{1}{2}hq[b(1 - 3\xi^2 - \eta^2) + 2c\xi\eta],$$
$$\sigma^{zz} = -\frac{hq}{s_{zzzz}}\left\{\alpha_{zz}\left(\xi^2 + \eta^2 - \frac{1}{2}\right) + [a(s_{\xi\xi zz} + s_{\eta\eta zz}) + cs_{\xi zzz} + bs_{\eta zzz}](1 - \xi^2 - \eta^2) - 2(as_{\eta\eta zz} + bs_{\eta zzz})\xi^2 - 2(as_{\xi\xi zz} + cs_{\xi zzz})\eta^2 + 2(2as_{\xi\eta zz} + bs_{\xi zzz} + cs_{\eta zzz})\xi\eta\right\}, \tag{16}$$

where a, b, c, and d are given by (14) and (15), σ^{ZZ} being given by

$$\sigma^{zz} = \frac{1}{s_{zzzz}}\left[\alpha_{zz}\left(\frac{\overline{Tx}}{\overline{x^2}}x + \frac{\overline{Ty}}{\overline{y^2}}y + \overline{T} - T\right) - (s_{xxxx}\sigma^{xx} + s_{zzyy}\sigma^{yy} + 2s_{zzxy}\sigma^{xy} + 2s_{zzxz}\sigma^{xz} + 2s_{zzyz}\sigma^{yz})\right], \tag{17}$$

which is a generalization of the formula given in [10] (formula (17.9), p. 90]. This σ^{ZZ} is not given, in general, in what follows.

The stresses near the boundaries may best be considered by introducing a local Cartesian system for each point on the boundary ellipse, the basis vectors coinciding with the unit vectors tangential (τ) and normal (ν) to the ellipse at that point. This system is defined by

$$\tau = R_1\xi\cos\psi - R_2\eta\sin\psi,$$
$$\nu = R_1\xi\sin\psi + R_2\eta\cos\psi,$$
$$\sin\psi = \frac{R_2\xi}{\sqrt{R_2^2\xi^2 + R_1^2\eta^2}},$$
$$\cos\psi = \frac{R_1\eta}{\sqrt{R_2^2\xi^2 + R_1^2\eta^2}}. \tag{18}$$

From (18) we find that on the cylindrical surface

$$\sigma^{rr} = -hqa\,\frac{3R_1^4\sin^4\theta+(R_1^4+4R_1^2R_2^2+R_2^4)\sin^2\theta\cos^2\theta+3R_2^4\cos^4\theta-R_1^4\sin^2\theta-R_2^4\cos^2\theta}{R_1^2\sin^2\theta+R_2^2\cos^2\theta},$$

$$\sigma^{rz} = \frac{1}{2}hq\left\{\frac{b\,[3R_2^2\cos^2\theta+(R_2^2+2R_1^2)\sin^2\theta-R_2^2]\cos\theta}{\sqrt{R_1^2\sin^2\theta+R_2^2\cos^2\theta}}\right.$$

$$\left.-\frac{c\,[3R_1^2\sin^2\theta+(R_1^2+2R_2^2)\cos^2\theta-R_1^2]\sin\theta}{\sqrt{R_1^2\sin^2\theta+R_2^2\cos^2\theta}}\right\},$$

where θ = arc tan (η/ξ), while $\sigma^{\nu\nu}$, $\sigma^{\nu\tau}$, and $\sigma^{\nu z}$ are zero, as the boundary conditions require.

It is convenient to put (16) in terms of a cylindrical coordinate system if the crystal is a circular cylinder:

$$\widehat{rr} = \sigma^{rr} = hq_0 a_0 (R^2 - r^2),$$

$$\widehat{r\varphi} = r\sigma^{r\varphi} = 0,$$

$$\widehat{\varphi\varphi} = r^2\,\sigma^{\varphi\varphi} = hq_0 a_0 (R^2 - 3r^2),$$

$$\widehat{rz} = \sigma^{rz} = \frac{1}{2}hq_0 (b_0 \sin\varphi + c_0 \cos\varphi)(R^2 - r^2),$$

$$\widehat{\varphi z} = r\sigma^{\varphi z} = \frac{1}{2}hq_0 (b_0 \cos\varphi - c_0 \sin\varphi)(R^2 - 3r^2). \qquad (20)$$

Here, a_0, b_0, c_0, and q_0 are given by (14) and (15) if ξ is replaced by x and η by y in the superscripts. The crystal may have a plane of elastic symmetry perpendicular to the axis of the cylinder, in which case the solution simplifies further if we introduce a coefficient A:

$$A = \frac{1}{2\,(\chi^{xx}+\chi^{yy})}\cdot\frac{\gamma_{xx}+\gamma_{yy}}{3n_{xxxx}+3n_{yyyy}+2n_{xxyy}+4n_{xyxy}} \qquad (21)$$

and takes the form

$$F = -\frac{1}{4}Ah(R^2 - r^2)^2, \quad \Psi = 0, \qquad (22)$$

$$\widehat{rr} = Ah(R^2 - r^2), \quad \widehat{\varphi\varphi} = Ah(R^2 - 3r^2), \quad \widehat{r\varphi} = \widehat{rz} = \widehat{\varphi z} = 0. \qquad (23)$$

Table 1 gives A for cylinders cut from various crystals to give this plane of elastic symmetry, in which all the formulas are in terms of the principal systems of crystal-physics coordinates,[4] the four- and two-place superscripts being replaced in accordance with the usual rules ([12], pp. 389-390).

As we would expect (see [2]), we have for an isotropic body that

$$A = \frac{\alpha}{16\varkappa}\cdot\frac{1}{s_{11}+s_{12}} = \frac{\alpha E}{16\varkappa(1-\nu)}, \qquad (24)$$

in which E is Young's modulus and ν is Poisson's ratio. All the formulas in the table become of this form if we put $s_{22} = s_{33} = s_{11}$, $s_{13} = s_{23} = s_{12}$, $s_{44} = s_{55} = s_{66} = 2(s_{11} - s_{12})$, $s_{14} = s_{25} = 0$, $\alpha_1 = \alpha_2 = \alpha_3 = \alpha$, $\varkappa_1 = \varkappa_2 = \varkappa_3 = \varkappa$.

3. Stresses in Crystal Plates

The temperature distribution in an anisotropic plate is defined by (5). The stress distribution corresponding to a general temperature distribution along the thickness of the plate has been derived [7], and for the particular temperature distribution of (5) we have

$$\sigma^{ik} = \frac{h}{6x^{zz}}\beta^{ik}(R^2 - 3z^2), \quad (i,\ k = 1,\ 2)$$
$$\sigma^{pz} = 0, \quad (p = 1,\ 2,\ 3). \qquad (25)$$

Here the β^{ik} are given by the following formulas if the superscripts are replaced in accordance with the usual rules:

$$\beta_m = \frac{\sum_n A_{mn}\alpha_n}{\Delta}, \quad (m, n = 1, 2, 6) \qquad (26)$$

where

$$\Delta = \begin{vmatrix} s_{11} & s_{12} & s_{16} \\ s_{12} & s_{22} & s_{26} \\ s_{16} & s_{26} & s_{66} \end{vmatrix},$$

and A_{mn} is the algebraic complement of the corresponding element in the determinant Δ. Detailed formulas have been tabulated [7] for the β^{ik} of crystal plates of various orientations and various classes of elastic symmetry.

One case of interest is a thin circular disc of radius R subject to a planar temperature distribution in the squares of the coordinates:

$$T = T_0 + k(x^2 + y^2 - R^2). \qquad (27)$$

The stress function may be put as follows by analogy with (22):

[4] See [11], pp. 271-273, 326, and 327, or [12], pp. 18-21, 44-45, and 50-53 for the orientation of the axes of these systems.

TABLE 1. Formulas for the Coefficients A

Elastic symmetry	Direction of cylinder axis	Formula for A
II. Monoclinic	Axis X_2	$\frac{1}{2(\varkappa_1+\varkappa_3)}\cdot\frac{s_{22}(\alpha_1+\alpha_3)-(s_{12}+s_{23})\alpha_2}{3(s_{11}s_{22}+s_{22}s_{33}-s_{12}^2-s_{23}^2)+2(s_{22}s_{13}-s_{12}s_{23})+s_{33}s_{55}-s_{35}^2}$
III. Orthorhombic	Axis X_1	$\frac{1}{2(\varkappa_2+\varkappa_3)}\cdot\frac{s_{11}(\alpha_2+\alpha_3)-(s_{12}+s_{13})\alpha_1}{3(s_{11}s_{22}+s_{11}s_{33}-s_{12}^2-s_{13}^2)+2(s_{11}s_{13}-s_{12}s_{13})+s_{11}s_{44}}$
	Axes X_2 and X_3	Derived from previous by permutation of subscripts
IV. Trigonal ($3; 2, 3\cdot m, \bar{6}\cdot m$)	X_1 axis or other two-fold axis	$\frac{1}{2(\varkappa_1+\varkappa_3)}\cdot\frac{(s_{11}-s_{12}-s_{13})\alpha_1+s_{14}\alpha_2}{3(s_{11}^2+s_{14}s_{33}-s_{12}^2-s_{13}^2)+2s_{13}(s_{11}-s_{12})+s_{14}s_{44}-s_{14}^2}$
V. Tetragonal ($\bar{4}\cdot m, 4; 2, 4, m\cdot 4; m$)	Axes X_1 and X_2	$\frac{1}{2(\varkappa_1+\varkappa_3)}\cdot\frac{(s_{11}-s_{12}-s_{13})\alpha_1+s_{14}\alpha_2}{3(s_{11}^2+s_{14}s_{33}-s_{12}^2-s_{13}^2)+2s_{13}(s_{11}-s_{12})+s_{14}s_{44}}$
	Axis X_3	$\frac{1}{2\varkappa_1}\cdot\frac{s_{12}\alpha_2-s_{11}\alpha_2}{6s_{14}s_{56}-8s_{14}^2+2s_{14}s_{66}+s_{56}s_{66}}$

TABLE 1 (continued).

Elastic symmetry	Direction of cylinder axis	Formula for A
Va. Tetragonal ($\bar{4}$, 4, 4:m)	Axis X_3	As above
VI. Hexagonal	Axis X_3	$\frac{1}{16\varkappa_1} \cdot \frac{s_{33}\alpha_1 - s_{13}\alpha_3}{s_{11}s_{33} - s_{13}^2}$
	Any direction perpendicular to X_3 axis	$\frac{1}{2(\varkappa_1 + \varkappa_3)} \cdot \frac{(s_{11} - s_{12} - s_{13})\alpha_1 + s_{11}\alpha_3}{3(s_{11}^2 + s_{11}s_{33} - s_{12}^2 - s_{13}^2) + 2s_{13}(s_{11} - s_{13}) + s_{11}s_{44}}$
VII. Cubic	X_1, X_2, and X_3 axes (directions of <100> type) *	$\frac{\alpha}{2\varkappa} \cdot \frac{s_{11} - s_{12}}{6s_{11}^2 + 2s_{11}s_{12} - 8s_{12}^2 + s_{11}s_{44}}$
	Direction of <110> type	$\frac{\alpha}{4\varkappa} \cdot \frac{2s_{11} - 2s_{12} + 3s_{44}}{6s_{11}(s_{11} + s_{12}) + 12s_{12}(s_{44} - s_{12}) + 11s_{11}s_{44} + s_{44}^2}$
	Direction of <111> type	$\frac{9\alpha}{8\varkappa} \cdot \frac{s_{44}}{2(s_{11}^2 + s_{11}s_{12} + s_{44}^2) - 4s_{12}^2 + 13s_{11}s_{44} + 20s_{12}s_{44}}$

*Given in [6].

$$F = -\frac{1}{4} B (R^2 - r^2)^2, \tag{28}$$

where

$$B = \frac{k(\alpha_{xx} + \alpha_{yy})}{3s_{xxxx} + 3s_{yyyy} + 2s_{xxyy} + 4s_{xyxy}}, \tag{29}$$

and the stress distribution becomes

$$\widehat{rr} = B(R^2 - r^2), \quad \widehat{\varphi\varphi} = B(R^2 - 3r^2), \quad \widehat{r\varphi} = 0. \tag{30}$$

4. Stresses in Spheres of Cubic Crystals

Here the temperature distribution is defined by (6), and this produces the following stress distribution:

$$\begin{aligned} \sigma^{xx} &= Ch(R^2 - x^2 - 2y^2 - 2z^2), & \sigma^{yz} &= Chyz, \\ \sigma^{yy} &= Ch(R^2 - 2x^2 - y^2 - 2z^2), & \sigma^{zx} &= Chzx, \\ \sigma^{zz} &= Ch(R^2 - 2x^2 - 2y^2 - z^2), & \sigma^{xy} &= Chxy, \end{aligned} \tag{31}$$

or in polar coordinates,

$$\widehat{rr} = Ch(R^2 - r^2), \quad \widehat{\vartheta\vartheta} = Ch(R^2 - 2r^2), \quad \widehat{r\vartheta} = 0. \tag{32}$$

Here,

$$C = \frac{2\alpha}{3\kappa} \cdot \frac{1}{8s_{11} + 12s_{12} + s_{44}}. \tag{33}$$

As we would expect [3], for an isotropic sphere:

$$C = \frac{\alpha}{15\kappa} \cdot \frac{1}{s_{11} + s_{12}} = \frac{\alpha E}{15\kappa(1 - \nu)}. \tag{34}$$

We are indebted to V. R. Regel' for suggesting the topic and for advice on the work, and to B. N. Grechushnikov and V. L. Indenbom for valuable discussions.

LITERATURE CITED

1. N.N. Lebedev, Thermal Stresses in the Theory of Elasticity [in Russian] (1937).
2. H. Adams and E.D. Williamson, "The annealing of Glass," J. Franklin Inst., 190, 597 (1920); 190, 835 (1920).
3. G.P. Ivantsov, The Heating of Metals [in Russian] (1948).
4. N. Yu. Taits, Technology of Heating Steel [in Russian] (1950).
5. A.V. Shubnikov, "Some aspects of the thermal deformation of crystals," Kristallografiya, 1, 1, 95-104 (1956).
6. B.N. Grechushnikov and D. Brodovskii, "Thermal stresses in cubic crystals," Kristallografiya, 1, 5, 596-598 (1956).
7. V.L. Indenbom, I.M. Sil'vestrova, and Yu.I. Sirotin, "Thermoelastic stresses in anisotropic plates," Kristallografiya, 1, 5, 599-602 (1956).
8. J. Nowinski and W. Olszak, "Naprezenia termiczne w grubosciennym walku anizotropowym," Arch. mech. stosowanej, 5, 221 (1953).
9. I.V. Mitskevich, "Some aspects of the theory of thermal conductivity for anisotropic solids," Zh. Éksperim. i Teor. Fiz., 26, 557-561 (1954).
10. S.G. Lekhnitskii, Theory of Elasticity of Anisotropic Bodies [in Russian] (1950).
11. A.V. Shubnikov, E.E. Flint, and G.B. Bokii, The Principles of Crystallography [in Russian] (1940).
12. W. Mason, Piezoelectric Crystals and Their Application in Ultrasonics [Russian translation] (1952).

SOVIET PHYSICS - CRYSTALLOGRAPHY VOL. 1, NO. 6 NOV.-DEC., 1956

PROPAGATION OF ELASTIC WAVES ALONG SPECIFIC DIRECTIONS IN CRYSTALS

K. S. Aleksandrov

Institute of Crystallography, Academy of Sciences of the USSR
Translated from Kristallografiya, Vol. 1, No. 6,
pp. 718-728, November-December, 1956
Original article submitted October 9, 1956

It has been found that there are specific directions of propagation of elastic waves in crystals belonging to different symmetry groups of the tensor of elastic constants. The specific directions are divided into several forms according to the character of the propagation of ultrasonic vibrations. It is shown that in the preparation of elastic shear waves in a crystal, the phenomena observed are in many respects similar to familiar optical phenomena. By means of quarter-wave crystal plates, it is possible to excite a circularly polarized ultrasonic shear wave in an isotropic body.

The classic theory of the elasticity of anisotropic media was developed in the 19th century in the works of Green, Christoffel, Kelvin, and other investigators [1] to explain optical phenomena in crystals on the basis of the mechanical theory of light. Direct confirmation of this theory could not then be made for elastic waves because of the inadequacy of experimental technique.

Currently, because of the development of methods of ultrasonic research, it is possible not only to confirm the position of the classic theory of elasticity, but, in a number of cases, to develop and amplify it. This question is dealt with in many recent articles [2-5,8] by foreign authors. Until now, however, as far as we are aware, there are no publications dealing directly with the analogy between the propagation of elastic and electromagnetic vibrations in crystals except slight references to this analogy in a few articles [2,8,10].

The purpose of the present work was to investigate the propagation of ultrasonic vibrations in specific directions in a crystal, and to draw an analogy between these phenomena and similar phenomena in optics.

Specific Directions of the Propagation of Elastic Waves in Crystals

It is sufficiently well known that three plane elastic waves may be propagated in an arbitrary direction in a crystal: one quasi-longitudinal wave and two quasi-transverse waves. The vectors of the particles displaced in the waves are perpendicular to each other and, in the general case, some of them may coincide with the wave normal.

Depending on the form of symmetry, many crystals may have specific directions for the propagation of plane elastic waves, directions in which purely transverse and longitudinal waves are propagated. Recently, Borgnis [2] has given a method of determining such specific directions for crystals of any symmetry.

Following this method, we shall determine the specific directions for crystals of the rhombic system, and derive from the expressions obtained specific directions also for crystals of symmetrical systems of higher symmetry (tetragonal, hexagonal, and cubic).

We shall denote by $\vec{n}$ the unit vector, determining the direction of propagation of the wave and determined by direction cosines l_1, l_2, l_3, while the vector of displacement of the particles in the wave connected with this direction, having the direction cosines m_1, m_2, m_3, will be denoted by $\vec{r}$. As shown previously [2,3], for any $\vec{n}$, the direction of the vector $\vec{r}$ and the velocity of propagation of the waves v_1 may be found from the system of equations

$$\begin{aligned} m_1\Gamma_{11}+m_2\Gamma_{12}+m_3\Gamma_{13}&=m_1\rho v^2,\\ m_1\Gamma_{12}+m_2\Gamma_{22}+m_3\Gamma_{23}&=m_2\rho v^2,\\ m_1\Gamma_{13}+m_2\Gamma_{23}+m_3\Gamma_{33}&=m_3\rho v^2, \end{aligned} \tag{1}$$

where $\Gamma_{ik}=\Gamma_{ki}$, for crystals of the rhombic system they have the form

$$\begin{aligned} \Gamma_{11}&=l_1^2c_{11}+l_2^2c_{66}+l_3^2c_{55},\\ \Gamma_{22}&=l_1^2c_{66}+l_2^2c_{22}+l_3^2c_{44},\\ \Gamma_{33}&=l_1^2c_{55}+l_2^2c_{44}+l_3^2c_{33},\\ \Gamma_{23}&=l_2l_3(c_{23}+c_{44}),\\ \Gamma_{13}&=l_1l_3(c_{13}+c_{55}),\\ \Gamma_{12}&=l_1l_2(c_{12}+c_{66}). \end{aligned} \tag{2}$$

Here, ρ is the density of the crystal and the c_{ik} are its elastic constants. The velocities of propagation of the three waves, connected with $\vec{n}$, may be obtained from the determinant of the system of equations (1)

$$\begin{vmatrix} \Gamma_{11}-\rho v^2 & \Gamma_{12} & \Gamma_{13}\\ \Gamma_{12} & \Gamma_{22}-\rho v^2 & \Gamma_{23}\\ \Gamma_{13} & \Gamma_{23} & \Gamma_{33}-\rho v^2 \end{vmatrix}=0. \tag{3}$$

To each value of the velocity v_i, obtained from (3), there correspond in equations (1) its permitted values of the direction cosines of the vector of displacement of the particles in the wave m_{i1}, m_{i2}, m_{i3}. For any one of the three values of the velocity, the quantities on the right-hand side of Eq. (1) may be regarded as components of a certain vector $\vec{p}_i\{m_{i1}\rho v_i^2;\ m_{i2}\rho v_i^2;\ m_{i3}\rho v_i^2\}$ coinciding in direction with the vector $\vec{r}$. The condition for the existence of specific directions of propagation of elastic waves in the crystal may then be written as follows:

$$\vec{r}_i\times\vec{n}=0 \quad \text{or} \quad \vec{p}_i\times\vec{n}=0. \tag{4}$$

Condition (4) means that one of the displacement vectors is parallel to the vector of the wave normal. Actually, if one of the three displacement vectors is parallel to the wave normal, and the displacement vectors are at right angles to each other, all three waves are pure, while the direction of the normal found is the specific direction. Condition (4) may be written otherwise:

$$l_1p_2-l_2p_1=0, \quad l_1p_3-l_3p_1=0, \quad l_2p_3-l_3p_2=0. \tag{4'}$$

Simple substitutions and replacement in (1) of m_k by l_k, in agreement with condition (4), for a crystal of the rhombic system, leads to Eq. (5), the solutions of which with respect to l_1, l_2, l_3 give the directions sought:

$$\begin{aligned} &l_1l_2[l_1^2(c_{11}-c_{12}-2c_{66})+l_2^2(-c_{22}+c_{12}+2c_{66})\\ &\quad+l_3^2(c_{12}+2c_{23}-c_{22}-2c_{44})]=0,\\ &l_2l_3[l_1^2(-c_{11}+c_{12}+2c_{66})+l_2^2(c_{22}+2c_{44}-c_{12}-2c_{66})\\ &\quad+l_3^2(c_{22}-c_{12}-2c_{23})]=0,\\ &l_3l_3[l_1^2(c_{12}+2c_{66}-c_{12}-2c_{55})+l_2^2(c_{22}-c_{22}-2c_{44})\\ &\quad+l_3^2(-c_{22}+c_{22}+2c_{44})]=0. \end{aligned} \tag{5}$$

Equations (5) are satisfied if

$$\begin{aligned} l_1=l_2&=0 \quad l_3=1\\ l_2=l_3&=0 \quad l_1=1\\ l_3=l_1&=0 \quad l_2=1. \end{aligned} \tag{6}$$

Thus, the directions of all three crystallographic axes in crystals of the rhombic system are specific propagation directions, independent of the relationships between the elastic constants of the crystal.

Furthermore, equations (5) are satisfied

$$\begin{aligned} &\text{for} \quad l_1=0 \quad \frac{l_2^2}{l_3^2}=\frac{c_{22}-c_{23}-2c_{44}}{c_{33}-c_{23}-2c_{44}},\\ &\text{for} \quad l_2=0 \quad \frac{l_3^2}{l_1^2}=\frac{c_{11}-c_{13}-2c_{55}}{c_{33}-c_{13}-2c_{55}},\\ &\text{for} \quad l_3=0 \quad \frac{l_2^2}{l_1^2}=\frac{c_{11}-c_{12}-2c_{66}}{c_{22}-c_{12}-2c_{66}}. \end{aligned} \tag{7}$$

Specific directions in planes perpendicular to one of the crystallographic axes exist only for definite relationships between the elastic constants of the crystal, when the numerators and denominators in expressions (7) have the same signs.

For the case $l_1\neq l_2\neq l_3\neq 0$, there may still be one more specific direction in a rhombic crystal, given by the direction cosines determined by the relationships

$$\frac{l_2^2}{l_3^2}=\frac{bd-kb-ad}{ac-bc-af}, \qquad \frac{l_1^2}{l_3^2}=\frac{df-kf+ck}{kb-bd+ad}, \tag{8}$$

where

$$\begin{aligned} a&=c_{11}-c_{12}-2c_{66}, & d&=c_{11}-c_{13}-2c_{55},\\ b&=c_{22}-c_{12}-2c_{66}, & f&=c_{23}-c_{23}-2c_{44},\\ c&=c_{23}-c_{12}-2c_{66}, & k&=c_{23}-c_{23}-2c_{44}. \end{aligned} \tag{9}$$

It is easy to find from expressions (6)-(8) specific directions also for crystals of the tetragonal, hexagonal, and cubic systems.

For example, for the cubic system, putting $c_{11}=c_{22}=c_{33}$, $c_{44}=c_{55}=c_{66}$, $c_{12}=c_{13}=c_{23}$, we obtain the specific directions

$$l_i = 1 \quad (i = 1, 2, 3) \tag{6'}$$

$$l_3 = 0, \quad l_1 = \pm l_2, \quad l_2 = 0, \quad l_3 = \pm l_1, \quad l_1 = 0, \quad l_2 = \pm l_3 \tag{7'}$$

$$\pm l_1 = \pm l_2 = \pm l_3 = \pm 1/\sqrt{3}. \tag{8'}$$

Equations (9) reduce to the form

$$a = b = \ldots = k = c_{11} - c_{12} - 2c_{44}, \tag{9'}$$

i.e., they characterize the so-called anisotropic crystal.

In the already cited article [2], the author, while finding the specific directions in crystals of the cubic system, failed to discover the directions expressed by formula (7') which will be discussed later.

Before proceeding to the investigation of the specific directions, two remarks must be made.

1. It is by no means necessary for all the specific directions determined from formulas (6)-(8) to exist in a crystal. Only formulas (6) are independent of the relationships between the elastic constants of a crystal, and the directions defined by formulas (6) always exist in crystals of the systems enumerated. With regard to the directions defined by formulas (7), they exist necessarily in crystals of the cubic system in planes perpendicular to the principal axes, but they may not be found in the other systems. The directions defined by formulas (8) certainly exist in crystals of the cubic system, agree with the directions defined by formulas (7) in crystals of the hexagonal system, and are very rarely found in crystals of the tetragonal and rhombic systems.

Thus, for example, for a Rochelle salt crystal, the directions defined by expression (8) do not exist, while of the three possible directions, defined by expression (7), only one exists in the XZ plane at an angle $\varphi = 15°20'$ to the X axis (for values of the elastic constants taken from [6]).

2. When speaking of a specific direction, it must not be forgotten that it may occur several times in a crystal, corresponding to the symmetry of the elastic properties of the crystal. The complete set of specific directions in crystals of all systems is shown in Fig. 1, where the light circles denote directions necessarily existing in the crystal, while the dots represent directions which are not to be found in some crystals of the given elasticity group. The specific directions are now shown in the bottom hemisphere.

Investigation of the Propagation of Ultrasonic Vibrations along Specific Directions in a Crystal

Figure 1 shows that the majority of specific directions of the propagation of elastic waves in a crystal are associated with the elements of sym-

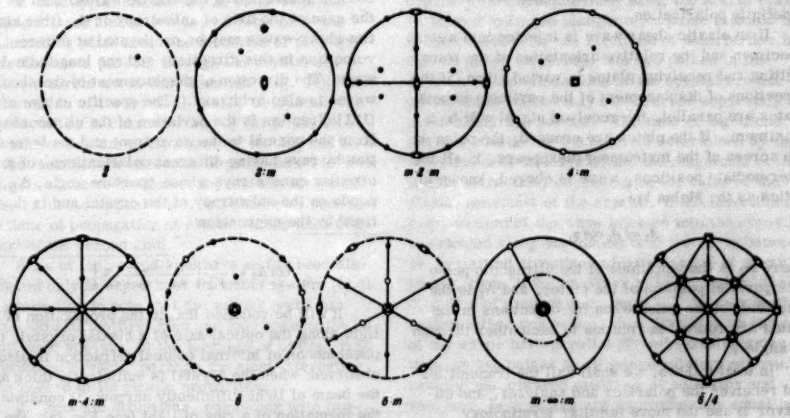

Fig. 1. Specific directions of propagation of elastic waves in crystals belonging to different symmetry groups of the tensor of elastic constants.

metry of the medium (coincide with the axes of symmetry or are situated in planes of symmetry). Knowing from equations (3) the velocities of propagation of the waves v_i in a specific direction $\{l_1, l_2, l_3\}$, if we find from equations (1) the direction cosines of the vectors of displacement in the waves, and carry out this investigation for all crystals, the specific directions may be divided into several groups.

1. In any specific direction coinciding with the axes of symmetry 3, 4, 6 of the elasticity group, it is possible for the purely longitudinal wave to be propagated at one velocity and the two shear waves at another velocity. With regard to the directions of displacement in the shear waves, equations (1) fail to give a definite answer in this case.

To confirm this statement, experiments were made on specimens cut normally to the axis of symmety of the elasticity group from NaCl and $NH_4H_2PO_4$ crystals, using an ultrasonic pulse apparatus [7] and two plates of Y-cut quartz, as transmitter and receiver. A short pulse of ultrasonic shear vibrations of frequency 1.67 Mc was injected into the crystal. The quartz plate at the other end of the crystal received the pulse passing through the crystal; after amplification, this pulse was applied to the plates of a cathode ray tube. A plate of Y-cut quartz transmits and receives ultrasonic vibrations with a fixed direction of displacement along the X axis, just as the polarizers and analyzers used in optics pass only light vibrations of a definite polarization.

If an elastic shear wave is injected into a glass specimen and the relative orientation of the transmitting and receiving plates is varied, then, if the directions of displacement of the particles in both plates are parallel, the received signal will be a maximum. If the plates are crossed, the pulse on the screen of the instrument disappears. In all the intermediate positions, a law is obeyed, known in optics as the Malus law,

$$A_1 = A_0 \cos\varphi,$$

where A_0 is the amplitude of the ultrasonic pulse with parallel position of the plates, and A_1 is the amplitude of the pulse when the directions in the plates are rotated in relation to each other through an angle φ.

In what follows, we shall call the transmitter and receiver the polarizer and analyzer, and endeavor to use the more familiar terminology adopted in optics, emphasizing the close analogy between the propagation of electromagnetic and elastic vibrations in crystals.

The experiments made showed that with any arbitrary direction of polarization of the transmitted ultrasonic wave and with crossed positions of polarizer and analyzer, the ultrasonic pulse was not received by the analyzer, and the wave was propagated in the crystal with given direction of polarization.

This case is to some extent analogous to the case of the propagation of light along the optical axis of a uniaxial inactive crystal. A plate, cut perpendicular to the optical axis and placed between crossed Nicols, remains dark on rotation of the microscope stage about the direction of propagation of the light. For this reason, we shall call the specific directions of propagation of elastic waves, coinciding with the 3,4,6 axes, axes of isotropy of the first kind.

It should be noted that in crystals there may be more than one such axis. In cubic crystals there are three such axes, in tetragonal, hexagonal, and trigonal crystals there is one, and in crystals of the remaining classes there are no such directions (see Fig. 1).

2. An exception to the case considered in 1 is provided by the [111] directions, coinciding with the axis of elasticity group $\bar{6}$ of crystals of the cubic system. As shown by de Klerk and Musgrave [8], in the propagation of an ultrasonic wave in the [111] direction, conditions are provided for the internal conical refraction of the elastic waves. Just as in the case of the axis of anisotropy of the first kind, two shear waves may be propagated at different velocities in this direction, and one longitudinal wave. The direction of displacement of the shear waves is also arbitrary. The specific nature of the [111] direction is the deviation of the ultrasonic ray from the normal to the wave front and the formation by rays having different polarizations of a circular cone of rays whose aperture angle, Δ_k, depends on the anisotropy of the crystal and is defined by the expression

$$\tan\Delta_k = \frac{1}{\sqrt{2}}\left|\frac{c_{11}-c_{13}-2c_{44}}{c_{11}-c_{12}+c_{44}}\right|. \qquad (10)$$

It will be recalled that in the propagation of light along the optical axis of a biaxial crystal, the phenomenon of internal conical refraction is also observed; when the crystal is sufficiently thick and the beam of light sufficiently narrow, it consists in the formation of a ring of light (see Fig. 2a), the diameter of which depends on the thickness of the

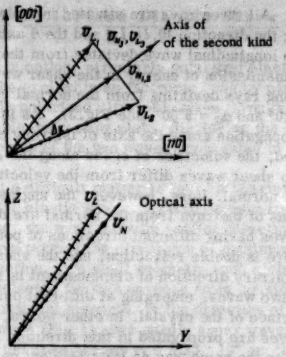

Fig. 2. a) Path of rays in internal conical refraction of light in biaxial crystals; b) path of rays in internal conical refraction of elastic waves in cubic crystals. v_{L1}, v_{L2}, v_{L3}) Velocities along the ray; v_{N1}, v_{N2}, v_{N3}) velocities along the normal corresponding to the two shear waves and one longitudinal wave.

crystal and the relationship between its optical constants [9]. If the phenomenon of internal conical refraction is examined in monochromatic polarized light, a luminous point will be seen, moving along a circumference during rotation of the polarizer.

In exactly the same way, in the case of the propagation of elastic waves, on rotation of the transmitting plate about the direction of propagation, the beam passing through the crystal describes a circle about this direction (Fig. 2b). The phenomenon of the internal conical refraction of elastic waves is characterized by large angles of refraction (for example, about 20° for KI) and also by the fact that the direction of propagation is here the axis of the refraction cone, and not its generatrix, as in the optical case. We shall call such directions of propagation of elastic waves axes of isotropy of the second kind.

Axes of the second kind have so far been discovered only in crystals of the cubic system [8]. It is interesting to note that the cubic crystal has three axes of the first kind and four axes of the second kind; speaking in the language of optics, it is a heptaxial crystal, perhaps the most interesting with regard to its elastic properties.

3. Specific directions, coinciding with twofold axes of symmetry, are widespread in crystals (Fig. 1). Analysis of Eqs. (2) and (3) in this case gives three different values of the velocity and three directions of displacement perpendicular to each other. For example, for a cubic crystal with propagation of an elastic wave in the [110] direction, the velocities of the waves v are equal, respectively, to

$$v_{[1\bar{1}0]} = [(c_{11} + c_{12} + 2c_{44})/2\rho]^{1/2},$$

$$v_{[11\bar{0}]} = [(c_{11} - c_{12})/2\rho]^{1/2}, \quad v_{[001]} = [c_{44}/\rho]^{1/2},$$

where the subscripts against the velocities denote the directions of displacement in each wave.

Investigations of the propagation of ultrasonic pulses in the directions considered have been carried out on specimens cut from cubic (rocksalt, potassium iodide), tetragonal (ammonium dihydrogen phosphate), trigonal (quartz), and rhombic (Rochelle salt) crystals.

As previously reported [10], analogy is observed in this case with optical phenomena occurring in the propagation of light perpendicular to the optical axis of a uniaxial inactive crystal. If a monochromatic beam of linearly polarized light is passed into a plate cut parallel to the optical axis of the crystal, and is regarded through an analyzer crossed with the polarizer, then on rotating the plate about the axis of the light beam, darkening of the plate will be seen every 90°, when the plane of vibrations of the incident light coincides with the plane of vibrations of one of the light waves propagated in the crystal.

As shown in [10], in the example of the propagation of ultrasonic pulses along the X axis of ammonium dihydrogen phosphate, a pulse injected into the crystal with any direction of polarization in the YZ plane, is divided into two pulses in the crystal. If the dimensions of the crystal are adequate, these pulses may be observed separately on the oscillograph screen. The time of lag of one pulse in relation to the other is determined by the dimensions of the crystal and the magnitude of the double refraction, depending on the value of the elastic constants of the crystal. If the direction of displacement of the wave injected into the crystal is oriented along the bisectrix of the angle between the permitted directions of polarization of shear waves, then, if the analyzer is rotated about the direction of propagation, there will be seen on the screen either one pulse, when the analyzer and one of the waves have parallel directions of polarization, or two pulses in all intermediate positions. In parallel and crossed positions of polarizer and analyzer, both pulses are approximately equal in amplitude, and the images on the screen of the cathode ray tube will be qualitatively identical [10].

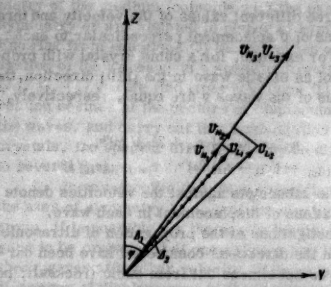

Fig. 3. Specific direction of propagation in the YZ plane in a beryllium crystal. v_{L1}, v_{L2}, v_{L3}) Velocities along the ray; v_{N1}, v_{N2}, v_{N3}) velocities along the normal, of the two shear waves and one longitudinal wave, respectively.

In what follows, we shall call the directions coinciding with the axes of isotropy of the second kind in the crystal the directions of maximum double refraction. There are three such directions in a rhombic crystal, four in a tetragonal crystal, six in a cubic crystal, and an infinite number in hexagonal crystals (any direction perpendicular to the 6 axis).

4. As an example of the specific directions situated in planes of symmetry, we shall examine the direction which may exist in crystals of the hexagonal system; it is defined by the formula

$$\tan\varphi = \frac{c_{33} - c_{13} - 2c_{44}}{c_{11} - c_{12} - 2c_{44}}, \qquad (11)$$

where φ is the angle reckoned from the 6 axis. In Fig. 1, the aggregate of such directions is shown by a dot-dash line.

For the example, we shall consider crystals of zinc and beryllium and use the nomenclature of their elastic constants given in [4]. Equation (11) shows that in a plane containing the principal angle, zinc has no specific directions differing from $\varphi = 0°$ and $\varphi = 90°$, which have already been considered. A beryllium crystal in this plane has a new specific direction defined by the cosines [0, 0.594, 0.805], i.e., $\varphi = 36.5°$.

Calculations give for this direction $[0, l_2, l_3]$ the following values for the speeds (vN_i) and directions of displacement of particles in the waves, $5.19 \cdot 10^5$ cm/sec and $5.80 \cdot 10^5$ cm/sec for shear waves; the directions of displacement give $[0, l_2, l_3]$; [1, 0, 0], and $[0, -l_3, l_2]$, respectively.

All three rays are situated in a plane containing the direction $[0, l_2, l_3]$ and the 6 axis, and only the longitudinal wave deviates from the normal. The transmission of energy in the shear waves occurs along rays deviating from the normal by angles $\Delta_1 = 4°20'$ and $\Delta_2 = 9°50'$ (see Fig. 3). As in the case of propagation along the axis of isotropy of the second kind, the velocities of sound along the ray for the two shear waves differ from the velocities along the normal. Here, however, the angles of deviations of the rays from the normal are different for waves having different directions of polarization; there is double refraction, and the shear wave with arbitrary direction of displacement is resolved into two waves, emerging at different points on the surface of the crystal. In other words, the shear waves are propagated in this direction in the crystal in the same way as light incident perpendicular to an arbitrarily cut plate of a biaxial crystal. In both cases, both waves deviate from the normal by different angles and have different normal and ray velocities.

5. With regard to the specific directions which do not coincide with the elements of symmetry of the medium and have not been especially investigated by us, it is possible to say merely that, according to the definition itself of specific directions (4), the longitudinal wave will be propagated along the normal. The points of emergence of rays of shear waves will be situated arbitrarily in space and the waves themselves will have different ray and normal velocities. In optics, this case is analogous to the foregoing.

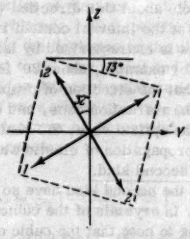

Fig. 4. Quarter-wave orientation of plate cut from quartz perpendicular to the X axis. 1-1 and 2-2) Directions of displacement of particles in waves propagated at velocities v_1 and v.

Circularly Polarized Elastic Shear Waves

Just as in optics, circularly polarized elastic waves may be excited in an isotropic body by passing a linearly polarized ultrasonic wave through a linearly double-refracting plate, displacing the phase difference of the two waves propagated in it by $\pi/2$.

It is not a difficult matter to make a quarter-wave plate for elastic waves. As will be seen from the foregoing, the most suitable are the directions which we have termed the directions of maximum double refraction. We shall calculate such a plate of quartz, selected for this purpose from considerations of mechanical strength. In the direction of the X axis in quartz (Fig. 1), two purely shear waves are propagated at velocities $v_1 = 3.33 \cdot 10^5$ cm/sec and $v_2 = 5.09 \cdot 10^5$ cm/sec. Figure 4 shows the polarization directions of these waves. In the same figure, the dashed line shows the method of cutting the plate. We determine the thickness of the plate, taking into consideration that the available apparatus [7] gives ultrasonic pulses of a frequency of 1.67 Mc. The phase difference G between the waves expressed in wavelengths is [11]:

$$G = d\left(\frac{1}{\lambda_1} - \frac{1}{\lambda_2}\right), \qquad (12)$$

where d is the plate thickness, λ_1 and λ_2 are the wavelengths, whence, for our case, d = 1.445 mm.

To reveal a circularly polarized elastic wave, the quarter-wave plate was stuck to a glass block with the dimensions 25 × 25 × 100 mm, and pulses of shear waves polarized in the direction of one of the edges of the plate (along the diagonal between the permitted polarization directions) were injected into the block through the plate. The pulse was received by the analyzer at the other end of the block and had approximately the same amplitude for any position of the analyzer. If a second-quarter plate was inserted between analyzer and block in crossed position with the former, compensation of the phase difference occurred, and on rotation of the analyzer the pulse reached a maximum value twice per revolution and disappeared twice.

With a quartz plate of double the thickness (d = 2.89 mm), the plane of polarization of the elastic wave could be rotated through 90°, which in optics is a characteristic feature of a half-wave plate.

Summary

On the basis of the method used by Borgnis [2], relationships have been derived for defining the specific directions of propagation of elastic waves in crystals of the rhombic system. From these equations, by means of various simplifications, corresponding expressions may be obtained for crystals of the tetragonal, hexagonal, and cubic systems.

It is shown that in crystals of the cubic system there are specific directions defined by formula (7') and not mentioned in [2]. A stereographic projection (Fig. 1) is given showing all the specific directions which may exist in the different groups of elastic symmetry (symmetry of the tensor of elastic constants).

An experimental investigation has been made of the propagation of ultrasonic vibrations along specific directions in various crystals. In all cases, an analogy has been found between the propagation of ultrasonic and light vibrations in crystals. On the basis of this analogy, all the specific directions in crystals have been divided into several groups, depending on the conditions of propagation of elastic waves in each direction.

A direct continuation of the analogy made is the production of quarter-wave plates for elastic waves, and the experimental production of circularly polarized elastic waves.

The aforementioned analogy is true only of shear waves and only in specific directions in the crystal. We have not considered the longitudinal wave, since, in any specific direction in the crystal, the longitudinal wave is propagated along a normal. In the experiment, transmitters of Y-cut quartz were used, giving a pure shear wave with sufficient approximation for qualitative experiments.

The case of the propagation of elastic waves in a crystal is to some extent a generalization with respect to the propagation of electromagnetic vibrations in crystals.

If later a general theory of the propagation and refraction of elastic waves in crystals were to be formulated and the Fresnel surfaces and Huygens structures, which have become classic for optics, were to be determined for elastic waves, the surfaces used in optics would form a special case of these surfaces. A considerable advance in this direction has been made in recent articles by Musgrave [3,4,5,6], although they are not free from individual errors and shortcomings.

The author is sincerely grateful to Academician A. V. Shubnikov for his general supervision of this work.

LITERATURE CITED

1. A. Love, Mathematical Theory of Elasticity

[Russian translation] (1935).
2. F.E. Borgnis, "Specific directions of longitudinal wave propagation in anisotropic media," Phys. Rev., 98, 1000-1005 (1955).
3. M.J.P. Musgrave, "On the propagation of elastic waves in aeolotropic media. I. General principles," Proc. Royal Soc., A226, 339-355 (1954).
4. M.J.P. Musgrave, "On the propagation of elastic waves in aeolotropic media. II. Media of hexagonal symmetry," Proc. Royal Soc., A226, 356-366 (1954).
5. G.F. Miller and M.J.P. Musgrave, "On the propagation of elastic waves in aeolotropic media. III. Media of cubic symmetry," Proc. Royal Soc., A236, 352-383 (1956).
6. S. Bhagavantam, "Elastic properties of single crystals and polycrystalline aggregates," Proc. Indian Acad. Sci., A41, 72-90 (1955).
7. K.S. Aleksandrov and O.V. Nosikov, "Instrument for the determination of the elastic constants of a crystal," Akusticheskii Zh., 2, 3, 244-247 (1956).
8. J. Klerk and M.J.P. Musgrave, "Internal conical refraction of transverse elastic waves in a cubic crystal," Proc. Phys. Soc., B68, 81 (1955).
9. M. Born, Optics [Russian translation] (1937), p. 318.
10. K.S. Aleksandrov, "Special case of the propagation of elastic waves in a crystal," Kristallografiya, 1, 1, 137-138 (1956).
11. A.V. Shubnikov, Optical Crystallography [in Russian] (1950).

PREPARATION OF SMALL SPHERES FROM SINGLE CRYSTALS

E. Sándor and P. Gado

Physics Institute, Budapest University

Translated from Kristallografiya, Vol. 1, No. 6,
pp. 729-732, November-December, 1956
Original article submitted March 28, 1956

An apparatus is described for forming spheres a few tenths of a millimeter in diameter. Experiments with various crystals are reported.

It is often difficult to calculate structure factors from measured intensities because it is very complicated to compute the absorption as a function of direction for a single crystal of irregular shape. This difficulty is very largely overcome if the crystal is cut to a shape such that the absorption is easily computed for all directions. The most convenient form is a sphere, and the absorption corrections for spherical crystals have been tabulated [1], so the calculations become quite simple.

Here we describe a device that enables one to cut a sphere of diameter 0.2 mm from a single crystal of any shape.

1. Principles and Design

Several devices have been described [2-5] for this purpose, the basic principle being as follows. The crystal is enclosed in a chamber coated with abrasive material and is caused to rotate freely; the crystal tends to rotate around its axis of largest moment of inertia, so the parts that strike the walls are the ends of the largest linear dimension. The result is that the crystal gradually acquires a shape having no largest dimension, i.e., a sphere. The crystal may be driven by centrifugal forces or by a jet of compressed air; the abrasive may be emery paper or grindstone material. The following conclusions may be drawn on methods previously described.

A. Compressed air is much preferable to centrifugal devices, because the crystal is then kept continuously on the wall, and so it becomes rounded much more rapidly. Moreover, compressed air is much less liable to damage the crystal, which is especially important for materials that cleave easily.

B. Previous devices experience some difficulty in reducing the diameter to 0.1-0.2 mm; many of them have gaps (e.g., between the fixed and moving parts, or between strips of emery paper) in which the small spheres become wedged. Also, emery paper becomes worn quite rapidly, and replacement represents an unnecessary difficulty.

We have designed a new instrument free from these deficiencies, which also has a special port through which the spheres are easily extracted without damage. The crystal is rounded by a carborundum grinding wheel of grain size 400 having an internal hole of V shape (Figs. 1 and 2). The compressed air enters this space via a small tangential channel. The large central holes on the two sides are sealed with close-fitting plates, one of which is fixed and has in its center a Lucite window. The other can be moved and has two ports, both closed by fine wire grids, one of which is flat and allows the air to escape. The other is convex and is used to insert and remove the crystals.

The adjustable plate is turned to expose the large grid; the crystal is placed in it, and the device is turned to allow the crystal to fall into the interior space. This hole is closed by a fine wire grid during the grinding. The crystal is subsequently extracted by opening the large grid again and tilting the device to cause the crystal to fall into it, perhaps with the aid of a slight puff of air. The crystal is then readily removed; forceps should not be used, especially for soft materials.

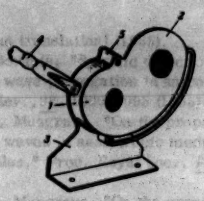

Fig. 1. Schematic of the device. 1) Grinding wheel; 2,3) closure plates; 4) air inlet; 5) holder for wheel.

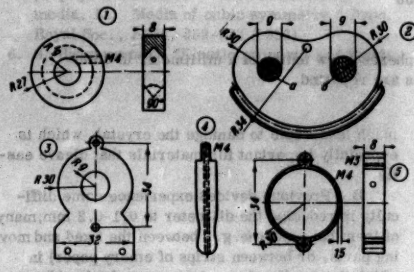

Fig. 2. Some components. 1) Carborundum wheel; 2) metal plate, 1.5 mm thick with (a) flat and (b) convex grids; 3) metal plate, 1.5 mm thick; 4) inlet; 5) wheel holder.

2. Tests on Materials

This device has been in use in our institute for about a year and has been used on various materials, as follows.

1. Careful operation has enabled us to produce spheres a few tenths of a millimeter in diameter from nearly all materials, the differences in diameter between directions not exceeding 1%. Difficulties were encountered only in the following cases.

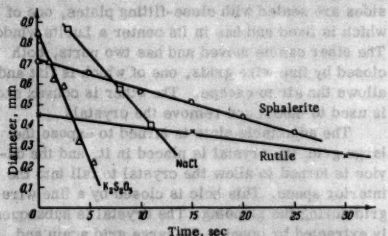

Fig. 3. Size as a function of time for various materials at a fixed air flow rate. The slopes of the lines cannot be compared directly, because the fixed rate was not the same for all materials; for instance, a high rate was used with the NaCl.

TABLE 1

Material	Δd, mm
Sphalerite (ZnS)	0.07
$K_2S_2O_5$	1.00
NaCl, KBr	0.04
$Na_2S_2O_3 \cdot 5H_2O$	0.30
Rutile (TiO_2)	0.01

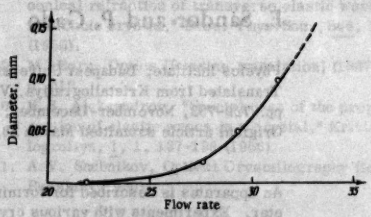

Fig. 4. Loss in diameter in 5 min for a sphalerite crystal as a function of flow rate (cm^3/sec).

A. Crystals that cleave readily are liable to split off small plates, so these are ground only to roughly spherical form (edges and corners removed). Examples are NaCl and KBr. Even these give satisfactory results if the device is operated carefully at a low speed with a fine wheel.

B. If the hardness varies a great deal with direction. The product may then be an ellipsoid rather than a sphere, the major axis corresponding to the direction of greatest hardness. This is the case for rutile, for example.

C. Crystals of very low melting point or showing transitions must be cooled suitably during grinding, on account of the heat produced. An example is $K_2S_2O_3 \cdot 2H_2O$, which loses one molecule

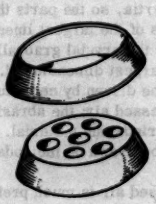

Fig. 5. Glass holder for storing crystal spheres.

of the water of crystallization between 17 and 30°C, and the other at 35°C.

2. The diameter has a linear relation to grinding time for a fixed air flow rate, the slope of the line being governed by the hardness (Fig. 3). Table 1 gives the reduction Δd in the diameter produced in 5 min with an air flow rate of 29 cm^3/sec.

3. Higher flow rates accelerate the reduction very greatly (roughly as the square of the rate, Fig. 4). Very high rates should not be used, on account of excessive danger of damage or even disintegration.

4. The small spheres are best stored in glass plates with small depressions ground in them, which should be fitted with suitable covers (Fig. 5).

LITERATURE CITED

1. H. T. Evans and M. G. Ekstein, "Tables of absorption factors for spherical crystals," Acta Cryst., 5, 540-542 (1952).
2. W. L. Bond, "Making small spheres," Rev. Sci. Instr., 22, 344 (1951).
3. P. Senio and Ch. W. Tucker, "Ceramic wheel sphere grinder," Rev. Sci. Instr., 25, 549 (1954).
4. W. L. Bond, "Small crystal spheres," Rev. Sci. Instr., 25, 401 (1954).
5. R. L. Whitmore, "Making small spheres," J. Sci. Instr., 26, 224 (1954).

BRIEF COMMUNICATIONS

A SYSTEM FOR MODELING CRYSTAL STRUCTURES AND PATTERNS

N. V. Belov

Institute of Crystallography, Academy of Sciences of the USSR

Translated from Kristallografiya, Vol. 1, No. 6,
pp. 733-734, November-December, 1956
Original article submitted September 11, 1956

The Komsomol'skaya Pravda Plant in Moscow has produced a plastic kit called "Mosaic" for constructing a variety of mosaics; it is intended mainly for stimulating conceptions of symmetry in children, but it is also of great value in instruction in crystallography, demonstration of atomic structures, and mineralogy. The hexagonal parts come in 5 colors, each fitting via a rod into a panel with a hexagonal net of holes. This gives a simple and cheap way (only 17 roubles, or less than the simplest crystal structure model) of constructing various patterns based on anion close packing with cations in the holes (many compounds and minerals consist essentially of patterns of this kind). Each hexagon may be considered as the projection along a triad axis of a Pauling octahedron, while a pattern built up from octahedra of different colors (i.e., cations) is (see [1] and [2]) present in many structures; sometimes it forms the entire structure.

"Mosaic" enables one to construct (or to have a student construct, in an examination) the following patterns given in [1,2]: corundum-mica, ilmenite, carbonate, spinel; rutile-cassiterite, diaspore-goethite, anatase-brookite-columbite; and numerous patterns for minerals with orthorhombic-monoclinic sequences: norbergite, chondrodite, humite, clinohumite, and olivine. The monticellite pattern may also be demonstrated in the latter. The pyroxene-ramsayite and amphibole patterns of [1] are also well shown, and careful inspection will reveal the "secret" pattern of chrysotile-asbestos (see [2], section V, p. 18), although there is nothing particularly secret about it.

The models made with "Mosaic" would be even better if the parts were not very flat hexagonal pyramids, but consisted of a triangle in a hexagon. This would give a complete imitation of an octahedron and would enable one to pass readily to arrays consisting of tetrahedra. It would probably be difficult to get the molds altered for this purpose, although it would not affect the beauty of the hexagons at all.

This kit will enable one to economize on paper printed with a hexagonal millimeter grid (in very short supply), which so far has been the basic medium for demonstrating and interpreting crystal structures on the basis of close packing.

LITERATURE CITED

1. N. V. Belov, Structures of Ionic Crystal [in Russian] (Moscow, 1947).
2. N. V. Belov, "Outlines of structural mineralogy, I-VII," Min. Sborn. L'vov Geol. Obshch. 3-10 (1949-1956).

SOVIET PHYSICS – CRYSTALLOGRAPHY VOL. 1, NO. 6 NOV.-DEC., 1956

ANOMALOUS POLARIZATION IN ROCHELLE-SALT CRYSTALS

V. A. Yurin

Institute of Crystallography, Academy of Sciences of the USSR
Translated from Kristallografiya, Vol. 1, No. 6,
pp. 734-736, November-December, 1956
Original article submitted September 3, 1956

Rochelle-salt crystals irradiated by the rays from Co^{60} show altered electrical polarization; the usual hysteresis loop (Fig. 1a) at a certain dose becomes a double one (Fig. 1b) typical of an antiferroelectric. Higher doses eliminate the loop; the polarization becomes linear (Fig. 1c).

The following aspects are of interest here.

1. Anomalous polarization as a function of temperature for weak and strong fields.

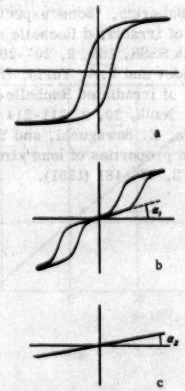

Fig. 1. Hysteresis loops of Rochelle salt; a) unirradiated; b) irradiated for 2 h; c) irradiated for 11 h 10 min. Temperature +18°C; frequency 50 cps; E_{max} = 1100 V/cm; dose rate 10^{19} eV/h-g.

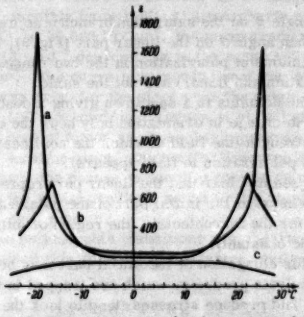

Fig. 2. Dielectric constant of Rochelle salt as a function of temperature; a) unirradiated; b) irradiated for 2 h; c) irradiated for 11 h 10 min. Dose rate, $0.1 \cdot 10^{19}$ eV/h-g; measurements made at 8 V/cm with a capacity bridge.

2. Changes in the domain structure and piezoelectric properties caused by irradiation.

The measurements were made always on the same specimens at increasing total dose levels, the measurements being performed in the intervals between successive doses.

Curve a of Fig. 2 shows the dielectric constant as a function of temperature for one of the specimens, which had the usual two peaks at the Curie points before irradiation. These peaks become lower and move together (curve b of Fig. 2) as the dose increases, the final result being a single broad hump (curve c). Curve b of Fig. 2 corresponds to the double hysteresis loop of Fig. 1b; curve c to Fig. 1c.

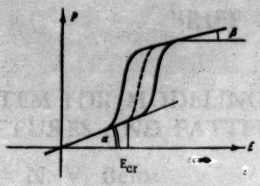

Fig. 3. Part of the double hysteresis loop given by Rochelle salt.

The hysteresis loop was recorded at the same time as the dielectric constant was measured with a bridge in weak fields. The dielectric constants deduced from the angles α_1 and α_2 of Figs. 1b, c agree closely with the values for curves b and c of Fig. 2.

Angle β on the saturation branch is appreciably less than angle α on the linear part (Fig. 3), so the mechanisms of polarization in the two ranges (saturation and linear) are not the same.

The domains in a specimen giving a double loop began to change in orientation only near the critical field strength (the field at which the nonlinear relation of polarization to field appears).

It seems clear that the linear part represents an extension of the initial part of the polarization curve for the ferroelectric (the region of initial dielectric constant).

This elongation of the initial part may be due to radiolysis products, which are trapped in the lattice and produce stresses (tend to lock the domains in position). This means that much higher field strengths are now needed in order to reorient the domains. Prolonged irradiation suppresses orientation change altogether. The crystal is thus in a different state, in which the antiparallel disposition of the domains gives rise to linear polarization for fields below the critical value; the similar linear region for an antiferroelectric arises from the antiparallel array of the dipoles in adjacent unit cells [3].

In some cases the domain structure became of smaller scale, whereas in others it was almost unaltered.

The piezoelectric constant g_{14} was measured on a 45° X-cut specimen in the intervals between successive doses; there was no appreciable change in this quantity.

This anomalous polarization resembles the polarization of an antiferroelectric and points to a close connection between the properties of ferroelectrics and antiferroelectrics, although there are marked differences also, of course. Rochelle salt is of special value here, because the type of polarization is readily altered by adjustment of the radiation dose, the two states being ferroelectric and similar to antiferroelectric.

We are indebted to I. S. Zheludev for direction of this work.

LITERATURE CITED

1. I. S. Zheludev, M. A. Proskurnin, V. A. Yurin, and A. S. Baberkin, "Some aspects of the polarization of irradiated Rochelle salt," Dokl. Akad. Nauk SSSR, 103, 2, 207-208 (1955).
2. I. S. Zheludev and V. A. Yurin, "Some physical properties of irradiated Rochelle-salt crystals," Izv. Akad. Nauk, 20, 2, 211-214 (1956).
3. G. Schirane, E. Sawaguchi, and Y. Takagi, "Dielectric properties of lead zirconate," Phys. Rev., 84, 3, 476-481 (1951).

THE MELTING POINT OF INDIUM AT PRESSURES UP TO 30,000 kg/cm^2

V. P. Butuzov and E. G. Ponyatovskii

Institute of Crystallography, Academy of Sciences of the USSR

Translated from Kristallografiya, Vol. 1, No. 6,
pp. 736-737, November-December, 1956
Original article submitted August 14, 1956

The range 1-30,000 kg/cm^2 was covered in these measurements on indium of 99.995% purity. The hydrostatic pressure was produced in a pressure amplifier designed at this institute [1]. The fluid was a mixture of isopentane with n-pentane, the pressure being measured to ±100 kg/cm^2 with a manganin manometer. The temperature was measured to ±1.5°C with an iron–nichrome thermocouple, the melting point being determined by differential temperature analysis with photographic recording. The methods have previously been described in detail [2].

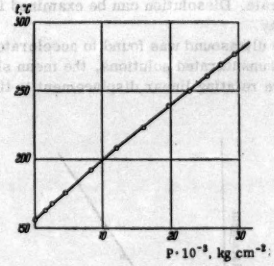

Fig. 1

Figure 1 shows the results; the melting point rises smoothly from 156°C at atmospheric pressure to 280°C at 30,000 kg/cm^2, the mean gradient being $4.13 \cdot 10^{-3}$ deg-cm^2/kg in the range 1-30,000 kg/cm^2. The curve is somewhat concave to the pressure axis, for the slope near the origin is $4.33 \cdot 10^{-3}$ deg-cm^2/kg. Oelsen et al. [3] give the latent heat of fusion at atmospheric pressure as 781 ± 4 cal/g-atom, which with Clapeyron's equation gives the change in specific volume on melting (from the initial gradient) as $2.93 \cdot 10^{-3}$ cm^3/g or 0.336 cm^3/g-atom.

No polymorphic transitions are observed throughout this range of temperatures and pressures.

LITERATURE CITED

1. V.P. Butuzov, G.P. Shakhovskii, and M.G. Gonikberg, "Pressure amplifiers for use at high temperatures and superhigh pressures," Tr. Inst. Kristallogr., 11, 233-238 (1955).
2. V.P. Butuzov, S.S. Boksha, and M.G. Gonikberg, "Polymorphic transitions of phosphorus at very high pressures," Dokl. Akad. Nauk SSSR, 108, No. 5 (1956).
3. W. Oelsen, O. Oelsen, and D. Thiel, "Präzisionsmessungen der Schmelzwärmen einiger Metalle," Z. Metall., 46, 8, 555-560 (1955).

EFFECTS OF ULTRASOUND ON THE GROWTH OF A SINGLE CRYSTAL OF POTASH ALUM

A. P. Kapustin and V. E. Kavalyunaite

Institute of Crystallography, Academy of Sciences of the USSR,
and Lenin Pedagogic Institute
Translated from Kristallografiya, Vol. 1, No. 6,
pp. 737-738, November-December, 1956
Original article submitted September 25, 1956

Ultrasound affects crystallization because it gives rise to numerous fresh nuclei in the supercooled material if a seed is already present. The precise number of nuclei may vary, which is reflected in the final polycrystalline structure. The effects of ultrasound on the latter have been examined many times, but the effects on single crystals have not been recorded. A growing crystal draws the molecules or groups it needs from the adjacent medium, so the major factors here are diffusion and concentration currents (for solutions) or self-diffusion and thermal conduction (for melts). It is debatable whether ultrasound influences exchange of molecules and diffusion, although these processes are basic to many of the effects of ultrasound.

We have examined the effects on the linear growth rates of the octahedron faces on single crystals of potash alum; the rates in the field were compared with those outside the field, the conditions otherwise being the same. The ultrasound was provided by a quartz plate driven at 2 Mc with a maximum intensity of 0.2 W/cm^2.

The beam passed through the bottom of the crystallizer, which was placed at the surface of a bath of transformer oil. The crystallizer was a double-walled glass vessel, the space between the walls containing circulating water at a constant temperature. The two crystallizers were connected in series in the water circuit. The growth rates were measured as the rates of displacement of the growth fronts as indicated by traveling microscopes reading to 0.01 mm. The temperature of the solution remained constant to 0.1°C; the saturation temperature was measured from concentration currents as viewed by schlieren methods.

The solution was run into the preheated crystallizers at a temperature of 7-8°C above its saturation point. The vessels were then quickly covered with lids having holes to admit the crystal holder and thermometer. The solutions were stirred thoroughly before the weighed seeds were inserted. Then the ultrasonic beam was directed into one vessel, while corresponding faces on both crystals were observed via the microscopes. The linear positions were recorded, initially every 15-30 min and then every hour (total duration of run 13-15 h). At the end the crystals were removed, dried, and weighed; the change in weight gave a check on the growth rate. Dissolution can be examined in the same way.

The ultrasound was found to accelerate dissolution in unsaturated solutions, the mean slope of the curve relating linear displacement to time be-

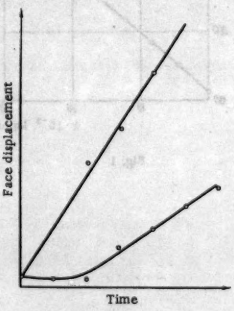

Fig. 1

ing about doubled. Again, the growth rate in a saturated solution was raised by the ultrasound; here the mean slope was increased by a factor of 2-3. The gain in weight in a period of 10-15 h was 50-60 mg; Fig. 1 illustrates the general behavior of the linear displacement. The ultrasound accelerated the growth of the face turned toward the source and also (to some extent) that of the other faces, because the relative increase in mass was always greater than for the control crystal.

The ultrasound had this pronounced effect on the growth only in weakly supersaturated solutions and at low intensities. High intensities merely produced the normal disintegration of the crystal.

REVIEW

APPLICATION OF THE DIFFRACTOMETER IN SOME STRUCTURE-ANALYSIS PROBLEMS

D. M. Kheiker and L. S. Zevin

All-Union Asbestos-Cement Research Institute

Translated from Kristallografiya, Vol. 1, No. 6, pp. 739-763, November-December, 1956
Original article submitted July 15, 1956

Introduction. §1. X-ray detectors. §2. Main parts of a diffractometer. §3. Intensity measurement, quantitative phase analysis. §4. Instrumental factors in shapes of diffraction peaks, crystallite-size determination. §5. Precision cell-parameter measurement. §6. Intensity measurements on single crystals. §7. Texture studies. §8. Other applications.

Introduction

Diffractometers are being increasingly used in x-ray structure analysis. These are instruments for recording the pattern and measuring the intensities with counters. There are types for use with powders, types for single-crystal studies, others for texture studies, and ones for special purposes. These instruments reduce the time needed while increasing the accuracy and sensitivity, which has meant more general use of x-ray structure analysis in research and (especially) industry.

The URS-50I x-ray equipment is in regular production in this country; it has ionization recording and is meant mainly for use with powders and in orienting piezoelectric crystals [1,2]. The general introduction of diffractometers in research and routine laboratories requires early exploitation of foreign work on devices of this type, together with development of methods adapted to the URS-50I and the design of new types of diffractometer custom-built for particular uses.

1. X-Ray Detectors

The detectors other than films are ionization chambers, Geiger counters, gas proportional counters, and scintillation counters. All of these reduce the time required and give the intensities directly. Counters are more sensitive and accurate than films and ionization chambers [3-6]; the error of measurement with a counter can be made as low as 1%.

Geiger counters are most commonly used in diffractometers [7-12] because the above advantages are here accompanied by good stability even in simple equipment. Gas proportional counters [12-15] and scintillation counters [15-21] have recently come into use for other reasons.

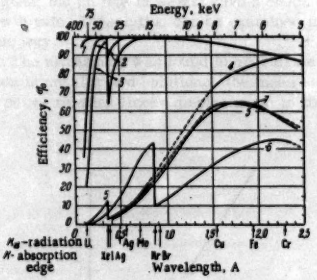

Fig. 1. Efficiency curves for counters: 1) scintillation counter with NaI(Tl) crystal of thickness 0.7 cm, with 127 μ Be window; 2) the same, 0.1 cm NaI(Tl), 127 μ Be; 3) 0.05 cm NaI(Tl), 127 μ Be; 4) proportional counter filled with Xe at 300 mm Hg, active length 2.7 cm, 127 μ Be window; 5) the same, 300 mm Hg of Xe, 2.7 cm, window 13 μ of mica + 127 μ Be; 6) the same, 500 mm Hg of Kr, 2.7 cm, 13 μ mica + 127 μ Be; 7) Geiger counter, 550 mm Hg of Ar, 10.0 cm, 13 μ mica.

TABLE 1. Comparison of Types of Counter

Type	Efficiency, %		Dead time, μsec	Discr. range, V	Discr. loss, %	Ratio of 102 line of graphite to x-ray background
	CuKα	MoKα				
Geiger	60*	13* 30**	200	–	–	2.3
Proportional	60*	13* 30**	1	6-10	20	4.3
Scintillation	96	99	1	5-10	15	4.5

*Filled with argon.
**Filled with krypton.

The most important characteristics of a counter are as follows.

Efficiency. This is defined as the ratio of the number of counts recorded to the number of quanta passing through the counter slit; it is directly related to the sensitivity and inversely related to the time needed to attain a given level of error. The efficiency of a Geiger counter [10,11,22] or proportional counter [22] is dependent on the absorption in the window material, the gas filling used, the active length, and the wavelength of the radiation. The efficiency is maximal at a certain wavelength; it falls toward short wavelengths because the radiation becomes more penetrating, and toward long wavelengths on account of increasing absorption in the window and in the dead space [12].

Thin windows of materials of low absorption are used to increase the efficiency at long wavelengths: 10 μ of mica (absorption coefficient for CuKα about 40 cm^{-1}), 20 μ of aluminum (40 cm^{-1}), and vacuum-tight beryllium 0.1 mm thick (1.6 cm^{-1}). The dead space is also minimized. The efficiency in the short-wave region is raised by filling the counter with heavy gases under increased pressure and by lengthening the counter. The strongly absorbing NaI(Tl) is used in optimal thickness in scintillation counters [22].

Figure 1 gives efficiency curves. An argon-filled Geiger counter and a xenon-filled proportional counter give efficiencies that fall rapidly toward short wavelengths; the efficiency for 1.54 Å (CuKα) is 60% but is only 13% for 0.71 Å (MoKα). This behavior produces an effect of partial filtration relative to films, especially if there is no absorption edge in the short-wave region of the continuum to delay the fall in efficiency. A krypton-filled proportional counter here gives much worse performance on CuKα, on account of its absorption edge at 0.87 Å, but it can be used with MoKα (0.71 Å) at an efficiency of some 30%. The scintillation counter gives nearly 100% efficiency in the range 5 to 75 keV, with some slight fall at long wavelengths due to absorption in the window.

Dead Time τ.[1] This determines the linear range of a Geiger counter, which has $\tau \cong 200$ μsec and so loses about 10% of the counts at 500 sec^{-1}. Proportional and scintillation counters have dead times less than 1 μsec, so the practical dead time is governed by the circuits and may be around a microsecond.

Energy Resolution. A Geiger counter produces a pulse whose height is independent of the energy deposited in the counter, whereas proportional and scintillation counters produce pulses proportional to the energy deposited. Discriminators can then be used to eliminate x-ray background [12-15]. The energy resolution of a proportional counter is 2-2.5 times better than that of a scintillation counter, but the latter is still adequate for many purposes (Table 1).

Electronic Systems. These employ standard circuits derived from nuclear physics; Fig. 2 shows the block diagram of the system commonly employed with a Geiger counter in recording x rays.

The other counters need two additional units: a linear amplifier and a single-channel analyzer. The EHT supply must also be more stable, and the circuits must have a dead time of about 1 μsec [23-25]. The system counts over a period set by the timer and also records the mean rate over the averaging time of the integrator.

2. Main Parts of a Diffractometer

A counter records the rays only over a narrow angular range at any one time; counter and speci-

[1] The time following the recording of a quantum for which the counter will not respond to a further quantum.

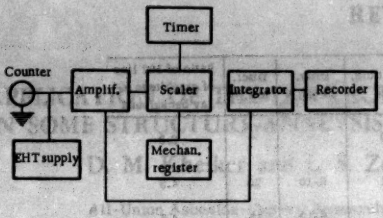

Fig. 2. Block diagram of a Geiger-counter system.

men must move, the angles being read with a goniometer.

Bragg-Brentano [7, 8, 26] or Zeeman-Bolin [27] focusing methods are used with powders to obtain adequate intensity in conjunction with good angular resolution. The first type is simpler in design, while the second enables one to use a broad divergent primary beam and is free from the difficulty of the Bragg system that all the reflections occur in planes parallel to the surface of the specimen. The Zeeman-Bolin method is thus preferable for phase analysis of specimens showing a preferred orientation.

The time distribution of the measurements implies that the primary beam must be of high stability. The two methods of stabilization are: (1) current and voltage stabilization at the x-ray tube [8, 26, 28]; (2) a monitor counter working from the primary beam, which controls the tube [29, 30]. The monitor counter can be used without tube control if it records an intensity proportional to that of the primary beam (e.g., from an aluminum foil placed in that beam), the other readings being taken as ratios to those from the monitor [31, 32].

3. Intensity Measurement and Quantitative Phase Analysis

The diffractometer has several differences from photographic methods in intensity measurement. The first arises from the random time distribution of the x-ray quanta, which produces a relative error inversely proportional to the square root of the number of quanta recorded. The second is that focusing methods and flat specimens must be used because the intensity is proportional to the number of crystals in the reflecting position, while the relative error in the intensity is inversely proportional to the square root of that number. The third is that the finite resolving time of the counter gives rise to additional errors in the intensity measurement.

Random Counting Error. The standard deviation σ of the measured intensity is $\sqrt{N}$ if the pulses are uniformly distributed, with $N = nT$, n being the count rate and T the counting time; the relative standard deviation η is $1/\sqrt{N}$. A background N_b causes the measured intensity to be the sum of the diffraction intensity and the background:

$$N = N_0 + N_b.$$

Then η for the diffraction intensity N_0 alone is

$$\eta = \frac{\sqrt{N + N_b}}{N - N_b} = \frac{\sqrt{K(K+1)}}{(K-1)\sqrt{nT}}, \qquad (3.1)$$

where $K = n/n_b$.

A line equal in intensity to the background ($K = 2$) requires three times the period needed to attain a given level of error in the absence of background (Fig. 3). The η applicable to a ratemeter employed for the same purpose with the counter at rest is [33]

$$\eta = \frac{1}{\sqrt{n \cdot 2RC}}, \qquad (3.2)$$

and so the effective counting time is double the time-constant of the RC circuit.

There are two cases to be considered in automatic recording:

A. $RC \gg \tau$, in which case the loss of charge during the time spent measuring the line is negligible, so the relative error in the measurement of the peak intensity is

$$\eta = \frac{1}{\sqrt{nRC}}. \qquad (3.3)$$

B. $\tau > RC$, which is intermediate between the first case and the fixed counter case. Here,

$$\eta = \frac{\sqrt{1 + \frac{RC}{4\tau\left(1 - \frac{RC}{\tau}\ln 2\right)}}}{\sqrt{2nRC}}. \qquad (3.4)$$

The error differs very little from that for a fixed counter under ordinary conditions: by 9% for $RC = 0.5\tau$, and by 4% for $RC = 0.25\tau$. The probability of a positive deviation of $4\sigma_B$ (in which σ_B is the probable deviation) is 0.0035, so it is best to check deviations from the mean background intensity in excess of $4\sigma_B$. Only deviations of width equal to that of the line, namely, $0.67\sqrt{n}/\sqrt{\tau + 2RC}$, should be checked, so the deviations to be checked are those equal to the line width and of height $4 \cdot 0.67\sqrt{n}/\sqrt{\tau + 2RC}$ [34]. High accuracy and sensitivity may be attained by increasing the counting time and taking readings on the pattern point by

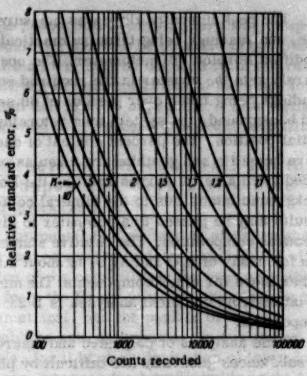

Fig. 3. Relation of random counting error to background rate; K is the ratio of total rate to background rate.

point [31], which can be done automatically [35, 36]. Another way of reducing the error is to minimize the background.

The background has the following components: (1) inherent counter background, (2) white radiation scattered by the specimen, (3) Compton scattering in specimen and air, (4) fluorescence in the specimen, (5) coherent scattering in the air, and (6) coherent scattering in the amorphous component of the specimen.

The first arises from cosmic rays and radioactive materials in the counter; it is minimized by shielding and by reducing the working or sensitive volume (all types of counter). The second is minimized by the use of a smoothed high-voltage supply to the x-ray tube and can be eliminated completely if a monochromator is used [37]. Fluorescence may be minimized by proper choice of working wavelength; in addition, the Compton, fluorescent, and white components may all be eliminated by placing a monochromator between specimen and counter [38].

The first four components lie at wavelengths other than the working wavelength, so they can be suppressed completely with discriminators. Coherent scattering in the air or amorphous binder cannot be eliminated by any energy-discrimination method, so particular attention has to be given to other techniques. Photographic methods employ a long collimator (which comes close to the specimen) and a trap for the beam, as well as evacuated cameras; a collimator may also be placed in front of the counter, and the volume traversed by the primary and diffracted rays may be evacuated [31].

The specimen should not contain a large amount of amorphous binder. The best materials are xylene, 5% Canada balsam in xylene, glycerol, or (best of all) no binder at all [39–41].

Most diffractometers employ a system that allows the use of a bent-crystal monochromator of symmetrical [31, 32, 41] or unsymmetrical [43] type. The discriminator and crystal monochromator may be further assisted by the use of fluorescence to produce monochromatic radiation [44]. Differential filters have been used to isolate the monochromatic part of the diffracted beam [9, 45].

Intensity Fluctuations from Variation in Number of Reflecting Particles. The crystals in a polycrystalline specimen may be randomly oriented (no preferred orientation), whereupon the relative standard deviation of the number in the reflecting position (and, hence, of the intensity) is given [46] by

$$\eta_l = \sqrt{\frac{8\pi\mu v_e R_g^2 \sin\theta}{Am\,(W_f + R_g\delta\theta)(H_f + H_z)}}, \qquad (3.5)$$

where μ is the absorption coefficient and v_e is the effective volume of a crystallite:

$$v_e = \sum v_i f_i,$$

f_i is the proportion of particles having volume v_i, R_g is the radius of the goniometer (distance from the principal axis to the counter slit), A is the cross section of the primary beam in a plane through the principal axis, m is the repeat of the plane, W_f is the transverse dimension of the projection of the focal spot, H_f is the lengthwise dimension of that projection, $\delta\theta$ is the half-width of the diffraction line, and H_z is the height of the counter slit.

Figure 4 gives the relative standard error as a function of the effective crystallite size and absorption coefficient.

Errors of the order of one percent require specimens crushed to a grain size of less than 5 μ [47]. Another method of reducing the error by a factor of 2–3 is to rotate the specimen in its own plane [48, 49].

Lost Counts. These are caused by the finite resolving time and represent one of the major obstacles to obtaining accurate intensities.

Two pulses separated by less than the resolving time will be counted as one. The pulses have a

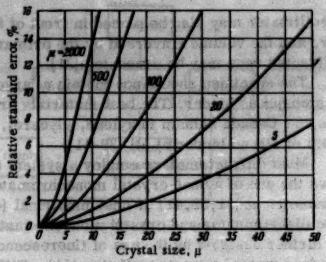

Fig. 4. Relative standard error in the intensity as affected by crystallite size and absorption coefficient μ.

uniform time distribution, so

$$N' = \frac{N_0'}{1 - N_0' \frac{\tau_r}{T}}. \qquad (3.6)$$

Here N' is the true number of counts, N_0' is the number observed, and τ_r is the resolving time (closely equal to the dead time).

There are several methods of measuring resolving times: the foils method [50-52], multiple-source methods [53], with an oscilloscope [54, 55], and by adjusting the circuit resolving time [9]. The oscilloscope method is the most accurate and reliable. Additional difficulties arise if the strength of the x-ray source varies; here, the loss is dependent on the exact time course of the intensity [4, 6, 9].

Major difficulties arise in quantitative phase analysis if the material has particles that readily take up a preferred orientation; great care must then be taken in specimen preparation, which must have no tendency to give rise to a preferred orientation [41]. It is also possible in this case to employ dilution with an amorphous phase, the relative intensity being extrapolated to zero content of that phase [56].

Use of an internal standard in phase analysis has reduced the relative error in the assay of α-quartz in industrial dust to about 2% when the quartz content is about 50% [57]. Residual austenite in steels has been determined in much the same way [4].

Black's work [58] on bauxites (evaluation of new deposits) gives a good illustration of the use of quantitative phase analysis. Here, use was made of one principal line from each of the minerals usually present in specimens: gibbsite, bohmite, kaolinite, hematite, goethite, and quartz.

The peak intensity alone was measured for each line, the readings being taken automatically with a modified Norelco diffractometer. The operator merely sets the counter in the required position, readings being taken over periods of 30 sec on line and background, the system then returning to the initial position. The percent content of each mineral (here hematite and goethite are taken as one) is deduced from a set of curves relating the line and background intensities to the mineral content. The results may be passed to a computer to give the chemical composition. The relative standard deviation for assay of H_2O and Al_2O_3 is about 1.5%, but rather more for other components. The mean-square deviation from chemical analyses is 1-2% for all components.

Phase analyses of polymers and macromolecular substances generally are difficult by photographic methods, so the diffractometer has become widely used here [59-62]. The holder for the polymer must allow recording of the radial and azimuthal distributions of the scattered radiation as well as deformation of the specimen. A thermostat is used to cover a range of temperatures [59]. The primary beam is rendered monochromatic by reflection from a flat crystal of pentaerythritol. A Soller collimator produces a wide parallel beam. The stability is provided by a ratio system based on a second counter. This apparatus has been used to measure the proportions of crystalline and amorphous phases at various temperatures in polyisobutene, natural rubber, polystyrene, polyethylene, and other such substances [60, 61]. The proportion of amorphous phase is indicated by the general scattering at θ between 0 and 60° relative to the integral scattering for an entirely amorphous specimen (one at a high temperature). However, it has been shown [62] that the proportion of amorphous phase during the crystallization of elastomers can be deduced quite accurately from the main amorphous ring.

Focused reflections have some disadvantages for organic materials. The irradiated area increases very greatly at small θ, which causes a marked shift in the peak intensity and unsymmetrical line broadening.

Transmission methods are free from these disadvantages; adequate intensity and resolution are obtained from broad divergent beams and a composite divergent slit in front of the counter [63]. This method has been used in research on the α-keratins [64].

Good resolution with broad beams in transmission may also be obtained with a focusing monochromator that collects the scattered rays [42].

The proportion of crystalline phase in an organic material that can be obtained in completely crystalline form may be deduced from the ratio of some strong crystal reflection to the same for a specimen that is 100% crystalline. This method has been applied to specimens of sodium penicillin [65].

4. Effects of Instrumental Factors on Line Shapes and Crystallite-Size Determination

Instrumental factors tend to alter the shape of a peak that otherwise is determined by the size distribution of the crystallites: the peak as a whole shifts from the Bragg position, the shape becomes unsymmetrical, and the peak is broadened.

Only the shift is important in qualitative phase analysis, for it hinders derivation of interplanar distances, whereas the broadening is basic to derivation of the size distribution; but all three effects are important in accurate measurements of cell parameters, especially the displacement from the Bragg position, which impairs identification of the center.

The final line shape is obtained by superimposing the following functions [66, 67].

1. The diffraction function $f(\Delta\theta)$, which is dependent on the size distribution of the crystals; $\Delta\theta$ is the deviation from the Bragg angle.
2. A function g_1 dependent on the spectrum of the source.
3. A function g_2 dependent on the source shape.
4. A function g_3 representing defocusing resulting from displacement of the plane of the specimen from the focal circle.
5. A function g_4 governed by the vertical divergence of the primary and scattered beams.
6. A function g_5 dependent on the penetration of the primary beam into the specimen.
7. A function g_6 dependent on the counter slit width.

Figure 5 shows the instrumental functions and the final shape.

The calculated shape agrees well with the observed one. The diffraction and instrumental widths are additive only for large θ; a correction curve has normally to be used. The high resolving power of the diffractometer extends the limit of crystallite size determination to 3000 Å. The following are the factors that broaden and displace the diffraction line.

Source Spectrum [68]. The form of g_1 is dependent on the line shape of the characteristic radiation and is given by

$$g_1 = K_1 \frac{1}{(\Delta\theta)^2 + \alpha_1^2}, \tag{4.1}$$

in which K_1 and α_1 are coefficients dependent on θ as well as on the half-width and wavelength. Any continuous component is symmetrical with respect to the Bragg position and is appreciable only at large θ.

Source Shape [2]. A Gauss function gives a good approximation to the actual distribution along the short axis of the projection of the focal spot, and so g_2 is given by

$$g_2 = e^{-K_2^2(\Delta\theta)^2}, \tag{4.2}$$

in which K_2 is a constant related to the half-width of the projection.

This half-width is about 0.02° in some diffractometers employing projection of the focal spot at an angle of 3°.

Defocusing [33]. The deviation from the Bragg position arising from deviation of the surface from the focal plane is

$$\Delta\theta = -\frac{x_3^2 \sin 2\theta}{2R_g^2}. \tag{4.3}$$

Here, x_3 is the distance from the center of the specimen and $x_3 \max = b_p/2$ is the half-width of the specimen.

The maximal deviation is given by

$$\Delta\theta_3' \max = -\frac{b_p^2 \sin 2\theta}{8R_g^2}. \tag{4.4}$$

The beam may not cover the specimen, in which case

$$\Delta\theta_3' \max = -\frac{b_g^2 \operatorname{ctg}\theta}{4R_g^2}, \tag{4.5}$$

in which b_g is the width of the section of the primary beam by a plane through the principal axis of the goniometer. The shape of the δ function broadened by defocusing is given by

$$g_3(\Delta\theta) \sim \frac{dx_3}{d\Delta\theta} \sim \frac{1}{\sqrt{\Delta\theta}}. \tag{4.6}$$

Vertical Divergence of Beams [69, 70]. Here, $\Delta\theta$ is governed by the height x_f of the focal point, the height x_p of the specimen, and the height x_z of the counter slit, all above the principal plane of the goniometer:

$$\Delta\theta = -\frac{\alpha^2 + \beta^2 - 2\frac{\alpha\beta}{\cos 2\theta}}{4} \operatorname{ctg} 2\theta, \tag{4.7}$$

$$(x_p - x_f)/R_g = \alpha, \tag{4.8}$$

$$(x_z - x_p)/R_g = \beta. \tag{4.9}$$

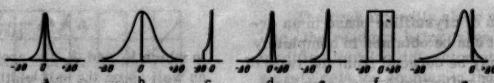

Fig. 5. Functions governing diffraction peak shape. a) Spectrum of source; b) source shape; c) defocusing; d) vertical divergence; e) absorption; f) counter slit width; g) final shape.

$$-\frac{H_f}{2} \leqslant x_f \leqslant \frac{H_f}{2}, \quad -\frac{H_P}{2} \leqslant x_P \leqslant \frac{H_P}{2},$$

$$-\frac{H_Z}{2} \leqslant x_Z < \frac{H_Z}{2}. \tag{4.10}$$

If the first and last heights are small relative to the second ($x_f \ll x_p$, $x_z \ll x_p$),

$$\alpha = -\beta = x_P / R_g,$$

$$\Delta\theta = -\frac{x_P^2 \operatorname{ctg}\theta}{2R_g^2}, \tag{4.11}$$

$$\Delta\theta_i^P \max = -\frac{H_P^2 \operatorname{ctg}\theta}{8R_g^2}. \tag{4.12}$$

If the first two are small relative to the third ($x_f \ll x_z$, $x_p \ll x_z$),

$$\alpha = 0, \quad \beta = x_Z / R_g.$$

$$\Delta\theta = -\frac{x_Z^2 \operatorname{ctg} 2\theta}{4R_g^2}. \tag{4.13}$$

$$\Delta\theta_i^Z \max = -\frac{H_Z^2 \operatorname{ctg} 2\theta}{16 R_g^2}. \tag{4.14}$$

Thus, in the particular cases we have

$$g_i(\Delta\theta) \sim \frac{1}{\sqrt{\Delta\theta}}. \tag{4.15}$$

$\Delta\theta$ may be positive or negative in the general case; the maximal negative values are given by (4.7)–(4.9) with

$$x_f = \frac{H_f}{2}, \quad x_P = -\frac{H_P}{2}, \quad x_Z = \frac{H_Z}{2},$$

and are put as

$$\Delta\theta_i^- \max = \frac{(H_P + H_f)^2 + (H_Z + H_P)^2 + \dfrac{2(H_P + H_f)(H_Z + H_P)}{\cos 2\theta}}{16 R_g^2} \operatorname{ctg} 2\theta. \tag{4.16}$$

The maximum positive values are given by

$$\frac{\partial(\Delta\theta_i \max)}{\partial x_P} = 0,$$

and are

$$\Delta\theta_i^+ \max = \frac{(h_f + h_Z)^2 \left(\dfrac{1}{\cos 2\theta} - 1\right)}{32 R_g^2} \operatorname{ctg} 2\theta. \tag{4.17}$$

Calculations agree closely with experiment [33].

Penetration of Beam [71]. Here, $\Delta\theta$ is related to the depth of the reflecting layer x_5 by

$$\Delta\theta = -\frac{x_5 \cos\theta}{R_g}. \tag{4.18}$$

The maximal deviation is

$$\Delta\theta_5 \max = \frac{d_0 \cos\theta}{R_g}, \tag{4.19}$$

in which $d_0 = x_5 \max$ is the specimen thickness. This penetration broadens the δ function in accordance with

$$g_5(\Delta\theta) \sim \frac{dx_5}{d\Delta\theta}\left(e^{-2\mu x_5 \operatorname{cosec}\theta}\right) \sim e^{-4\Delta\theta}. \tag{4.20}$$

Finite Counter Slit Width. This transforms a δ function to a rectangular function.

5. Precision Measurement of Cell Parameters

It will be clear from the above that the following factors that cause asymmetric broadening will displace the peak: (1) defocusing (from flat form of specimen), (2) vertical divergence, (3) penetration.

In addition, the goniometer must be correctly adjusted and must be properly set relative to the focus of the x-ray tube.

Defocusing shifts the center of a δ function by

$$\Delta\theta_0 = \frac{\int_0^{\Delta\theta\max} g\,\Delta\theta d(\Delta\theta)}{\int_0^{\Delta\theta\max} g d(\Delta\theta)} = \frac{\Delta\theta_3 \max}{3}. \tag{5.1}$$

Figure 6 shows the two cases arising for a triangular line.

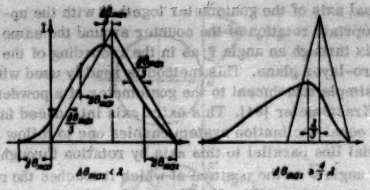

Fig. 6. Displacement of the peak of a triangular line of half-width λ due to unsymmetrical broadening.

The peak is shifted by $\Delta\theta_3 \max/4$ in the first case and by $\lambda/3$ in the second. Alternatively, the shift might be deduced by reference to the line joining the middle of the horizontal intercepts, in which case it is $\Delta\theta_3 \max/3$, and so coincides with the shift in the center of gravity.

It is difficult to deduce the shift due to vertical divergence for the general case; but for the cases of spot and slit heights small relative to specimen height, or spot and specimen heights small relative to slit height, we have, respectively,

$$\Delta\theta_1^p \max = -\frac{H_p^2 \operatorname{ctg}\theta}{8R_g^2}$$

and

$$\Delta\theta_1^z \max = -\frac{H_z^2 \operatorname{ctg} 2\theta}{4R_g^2},$$

which are analogous to (4.4) and imply a shift in the peak of

$$\frac{\Delta\theta_1 \max}{3}.$$

A Soller collimator gives a shift of

$$\frac{\sigma^2 \operatorname{ctg} 2\theta}{12},$$

in which σ is the distance between adjacent plates divided by the length of these. The shift due to penetration into a specimen of thickness t is given by (4.20) and (5.1) as

$$\Delta\theta_0 = \frac{\sin 2\theta}{4\mu R_g} - \frac{d_0 \cos\theta}{R_g(e^{2\mu d_0 \operatorname{cosec}\theta} - 1)}. \qquad (5.2)$$

Displacement of the surface from the axis by a distance s causes the peak to move through an angle

$$\frac{s\cos\theta}{R_g}.$$

The over-all shift is then

$$\Delta\theta_0^z = -\frac{3H_p^2 \sin 2\theta}{24R_g^2} - \frac{H^2 \operatorname{ctg} 2\theta}{12} - \left(\frac{\sin 2\theta}{4\mu R_g} - \frac{d_0 \cos\theta}{R_g(\exp(2\mu d_0 \operatorname{cosec}\theta) - 1)}\right) - \frac{s\cos\theta}{R_g}. \qquad (5.3)$$

The errors arising in the interplanar distances from these factors may [4, 71, 72] be eliminated[2] in a $\cos^2\theta$ extrapolation (Fig. 7). The counter zero may be determined precisely in several ways, the screen method [73] being the most accurate, as this gives the setting to 0.001°.

The parameters of cubic lattices have been determined for polycrystalline specimens in absolute terms to within the error (±0.004%) with which the wavelength of CuKα is known by applying these methods of extrapolation and zero setting; the relative accuracy was substantially higher, especially when thermostatic control and point-by-point readings were used, 2θ being found to 0.001° [72].

Also, θ in the range 78-88° may be measured [74] by using a counter with a ring slit.

A Laue goniometer may also be used to examine lattice symmetry and distortion.

A proportional counter working into a multichannel analyzer can overcome any uncertainty in wavelength measurement and so can give exact lattice parameters [75].

6. Intensity Measurement on Single Crystals

Ionization methods for integral intensity here are of high accuracy and sensitivity; the time required is also reduced. The last feature is very important, on account of advances in direct sign determination and electron-density calculation by computer. For instance, the intensities of 2485 reflections were measured in 55 h with a diffractometer, of which 24 h were accounted for by accessory operations [76].

Fig. 7. Relation of line shift to θ.

[2] This is not so for the shift due to vertical divergence, though it may be that more exact correction for this divergence is responsible for the higher accuracy of lattice parameters obtained by extrapolation.

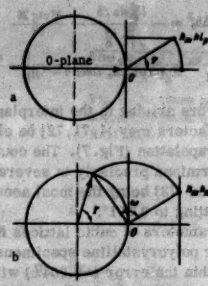

Fig. 8. The equatorial method of measuring single-crystal intensities. a) Plane of primary beam and principal axis; b) equatorial plane.

Photographic methods for integral intensity record for reciprocal-lattice planes separately: one coordinate must thus be known, the other two coordinates being deduced from the position of the spot on the pattern. Beams reflected at different angles meet on their way to the film in layer photography, whereas the crystal must be coupled to the counter in ionization methods, for which purpose all three coordinates must be known in the general case. The reflections may be recorded in sequence with a counter, instead of layer by layer.

Types of layer recording have been described with the counter set up on a Weisenberg instrument to employ the plane angle method [77] or any type of layer recording [78]: equal-inclination, perpendicular beam, plane angle, and constant cone.

A goniometer head rotating around the counter axis enables one to record only one reciprocal-lattice plane without remounting the crystal, this passing through the origin node and being perpendicular to that axis [79, 80]. Simultaneous motion of the counter around an axis in the equatorial plane enables one to use the perpendicular-beam method [81]. A special goniometer for use with the equal-inclination method provides variation of the angle between the primary beam and the common axis of crystal and counter [82]. Polar recording requires an additional axis of rotation for the crystal in the equatorial plane and parallel to the closest-packed rows in the reciprocal lattice [71, 83, 84].

This axis in the equatorial method enables one to displace the line $h_m k l_p$ (Fig. 8) through an angle φ in the equatorial plane. The nodes in this series are then brought to the reflecting position by rotating the crystal through an angle ω around the principal axis of the goniometer together with the appropriate rotation of the counter around the same axis through an angle Υ, as in the recording of the zero-layer plane. This method is readily used with a simple attachment to the goniometer of a powder diffractometer [84]. This extra axis introduced into an equal-inclination system enables one to follow a nodal line parallel to this axis by rotation through an angle $\bar{\varphi}$ to the position at which it touches the reflection sphere (Fig. 9). The equal-inclination method ($\mu = -\nu$) applied to nodal series so placed merely requires ω (counter angle) and Υ related by $\Upsilon = 2\omega$, which implies a simple kinematic coupling. The latter feature greatly reduces the number of special setting operations in this method (called tangential). Other possibilities appear if the attachment to the powder goniometer contains a further axis Φ (Fig. 10) that itself may rotate around another axis X of the attachment, this axis being perpendicular to Φ and lying in the equatorial plane (these two additional axes form an Euler system in conjunction with the principal axis Ω of the goniometer). This attachment allows one to record reciprocal-lattice nodes by the cone method [76], in which the crystal is set with one axis (e.g., b^*) along the Φ axis; the X axis is set perpendicular to the plane that bisects 2θ, and the Φ axis is inclined by an angle x by rotation around the X axis. Then the crystal is turned through φ around the Φ axis to bring into the reflecting position in the equatorial plane all nodes lying on a cone with the b^* axis as its axis and a vertex angle of x, the radius vector corresponding to θ.

It is usual to measure the integral intensity in one of two ways: with a wide slit or with a convergent beam. The counter is kept fixed in the first method, the slit being opened to accept the entire reflected beam and the crystal being oscillated over a narrow range around the reflecting position. Crystal and counter are stationary in the second method, which takes less time; but it requires a uniformly emitting spot of appropriate size [9, 85].

A recent description [82] concerns a diffractometer that records the intensity, crystal angle, and counter angle for a single crystal, this information being sufficient to give the F^2 solid.

This instrument employs equal inclination, the counter moving through half a slit width during a complete rotation of the crystal, which provides all combinations of the two angles and so brings all nodes of the layer plane into the reflecting position.

A system of relays is used to slow the motion of crystal and counter on reflections and to give high speeds on background measurements. This

Fig. 9. The tangential method of measuring the integral intensity from a single crystal. a) Plane of primary beam and principal axis; b) plane P.

saves much time, and the device thus provides rapid construction of reciprocal-lattice planes.

Another automatic system employs a computer to derive the setting angles of counter and crystal from the known cell parameters.

A servo system employing selsyns would appear best for setting these angles, as in a neutron-diffraction goniometer [86].

7. Textures

The accuracy and rapidity of counter methods as applied to pole figures makes these essentially better than photographic ones here; such a figure can be recorded in about an hour for a given plane with a powder diffractometer. Texture studies merely require some minor modifications to allow rotation of the specimen around two mutually perpendicular axes. The intensities provided by the required plane are measured with the counter fixed at the appropriate θ, which makes the absorption and scattering volume corrections much simpler than those for the photographic method. There are two mutually complementary methods in the construction of pole figures: transmission and reflection. The first gives the outer part of the figure, while the second gives the central part.

The principles of the transmission method are detailed in [87]. A thin specimen is mounted in a holder providing rotation around an axis perpendicular to its surface and around an axis coincident with the goniometer axis. The counter is fixed at the Bragg angle for the appropriate plane (Fig. 11), while the specimen rotates around the goniometer axis. The intensity corresponding to a diameter of the pole figure is recorded. The process is then repeated with the specimen turned through an angle around the D axis, which gives the intensity distribution along a diameter at an angle β to the previous one, etc.

This method avoids the construction of Wulff nets; it needs only polar nets. The change in the position of the specimen relative to the beam requires correction for the geometrical path of the beam in the specimen [88]. The formula given in the original paper is correct for rotation angles α up to 40-50°. This method does not give the central part of the figure, because the beam is cut off by the holder in this range.

The above scheme has been used with slight changes in the slit system to give a marked simplification in the calculations [89]. Broad divergent beams and a narrow counter slit are used, so only the central part of the diffraction peak is recorded. The diffracted intensity is then independent of the angle of rotation over a fairly wide range (deviation from the Bragg angle by up to 40°) for specimens of a certain thickness; the absorption and scattering-volume corrections are then eliminated.

The complete pole figure may be recorded, and absorption corrections eliminated, by replacing the rotation around an axis perpendicular to the plane

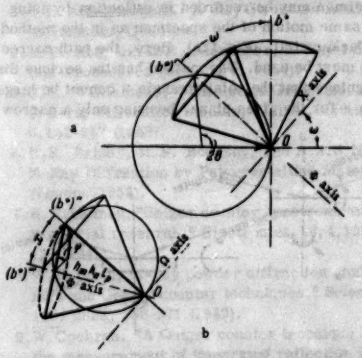

Fig. 10. The cone method for single crystals. a) Equatorial plane; b) O(b*)' section.

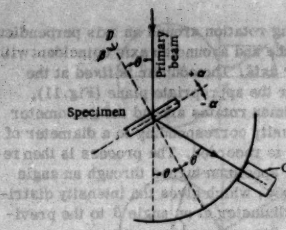

Fig. 11. Method of turning specimen in texture examination by transmission.

by examination of a series of cylindrical specimens [90], the axis of each lying in the rolling plane, each having a different angle to the rolling direction. The scattered intensity is measured in a plane perpendicular to the axis of the specimen. The rotation of the specimen is coupled to that of the recorder chart.

An automatic device [91] has been described for use with thin specimens in transmission. The specimen is rotated continuously around axis D (Fig. 11), which is synchronously coupled to the rotation of the polar net in the recorder. The specimen is rotated in steps of 5° around the axis of the goniometer, this being coupled to the radial position of the pen in the recorder. The correction for the geometrical path of the rays is performed automatically. The intensity scale has seven steps, the pen having accordingly seven colors. Contours can then be drawn in directly via lines of the same color.

The central part of the figure for a massive specimen may be recorded in reflection by using the same motion of the specimen as in the method of Decker et al. (Fig. 12a). Here, the path correction must be used. The method has the serious disadvantage that the rotation angle α cannot be larger than θ for the given plane, because only a narrow

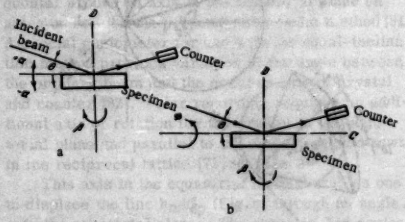

Fig. 12. Methods of rotating the specimen in texture studies in reflection.

central part of the pole figure is recorded [92]. A more generally applicable method was described by Schulz [93]. The vertical slit system in the spectrometer is replaced by a set of horizontal slits that produce a beam parallel in the vertical plane but divergent in the horizontal plane. The specimen rotates around axis D and also around the line of intersection of its plane with the principal plane of the goniometer (C in Fig. 12b).

The specimen and counter are set to the position corresponding to the interplanar distance. Rotation on the C axis corresponds to recording along a diameter of the figure. The absorption is such that the intensity should not be dependent on Φ, but the intensity is actually found to fall at large Φ, on account of inevitable defocusing during rotation on C, which causes broadening of the peak [94]. This effect may be reduced by widening the counter slit, at the expense of loss of resolution. Satisfactory results are obtained up to $\Phi = 40°$ under these conditions.

An automatic specimen holder has been made for use in Schulz's method, which overcomes the following problems: exact and rapid setting of the specimen, increasing the surface area involved in the reflection for specimens with rather large crystals, and automatic intensity recording for specified positions of the specimen [95, 96].

Schulz's method forms the basis of a goniometer for examining preferred orientation [97]. The drive rotates the specimen continuously around the D axis (Fig. 12b), one turn around this corresponding to 10° around the C axis. The normals to the chosen plane then describe spiral paths on the stereographic projection. The intensity is recorded on a synchronized chart, from which it is transferred to the pole figure.

The accuracy may be improved by placing one spiral in another to give the turns separations of 5°, 2.5°, etc.

Schulz's method in reflection gives good results for the central part (up to 40°), while the method of Decker et al. [98] gives good results for the outer region.

The complete pole figure may also be constructed by the method of Decker et al. with only one holder, which is used in transmission and in reflection. Good overlap between the two regions is provided by recording a higher-order reflection from the same plane [99].

Precision intensity recording has allowed the diffractometer to be applied to orientation studies of crystallites in cellulose, textile fibers, etc. [100]. The holder for use with these [101] enables one to

record the azimuthal and radial intensity distributions for specimens varying in degree of elongation.

8. Other Applications

Quenching (the usual method for examining the kinetics of high-temperature phase transitions) is not suitable for many materials. The diffractometer does not need long exposures and so allows one to follow phase transformations at the transition temperature [102-104]. The main difficulty with high-temperature x-ray cameras (protection of the film) is absent here, and diffractometers can be used with furnaces going up to 1600°C or more [105]. The heater may be tungsten wire (1200°C) [91], platinum wire (1500°C) [106], or tantalum foil (1600°C) [105]. The furnace must be evacuated or filled with inert gas, to avoid oxidation or decarburization of the specimen. A stream of hot inert gas [107] may be used at 600-900°C, the outer jacket of the furnace, together with any external heaters and screens, having slots to pass the beams. The top and bottom plates are water-cooled, to protect the goniometer mechanisms. Specimen temperatures around 600°C may be produced simply by heating the holder [110]. Examples of this type of use are the isothermal decomposition of austenite in steel containing 2.5% Ni [103], structure determination for α-$CaO \cdot 2SiO_2$ [106], and ordering in CuZn and Cu_3Au crystals at high temperatures [108].

The holder may be of insulating plastic for work at low temperatures [109,111]; the metal parts leading to the goniometer are fitted with heater spirals. The low temperature is produced by direct contact with liquid nitrogen [111,112] or by a jet of cold gas [109].

Single crystals may be oriented rapidly [113], the counter being set at 2θ and the crystal being turned about two mutually perpendicular axes to locate the appropriate plane. Two such planes are used with a stereographic projection to find the coordinates of a third plane, which is set up in order to check the diffractometer settings.

Highly radioactive specimens represent a special problem; the detector should respond only to the characteristic x rays used. There are two lines of attack here: use of a double-crystal system [114, 115] and differential discrimination with scintillation or proportional counters [15,21]. The second crystal acts as a focusing monochromator (the first crystal is the specimen); it is set up between specimen and counter to direct only the characteristic radiation to the latter. A piece of lead is placed between specimen and counter. A modification that avoids moving the counter with its heavy shield is to rotate the x-ray tube and specimen around the goniometer axis, but this method generally has the disadvantages of great loss of intensity at the second crystal and complexity in the goniometer. The discriminator methods are free from these; standard goniometers may be used. Scintillation counters are of lower energy resolution than gas counters, but they both provide recording free from background caused by the specimen, with loss of only 15-20% of the characteristic radiation.

* * *

It will be clear from this survey that the diffractometer should find steadily increasing use in many forms of structure analysis, as in quantitative phase analysis, line profile examination, cell parameter determination, texture studies, intensity measurement for single crystals at high and low temperatures, and with radioactive specimens.

These applications will be facilitated by:

1. Provision of attachments to the URS-50I to adapt it for these applications;
2. Design of specialized diffractometers, especially for use with single crystals and textures.

LITERATURE CITED

1. Yu. K. Ioffe, "The URS-50I and URS-25I x-ray equipments for structure analysis with ionization recording," Kristallografiya, 1, 4, 460-467 (1956).
2. The URS-50I X-ray Equipment for Structure Analysis with Ionization Recording (Description and Instructions for Use) [in Russian] (1955).
3. A.I. Kitaigorodskii, X-Ray Structure Analysis [in Russian] (1950).
4. H.P. Klug and L.A. Alexander, X-Ray Diffraction Procedures (New York, 1954).
5. G.K. Williamson, "The use of Geiger counters in x-ray diffraction studies," J. Inst. Metals, 81, 6, 152-157 (1953).
6. H.S. Peiser, H.P. Rooksby, and A.J.S. Nilson, X-Ray Diffraction by Polycrystalline Materials (London, 1955).
7. H. Friedman, "Geiger counter spectrometer for industrial research," Electronics, 18, 4, 132-137 (1945).
8. W. Parrish, "X-ray powder diffraction analysis film and Geiger counter techniques," Science, 110, 2858, 368-371 (1949).
9. W. Cochran, "A Geiger counter technique for the measurement of integrated reflection intensity," Acta Crystallogr., 3, 4, 268-278 (1950).

10. M.A. Blockhin, "Chemical analysis by x-ray fluorescence," Zav. Lab., 16, 8, 941-948 (1950).
11. M.A. Blockhin, "X-ray analysis by fluorescence," Zav. Lab., 16, 6, 681-687 (1950).
12. U.W. Arndt, "The use of Geiger and proportional counters in x-ray diffraction studies," Atomics, 4, 9, 217-225 (1953).
13. U.W. Arndt, W.A. Coates, and D.P. Riley, "A proportional-counter technique for measuring x-ray scattering from powders, fibers, and liquids," Proc. Phys. Soc., B, 66, 12, 1009-1016 (1953).
14. A.R.B. Skertchly, "Proportional counter tube for x-ray diffraction analysis," Rev. Sci. Instr., 27, 5, 324-326 (1956).
15. T.R. Kohler and W. Parrish, "X-ray diffractometry of radioactive samples," Rev. Sci. Instr., 26, 4, 374-379 (1955).
16. I.C.M. Brentano and I. Ladany, "Scintillation counting of low-energy photons and its use in x-ray diffraction," Rev. Sci. Instr., 25, 10, 1028-1029 (1954).
17. H.I. West, W.E. Meyerhof, and Hofstadter, "Detection of x rays by means of NaI(Tl) scintillation counters," Phys. Rev., 81, 1, 141-142 (1951).
18. I.C.M. Brentano and I. Ladany, "The recording of x-ray diffraction patterns by a scintillation counter," Phys. Rev., 92, 3, 850 (1953).
19. L.M. Belyaev, K.I. Narbut, E.L. Stolyarova, I.E. Konstantinov, V.A. Alekseev, and A.B. Gil'varg, "Use of a scintillation counter in recording x-ray spectra," Fifth All-Union Conference on X-Ray Applications [in Russian] (Leningrad, 1955).
20. I.T. Nelson and R.T. Ellickson, "Scintillation counter for detection of x rays," J. Opt. Soc., 45, 11, 984-986 (1955).
21. M.A. Bredig, G.E. Klein, and B.S. Borie, "X-ray diffractometer for highly radioactive materials," Rev. Sci. Instr., 26, 6, 610 (1955).
22. J. Taylor and W. Parrish, "Absorption and counting efficiency data for x-ray detectors," Rev. Sci. Instr., 26, 4, 367-373 (1955).
23. N.O. Chechik, S.M. Fainshtein, and T.M. Lifshits, Electron Multipliers [in Russian] (Moscow, 1954).
24. T.M. Lifshits, "Use of electron multipliers in counting elementary particles and quanta," UFN, 50, 3, 365-432 (1953).
25. B. Astrom, "A scintillation spectrometer," Arkiv. Fys., 7, 3, 241-245 (1954).
26. A.R. Lang, "A versatile x-ray diffractometer for single-crystal and powder studies," J. Sci. Instr., 33, 4, 138-141 (1956).
27. G. Wassermann and J. Wiewiorowsky, "Über ein Geiger–Zählrohr Goniometer nach dem Seemann–Bohlin–Prinzip," Z. Metall., 44, 12, 567-570 (1953).
28. A.I. Froiman, "Some aspects of x-ray methods based on counters," Izv. Akad. Nauk SSSR, Ser. Fiz., 17, 2, 237-241 (1953).
29. D.G. Cole and E. Gillam, "On monitoring a Geiger-counter spectrometer beam," J. Sci. Instr., 30, 11, 429-430 (1953).
30. R. Rabilion, "Montage Goniometrique a rayonnement mono ou polychromatique auto-stabilisé," Acta Crystallogr., 7, 10, 618 (1954).
31. W.H. Hall, U.W. Arndt, and R.A. Smith, "A Geiger counter spectrometer for the measurement of Debye and Scherrer line shapes," Proc. Phys. Soc., A62, 10, 631-638 (1949).
32. R.A. Coyle, K.F. Hale, and C. Wainwright, "The design and operation of a precision Geiger–Müller counter x-ray diffraction spectrometer," J. Sci. Instr., 30, 5, 151-155 (1953).
33. A. Trost, "Einfluß der geometrischen Größen und der Zeitkonstantan auf die Genauigkeit von Röntgeninterferenzmessungen mit einem Zählrohr Goniometer," Z. Angew. Phys., 7, 10, 469-478 (1955).
34. C. Wainwright, "The use of the Geiger–Müller counter x-ray spectrometer in an x-ray laboratory with special reference to automatic recording," Brit. J. Appl. Phys., 2, 6, 157-163 (1951).
35. A.R. Land, "A printing recorder for use in conjunction with scaling units," J. Sci. Instr., 29, 6, 176-178 (1952).
36. J.W. Hughes and E.K. Pike, "A monitored Geiger counter x-ray powder diffractometer with automatic recording," J. Sci. Instr., 33, 5, 204 (1956).
37. Ya.I. Graevskaya, V.I. Iveronova, and V.P. Tarasova, "A specialized equipment for measuring x-ray reflection intensities with Geiger counters," Kristallografiya, 1, 4, 442-445 (1956).
38. B.R. Banerjee, "Reflected beam x-ray monochromator for Geiger counter diffractometry," Rev. Sci. Instr., 26, 6, 564-565 (1955).
39. W.H. Hall and G.K. Williamson, "The diffraction pattern of cold metals. II. Changes in integrated intensity," Proc. Phys. Soc., B64, 11, 946-953 (1951).
40. D. Schröder, "Die röntgenographische Untersuchung von Tonmineralen nach dem Zählrohrverfahren," Z. Pflanzenernähr. Düng Boden-

kunde, 62, 2, 148-158 (1953).
41. G. L. McCreery, "Improved mount for powdered specimens used on the Geiger counter x-ray spectrometer," J. Am. Ceram. Soc., 32, 4, 141-146 (1949).
42. A. R. Long, "Diffracted-beam monochromatization techniques in x-ray diffractometry," Rev. Sci. Instrum., 27, 1, 17-25 (1956).
43. G. Frohnmeyer and H. Richter, "Ein lichtstarkes Fokussierungverfahren für Strukturbestimmungen mit dem Zählrohrgoniometer," Naturwiss., 42, 9, 256-257 (1955).
44. R. J. Weiss, J. J. DeMarco, and G. Weremchuk, "Conversion of Norelco fluorescent spectrograph to an x-ray diffractometer," Acta Cryst. 7, 89, 599-600 (1954).
45. J. A. Soules, W. L. Gordon, and C. H. Shaw, "Design of differential x-ray filters for low-intensity scattering experiments," Rev. Sci. Instr., 27, 1, 12-14 (1956).
46. L. Alexander, H. P. Klug, and E. Kummer, "Statistical factors affecting the intensity of x rays diffracted by crystalline powders," J. Appl. Phys., 19, 8, 742-753 (1948).
47. H. P. Klug, L. Alexander, and E. Kummer, "Quantitative analysis with the x-ray spectrometer (Accuracy and reproducibility)," Analyt. Chem., 20, 7, 607-609 (1948).
48. E. F. Champaygne, "Rotating sample holder for x-ray diffraction studies," Rev. Sci. Instr., 17, 9, 345 (1946).
49. P. N. Bestelink, D. R. Holmes, and M. A. D. Phil, "A dual-purpose specimen spinner for transmission and reflection x-ray diffraction," J. Sci. Instr., 33, 7, 281-282 (1956).
50. K. Lonsdale, "Note on quantitative analysis by x-ray diffraction methods," Am. Mineral., 32, 90-92 (1948).
51. K. Lonsdale, "Geiger-counter measurements of Bragg and diffuse scattering of x rays by single crystals," Acta Crystall., 1, 1, 12-20 (1948).
52. L. Alexander, E. Kummer, and H. P. Klug, "Dead time and nonlinearity characteristics of the Geiger-counter x-ray spectrometer," J. Appl. Phys., 20, 8, 735-740 (1949).
53. Y. Beers, "A precision method for measuring Geiger counter resolving times," Rev. Sci. Instr., 73, 2, 72-76 (1942).
54. H. G. Stever, "Discharge mechanism of fast G-M counters from the dead time experiment," Phys. Rev., 61, 1-2, 38-52 (1942).
55. R. Pepinsky, P. Jarmotz, H. M. Long, and D. Sayre, "Recovery time of Geiger counters for x-ray intensity measurement," Rev. Sci. Instr., 19, 1, 51-52 (1948).
56. J. Manson, "Preferred orientation of platelets in x-ray diffractometer powder samples," J. Appl. Phys., 26, 10, 1254-1256 (1955).
57. H. P. Klug, "Quantitative analysis of powder mixtures with Geiger-counter spectrometer," Anal. Chem., 25, 5, 704-708 (1953).
58. R. H. Black, "Analysis of bauxite exploration samples (An x-ray diffraction method)," Anal. Chem., 25, 5, 743-748 (1953).
59. S. Krimm and R. S. Stein, "An x-ray spectrometer for polymer studies," Rev. Sci. Instr., 22, 12, 920-925 (1951).
60. S. Krimm and A. V. Tobolsky, "Quantitative x-ray studies of order in amorphous and crystalline polymers. Scattering from various polymers and a study of glass transition in polystyrene and polymethylmetacrylate," J. Textile Research, 21, 11, 805-822.
61. S. Krimm and A. V. Tobolsky, "Quantitative x-ray studies of order in amorphous and crystalline polymers. Quantitative x-ray determination of crystallinity in polyethylene," J. Polym. Science, 7, 1, 57-76 (1951).
62. L. Alexander, S. Ohlberg, and G. R. Taylor, "X-ray diffraction studies of crystallization in elastomers," J. Appl. Phys., 26, 9, 1068-1074 (1955).
63. A. R. Lang, "Focusing transmission specimen technique for the x-ray diffractometer," Rev. Sci. Instr., 26, 7, 680-689 (1955).
64. A. R. Lang, "An x-ray study of α-keratin. II. Diffraction measurements of the complete diffraction pattern of Canadian porcupine quill," Acta Cryst., 9, 5, 446-451 (1956).
65. C. L. Christ, R. B. Barnes, and E. F. Williams, "Organic quantitative analysis using the Geiger-counter x-ray spectrometer," Anal. Chem., 20, 9, 789-795 (1948).
66. L. Alexander, "Geometrical factors affecting the contours of x-ray spectrometer maxima. I. Factors causing asymmetry," J. Appl. Phys., 19, 11, 1068-1071 (1948).
67. L. Alexander, "The synthesis of x-ray spectrometer line profiles with application to crystallite size measurements," J. Appl. Phys., 25, 2, 155-161 (1954).
68. H. Ekstein and S. Liegel, "Limits of accuracy in the determination of lattice parameters and stresses by the Debye–Scherrer method," Acta Crys., 2, 99-104 (1949).
69. J. N. Eastabrook, "Effect of vertical divergence on the displacement and breadth of x-ray powder diffraction lines," Brit. J. Appl. Phys., 3,

11, 349-352 (1952).
70. L. Alexander, "The effect of vertical divergence on x-ray powder diffraction lines," Brit. J. Appl. Phys., 4, 3, 92-93 (1953).
71. A. J. C. Wilson, "Geiger-counter x-ray spectrometer. Influence of size and absorption coefficient of specimen on position and shape of powder diffraction maxima," J. Sci. Instr., 27, 12, 321-325 (1950).
72. A. Smakula and J. Kalnajs, "Precision determination of lattice constants with a Geiger-counter x-ray diffractometer," Phys. Rev., 99, 6, 1737-1743 (1955).
73. M. Tournarie, "Reglage absolu d'un goniometre a compteur de Geiger-Müller," J. Phys. et Rad., 15, 1, 11A-15A (1954).
74. R. Berthold and V. Gerold, "Ein neues Verfahren zum Ausmessen letzten Debye-Scherrer Linien mit dem Zählrohr," Z. Metall., 46, 9, 599-601 (1955).
75. A. R. B. Skertchly, "The Laue goniometer and its use as a proportional diffractometer," Acta Cryst., 9, 3, 320-321 (1956).
76. T. C. Furnas and D. Harker, "Apparatus for measuring complete single crystal x-ray diffraction data by means of a Geiger-counter diffractometer," Rev. Scient. Instrum., 26, 5, 449-453 (1955).
77. D. F. Clifton, A. Filler, and D. McLachlan, "Adaptation of a Geiger counter to the Weisenberg camera," Rev. Sci. Instrum., 22, 12, 1024-1025 (1951).
78. H. T. Evans, "Use of Geiger counter for the measurements of x-ray intensities from small single crystals," Rev. Sci. Instrum., 24, 2, 156-161 (1953).
79. G. S. Zhdanov and G. A. Gol'der, "Use of the Geiger-Müller counter in x-ray structure analysis," Collection: Application of X-rays in the Examination of Materials [in Russian] (1949), pp. 420-424.
80. S. C. Abrahams, and H. J. Grenville-Wells, "Single-crystal adaptor for the Norelco high-angle diffractometer," Rev. Sci. Instrum., 25, 5, 519-520 (1954).
81. R. Pepinsky and B. C. Frazer, "Modification of General Electric SPG goniometer for single-crystal neutron diffraction measurements," Rev. Sci. Instrum., 26, 4, 402-403 (1955).
82. W. L. Bond, "A single-crystal automatic diffractometer. I," Acta Cryst., 8, 12, 741-746 (1955).
83. F. L. Hirschfeld and G. M. J. Schmidt, "Geiger-counter measurements of single-crystal Bragg reflections. The geometrical problem," Bull. Res. Council Israel, 3, 37-45 (1953).
84. M. M. Umanskii and D. M. Kheiker, "X-ray goniometric methods of examining crystals," Kristallografiya, 1, 4, 459-466 (1956).
85. A. R. Lang, "Suggested necessary condition for successful use of stationary crystal integrated reflection measuring method with the counter spectrometer," Rev. Sci. Instrum., 25, 10, 1039-1040 (1954).
86. R. Pepinsky, B. C. Frazer, and M. L. McKlown, "New goniometers for single-crystal neutron diffraction studies," Rev. Sci. Instrum., 25, 7, 699-703 (1954).
87. B. F. Decker, E. T. Asp, and D. Harker, "Preferred orientation using a Geiger-counter x-ray diffraction goniometer," J. Appl. Phys., 19, 4, 388-392 (1948).
88. S. VanBeatty, "Intensity correction factors for x-ray spectrometer transmission pole figure determinations," J. Appl. Phys., 21, 9, 940-941 (1950).
89. L. G. Schulz, "Determination of preferred orientation in flat transmission samples using a Geiger-counter x-ray spectrometer," J. Appl. Phys., 20, 11, 1033-1036 (1949).
90. J. T. Norton, "A technique for quantitative determination of texture of sheet metals," J. Appl. Phys., 19, 12, 1176-1178 (1948).
91. A. H. Geisler, "Automatic pole figure recorder," Rev. Sci. Instrum., 25, 8, 727-732 (1954).
92. M. Field and E. Merchant, "Reflection method of determining preferred orientation of the Geiger-counter spectrometer," J. Appl. Phys., 20, 8, 741-745 (1949).
93. L. G. Schulz, "A direct method of determining preferred orientation of a flat reflection sample using a Geiger-counter x-ray spectrometer," J. Appl. Phys., 20, 11, 1030-1033 (1949).
94. W. P. Chernock and P. A. Beck, "Analysis of certain errors in the x-ray reflection method for the quantitative determination of preferred orientation," J. Appl. Phys., 23, 3, 341-345 (1953).
95. W. P. Chernock, M. H. Mueller, H. R. Fisch, and P. A. Beck, "An automatic x-ray reflection specimen holder for the quantitative determination of preferred orientation," Rev. Sci. Instrum., 24, 10, 925-928 (1953).
96. J. Singer, "Jig for aligning specimens on pole figure goniometers," Rev. Scient. Instrum., 26, 10, 963-964 (1955).
97. A. N. Holden, "A spiral-scanning x-ray reflection goniometer for the rapid determination of

preferred orientation," Rev. Sci. Instrum., 24, 1, 10-12 (1953).
98. H. Hu, and P. A. Beck, "Rolling texture in aluminium," J. Metals, 188, 10, 1214-1215 (1950).
99. M. Schwartz, "Method for obtaining complete quantitative pole figures for flat sheets using one sample and one sample holder," J. Appl. Phys., 26, 12, 1507-1513 (1955).
100. B. Irvin and F. B. Breazeale, "The adaptation of the Norelco high-angle spectrometer to the measurement of the x-ray diffraction of fibers," Rev. Sci. Instrum., 24, 8, 627-631 (1953).
101. L. Segal, J. J. Creely, and C. M. Conrad, "A rotating specimen mount for use with x-ray spectrometer in measuring crystallite orientation of cellulosic and other textile fibers," Rev. Sci. Instrum., 21, 5, 431-435 (1950).
102. L. S. Birks and H. Friedman, "A high-temperature x-ray diffraction apparatus," Rev. Sci. Instrum., 18, 8, 576-580 (1947).
103. H. T. Heal, and H. Mykura, "An x-ray method for the study of phase changes at high temperatures," Metal Treatment, 17, 63, 129-135 (1950).
104. N. A. Toropov, D. F. Konovalov, A. I. Efremov, and G. V. Anan'eva, "X-ray analysis by ionization in the examination of cements," Tsement, 3, 17-20 (1954).
105. P. Chiotti, "Adaptation of a Geiger-counter x-ray diffractometer for high-temperature investigations," Rev. Sci. Instrum., 25, 7, 683-688 (1954).
106. V. Valkenburg and H. F. McMurdie, "High-temperature x-ray diffraction apparatus," Am. Ceram. Soc., Bull., 26, 5, 139-142 (1947).
107. G. K. Williamson and A. Moore, "A precision high-temperature specimen chamber for an x-ray diffractometer," J. Sci. Instrum., 33, 3, 107-110 (1956).
108. D. T. Keating and B. E. Warren, "Long-range order in beta-brass and Cu_3Au," J. Apply. Phys., 22, 3, 286-290 (1951).
109. N. H. Smith and H. H. Heady, "Identification of frozen liquid samples with the x-ray diffractometer," Anal. Chem., 27, 6, 883-888 (1955).
110. E. A. Wood, "Heated sample holder for x-ray diffractometer work," Rev. Sci. Instrum., 27, 1, 60 (1956).
111. B. A. Calhoun and S. C. Abrahams, "A low-temperature adaptor for the Norelco high-angle spectrometer," Rev. Sci. Instrum., 24, 5, 397 (1953).
112. R. Keeling, B. C. Frazer, and R. Pepinsky, "Low-temperature x-ray goniometer for structural studies of crystal transition," Rev. Sci. Instrum., 24, 12, 1087-1095 (1953).
113. J. A. James, "Orientation of crystals using a Geiger-counter x-ray spectrometer," J. Scient. Instrum., 27, 12, 324 (1950).
114. S. T. Konobeevskii, B. M. Levitskii, and Yu. A. Martynyuk, "A new method of x-ray structure analysis for radioactive materials," Zh. Tekhn. Fiz., 26, 4, 870-873 (1956).
115. W. V. Cummings, J. D. C. Caultz, and M. J. Sanderson, "Double diffracting x-ray spectrometer for study of irradiated materials," Rev. Sci. Instrum., 26, 1, 5-13 (1955).

LETTER TO THE EDITORS

METHODS OF REPRESENTING THE CUBIC SPACE GROUPS

N. V. Belov

Institute of Crystallography, Academy of Sciences of the USSR

Translated from Kristallografiya, Vol. 1, No. 6,
pp. 764-768, November-December, 1956
Original article submitted September 11, 1956

The second edition of the International Tables for the Identification of Crystal Structures appeared in 1952. This consisted almost entirely of information on the space groups, but diagrams for all the cubic groups were omitted by the editors because the specialists they had consulted were of the opinion that those in the first edition were incomplete but at the same time overcomplicated and obscure, which made them of little real value.

This omission gave rise to objections from many crystallographers, and Pauling spoke for these in Acta Crystallographica when he stated that, if we rule out the incorrect reference of the reader (for the cubic groups) for part of the data to one or two of the simpler groups, the diagrams of the first edition were satisfactory (in which I agree with him); and further, the diagrams for the space groups are of value in instruction as well as for reference purposes, for without them we cannot have a sufficiently detailed study of the space groups as the basis of structure analysis.

The editors agreed with these objections and promised to publish the diagrams for the cubic groups as a special supplement to the first volume;

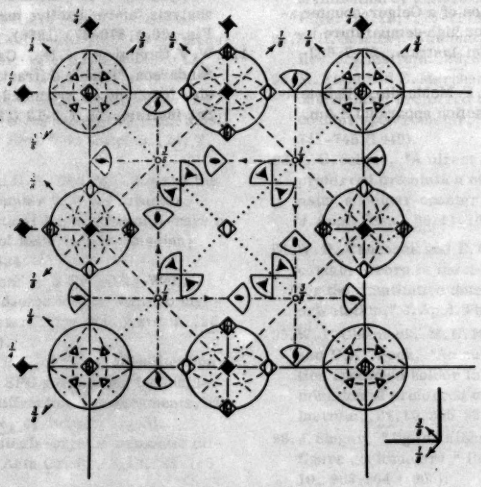

Fig. 1. Lonsdale and Henry's draft of a diagram of the symmetry elements in group O_h^7 = Fd3c; the top left quadrant of the projection on a cube face is shown.

but this promise has remained unfulfilled although four years have elapsed, because the editors have not yet been able to decide on the best method of representing the cubic diagrams.

Only in August of this year did I receive from Professor Lonsdale (chairman of the editorial committee) a letter enclosing a diagram for one of the most complicated holohedral cubic groups (Fig. 1), with a request that I bring these draft diagrams to the notice of our crystallographers by publishing them in this journal together with my reply to Professor Lonsdale and my proposed diagram (Fig. 2) for this group. This diagram has been drawn up largely in accordance with the method of representation chosen by the British editors.

It will be seen that the most novel feature is that stereographic projections are used at the points where the largest numbers of symmetry elements coincide, and these the crystallographer may most readily employ to envisage the orientation of the intersecting symmetry elements. Excerpts from these projections even show the individual elements such as inclined triad and diad axes (rotation or screw).

The editors also consider that their diagrams have the great advantage of a marked reduction in the number of symbols needed; in particular, they consider it possible to avoid altogether the 15 symbols for (mainly) inclined elements that were used solely for the cubic groups in the first edition (but it is not clear why they considered this a disadvantage).

The following is my reply to Professor Lonsdale, with the introductory and final sentences deleted.

I have made a careful study of your proposed diagram (of the symmetry elements) for group O_h^8 = Fd3c and have some comments on the proposed new method of representation.

1. The replacement of an insignificant square with a single diagonal by a stereographic projection appears very effective. There is no doubt that such projections are especially valuable in space groups for crystallographers of orthodox background in mineralogical crystallography, but I consider that the method has not been carried to its logical conclusion in the proposed draft, and also (and in part because) this has disadvantageous effects for other details, as I show below.

2. How do the signs for inversion axes at level $\frac{1}{4}$ appear at the poles x and $\bar{x}$ (at y and $\bar{y}$ on the other edge) on the projection representing the intersecting symmetry elements at $\frac{1}{4}$ of the edge at level 0? I do not see why at these poles we do not have the signs for the 4_1 and 4_3 screw axes emerging at level 0; and then the signs for the inversion axes (at level $\frac{1}{4}$) would have to be displaced to the margin. Conversely, the stereographic projection around the origin of the cell must be supplemented with signs for the inversion or diad axes mentioned in the next point. The marginal signs are best given as in the International Tables of 1935.

3. Do we denote the emergence of a horizontal axis by the sign for an inversion axis or by that for a diad axis? The proposed diagram nowhere distinguishes the special points of (horizontal) inversion axes, and we are forced to envisage them as occurring exactly in the middle between two points of emergence (from the poles of the stereographic projection) of the inversion axis. This is incorrect as regards method, on account of the special role of these special points, which is so important that the origin of the cell is taken at such a point in many groups.

I consider that it is absolutely necessary to use the mirrors (used in the 1935 edition) that cut across the diad axes and so indicate these points, and that these should be used in that form. In particular, I am unable to see how you can otherwise denote these special points in group T_d^6 = I43d (p. 334 of the 1935 edition) or O_h^{10} = Ia3d.

Mirrors with the heights stated must be shown for vertical inversion axes as well as horizontal ones. If these points are not overlapped from above by signs for other axes (e.g., screw ones) in the projection, the method of symbolizing them can give rise to no doubt; if this occurs, the mirrors are shown by the side. This displacement of the mirrors, if these lie within the stereographic projection, cannot give rise to doubt as to the position of the points. If mirrors are used, we should denote the emergence of an inversion axis from a pole of a stereographic projection by a simple arrow. This is shown to be correct by the next point.

4. It is usual in group O_h^8 = Fd3c to locate the origin not at a center of symmetry (where the symmetry is 6) but at point T = 23, where the symmetry is higher (namely, 12); but this is in no way reflected in the stereographic projection around the origin, from whose poles emerge neither diad axes nor inversion ones, whose existence must be deduced by resort to another stereographic projec-

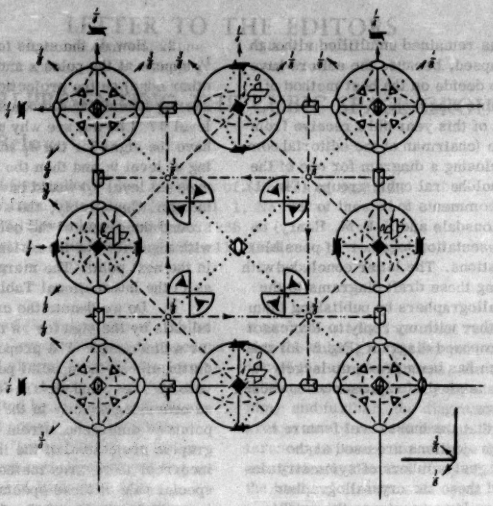

Fig. 2. Draft diagram for space group O_h^8 proposed here.

tion, namely, that for point ¼ on an edge. Diad or inversion axes essentially must be shown in the stereographic projection around the origin in order not to confuse nonspecialists, especially those (e.g. students) largely unfamiliar with the space groups.

5. In this context the polyhedra of points in general positions (given in the 1935 tables) are not unnecessary, as you state in your explanatory text for the diagram. They identify directly the complex of symmetry T = 23 at the 16 corresponding points of the elementary cube. Of course, it is hardly an advantage of the diagram for O_h^8 that one can see only half of these polyhedra, and that all of the points of these have commas. I consider that all that is necessary (leaving out reference to previous pages) is to show the polyhedra at levels 0 and ¼ (half with commas and half without) and to mention that they overlap at levels ½ and ¾ with enantiomorphic polyhedra, which would be absolutely clear.

6. Your symbols for triad and diad axes (rotation or screw) are evidently excerpts from the stereographic projections where they do not appear in the symmetry complex shown on the complete stereographic projection; they are larger for the triad axes but very small for the diad ones. This is good for the triad axes but not good for the diads. The method used in the 1935 tables is better and clearer.

My diagram for group O_h^8 = Fd3c has been drawn up in accordance with the above remarks, but it conforms generally to your basic principle; in it there is an illogical feature. I have not denoted a horizontal inversion axis by a distinct sign at all, but have everywhere inserted the symbol for a triad inversion axis (triangle with blank circle). I recognize that this is incorrect, since even the beginner would find it difficult to imagine to which closest triad axis we assign a center of symmetry of height ⅛ or ⅜. It would be more logical to delete the blank circles from the signs for the triad axes altogether.

7. I also raise the question of the representation of d planes, for which I have proposed[1] a representation without arrows, though this may not be very convenient for graphic reproduction. Why not represent diamond planes by two bars and two points, to distinguish them from ordinary inclined planes?

8. The symmetry complex T = 23 is used in the diagram to distinguish (a) positions without parameters; centers of symmetry are used to show

[1]Dokl. Akad. Nauk SSSR, 59, 4, 701-702 (1948).

(c) positions of symmetry $C_{3i} = \bar{3}$; and mirrors to show (d) positions (also without parameters) with $S_4 = \bar{4}$. We are left with no symbols for the no less important (b) positions with symmetry $D_3 = 32$; it would be very appropriate to indicate these (above and below the centers of symmetry) by a sign representing a quartz crystal, though I accept that this is only a pious hope. I regret that I am unable to discuss all the cubic groups in detail, because this would undoubtedly raise other points.

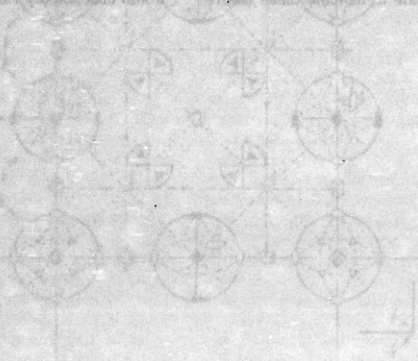

Fig. 1. [illegible] for space group O_h^1.

INDEX

Soviet Physics – Crystallography 1956

Volume 1, Numbers 1-6

INDEX

Soviet Physics — Crystallography 1956

Volume 1, Numbers 1–6

AUTHOR INDEX

	VOL.	PAGE	RUSS. PAGE
Ablov, A. V., see G. B. Bokii	1	36	49
Aleksandrov, K. S., Special Case of the Propagation of Elastic Waves in Crystals	1	104	138
Aleksandrov, K. S., and V. Ya. Khaimov-Mal'kov, Rotation of the Plane of Polarization of an Elastic Shear Wave	1	292	373
Aleksandrov, K. S., Propagation of Elastic Waves along Specific Directions in Crystals	1	563	718
Auleitner, Yu. K., see L. I. Tatarinova	1	426	537
Bagdasarov, Kh. S., and A. P. Kapustin, Production of Etch Figures by Means of Ultrasonic Vibrations	1	107	139
Bakakin, V. V., and N. V. Belov, A Rational Method of Deriving the Various Close-Packed Arrays of Spheres	1	391	491
Baranskii, K. N., L. A. Gribov, and V. P. Prikhod'ko, Crystals of Complex Compounds of Metals of the Platinum Group (Part 13)	1	280	361
Baranskii, K. N., L. A. Gribov, and V. P. Prikhod'ko, Refractive Indices of Rochelle Salt Near Phase-Transition Points	1	287	368
Batsanov, S. S., Relation between the Melting Points and Refractive Indices of Ionic Crystals	1	108	140
Batsanov, S. S., and A. S. Sonin, Refractions for Hydrogen Bonds in Inorganic Compounds (Part 2)	1	249	321
Batsanov, S. S., Refractions of Hydrogen Bonds in Inorganic Compounds (Part 3)	1	254	328
Batsanov, S. S., and E. D. Ruchkin, Ionic Radii and Refractions for Group VIII Metals	1	468	595
Batsanov, S. S., see G. B. Bokii	1	60	81
Belov, K. P., A. V. Zalesskii, and A. S. L'vova, Susceptibility of Pyrrhotine as a Function of Temperature	1	549	696
Belov, N. V., and T. N. Tarkhova, Color Symmetry Groups	1	5	4
Belov, N. V., and T. N. Tarkhova, The Strips Method of Computing Fourier Analyses in Crystal Structure Analysis	1	99	132
Belov, N. V., and T. N. Tarkhova, A Nomographic Method of Calculating Structure Factors	1	180	235
Belov, N. V., and T. N. Tarkhova, The 48-Hedron Group	1	278	360
Belov, N. V., The One-Dimensional Infinite Crystallographic Groups	1	372	474
Belov, N. V., Moorish Patterns of the Middle Ages and the Symmetry Groups	1	482	610
Belov, N. V., and T. N. Tarkhova, Color Symmetry Groups	1	487	619
Belov, N. V., Three-Dimensional Mosaics with Colored Symmetry	1	489	621
Belov, N. V., A System for Modeling Crystal Structures and Patterns	1	574	733
Belov, N. V., Methods of Representing the Cubic Space Groups	1	596	764
Belov, N. V., see V. V. Bakakin	1	391	491
Belov, N. V., see E. G. Fesenko	1	131	171
Belov, N. V., see N. I. Shulepova	1	467	594
Bokii, G. B., T. I. Malinovskii, and A. V. Ablov, Structure of the Dihalide-Diamines of Cobalt	1	36	49
Bokii, G. B., and S. S. Batsanov, New Ionic Refraction Values	1	60	81

	VOL.	PAGE	RUSS. PAGE
Bokii, G. B., and T. S. Khodashova, An X-Ray Study of Crystals of $InF_3 \cdot 3H_2O$	1	152	197
Brodovskii, D., see B. N. Grechushnikov	1	470	597
Broude, V. L., and A. F. Prikhot'ko, Structural Changes in Crystals Studied on Low-Temperature Spectra	1	258	334
Burovaya, É. E., Crystals of Complex Compounds of Metals of the Platinum Group (Part 14)	1	284	365
Butuzov, V. P., and E. G. Ponyatovskii, The Polymorphic Transitions of Bismuth at High Pressures	1	453	572
Butuzov, V. P., and E. G. Ponyatovskii, The Melting Point of Indium at Pressures up to 30,000 kg/cm^2	1	577	736
Chentsova, L. G., Nature of the Color Centers in Smoky Quartz	1	384	484
Chernov, A. A., Tangential Growth Rates of Elementary Layers on the Surface of a Crystal	1	88	119
Chernov, A. A., Evaluation of Transformation Times for Inclusions and Dendritic Crystals	1	460	583
Distler, G. I., The Optical Parameters of New Ultraviolet Polarizers	1	161	218
Distler, G. I., and E. V. Parvova, Development and Testing of Heat-Resisting Polarizers	1	171	221
Dukova, E. D., see G. G. Lemmlein	1	84	112
Dukova, E. D., see G. G. Lemmlein	1	269	351
Dukova, E. D., see G. G. Lemmlein	1	375	477
Dvoryankin, V. F., see B. K. Vainshtein	1	493	626
Ezhkova, Z. I., see G. S. Zhdanov	1	210	271
Fesenko, E. G., I. M. Rumanova, and N. V. Belov, Crystal Structures of Zoisite	1	132	171
Fesenko, E. G., and O. I. Prokopalo, Isomorphism of the Ferrates and Titanates of Strontium, Barium, and Lead	1	412	520
Fesenko, E. G., and O. I. Prokopalo, Isomorphous Mixtures of Barium Titanate and Ferrate	1	553	703
Firsova, M. M., see V. G. Zubov	1	454	546
Firsova, M. M., see V. G. Zubov	1	439	555
Frank-Kamenetskii, V. A., M. A. Rumsh, and A. I. Komkov, The KRON-1 X-Ray Camera for Examining Euhedral and Irregular Crystals	1	367	468
Fridkin, V. M., Some Results on the Photoelectret State in Sulfur Single Crystals	1	441	557
Fridkin, V. M., Depolarization of Photopolarized Sulfur Single Crystals at Various Temperatures	1	546	692
Fridkin, V. M., see A. I. Froiman	1	236	342
Froiman, A. I., and V. M. Fridkin, The Heterocharge on Carnauba Wax Electrets	1	263	342
Gado, P., see E. Sándor	1	571	729
Gliki, N. V., I. A. Pleteneva, and V. A. Timofeeva, Spiral Growth Layers on Barium Titanate Crystals	1	478	607
Gol'der, G. A., see E. A. Gribova	1	39	53
Graevskaya, Yu. I., V. I. Iveronova, and V. P. Tarasova, A Specialized Geiger Counter Apparatus for Intensity Measurement of X-Ray Reflections	1	350	442
Grechushnikov, B. N., and D. Brodovskii, Thermal Stresses in Cubic Crystals	1	470	597
Gribov, L. A., see K. N. Baranskii	1	280	361
Gribov, L. A., see K. N. Baranskii	1	287	368
Gribova, E. A., G. S. Zhdanov, and G. A. Gol'der, An X-Ray Structural Study of Indigo and Thioindigo	1	39	53

	VOL.	PAGE	RUSS. PAGE
Gudkov, L. S., see E. S. Makarov	1	511	650
Indenbom, V. L., I. M. Sil'vestrova, and Yu. I. Sirotin, Thermoelastic Stresses in Anisotropic Plates	1	472	599
Ioffe, Yu. K., The URS-50I and URS-25I X-Ray Diffractometers for Structure Analysis	1	362	460
Iveronova, V. I., see Yu. I. Graevskaya	1	350	442
Kamentsev, I. E., The Oriented Crystallization of Potassium Iodide and Bromide on Muscovite	1	185	240
Kapustin, A. P., and V. E. Kavalyunaite, Effects of Ultrasound on the Growth of a Single Crystal of Potash Alum	1	578	737
Kapustin, A. P., see Kh. S. Bagdasarov	1	107	139
Kapustinskii, A. F., Constancy and Multiple Proportions as Fundamental Principles in Crystallography and Chemistry	1	67	90
Kapustinskii, A. F., Atomic and Ionic Dimensions of the Transuranium Elements in Crystals	1	304	382
Kavalyunaite, V. E., see A. P. Kapustin	1	578	737
Kaverin, S. V., see Z. G. Pinsker	1	48	66
Khaimov-Mal'kov, V. Ya., see K. S. Aleksandrov	1	292	373
Kheiker, D. M., and L. S. Zevin, Application of the Diffractometer in some Structure-Analysis Problems	1	580	739
Kheiker, D. M., see M. M. Umanskii	1	353	446
Khitrova, V. I., see Z. G. Pinsker	1	231	300
Khodashova, T. S., see G. B. Bokii	1	152	197
Kholodenko, L. P., Theory of Hysteresis Effects in Barium Titanate	1	311	393
Khotsyanova, T. L., Structure of Diphenyliodonium Chloride and Iodide	1	415	524
Khotsyanova, T. L., and Yu. T. Struchkov, The Crystal Structure of Tetraphenylphosphonium Iodide and the Configuration of Tetraaryl Ions and Molecules	1	527	669
Kitaigorodskii, A. I., Determination of the Sign of Structure Amplitudes	1	12	14
Klassen-Neklyudova, M. V., and A. A. Urusovskaya, Influence of Non-uniform Stressed State on the Mechanism of the Plastic Deformation of Thallium and Cesium Halides	1	323	410
Klassen-Neklyudova, M. V., and A. A. Urusovskaya, Study of the Structure of Kink Bands in Thallium Halide Crystals	1	446	564
Kliya, M. O., The Transformation Mechanism for Dendritic Crystals	1	456	577
Kolontsova, E. V., I. V. Telegina, and G. M. Plavnik, Structure of Fault (Kink) Bands of Certain Ionic Crystals	1	331	419
Komkov, A. I., see V. A. Frank-Kamenetskii	1	367	468
Kosevich, V. M., see V. I. Startsev	1	336	425
Kosevich, V. M., see V. I. Startsev	1	339	429
Kurov, G. A., and Z. G. Pinsker, Nature of Amorphous Antimony	1	320	407
Kvitka, S. S., A Flat-Crystal Monochromator for the BSV-4 Tube	1	386	485
Lemmlein, G. G., and E. D. Dukova, Tangential Growth Rates of Elementary Layers on Paratoluidine Crystals	1	84	112
Lemmlein, G. G., and E. D. Dukova, Formation of Screw Dislocations in the Growth Process of a Crystal	1	269	351
Lemmlein, G. G., and E. D. Dukova, Attraction between Centers of Spirals of Opposite Sign during Crystal Growth	1	375	477
Levdik, V. A., see E. S. Makarov	1	506	644
Lobachev, A. N., see B. K. Vainshtein	1	370	472
L'vova, A. S., see K. P. Belov	1	549	696
Makarov, E. S., and S. I. Vinogradov, Crystal Structure of Th_2Zn_{17} and U_2Zn_{17}	1	499	634
Makarov, E. S., and V. A. Levdik, Crystal Structure of UGa and UGa_2	1	506	644

	VOL.	PAGE	RUSS. PAGE
Makarov, E. S., and L. S. Gudkov, X-Ray Diffraction Study of Thorium–Zinc Alloys	1	511	650
Makarov, V. M., see I. S. Zheludev	1	289	370
Malinovskii, T. I., see G. B. Bokii	1	36	49
Mikheeva, L. F., see I. A. Yakovlev	1	91	123
Miller, A. I., see Z. G. Pinsker	1	183	239
Orekhvo, O. S., see Z. G. Pinsker	1	183	239
Ormont, B. F., On the Possibility of Forming the Structure of the Deuterides (Hydrides) of Metals, Retaining Hydrogen Molecules or Pairs of Atoms in the Lattice	1	110	142
Parvov, V. F., see I. S. Zheludev	1	382	482
Parvova, E. V., see G. I. Distler	1	171	221
Pinsker, Z. G., and S. V. Kaverin, Electron-Diffraction Determination of the Structure of Iron Carbide Fe_4C	1	48	66
Pinsker, Z. G., O. S. Orekhvo, and A. I. Miller, An Electron-Diffraction Study of Bi and Sb Alloys and Certain of Their Oxides	1	183	239
Pinsker, Z. G., and V. I. Khitrova, Study of the Structure of some Four-Component Alloys of Tl–Sb–As–Se	1	231	300
Pinsker, Z. G., see G. A. Kurov	1	320	407
Pinsker, Z. G., see S. A. Semiletov	1	161	209
Pinsker, Z. G., see L. I. Tatarinova	1	426	537
Plavnik, G. M., see E. V. Kolontsova	1	331	419
Pleteneva, I. A., see N. V. Gliki	1	478	607
Ponyatovskii, E. G., see V. P. Butuzov	1	453	572
Ponyatovskii, E. G., see V. P. Butuzov	1	577	736
Porai-Koshits, M. A., Derivation of Working Formulas for the Electron Density and Structure Amplitudes from the Symmetry and Antisymmetry of Trigonometric Functions	1	22	27
Porai-Koshits, M. A., Application of Computers to X-Ray Structural Calculations	1	193	248
Porai-Koshits, M. A., Structure of Cesium-Tetrachlorocobaltate Crystals Cs_2CoCl_4	1	224	291
Pozdnyakov, P. G., Growth of Crystals of Ethylene Diamine Tartrate	1	175	228
Pozdnyakov, P. G., Preparation of Lithium Sulfate Crystals	1	275	356
Pozdnyakov, P. G., Preparation of Potassium Tartrate Crystals	1	464	589
Prikhod'ko, V. P., see K. N. Baranskii	1	280	361
Prikhod'ko, V. P., see K. N. Baranskii	1	287	368
Prikhot'ko, A. F., see V. L. Broude	1	258	334
Prokopalo, O. I., see E. G. Fesenko	1	412	520
Prokopalo, O. I., see E. G. Fesenko	1	533	703
Rannev, N. V., see G. S. Zhdanov	1	407	514
Rogachev, D. L., see A. I. Zaslavskii	1	123	159
Ruchkin, E. D., see S. S. Batsanov	1	468	595
Rumanova, I. M., see E. G. Fesenko	1	132	171
Rumsh, M. A., see V. A. Frank-Kamenetskii	1	367	468
Sándor, E., The Study of Poorly-Formed Single Crystals of Unknown Symmetry with an X-Ray Goniometer	1	533	677
Sándor, E., and P. Gado, Preparation of Small Spheres from Single Crystals	1	571	729
Semiletov, S. A., and Z. G. Pinsker, Electron-Diffraction Study of the Degree of Perfection of Germanium Single Crystals	1	161	209
Semiletov, S. A., Electron-Diffraction Study of the Structures of Thin Layers of Cadmium Sulfide, Selenide, and Telluride	1	236	306

	VOL.	PAGE	RUSS. PAGE
Semiletov, S. A., Electron-Diffraction Determination of the Structure of Antimony Telluride	1	317	403
Semiletov, S. A., Electron-Diffraction Study of the Structure of Germanium Films Obtained at Vacuum Deposition	1	430	542
Shal'nikova, N. A., and I. A. Yakovlev, X-Ray Diffraction Study of the Crystal-Lattice Constants and Thermal-Expansion Coefficients of Leucosapphire and Ruby	1	420	531
Shendrik, T. N., see Yu. N. Venevtsev	1	516	657
Shkol'nikova, L. M., see E. A. Shugam	1	378	478
Shubnikov, A. V., Some Peculiarities in the Thermal Deformation of Crystals	1	71	95
Shubnikov, A. V., On the Absence of a Definite Connection Between the Homology of the External Form of Crystals and That of Their Optical Indicatrices	1	191	246
Shubnikov, A. V., Some Aspects of the Crystallization of Diphenylamine	1	295	374
Shubnikov, A. V., Lecture Experiment for Demonstrating Rhythmic Growth in Salol Crystals	1	477	606
Shubnikov, A. V., Ansheles's Comments on "A Traditional Error and the Many Ways in Which It Appears"	1	484	614
Shugam, E. A., and L. M. Shkol'nikova, A Study of the Crystal Structures of Aluminum and Chromium Acetylacetonates	1	378	478
Shulepova, N. I., and N. V. Belov, Symmetry of Patterson Syntheses (Functions)	1	467	594
Shuvalov, L. A., see I. S. Zheludev	1	537	681
Sil'vestrova, I. M., see V. L. Indenbom	1	472	599
Sirotin, Yu. I., Stresses Produced by Heating and Cooling in Single Crystals	1	556	708
Sirotin, Yu. I., see V. L. Indenbom	1	472	599
Sit'ko, R. Ya., see I. S. Zheludev	1	543	689
Smirnova, N. L., Structure Types with Atomic Close Packing: Possible Structure Types for the Composition AB_3	1	128	165
Smirnova, N. L., Structure Types with Closest Atomic Packing: Possible Structure Types for the AB_4 Composition	1	399	502
Sonin, A. S., see S. S. Batsanov	1	249	321
Startsev, V. I., V. M. Kosevich, and Yu. S. Tomenko, Study of the Intersection of Twin Layers in Calcite Single Crystals	1	336	425
Startsev, V. I., V. M. Kosevich, and Yu. S. Tomenko, Study of the Intersection of Twinning Layers in Single Crystals of Antimony, Bismuth, and Zinc	1	339	429
Stasova, M. M., see B. K. Vainshtein	1	241	311
Struchkov, Yu. T., see T. L. Khotsyanova	1	527	669
Syrkin, L. N., Study of the Form of Potential Relief for Ions in Crystals of the Perovskite Type	1	212	274
Tarasova, V. P., see Yu. I. Graevskaya	1	350	442
Tarkhova, T. N., see N. V. Belov	1	5	4
Tarkhova, T. N., see N. V. Belov	1	99	132
Tarkhova, T. N., see N. V. Belov	1	180	235
Tarkhova, T. N., see N. V. Belov	1	278	360
Tarkhova, T. N., see N. V. Belov	1	487	619
Tatarinova, L. I., Electron-Diffraction Study of Amorphous GaSe	1	423	534
Tatarinova, L. I., Yu. K. Auleitner, and Z. G. Pinsker, Electron-Diffraction Study of GaSe	1	426	537
Telegina, I. V., see E. V. Kolontsova	1	331	419
Timofeeva, V. A., see N. V. Gliki	1	478	607

	VOL.	PAGE	RUSS. PAGE
Tomenko, Yu. S., see V. I. Startsev	1	336	425
Tomenko, Yu. S., see V. I. Startsev	1	339	429
Tsinober, L. I., Spiral Structure of Accesory Growth on (0001) Surfaces of Artificial Quartz Crystals	1	480	609
Umanskii, M. M., and D. M. Kheiker, Methods of X-Ray Goniometry for Examining Crystals	1	353	446
Umanskii, M. M., see G. S. Zhdanov	1	210	271
Umanskii, M. M., see V. V. Zubenko	1	346	436
Urusovskaya, A. A., see M. V. Klassen-Neklyudova	1	323	410
Urusovskaya, A. A., see M. V. Klassen-Neklyudova	1	446	564
Vainshtein, B. K., The Kinematic Theory of Reflection Intensities on Electron-Diffraction Patterns. Part 1: Spot Patterns	1	15	17
Vainshtein, B. K., Derivation of the Formula for the Temperature Factor from a Convolution Theorem	1	103	137
Vainshtein, B. K., Kinematic Theory of Intensities in Electron-Diffraction Patterns. Part 2: Patterns from Textures and Polycrystalline Aggregates	1	117	150
Vainshtein, B. K., and M. M. Stasova, Electron-Diffraction Study of Cryptohalite	1	241	311
Vainshtein, B. K., and A. N. Lobachev, Differentiation of Dynamic and Kinematic Types of Scattering in Electron Diffraction	1	370	472
Vainshtein, B. K., Accuracy of Fourier Series for the Potential in Electron Diffraction	1	394	495
Vainshtein, B. K., and V. F. Dvoryankin, Effects of Bonding on Electron Scattering by Atoms	1	493	626
Varfolomeeva, L. A., see G. S. Zhdanov	1	210	271
Vasin, I. G., see M. I. Yaroslavskii	1	475	603
Velichkina, T. S., see I. A. Yakovlev	1	91	123
Venevtsev, Yu. N., G. S. Zhdanov, and T. N. Shendrik, X-Ray Diffraction Study of the $PbTiO_3$–"$PbSnO_3$" System	1	516	657
Vinogradov, S. I., see E. S. Makarov	1	499	634
Vorontsova, L. G., see G. S. Zhdanov	1	44	61
Yakovlev, I. A., L. F. Mikheeva, and T. S. Velichkina, The Molecular Scattering of Light and the $\alpha \rightleftharpoons \beta$ Transformation in Quartz	1	91	123
Yakovlev, I. A., see N. A. Shal'nikova	1	420	531
Yaroslavskii, M. I., and I. G. Vasin, Resonant Plates Cut from Brazilian-Law Quartz Twins	1	475	603
Yavorskii, I. V., Geometry of the Diffraction Picture for Dynamic Interaction of X-Rays with a Crystal	1	221	287
Yurin, V. A., Anomalous Polarization in Rochelle-Salt Crystals	1	575	734
Zalesskii, A. V., see K. P. Belov	1	549	696
Zaslavskii, A. I., and D. L. Rogachev, Determination of the Laue Class and Orientation for an Unfacetted Crystal from a Single Pattern Recorded with Polychromatic Radiation from the Crystal at Rest	1	123	159
Zevin, L. S., see D. M. Kheiker	1	580	739
Zhdanov, G. S., Z. V. Zvonkova, and L. G. Vorontsova, X-Ray Structural Study of a Methylene Blue Dye	1	44	61
Zhdanov, G. S., M. M. Umanskii, L. A. Varfolomeeva, Z. I. Ezhkova, and Z. K. Zolina, X-Ray Determination of Unit Cells and Space Groups of the Piezoelectric Crystals $KLiC_4H_4O_6 \cdot H_2O$, $NH_4LiC_4H_4O_6 \cdot H_2O$, $NaHC_4H_4O_6 \cdot H_2O$ and $(NH_4)_2C_4H_4O_6$	1	210	271
Zhdanov, G. S., Z. V. Zvonkova, and N. V. Rannev, X-Ray Structural Study of Lead Diethyldithiocarbamate	1	407	514

	VOL.	PAGE	RUSS. PAGE
Zhdanov, G. S., see E. A. Gribova	1	39	53
Zhdanov, G. S., see Yu. N. Venevtsev	1	516	657
Zhdanov, G. S., see N. N. Zhuravlev	1	158	205
Zhdanov, G. S., see N. N. Zhuravlev	1	404	509
Zheludev, I. S., Dielectric Ellipsoids and Dielectric-Constant Surfaces	1	79	105
Zheludev, I. S., and V. M. Makarov, Measurement of Pressure in Explosions of Gaseous Mixtures by Means of a Piezoelectric Gauge	1	289	370
Zheludev, I. S., and V. F. Parvov, Phase Transitions and Domain Structure in Barium Titanate at 120 and 5°C	1	382	482
Zheludev, I. S., and L. A. Shuvalov, Ferroelectric Phase Transitions and Crystal Symmetry	1	537	681
Zheludev, I. S., and R. Ya. Sit'ko, Behavior of Rochelle Salt Domains in Alternating Electric Fields	1	543	689
Zhuravlev, N. N., and G. S. Zhdanov, Metallographic and X-Ray-Diffraction Study of Alloys in the Germanium-Rhodium System	1	158	205
Zhuravlev, N. N., Microscope and X-Ray Structural Study of Cobalt-Antimony Alloys	1	402	506
Zhuravlev, N. N., and G. S. Zhdanov, X-Ray Diffraction Determination of the Structure of $CoSb_3$, $RhSb_3$, and $IrSb_3$	1	404	509
Zhuravlev, N. N., Determination of the Structure of SiB_6 by X-Ray Diffraction	1	524	666
Zolina, Z. K., see G. S. Zhdanov	1	201	271
Zubenko, V. V., and M. M. Umanskii, X-Ray Measurement of Coefficients of Thermal Expansion of Polycrystalline Materials in the Range −50 to +100°C	1	346	436
Zubov, V. G., A Simple Method of Observing a Phase Transition in Quartz Single Crystals	1	188	243
Zubov, V. G., and M. M. Firsova, Measurement and Recalculation of the Dynamic Elastic Constants for Quartz	1	434	546
Zubov, V. G., and M. M. Firsova, Some Aspects of the Diffraction of Light by Ultrasonic Waves in Quartz	1	439	555
Zvonkova, Z. V., A Crystallochemical Study of the Nature of the Donor–Acceptor Bond in Boron Complexes	1	54	73
Zvonkova, Z. V., Use of Direct X-Ray Structure Analysis Methods in Chemical Crystallography	1	497	631
Zvonkova, Z. V., see G. S. Zhdanov	1	44	61
Zvonkova, Z. V., see G. S. Zhdanov	1	407	514
Zvyagin, B. B., An Electron-Diffraction Study of the Hydromicas	1	166	214

SUBJECT INDEX

Articles are classified under the following headings:

THEORETICAL CRYSTALLOGRAPHY
- Symmetry
- Other generalizations of symmetry
- Theory of the solid state
- Theory of crystal growth, theory of dislocations
- Theory of the scattering of x-rays, electrons and neutrons
- Theory of crystal structure determination

CRYSTAL STRUCTURES—ATOMIC ARRANGEMENTS
- Metals and alloys (x-ray diffraction, electron diffraction)
- Simple and binary inorganic compounds (x-ray diffraction)
- Simple and binary inorganic compounds (electron diffraction)
- Ternary and more complicated inorganic compounds (x-ray diffraction)
- Ternary and more complicated inorganic compounds (electron diffraction)
- Minerals (except silicates)
- Silicates
- Complex compounds
- Organic compounds
- Apparatus for structure studies
- Experimental methods for studying structures
- Computing methods involving structures

CRYSTALLOGRAPHIC PHYSICAL CHEMISTRY
- General problems of crystal chemistry
- Chemical binding in crystals
- Phase changes, constitution diagrams

STRUCTURES OF REAL CRYSTALS
- Imperfections, special diffraction methods for: degree of dispersion, distortion, mozaicity, concentration inhomogeneity, etc. (See also: theory of scattering)

CRYSTAL OPTICS
- Problems of optical crystallography
- The study of crystals by optical methods
- Spectroscopic studies of crystals
- Electro-optical properties of crystals

ELECTRICAL PROPERTIES OF CRYSTALS
- Structures and electrical properties of ferroelectrics and piezoelectrics
- Domain structures of ferroelectrics
- Electrical properties of ferroelectrics. Pyroelectrics
- Electrical properties of linear dielectrics
- Electrets and photoelectrets

MAGNETIC PROPERTIES OF CRYSTALS

MECHANICAL PROPERTIES OF CRYSTALS
Plastic deformation
Twinning
Internal strains
Elasticity of crystals, internal friction

THERMAL PROPERTIES

PRODUCTION OF CRYSTALS
Crystallization from the gas phase
Crystallization from solution
Crystallization from the melt
Etching of crystals
External morphology
Internal morphology
The growing of crystals
Apparatus for studying the growth of crystals; grinding, cutting, and other shaping of crystals

ANNIVERSARIES

OBITUARIES OF SCIENTISTS

MISCELLANEOUS

THEORETICAL CRYSTALLOGRAPHY

	VOL.	PAGE	RUSS. PAGE
Symmetry			
The 48-Hedron Group. N.V. Belov and T.N. Tarkhova	1	278	360
One-Dimensional Infinite Crystallographic Groups. N.V. Belov	1	372	474
Moorish Patterns of the Middle Ages and the Symmetry Groups. N.V. Belov	1	482	610
Ferroelectric Phase Transitions and Crystal Symmetry. I.S. Zheludev and L.A. Shuvalov	1	537	681
Methods of Representing the Cubic Space Groups. N.V. Belov	1	596	764
Other Generalizations of Symmetry			
Color-Symmetry Groups. N.V. Belov and T.N. Tarkhova	1	5	4
Color-Symmetry Groups. N.V. Belov and T.N. Tarkhova	1	487	619
Three-Dimensional Mosaics with Colored Symmetry. N.V. Belov	1	489	621
Theory of the Solid State			
Study of the Form of Potential Relief for Ions in Crystals of the Perovskite Type. L.N. Syrkin	1	212	274
Theory of Hysteresis Effects in Barium Titanate. L.P. Kholodenko	1	311	393
Theory of Crystal Growth, Theory of Dislocations			
Tangential Growth Rates of Elementary Layers on the Surface of a Crystal. A.A. Chernov	1	88	119

	VOL.	PAGE	RUSS. PAGE
Evaluation of Transformation Times for Inclusions and Dendritic Crystals. A.A. Chernov	1	460	583
Theory of the Scattering of X Rays, Electrons, and Neutrons			
Kinematic Theory of Reflection Intensities on Electron-Diffraction Patterns. Part 1. Spot Patterns. B.K. Vainshtein	1	15	17
Derivation of the Formula for the Temperature Factor from a Convolution Theorem. B.K. Vainshtein	1	103	137
Kinematic Theory of Intensities in Electron-Diffraction Patterns. Part 2. Patterns from Textures and Polycrystalline Aggregates. B.K. Vainshtein	1	117	150
Geometry of the Diffraction Picture for Dynamic Interaction of X Rays with a Crystal. I.V. Yavorskii	1	221	287
Differentiation of Dynamic and Kinematic Types of Scattering in Electron Diffraction. B.K. Vainshtein and A.N. Lobachev	1	370	472
Effects of Bonding on Electron Scattering by Atoms. B.K. Vainshtein and V.F. Dvoryankin	1	493	626
Theory of Crystal Structure Determination			
Determination of the Sign of Structure Amplitudes. A.I. Kitaigorodskii	1	12	14
Accuracy of Fourier Series for the Potential in Electron Diffraction. B.K. Vainshtein	1	394	495
Symmetry of Patterson Syntheses (Functions). N.I. Shulepova and N.V. Belov	1	467	594
Use of Direct X-Ray Structure Analysis Methods in Chemical Crystallography. Z.V. Zvonkova	1	497	631
CRYSTAL STRUCTURES - ATOMIC ARRANGEMENTS			
Metals and Alloys (X-Ray Diffraction, Electron Diffraction)			
Metallographic and X-Ray Diffraction Study of Alloys in the Germanium-Rhodium System. N.N. Zhuravlev and G.S. Zhdanov	1	158	205
Electron-Diffraction Study of Bi and Sb Alloys and Certain of Their Oxides. Z.G. Pinsker, O.S. Orekhvo, and A.I. Miller	1	183	239
Microscope and X-Ray Structural Study of Cobalt-Antimony Alloys. N.N. Zhuravlev	1	402	506
X-Ray Diffraction Determination of the Structure of $CoSb_3$, $RhSb_3$, and $IrSb_3$. N.N. Zhuravlev and G.S. Zhdanov	1	404	509
Crystal Structure of Th_2Zn_{17} and U_2Zn_{17}. E.S. Makarov and S.I. Vinogradov	1	499	634
Crystal Structure of UGa and UGa_2. E.S. Makarov and V.A. Levdik	1	506	644
X-Ray Diffraction Study of Thorium-Zinc Alloys. E.S. Makarov and L.S. Gudkov	1	511	650
Simple and Binary Inorganic Compounds (X-Ray Diffraction)			
X-Ray Diffraction Study of the Crystal-Lattice Constants and Thermal-Expansion Coefficients of Leucosapphire and Ruby. N.A. Shal'nikova and I.A. Yakovlev	1	420	531
Determination of the Structure of SiB_6 by X-Ray Diffraction. N.N. Zhuravlev	1	524	666
Simple and Binary Inorganic Compounds (Electron Diffraction)			
Electron-Diffraction Determination of the Structure of Iron Carbide Fe_4C. Z.G. Pinsker and S.V. Kaverin	1	48	66
Electron-Diffraction Study of the Structures of Thin Layers of Cadmium Sulfide, Selenide, and Telluride. S.A. Semiletov	1	236	306

	VOL.	PAGE	RUSS. PAGE
Electron-Diffraction Determination of the Structure of Antimony Telluride. S.A. Semiletov	1	317	403
Electron-Diffraction Study of Amorphous GaSe. L.I. Tatarinova	1	423	534
Electron-Diffraction Study of GaSe. L.I. Tatarinova, Yu.K. Auleitner, and Z.G. Pinsker	1	426	537
Electron-Diffraction Study of the Structure of Germanium Films Obtained by Vacuum Deposition. S.A. Semiletov	1	430	542
Ternary and More Complicated Inorganic Compounds (X-Ray Diffraction)			
X-Ray Study of Crystals of $InF_3 \cdot 3H_2O$. G.B. Bokii and T.S. Khodashova	1	152	197
Ternary and More Complicated Inorganic Compounds (Electron Diffraction)			
Study of the Structure of Some Four-Component Alloys of Tl-Sb-As-Se. Z.G. Pinsker and V.I. Khitrova	1	231	300
Minerals (Except Silicates)			
Electron-Diffraction Study of Cryptohalite. B.V. Vainshtein and M.M. Stasova.	1	241	311
Silicates			
Crystal Structure of Zoisite. E.G. Fesenko, I.M. Rumanova, and N.V. Belov	1	132	171
Electron-Diffraction Study of the Hydromicas. B.B. Zvyagin	1	166	214
Complex Compounds			
Structure of the Dihalide-Diamines of Cobalt. G.B. Bokii, T.I. Malinovskii, and A.V. Ablov	1	36	49
Structure of Cesium-Tetrachlorocobaltate Crystals Cs_2CoCl_4. M.A. Porai-Koshits	1	224	291
Study of the Crystal Structure of Aluminum and Chromium Acetylacetonates. E.A. Shugam and L.M. Shkol'nikova	1	378	478
X-Ray Structural Study of Lead Diethyldithiocarbamate. G.S. Zhdanov, Z.V. Zvonkova, and N.V. Rannev	1	407	514
Organic Compounds			
X-Ray Structural Study of Indigo and Thioindigo. E.A. Gribova, G.S. Zhdanov, and G.A. Gol'der	1	39	53
X-Ray Structural Study of a Methylene Blue Dye. G.S. Zhdanov, Z.V. Zvonkova, and L.G. Vorontsova	1	44	61
Structure of Diphenyliodonium Chloride and Iodide. T.L. Khotsyanova	1	415	524
Crystal Structure of Tetraphenyl Phosphonium Iodide and the Configuration of Tetraaryl Ions and Molecules. T.L. Khotsyanova and Yu.T. Struchkov	1	527	669
Apparatus for Structure Studies			
X-Ray Measurement of Coefficients of Thermal Expansion of Polycrystalline Materials in the Range −50 to +100°C. V.V. Zubenko and M.M. Umanskii	1	346	436
Specialized Geiger Counter Apparatus for Intensity Measurement of X-Ray Reflections. Y.I. Graevskaya, V.I. Iveronova, and V.P. Tarasova	1	350	442
URS-50I and URS-25I X-Ray Diffractometers for Structure Analysis. Yu.K. Ioffe	1	362	460
KRON-1 X-Ray Camera for Examining Euhedral and Irregular Crystals. V.A. Frank-Kamenetskii, M.A. Rumsh, and A.I. Komkov	1	367	468

	VOL.	PAGE	RUSS. PAGE
Flat-Crystal Monochromator for the BSV-4 Tube. S.S. Kvitka	1	386	485
Application of the Diffractometer in Some Structure-Analysis Problems. D.M. Kheiker and L.S. Zevin	1	580	739
Experimental Methods for Studying Structures			
Determination of the Laue Class and Orientation for an Unfacetted Crystal from a Single Pattern Recorded with Polychromatic Radiation from the Crystal at Rest. A.I. Zaslavskii and D.L. Rogachev	1	123	159
Methods of X-Ray Goniometry for Examining Crystals. M.M. Umanskii and D.M. Kheiker	1	353	446
Study of Poorly Formed Single Crystals of Unknown Symmetry with an X-Ray Goniometer. E. Sándor	1	533	677
Computing Methods Involving Structures			
Derivation of Working Formulas for the Electron Density and Structure Amplitudes from the Symmetry and Antisymmetry of Trigonometric Functions. M.A. Porai-Koshits	1	22	27
Strips Method of Computing Fourier Analyses in Crystal Structure Analysis. N.V. Belov and T.N. Tarkhova	1	99	132
Nomographic Method of Calculating Structure Factors. N.V. Belov and T.N. Tarkhova	1	180	235
Application of Computers to X-Ray Structural Calculations. M.A. Porai-Koshits	1	193	248
CRYSTALLOGRAPHIC PHYSICAL CHEMISTRY			
General Problems of Crystal Chemistry			
Possibility of Forming the Structure of the Deuterides (Hydrides) of Metals, Retaining Hydrogen Molecules or Pairs of Atoms in the Lattice. B.F. Ormont	1	110	142
Structure Types with Atomic Close Packing: Possible Structure Types for the Composition AB_3. N.L. Smirnova	1	128	165
A Rational Method of Deriving the Various Close-Packed Arrays of Spheres. V.V. Bakakin and N.V. Belov	1	391	491
Structure Types with Closest Atomic Packing: Possible Structure Types for the AB_4 Composition. N.L. Smirnova	1	399	502
Chemical Binding in Crystals			
Crystallochemical Study of the Nature of the Donor–Acceptor Bonds in Boron Complexes. Z.V. Zvonkova	1	54	73
New Ionic Refraction Values. G.B. Bokii and S.S. Batsanov	1	60	81
Constancy and Multiple Proportions as Fundamental Principles in Crystallography and Chemistry. A.F. Kapustinskii	1	67	90
Refractions for Hydrogen Bonds in Inorganic Compounds – Part 2. S.S. Batsanov and A.S. Sonin	1	249	321
Refractions of Hydrogen Bonds in Inorganic Compounds – Part 3. S.S. Batsanov	1	254	328
Atomic and Ionic Dimensions of the Transuranium Elements in Crystals. A.F. Kapustinskii	1	304	382
Ionic Radii and Refractions for Group VIII Metals. S.S. Batsanov and E.D. Ruchkin	1	468	595

	VOL.	PAGE	RUSS. PAGE
Phase Changes, Constitution Diagrams			
A Simple Method of Observing a Phase Transition in Quartz Single Crystals. V.G. Zubov	1	188	243
Nature of Amorphous Antimony. G.A. Kurov and Z.G. Pinsker	1	320	407
Polymorphic Transitions of Bismuth at High Pressures. V.P. Butuzov and E.G. Ponyatovskii	1	453	572
STRUCTURES OF REAL CRYSTALS			
Imperfections, Special Diffraction Methods for: Degree of Dispersion, Distortion, Mozaicity, Concentration Inhomogeneity, etc. (See Also: Theory of Scattering)			
Electron-Diffraction Study of the Degree of Perfection of Germanium Single Crystals. S.A. Semiletov and Z.G. Pinsker	1	161	209
CRYSTAL OPTICS			
Problems of Optical Crystallography			
Dielectric Ellipsoids and Dielectric-Constant Surfaces. I.S. Zheludev	1	79	105
On the Absence of a Definite Connection between the Homology of the External Form of Crystals and That of Their Optical Indicatrices. A.V. Shubnikov	1	191	246
The Study of Crystals by Optical Methods			
Relation between the Melting Points and Refractive Indices of Ionic Crystals. S.S. Batsanov	1	108	140
Nature and the Color Centers in Smoky Quartz. L.G. Chentsova	1	384	484
Spectroscopic Studies of Crystals			
Molecular Scattering of Light and the $\alpha \rightleftarrows \beta$ Transformation in Quartz. I.A. Yakovlev, L.F. Mikheeva, and T.S. Velichkina	1	91	123
Optical Parameters of New Ultraviolet Polarizers. G.I. Distler	1	169	218
Development and Testing of Heat-Resisting Polarizers. G.I. Distler and E.V. Parvova	1	171	221
Structural Changes in Crystals Studied on Low-Temperature Spectra. V.L. Broude and A.F. Prikhot'ko	1	258	334
Electro-optical Properties of Crystals			
Refractive Indices of Rochelle Salt near Phase-Transition Points. K.N. Baranskii, L.A. Gribov, and V.P. Prikhod'ko	1	287	368
Some Aspects of the Diffraction of Light by Ultrasonic Waves in Quartz. V.G. Zubov and M.M. Firsova	1	439	555
Resonant Plates Cut from Brazilian-Law Quartz Twins. M.I. Yaroslavskii and I.G. Vasin	1	475	603
ELECTRICAL PROPERTIES OF CRYSTALS			
Structures and Electrical Properties of Ferroelectrics and Piezoelectrics			
X-Ray Determination of Unit Cells and Space Groups of the Piezoelectric Crystals $KLiC_4H_4O_6 \cdot H_2O$, $NH_4LiC_4H_4O_6 \cdot H_2O$, $NaHC_4H_4O_6 \cdot H_2O$, and $(NH_4)_2C_4H_4O_6$. G.S. Zhdanov, M.M. Umanskii, L.A. Varfolomeeva, Z.I. Ezhkova, and Z.K. Zolina	1	210	271

	VOL.	PAGE	RUSS. PAGE
Isomorphism of the Ferrates and Titanates of Strontium, Barium, and Lead. E.G. Fesenko and O.I. Prokopalo	1	412	520
X-Ray Diffraction Study of the $PbTiO_3$–"$PbSnO_3$" System. Yu.N. Venevtsev, G.S. Zhdanov, and T.N. Shendrik	1	516	657
Isomorphous Mixtures of Barium Titanate and Ferrate. E.G. Fesenko and O.I. Prokopalo	1	553	703
Domain Structures of Ferroelectrics			
Phase Transitions and Domain Structure in Barium Titanate at 120 and 5°C. I.S. Zheludev and V.F. Parvov	1	382	482
Electrical Properties of Ferroelectrics. Pyroelectrics			
Behavior of Rochelle Salt Domains in Alternating Electric Fields. I.S. Zheludev and R.Ya. Sit'ko	1	543	689
Anomalous Polarization in Rochelle-Salt Crystals. V.A. Yurin	1	575	734
Electrets and Photoelectrets			
Heterocharge on Carnauba Wax Electrets. A.I. Froiman and V.M. Fridkin	1	263	342
Some Results on the Photoelectret State in Sulfur Single Crystals. V.M. Fridkin	1	441	557
Depolarization of Photopolarized Sulfur Single Crystals at Various Temperatures. V.M. Fridkin	1	546	692
MAGNETIC PROPERTIES OF CRYSTALS			
Susceptibility of Pyrrhotine as a Function of Temperature. K.P. Belov, A.V. Zalesskii, and A.S. L'vova	1	549	696
MECHANICAL PROPERTIES OF CRYSTALS			
Plastic Deformation			
Influence of Nonuniform Stressed State on the Mechanism of the Plastic Deformation of Thallium and Cesium Halides. M.V. Klassen-Neklyudova and A.A. Urusovskaya	1	323	410
Structure of Fault (Kink) Bands of Certain Ionic Crystals. E.V. Kolontsova, I.V. Telegina, and G.M. Plavnik	1	331	419
Study of the Structure of Kink Bands in Thallium Halide Crystals. M.V. Klassen-Neklyudova and A.A. Urusovskaya	1	446	564
Twinning			
Study of the Intersection of Twin Layers in Calcite Single Crystals. V.I. Startsev, V.M. Kosevich, and Yu.S. Tomenko	1	336	425
Study of the Intersection of Twinning Layers in Single Crystals of Antimony, Bismuth, and Zinc. V.I. Startsev, V.M. Kosevich, and Yu.S. Tomenko	1	339	429
Internal Strains			
Thermal Stresses in Cubic Crystals. B.N. Grechushnikov and D. Brodovskii	1	470	597
Thermoelastic Stresses in Anisotropic Plates. V.L. Indenbom, I.M. Sil'vestrova, and Yu.I. Sirotin	1	472	599
Stresses Produced by Heating and Cooling in Single Crystals. Yu.I. Sirotin	1	556	708

Elasticity of Crystals, Internal Friction	VOL.	PAGE	RUSS. PAGE
Special Case of the Propagation of Elastic Waves in Crystals. K.S. Aleksandrov.	1	104	138
Rotation of the Plane of Polarization of an Elastic Shear Wave. K.S. Aleksandrov and V.Ya. Khaimov-Mal'kov	1	292	373
Measurement and Recalculation of the Dynamic Elastic Constants for Quartz. V.G. Zubov and M.M. Firsova	1	434	546
Propagation of Elastic Waves along Specific Directions in Crystals. K.S. Aleksandrov.	1	563	718
THERMAL PROPERTIES			
Some Peculiarities in the Thermal Deformation of Crystals. A.V. Shubnikov	1	71	95
PRODUCTION OF CRYSTALS			
Crystallization from the Gas Phase			
Tangential Growth Rates of Elementary Layers on Paratoluidine Crystals. G.G. Lemmlein and E.D. Dukova	1	84	112
Attraction between Centers of Spirals of Opposite Sign during Crystal Growth. G.G. Lemmlein and E.D. Dukova	1	375	477
Crystallization from Solution			
Transformation Mechanism for Dendritic Crystals. M.O. Kliya	1	456	577
Effects of Ultrasound on the Growth of a Single Crystal of Potash Alum. A.P. Kapustin and V.E. Kavalyunaite	1	578	737
Crystallization from the Melt			
Some Aspects of the Crystallization of Diphenylamine. A.V. Shubnikov	1	295	374
Lecture Experiment for Demonstrating Rhythmic Growth in Salol Crystals. A.V. Shubnikov.	1	477	606
Etching of Crystals			
Production of Etch Figures by Means of Ultrasonic Vibrations. Kh.S. Bagdasarov and A.P. Kapustin	1	107	139
External Morphology			
Oriented Crystallization of Potassium Iodide and Bromide on Muscovite. I.E. Kamentsev	1	185	240
Crystals of Complex Compounds of Metals of the Platinum Group. Part 13. K.N. Baranskii, L.A. Gribov, and V.P. Prikhod'ko	1	280	361
Crystals of Complex Compounds of Metals of the Platinum Group. Part 14. É.E. Burovaya	1	284	365
Spiral Growth Layers on Barium Titanate Crystals. N.V. Gliki, I.A. Pleteneva, and V.A. Timofeeva	1	478	607
Spiral Structure of Accessory Growth on (0001) Surfaces of Artificial Quartz Crystals. L.I. Tsinober.	1	480	609
Internal Morphology			
Formation of Screw Dislocations in the Growth Process of a Crystal. G.G. Lemmlein and E.D. Dukova	1	269	351

	VOL.	PAGE	RUSS. PAGE
The Growing of Crystals			
Growth of Crystals of Ethylene Diamine Tartrate. P.G. Pozdnyakov	1	175	228
Preparation of Lithium Sulfate Crystals. P.G. Pozdnyakov	1	275	356
Preparation of Potassium Tartrate Crystals. P.G. Pozdnyakov	1	464	589
Apparatus for Studying the Growth of Crystals; Grinding, Cutting, and Other Shaping of Crystals			
Preparation of Small Spheres from Single Crystals. E. Sándor and P. Gado	1	571	729
ANNIVERSARIES			
German Stepanovich Zhdanov	1	301	379
OBITUARIES OF SCIENTISTS			
Pierre Curie	1	115	147
In Memory of A.K. Boldyrev. V.I. Mikheev, I.I. Shafranovskii, and A.V. Shubnikov	1	207	267
MISCELLANEOUS			
Measurement of Pressure in Explosions of Gaseous Mixtures by means of a Piezoelectric Gauge. I.S. Zheludev and V.M. Makarov	1	289	370
Ansheles's Comments on "A Traditional Error and the Many Ways in Which It Appears." A.V. Shubnikov	1	484	614
System for Modeling Crystal Structures and Patterns. N.V. Belov	1	574	733
Melting Point of Indium at Pressures up to 30,000 kg/cm^2. V.P. Butuzov and E.G. Ponyatovskii	1	577	736